

REPORT DOCUMENTATION PAGE

Public reporting burden for this collection of information is estimated to average 1 hour per response, including gathering and maintaining the data needed, and completing and reviewing the collection of information collection of information, including suggestions for reducing this burden to Washington Headquarters, Davis Highway, Suite 1204 Arlington, VA 22202-4302, and to the Office of Management and Budget.

AFRL-SR-BL-TR-00-

0611

1 sources.
t of this
Jefferson
13.

1. AGENCY USE ONLY (Leave blank)

2. REPORT DATE

28 Dec 98

3. REPORT NUMBER
F. Report 1 Sep 93 - 31 Aug 98

4. TITLE AND SUBTITLE

Regional Seismic Event Identification and Improved Locations with Small Arrays

5. FUNDING NUMBERS

Contract # F49620-93-1-0508

6. AUTHOR(S)

Jean-Bernard Minster

7. PERFORMING ORGANIZATION NAME(S) AND ADDRESS(ES)

The Regents of the University of California
Scripps Institution of Oceanography
IGPP 0225, 9500 Gilman Drive
La Jolla, California 92093-0225

8. PERFORMING ORGANIZATION
REPORT NUMBER

9. SPONSORING/MONITORING AGENCY NAME(S) AND ADDRESS(ES)

AFOSR/NM
110 Duncan Ave. Suite B115
Bolling AFB DC 20332-0001
Program Manager: Dr. Henry Radoski

10. SPONSORING /MONITORING
AGENCY REPORT NUMBER

11. SUPPLEMENTARY NOTES

12a. DISTRIBUTION/AVAILABILITY STATEMENT

Approved for public release, distribution unlimited

12b. DISTRIBUTION CODE

13. ABSTRACT (Maximum 200 words)

We isolated the effect of structure immediately beneath seismic stations on seismic waveforms by determining the inference of velocity discontinuities beneath a single broadband 3-component seismic station using receiver functions, in which the P-to-S converted phases generated beneath a seismic station are isolated by deconvolution of the horizontal component seismograms by the vertical. We improve the deconvolution itself by the development of a time domain inversion for the receiver function. We extend the technique's application to an area of complex structure, using data collected at Piñon Flat Observatory, California, where we improve understanding of the region's structure and tectonic framework. We then used near-receiver-scattered component of teleseismic code to calibrate site amplifications for the southern California seismic network. We also developed and applied appropriate statistical analysis tools to permit accurate estimation of the site amplifications from the doubly censored non-Gaussian data. The main purpose of estimating site amplifications has been to enable isolation of propagation effects on Lg amplitudes, which is important to understand for accurate monitoring of nuclear testing. We conclude with the application of the site amplifications to Lg of regional events, demonstrating that they are successful in isolating propagation from site effects on Lg amplitudes.

14. SUBJECT TERMS

15. NUMBER OF PAGES

191

16. PRICE CODE

17. SECURITY CLASSIFICATION

OF REPORT

unclassified

18. SECURITY CLASSIFICATION

OF THIS PAGE

unclassified

19. SECURITY CLASSIFICATION

OF ABSTRACT

unclassified

20. LIMITATION OF ABSTRACT

SAR

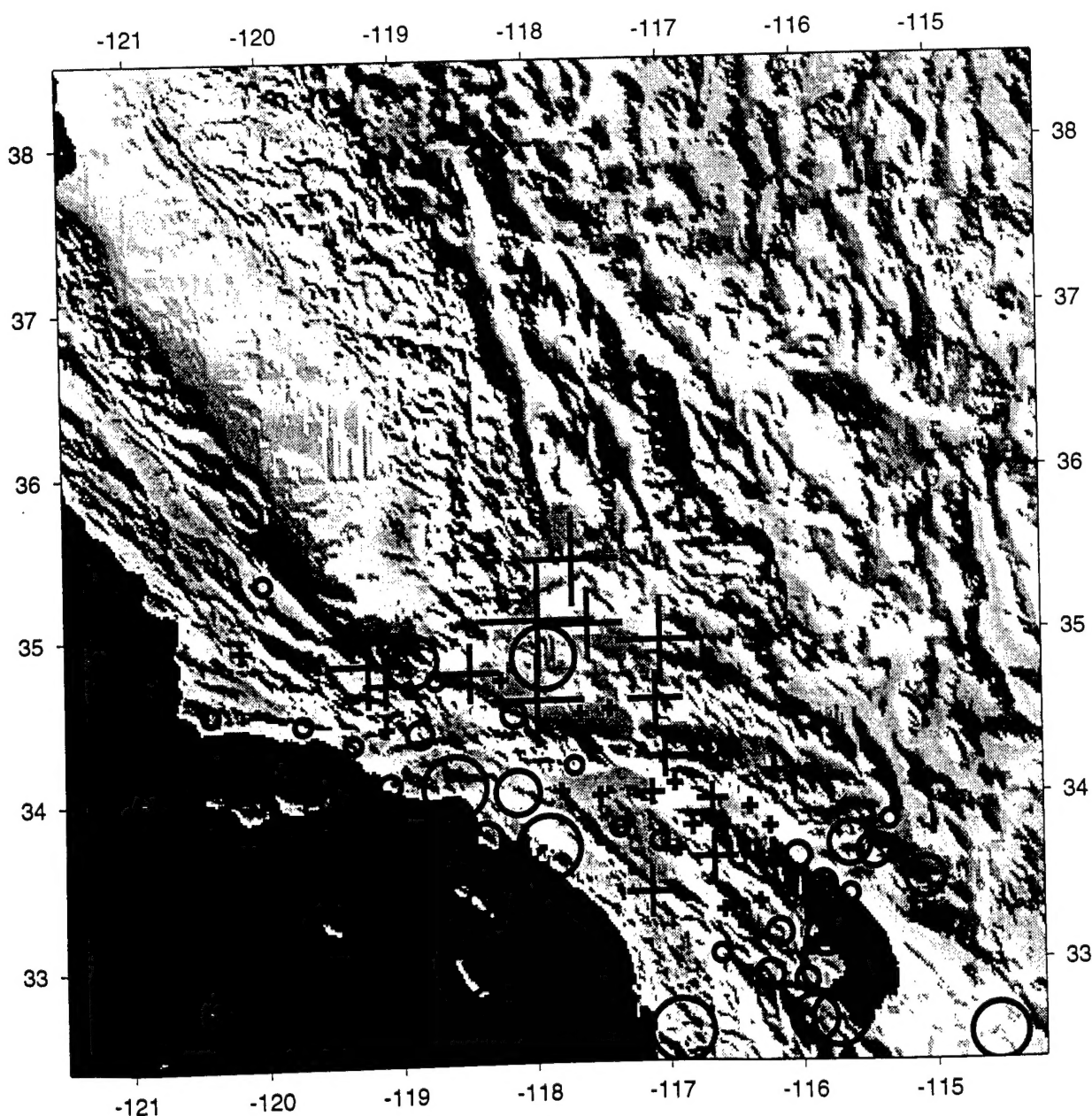
NSN 7540-01-280-5500

Standard Form 298 (Rev 2-89)
Prescribed by ANSI Std. Z39-18
298-102

The Effects of Near-Receiver Structure on Teleseismic and Regional Waveforms

by

Glenn Eli Baker



University of California, San Diego
Scripps Institution of Oceanography
1996

DTIC QUALITY INSPECTED 4

20001120 204

University of California, San Diego

The Effects of Near-Receiver Structure on Teleseismic and Regional Waveforms

A dissertation submitted in partial satisfaction of the
requirements for the degree Doctor of Philosophy
in Earth Sciences

by

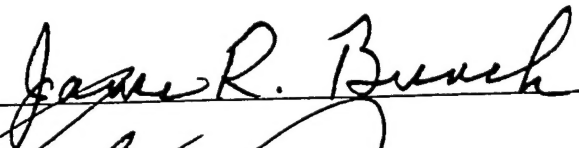
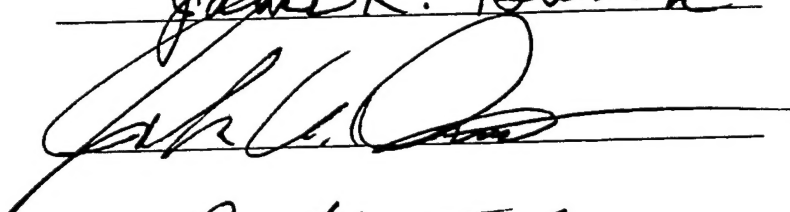

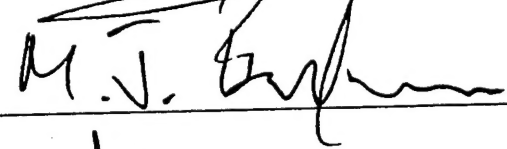
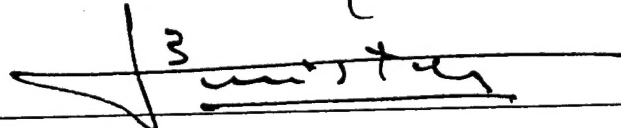
Glenn Eli Baker

Committee in charge:

Professor Jean-Bernard H. Minster
Professor T. Guy Masters
Professor John A. Orcutt
Professor Michael J. Buckingham
Professor James R. Bunch

1996

The dissertation of Glenn Eli Baker is approved, and it
is acceptable in quality and form for publication on
microfilm:





 Chair

University of California, San Diego

1996

Table of Contents

Signature Page	iii
Table of Contents	iv
List of Figures and Tables	ix
Acknowledgments	xxii
Vita	xxiv
Abstract	xxvii
 Chapter 1. Introduction to the Dissertation	 1
Goals and Research Accomplished	1
 Chapter 2. Constraints on crustal structure and complex Moho topography beneath Piñon Flat, California, from teleseismic receiver functions	 4
Abstract	4
Introduction	4
Tectonic and Geological Setting	6
Data	8
Forward Modeling	10
Complex Moho Topography near the San Jacinto Mt/Salton Trough Transition	15
Tangential Component Receiver Functions and Dipping Structure	30
Tectonic Implications	34
Crustal Low-Velocity Zone, Rheology or Lithology?	34
Moho Topography	36
Conclusions	39
References	41

Chapter 3. Uncertainty of Receiver Function Waveforms and Implications for Modeling	45
Abstract	45
Bootstrap Estimate of the Standard Deviation	48
Confidence Intervals on Velocity Jump Amplitudes	48
Amplitude Bias due to the Deconvolution	50
The Effect of Additive Noise	53
The Effects of Regularization on Receiver Function Waveforms	59
Averaging Functions - Preserving Absolute Amplitudes	62
Averaging Functions - Estimating the Effects of Deconvolution on the Waveform.....	64
Relationship Between Receiver Function Amplitude, Model Velocity, and Estimated Depths	66
Other Sources of Uncertainty	73
Error in Receiver Function Amplitudes due to Scattering along the Paths of Different Phases	73
Errors in Model Parameters due to Inappropriate Assumptions of Incidence or Backazimuth	75
Conclusions	76
References	79
Chapter 4. The Role of Seismology in Monitoring Nuclear Testing	81
Introduction	81
Errors in Regional Nuclear Discriminants due to Path Effects	82
The Importance of Fine Scale Observations	85
The Need for Site Amplifications	95
References	97

Chapter 5. Iterative Reweighting for Estimation of Magnitude and Site Amplifications from Doubly Censored and Corrupted Data	99
Abstract	99
Problems Addressed	97
The Problem of Site Amplification and Magnitude Estimation from SCSN Data	100
Robust Reweighting	103
Trade-offs between the Standard	
Least Squares and the Robust Solutions	108
The Effect of Robust Reweighting on Real Data	110
Incorporating Censored Data into Parameter Estimates: Previous Work in Magnitude Estimation	115
Derivation of the Likelihood Function	115
Maximizing the Likelihood Function by Iteratively Solving a Linearized Equation	118
The Practical Effects of Iterative	
Reweighting to Incorporate Censored Data	120
Conclusions	122
References	124
Appendix 5.1: Validity of <i>a priori</i> Weighting by Ratios of Signal to Pre-event Noise	125
Chapter 6. Diffuse Coda Site Amplifications in southern California and the Nature of Lg Waves	128
Abstract	128
Introduction	129
Motivation - Isolating Site Effects from Propagation Effects on Absolute Amplitudes	129
What Controls Site Amplifications?	131

What is Lg?	134
What is Diffuse Coda and is it an Isotropic Source of Lg-like Energy	137
Implications for a Study of Lg Propagation	139
Isolation of the Diffuse Component of Teleseismic Coda	141
How Sensitive are Site Amplifications to Differences Between Signal Parameters?	148
Sensitivity to Wavetype	148
Comparison of Site Amplifications from Diffuse Coda of Deep and Shallow Events	148
Comparison of Site Amplifications from Diffuse Coda and Local S-Wave Coda	152
Conclusions	157
References	159
Chapter 7. Conclusion to the Dissertation	162
Introduction	162
What we Learned that Indicated that Site Amplifications are Important	162
Application of Site Amplifications	165
Discussion of the Application of Site Amplifications and Future Work	177
Conclusions	181
References	183
Appendix A. Simultaneous Time-domain Deconvolution with application to the computation of receiver functions	184
Summary	184
Problems Noted with the Existing Deconvolution Method	184
Simultaneous Deconvolution	186
Examples	187

Conclusions	189
Acknowledgments	190
References	190

List of Figures and Tables

	page
Chapter 2	
Figure 2.1	5
<p>Shaded relief map of the area around PFO, CA. The San Jacinto and San Andreas faults are shown to the southwest and northeast of PFO respectively. Some smaller cross-faults near PFO, referred to in the text, are included (from Rogers, 1965). The circle about PFO is of 10 km radius. The sea level contour is indicated by a dashed line.</p>	
Figure 2.2	9
<p>Station-centered plot of 117 events at PFO by ray parameter and backazimuth. Circles, from the outermost inward, are at 0.08, 0.06, and 0.04 sec/km. Nearby events have been grouped according to ray parameter and backazimuth (the events in each group are encircled). The numbers correspond to the receiver functions in figure 8. Isolated events are used in the individual analyses discussed in the text.</p>	
Figure 2.3	11
<p>Receiver functions calculated for events binned by ray parameter only. The average distance in degrees for each set of events is to the left of each trace.</p>	
Figure 2.4	13
<p>Incremental development of a simple velocity model. On the right side, the receiver function from the steepest incidence angle group of figure 3 is plotted as a solid line and the synthetic receiver function corresponding to the velocity model shown to the left is plotted as a dashed line. Phases indicated in the synthetics are due to the newest feature of each successive model.</p>	
Figure 2.5	16
<p>Two velocity models which fit the data equally well based on forward modeling.</p>	
Figure 2.6	16
<p>Synthetic receiver functions for the simple (dotted) and modified (dashed) models compared to the data (solid). Comparisons are made for the steepest (bottom) and second steepest incidence (top) group receiver functions of figure 3.</p>	

Figure 2.7	18
Ray paths of converted and reverberated phases for horizontal and dipping interfaces. Note the difference in horizontal distance from the station sampled by similar phases updip relative to downdip.	
Figure 2.8	19
Receiver functions, low-pass filtered below 1 hertz, for the event groups pictured in figure 2, with group numbers of figure 2 above each trace. Average backazimuth and distance for each group is to the left of the traces. Note the variability of the Moho Ps-P time at about 4 seconds (downward arrow). Upward arrow indicates negative peak after Moho Ps.	
Figure 2.9	20
Moho Ps-P times for individual events, plotted on the same station centered plot as in figure 2. The distinctive pattern of longer times to the northwest and shorter times to the southeast in the data (top plot) is well matched by synthetics calculated for a 32 km deep 6.3 km/sec layer over a half space dipping 20 degrees to the northwest.	
Figure 2.10	21
Contour plot of the demeaned one norm of observed-minus-predicted Moho Ps-P times in seconds, for dipping planar layer over a half space models ranging over all strikes and dips up to 300 in 50 increments. The minimum is at 15 to 20 degrees northwest dip.	
Figure 2.11	22
Demeaned Moho Ps-P time residuals for a 6.3 km/sec 32 km deep layer over a half space dipping 20 degrees northwest (left). Points are plotted at the horizontal distance and backazimuth from the station that the Ps converted phase would be generated at the Moho and are scaled by the size of the residual. Note that for this model, all rays cross the Moho directly beneath or to the southeast of the station. The dashed line running 120 south of east indicates the position of one of the cross sections of figure 17. Demeaned Moho Ps-P time residuals relative to a 6.3 km/sec 30 km deep horizontal layer over a half space (right). Note not only the greater consistency in residual times for the dipping model, but what different areas of the Moho are sampled in each model.	
Figure 2.12	25
Moho Ps/P amplitude ratios for receiver functions of groups of figure 2, on the same station centered plot. Azimuthal variation observed in the data (left) is roughly matched by synthetics for the same 6.3 km/sec 32 km deep layer over a half space dipping 20 degrees northwest. Absolute values of the amplitudes are not important (see the discussion regarding uncertainty). Only relative amplitudes at different azimuths are used to infer dip direction. Plus symbols indicate reversed polarity of the Ps arrival.	

Figure 2.13	27
Normalized P waves (vertical recordings) of impulsive events from group 5 of figure 2 (top five traces), aligned by arrival time, and their stack (bottom trace).	
Figure 2.14	27
Stacks for the 4 groups containing impulsive events. PpPmp-P times are listed above the presumed PpPmp arrival of each trace. The position of each group is indicated, with the circle scaled by the residual relative to the flat-lying 6.3 km/sec 30 km deep layer over a half space of figure 11 (so as to account for the effect of variations in ray parameter between groups).	
Figure 2.15	29
Tangential component of mislocation vectors for initial P waves at PFO (top) and for a layer over a half space dipping 20 degrees towards S40W (bottom). Circles are at 100, 250, and 400 incidence. Predicted positions of the events are plotted as disks. Arrows point to the measured positions of the events. Eighteen of twenty one mislocation vectors in the northwest quadrant are pointing clockwise, with a mean of nearly 5 degrees, the southeast quadrant has a mean tangential mislocation of 2.5 degrees counterclockwise with sixteen of twenty one events consistent in direction, while the southwest quadrant mislocation vectors are much less consistent and have a mean of 1.5 degrees clockwise.	
Figure 2.16	32
Radial (solid line, upper trace) and tangential (solid line, second trace) receiver functions of group 5 (from figure 2), and their point-by-point product, indicating their coherence (solid line, lower trace). Synthetic receiver functions and their coherence (dashed lines) are shown below the data traces, for the refined model of figure 5 in which the shallowest discontinuity dips 150 southward. Vertical lines through the traces delineate the windows for which particle motion is plotted below (the upper row is the for the data and the lower row is for the synthetics).	
Figure 2.17	37
North-south (upper left) and nearly east-west (upper right) topographic cross-sections through PFO. The position of the second cross-section is indicated by a dashed line through the center of the circle in the left side of figure 11. PFO's position is indicated by the triangle. The lower plots indicate Moho depth for each cross-section inferred by assuming Airy isostasy with the depth of compensation at the Moho. The short horizontal bars are estimates of Moho depth based on receiver function	

each signal to noise level (the maximum signal peak to rms pre-event noise levels, S/N , are listed to the left of each set of traces). The receiver functions for 25 such synthetic seismograms (with different source functions and noise windows, but the same S/N levels), are shown on the right, with the mean and 2 standard deviations uncertainty listed for the P and Ps amplitudes and the Ps-P timing error of each set.

Figure 3.7	61
Comparison of a stack of 25, $S/N=10$, receiver functions (bottom right) with a synthetic receiver function for the same layer over a half space model after convolution with the averaging function (averaging function is upper left and convolution with synthetic is upper right). The sidelobes of the averaging function are very much smaller than those of the receiver function. A more accurate estimate of the effects of deconvolution on the receiver function is shown on the lower left (discussed in text).	
Figure 3.8	63
Eigenvectors of the ATA matrix (where A is the convolution matrix of the vertical seismograms) for the receiver function shown in figure 1. The smallest eigenvalues are associated with high frequency oscillations.	
Figure 3.9	68
a) Velocity model used for OBN data. b) Fit of the synthetic from the model in (a) (dashed line) to the OBN data (solid line).	
Figure 3.10	69
VSS for data recorded at OBN. Upper left, view in 3-space. Upper right, view in V_p -depth space. Lower left, view in V_s -depth space. Lower right, view in V_p - V_s space.	
Figure 3.11	72
a) The simple velocity model adopted for demonstration of the effects of moveout with ray parameter (solid line) and $\pm 10\%$ perturbations to that model (dashed lines). b) Receiver functions calculated for the models of figure 11a, for a ray parameter of 0.04. c) The same for a ray parameter of 0.06, and d) the same for a ray parameter of 0.08.	
Figure 3.12	74
a) The same velocity model of figure 11a (solid line), and a velocity model with 2% lower S-wave velocity than the dashed line model of figure 11a. b) Synthetic receiver functions for the velocity models of (a), showing no difference in arrival times.	
Figure 3.13	77
Receiver functions for the same layer over a half space model used for all synthetics in this paper. The solid line shows the ideal receiver function. The long and short dashed lines respectively show receiver functions for which	

the ray arrives with plus and minus 3 degrees difference in incidence angle from that expected. The P and Ps amplitudes for each are shown.

Chapter 4

Figure 4.1	84
Peak $\log(Lg/Pg)$ amplitude ratios for a subset of SCSN data, corrected to the WWSSN response. Earthquake records are plotted as crosses and explosion records are plotted as circles. The discrimination line separating earthquakes and explosions matches that found by Taylor et. al. (1986) for the western U.S. We will address whether the scatter and misidentification (i.e. symbols on the "wrong side" of the line) is due to identifiable propagation effects.	
Figure 4.2	86
Map of southern California seismic network stations (triangles) with regional earthquakes (asterisks) and explosions (circles) that are discussed in the chapter.	
Figure 4.3	87
Results of $\log(Lg/Pg)$ discrimination using southern California network recordings for 4 nuclear explosions. Crosses indicate identification of the source as an earthquake. Circles indicate identification as an explosion. Symbols are scaled by their distance from the discrimination level of figure 1. The smaller explosions, Floydada (1991, day 227, figure 3a) and Coso (1991, day 67, figure 3b), are misclassified more frequently than the larger explosions, Lubbock (1991, day 291, figure 3c) and Hoya (1991, day 257, figure 3d). The sampling is biased because of the limited dynamic range of the instruments, leading to clipped records at short distances for large events, and low signal to noise level records at long distances for small events.	
Figure 4.4	88
To examine possible geographic variation in the pattern of $\log(Lg/Pg)$ amplitudes, we standardize the distribution of each event's discriminant values (i.e. remove the mean and normalize so that one standard deviation equals 1.0). The result above is for Hoya (figure 3d). Here, symbol size is scaled by proximity to the mean, with crosses positive and circles negative. Note that the crosses appear to be in the same region in which misclassifications occurred for the smaller explosions.	
Figure 4.5	88
The normalization described in figure 4 was performed for 10 nuclear explosions. The mean for each station, for all the events it recorded, was then plotted above, revealing a distinct geographic pattern. Although we have ignored the possible effects of the bias in sampling (nearer stations recording more small events and more distant stations recording larger events), inspection of results for individual events suggests that the pattern is robust. That the pattern appears to be common to all events, whose sources	

span 50 km within NTS, argues against near source scattering strongly affecting the discriminant values.

- Figure 4.6 89
 Log(Lg/Pg) amplitude ratios for earthquake no. 4 ($M_b = 3.8$) of figure 2. As in figure 3, crosses are "earthquake-like" values scaled by distance above the discrimination line of figure 1, and circles represent "explosion-like" values scaled by distance below the line. For this shallow earthquake (~ 2 km depth), most (100 out of 150) recordings misclassify the event as an explosion. This serves as a warning that, even if we develop perfect path corrections, there will be anomalous events.
- Figure 4.7 89
 Normalized log(Lg/Pg) amplitude ratios, as in figure 4, for earthquake number 4 (figures 2 and 6). The relative pattern of large and small Lg to Pg amplitude ratios is quite similar to that observed for the nuclear explosions (figure 5), further indicating that neither source radiation or near source scattering is important to the pattern of Lg/Pg amplitude ratio variations.
- Figure 4.8 90
 Event classification as in figure 6, for earthquake no. 3 ($M_b = 4.4$) of figure 2. All of the stations at which the event is misclassified are clustered at the greatest distance from the source. Although this alone might suggest a potential distance, or near-receiver scattering, or receiver site effect, we find a very different pattern for earthquake no. 1 (figure 9).
- Figure 4.9 90
 Event classification as in figures 6 and 8 for earthquake no. 1 ($M_b = 4.2$) of figure 2. In contrast to figure 8, the distinct area of misclassifications is nearest the source, and at a completely different set of stations. Taken together, this figure and figure 8 indicate that neither distance, near-receiver scattering, or site effects control the pattern of relative Lg to Pg amplitudes in any simple way.
- Figure 4.10 91
 Event classification as in figures 6, 8, and 9, for earthquake no. 6 ($M_b = 4.2$) of figure 2. There are almost no misclassifications for this event. The two areas in which the smaller amplitude ratios cluster (in the center and at the northwest edge of the network), are distinct from the areas of smaller amplitude ratio for the events from different azimuths (figures 6, 8, and 9), strengthening the argument against any influence of distance, near-receiver scattering, or site effects.
- Figure 4.11 91
 Pn first motion polarity for earthquake number 1 (figures 2 and 9). Triangles indicate positive first motion, and circles, negative. If the source radiation controlled the pattern of Lg/Pg amplitude ratio variation observed, we might expect higher Lg/Pg amplitude ratios to be recorded along P-nodal lines. Here, the polarities suggest a possible P-nodal plane running roughly

northwest-southeast, correlating in no way with the amplitude ratio pattern observed.

Figure 4.12	92
Event classification as in figures 6, 8, 9, and 10, for earthquake no. 2. There were relatively fewer observations for this $M_b = 5.4$ event, due to clipping, than were available for the nearby earthquake no. 3 (figure 8), but the pattern of misclassifications is similar. We can compare this result to one predicted by the known source focal mechanism.	

Figure 4.13	92
Ratio of predicted S to P amplitudes radiated from the source of earthquake no. 2. The relative amplitudes have been normalized as in figure 4. The largest crosses are in the vicinity of the P node, just the opposite of the observed pattern, suggesting that at least at approximately 1 Hz and in that distance range, the focal mechanism has little effect on the observed L_g and P_g amplitudes.	

Chapter 5

Figure 5.1	106
Penalty functions (upper left) for misfit of least squares, L_1 -norm, and Hampel 17a solutions and their 1st and 2nd derivatives, i.e., influence functions (upper right) and the values for robust weights (lower left). Note that the L_1 -norm does not have a true influence function, as its robust weights would approach infinity near zero misfit. It is included here for comparison with the other solutions.	

Table 5.1	110
Differences in mean errors between the least squares (second and third columns) and robust (rightmost two columns) solutions to synthetic data with normal (top row) and exponential (second row) noise, and large outliers (bottom rows).	

Figure 5.2	112
Quantile-quantile plots for the misfits from the least squares (top), and robustly reweighted solution (bottom). If the misfits were normally distributed, the points would lie along the diagonal plotted. The large deviation of points from the diagonal, for the least squares misfits, beginning at approximately 2 standard deviations, indicates that the distribution of the misfits is much heavier-tailed than the normal distribution. The very large outliers most likely indicate outright blunders in the data.	

Figure 5.3	113
Plots of robust weights vs. event dates (top row) for two of the stations most affected by the robust reweighting, showing a distinct grouping of low weights within specific time periods. Pre-event noise levels vs. event dates (middle row) indicate that magnification was likely significantly lower than was recorded in instrument parameter logs for station SBK (left column)	

during that time period. The robust weights are plotted vs. the pre-event noise levels in the bottom row. The correlation is perfect for SBK, but more muddled for LUC (right column)

Table 5.2	122
Differences between site amplifications for the SCSN with and without incorporating censored data.	
Table 5A.1	127
Differences between unweighted and <i>a priori</i> weighted least squares site amplification estimates. The robust estimates are effectively the same whether we being with or without <i>a priori</i> weighting, and we see that the <i>a priori</i> weighted values are always closer to the presumably more accurate robustly weighted values.	
 Chapter 6	
Figure 6.1	130
Stations of the southern California seismic network for which site amplifications were calculated.	
Figure 6.2	132
Vertical amplification at a free surface for incoming P-waves (top) and S-waves (bottom) as a function of incidence angle.	
Figure 6.3	143
Map of teleseismic sources. Shallow source epicenters are indicated by circles, and deep source epicenters by inverted triangles. Symbols are scaled by magnitude.	
Figure 6.4	145
Correlation coefficients of the teleseismic coda from 21 to 61 seconds after the initial P arrival, for each pair of SCSN stations recording a deep event, vs. interstation spacing, before (top) and after beam removal (bottom). The m_b 6.5, 606 km deep event was 73° from southern California. The mean correlation coefficient was 0.055 before beam removal and 0.008 after, and the slope was virtually zero, indicating complete removal of the coherent coda.	
Figure 6.5	145
Correlation coefficients of the teleseismic coda from 20 to 45 seconds after the initial P arrival, for each pair of SCSN stations recording a shallow event, vs. interstation spacing, before (top) and after beam removal (bottom). The m_b 6.2, 10 km deep event was 51° from southern California. The mean correlation coefficient was 0.162 before beam removal and 0.006 after, and the slope was virtually zero, indicating complete removal of the coherent coda.	

Figure 6.6	147
Correlation coefficients of the teleseismic coda from 40 to 95 seconds after the initial P arrival, for each pair of SCSN stations recording a shallow event, vs. interstation spacing, before beam removal (top), and after beam removal (bottom). The Mb 6.5, 19 km deep event was 53° from southern California. The mean correlation coefficient was 0.431 before beam removal and -0.005 after. There is a significant increase in the correlation coefficients with decreasing interstation spacing, indicating incomplete removal of the coherent coda. The zero distance intercept was 0.052. In this case, the coda window chosen included the PcP arrival, which is usually, but not always, insignificant, and which may have been the source of the coherent coda, although PcP was not visible in a record section. Some other shallow events had even more coherent coda, with no apparent cause. Those events usually were less distant than the average.	
Figure 6.7	149
Record section for the shallow event with the largest percentage of coherent coda. The event was reported to be at 17 km depth, and we see the depth phases pP and sP as predicted for that depth, at approximately 6 and 8 seconds after the initial P arrival. Some energy is also visible at 18 seconds after P, the time predicted for PcP. The coda window used was from 25 to 80 seconds after the initial P arrival, where no major phases were predicted to arrive. However, there is a very large coherent phase with similar moveout to the initial arrival, at about 45 seconds after the initial arrival.	
Figure 6.8	150
Record section for the diffuse coda of the event of figure 7. With the beam removed from each individual trace, the coherent phases that were prominent in the time window used for calibration in figure 7 are no longer apparent.	
Figure 6.9	151
Correlation coefficients of the teleseismic coda from 25 to 80 seconds after the initial P arrival, for each pair of SCSN stations recording the shallow event of figure 7. The increase in correlation coefficient with decreasing station spacing indicates that not all of the steeply incident P-wave energy was coherent. After beam removal, the zero distance intercept was 0.056. The large decrease however, in the mean value, from 0.434 before beam removal to -0.002 after, indicates that most of the coherent coda energy was removed.	
Figure 6.10	153
Comparison of diffuse coda site amplifications calculated from just the coda of the 20 deep events and those calculated from just the coda of the 20 shallow events. The vertical lines represent 2 standard deviations uncertainty about the deep event coda site amplifications, and the horizontal lines represent the same for the shallow event coda site amplifications.	

Figure 6.11	155
<p>Comparison of diffuse coda site amplifications versus 1.5 Hz local S-wave coda site amplifications of Su and Aki (1995) for sites with amplifications less than 3.0 (upper left). The coefficient of determination is measure of how meaningful it is to relate two variables by a sloping line (i.e. $Y=aX+b$). Specifically, the coefficient of determination, r^2, is given by $r^2=1-SSE/SST$, where the sum of the squared error, $SSE = \sum y_i^2 - b\sum y_i - a\sum x_i y_i$, is a measure of how much variation is left unexplained by the model, and the total squared error, $SST = \sum y_i^2 - (\sum y_i)^2/n$, is a measure of the total amount of variation in the observed values of the dependent variable. Thus SSE/SST is the proportion of the total variation that is not predicted by the linear model, and r^2 is the proportion of variation in the dependent variable that is predicted by the linear model. The correlation between the local S-wave coda amplifications at 1.5 Hz and the diffuse coda amplifications is about as good as between the local S-wave coda amplifications at 1.5 Hz and at 3 Hz (upper right). The correlation is much poorer for larger differences in frequency at the same site (lower plots).</p>	
Figure 6.12	156
<p>Comparison of diffuse coda site amplifications versus local 1.5 Hz S-wave coda site amplifications of Su and Aki (1995) for all amplifications (upper left). The linear relationship seen in figure 9 breaks down for the highest amplification sites, with approximately 5 times higher amplification estimated from the 1.5 Hz local S-wave coda than from the diffuse coda. The local S-wave coda site amplifications are also much greater at 1.5 and 3 Hz (upper right), than at 6 and 12 Hz (lower plots).</p>	
Chapter 7	
Figure 7.1	167
<p>Log(Lg/Pg) amplitude ratios recorded at SCSN stations for event number one of figure 4.2. The values are demeaned, with values greater than the mean plotted as crosses and those less than the mean plotted as circles. Symbols are scaled by distance from the mean. Arrows indicate the propagation direction.</p>	
Figure 7.2	168
<p>Lg amplitudes, after correction for site amplifications, for event one.</p>	
Figure 7.3	169
<p>Pg amplitudes, after correction for site amplifications, for event one.</p>	
Figure 7.4	171
<p>Log(Lg/Pg) amplitude ratios for event number three of figure 4.2</p>	

Figure 7.5	172
Lg amplitudes, after correction for site amplifications, for event three.	
Figure 7.6	173
Pg amplitudes, after correction for site amplifications, for event three.	
Figure 7.7	174
Log(Lg/Pg) amplitude ratios for a nuclear explosion at NTS.	
Figure 7.8	175
Lg amplitudes, after correction for site amplifications, for the NTS event.	
Figure 7.9	176
Pg amplitudes, after correction for site amplifications, for the NTS event.	
Figure 7.10	178
Log(Lg/Pg) amplitude ratios for event number six of figure 4.2.	
Figure 7.11	179
Lg amplitudes, after correction for site amplifications, for event six.	
Figure 7.12	180
Pg amplitudes, after correction for site amplifications, for event six.	
 Appendix A	
Figure 1	185
The top panel shows receiver functions computed by frequency-domain deconvolution of 14 events at Arti, Russia (ARU). The middle panel shows the stack of these 14 receiver functions and the traces representing \pm two standard deviations of the mean. The bottom panel shows the receiver function computed using simultaneous time-domain deconvolution of the same 14 events and the traces representing \pm two standard deviations of the mean.	
Figure 2	187
Misfit versus model-norm size for various Lagrange multipliers (μ) applied to the simultaneous deconvolution to compute the receiver function shown on the bottom of Fig. 1. The misfit is defined as the rms difference between the observed radial component of the seismograms and those predicted by a reconvolution of the receiver function with the vertical component. The model-norm size for this example is defined as the rms sum of all the components of the receiver function. To compute the receiver function shown on the bottom panel of Fig. 1 we used $\mu = 10^2$.	
Table 1	187
Velocity model used to generate the synthetic seismograms.	

- Figure 3 188
The uppermost 'idealized receiver function' was produced by deconvolution of noise-free synthetic seismograms (assuming a delta-function source). The bottom and middle receiver functions were computed by simultaneous deconvolution of five and 25 synthetic seismograms (described in the text) respectively. The numbers plotted above each of the receiver functions, on this as well as all the following figures, are the rms misfits between all of the observed horizontal components of the seismograms and the convolution products of the receiver function and the respective vertical components. The seismograms were weighted for the rms misfit calculation just as they were for the deconvolution.
- Figure 4 188
The uppermost 'idealized receiver function' was produced by deconvolution of noise-free synthetic seismograms (assuming a delta-function source). The second and third receiver functions from the top were computed by stacking 25 and five receiver functions (respectively), each computed by single-event frequency-domain deconvolution of the same synthetic seismograms as used to produce Fig. 2. The bottom receiver function was computed by the frequency-domain deconvolution of the uncut vertical components (see text) from the respective 25 horizontal components followed by stacking.
- Figure 5 188
(Top) receiver function produced by simultaneous time-domain deconvolution of 25 events recorded at PFO. (Bottom) receiver function was computed by stacking 25 receiver functions computed individually from the same recordings by spectral division. Each of these traces was normalized by their peak amplitude.
- Figure 6 189
Receiver functions computed by simultaneous lower-bounded deconvolution of the 25 synthetic seismograms used in computing Figs. 3 and 4. The top receiver function has a lower bound of zero. The lower-bound constraint decreases from top to bottom. The bottom receiver function has no lower-bound constraint. Numbers above the traces are the rms misfits.
- Figure 7 190
Receiver functions computed by simultaneous lower-bounded deconvolution of the 25 synthetic seismograms used in computing Fig. 5. The top receiver function has a lower bound of zero. The lower-bound constraint decreases from top to bottom. The bottom receiver function has no lower bound constraint. Numbers above the traces are the rms misfits.

Acknowledgments

The generous contribution of time and energy by many people has helped me reach the point of finishing my Ph.D. in seismology.

At IGPP, it began with the dedication of the faculty to teaching the first year classes. Guy Masters had more well thought out, useful, and challenging homework assignments than I had ever been presented with. George Backus, Guy Masters, John Orcutt, and Bob Parker all provided clear and comprehensive class notes for the material they covered. All that effort to provide the students with a solid basis in geophysics is thoroughly appreciated. During that first year, Jon Berger provided my support without asking for any work in return, but only asking that I learn as much as I could from the classes. Holly Given regularly went out of her way to ease my transition into doing seismology here, introducing me to the available software and to broadband data.

Much of my basic understanding of the field has been learned from my fellow students. I spent long days and nights working out problems, often with Joydeep Bhattacharyya. When we got stuck, we could always count on older students, especially Rudy Widmer, to clear up our confusion. When I started doing research full time, my first project was joint with Harold Gurrola, whose refreshingly unpretentious perspective on the work we were doing was thoroughly appreciated. I was especially lucky to share an office for a couple of years with Jeff Hanson, who regularly asked me fundamental seismology questions. As I was invariably unable to answer them, Jeff would start examining them at a very basic level, figure out the answers, and explain them to me. He was also willing to do that with any question I had, whether it was fundamental, or a particular problem I was having in my research. Hadley Johnson helped me many times to overcome data analysis problems, especially

helping me bridge the gap between theory and practicality. Greg Anderson read chapters 6 and 7 of my thesis with remarkable thoroughness. My wife, Irina Gorodnitsky, helped me in many ways throughout graduate school. She provided advice on mathematical problems all along, and her proof-reading of chapter 5 made its presentation much clearer.

Both IGPP faculty and visitors to Scripps also greatly influenced my work. Larry Burdick got me started looking at regional phases. Vernon Cormier spent days patiently explaining the details of ray synthetic seismograms, which helped me to understand both their utility and limitations. Steve Day helped me solve a number of specific problems, always somehow making it seem like I was doing him a favor. Steve also was a patient and thoughtful sounding board when I needed perspective on the direction my research was taking. George Zandt helped me greatly with the receiver function work; asking difficult questions, picking out the weakest points of my work, and then helping answer the questions, so making the work stronger. My understanding of Lg propagation was significantly increased through a series of discussions with Greg Wagner. Guy Masters spent a great deal of time and energy listening to whatever I was stuck on, thinking it through, and coming up with good suggestions. Bernard Minster had the unenviable task of reading everything I wrote. His efforts have made the presentation of this work clearer, more concise, and more comprehensible. Bernard's criticism of the work also made it much stronger than it would otherwise have been.

Chris Garrod, Paul Rasmussen, Hal Skelly, and Nadya Williams have all helped me with computer problems. Katrin Hafner's help in obtaining SCSN data was invaluable, as was Lisa Wald's help in determining SCSN instrument responses.

Vita

December 12, 1956 - Born - Quincy, Florida

- | | |
|------|--|
| 1979 | B.Sc., Geology, University of Washington, Seattle, Washington |
| 1985 | M.Sc., Geophysics, University of Washington, Seattle, Washington |
| 1996 | Ph.D., Earth Sciences, UCSD, San Diego, California |

Publications

Peer Review Journal Articles

- Baker, G.E., and J.B. Minster (1996), Iterative reweighting for estimation of site amplifications and event magnitudes from doubly censored and corrupted data, *submitted to Geophys Jour Intl*
- Baker, G.E., J.B. Minster, G. Zandt, and H.G. Gurrola (1996), Constraints on crustal structure and complex Moho topography beneath Piñon Flat, California, from teleseismic receiver functions, *Bull. Seism. Soc. Am.*, *in press*
- Baker, G.E., H.G. Gurrola, J.B. Minster, and G. Zandt (1996), Uncertainty of receiver function waveforms and implications for modeling, *Bull. Seism. Soc. Am.*, accepted with revisions
- Gurrola, H.G., G.E. Baker, and J.B. Minster (1995), Simultaneous time-domain deconvolution with application to receiver functions, *Geophys. J. Intl.*, **120**, 537-543
- C. Weaver and G.E. Baker, (1988), Geometry of the Juan de Fuca Plate beneath Washington and northern Oregon from seismicity, *Bull. Seism. Soc. Am.* **78**, 264-275
- Baker, G.E. and C. A. Langston (1987), Source parameters of the 1949 magnitude 7.1 south Puget Sound, Washington, earthquake as determined from long-period body waves and strong ground motions, *Bull. Seism. Soc. Am.* **77**, 1530-1557

Conference Proceedings Articles

- Baker, G.E. and, J.B. Minster (1996), Quantifying the attenuation and blockage of Lg and robust statistical estimates of site amplifications at SCSN stations, *Proceedings 18th Annual Seismic Research Symposium*, DARPA
- Baker, G.E. and, J.B. Minster (1995), Lg site amplification calibration for isolation of Lg propagation effects, *Proceedings 17th Annual Seismic Research Symposium*, DARPA
- Baker, G.E., V. Cormier., and J.B. Minster (1994), Effects on Pn, Pg, and Lg Amplitudes of Nuclear Explosion Waveforms Recorded in Southern California, *Proceedings 16th Annual Seismic Research Symposium*, DARPA
- Baker, G.E., L.J. Burdick, and J.B. Minster (1993), Regional broadband waveforms: individual station and three component array analysis of nuclear explosion sources crossing a southern California path, *Proceedings 15th Annual Seismic Research Symposium*, DARPA, 8-14

Abstracts

- Baker, G. E., H.G. Gurrola, and J.B. Minster (1996), Iterative reweighting for estimation of site amplifications from doubly censored and corrupted data: Results for the southern California seismic network, *EOS, Trans. AGU*, **77**
- Gurrola, H.G., G.E. Baker, and J.B. Minster (1996), Resolution of receiver function waveforms and resulting limitations in the modeling of Earth structure, *EOS, Trans. AGU*, **77**
- Baker, G. E., and J.B. Minster (1995), Site amplifications at southern California network stations, estimated from near-receiver scattered teleseismic coda., *EOS, Trans. AGU*, **76**, p. 365
- Baker, G. E., and J.B. Minster (1995), Effects of laterally varying structure on the performance of regional body-wave based discriminants, *NATO Advanced Study Institute on Monitoring a Comprehensive Test Ban Treaty*, Algarve, Portugal
- Baker, G. E., J.B. Minster, and V. Cormier (1994), Variations in Pn, Pg, and Lg amplitudes in Southern California, *EOS, Trans. AGU*, **75**, p. 483
- Baker, G. E., and J.B. Minster (1993), Analyses of broadband station, short period network, and 3-component array recordings of NTS nuclear explosions, *EOS, Trans. AGU*, **74**, p. 424
- Baker, G. E., G. Zandt, and J.B. Minster (1992), Crust and upper mantle structure beneath Piñon Flat, CA from receiver functions and PmP, Sp, and Pn observations. *EOS, Trans. AGU*, **73**, p. 198
- Baker, G. E., H.G. Gurrola, and J.B. Minster (1992), New receiver function techniques and application to the IRIS/IDA station at Piñon Flat Observatory (PFO), *Frontiers of Broad Band Seismology*, U.C. Berkeley
- Baker, G. E., H.G. Gurrola, and J.B. Minster (1990), Crustal structure at Piñon Flat Observatory from receiver functions, *EOS, Trans. AGU*, **71**, p. 1437
- Baker, G. E. (1984), A long period focal mechanism for the magnitude 7.1 South Puget Sound, Washington event of April 13, 1949, *EOS, Trans. AGU*, **65**, p. 986

Abstract of the Dissertation

The Effects of Near-Receiver Structure on Teleseismic and Regional Waveforms

by

Glenn Eli Baker

Doctor of Philosophy in Earth Sciences

University of California, San Diego, 1996

Professor Jean-Bernard Minster, Chairman

The two distinct parts to this dissertation deal with isolating the effect of structure immediately beneath seismic stations on seismic waveforms. The first part deals with the inference of velocity discontinuities beneath a single broadband 3-component seismic station using receiver functions, in which the P-to-S converted phases generated beneath a seismic station are isolated by deconvolution of the horizontal component seismograms by the vertical.

We improve the deconvolution itself by the development of a time domain inversion for the receiver function. We extend the technique's application to an area of complex structure, using data collected at Piñon Flat Observatory, California, where we improve understanding of the region's structure and tectonic framework. We are able to make inferences about complex Moho topography and corroborate them using observations of P-PmP differential times, and P-wave polarizations. We also analyze the uncertainties in receiver function waveforms using both synthetic and

real data, demonstrating that regularized deconvolution of noisy seismograms significantly biases receiver function amplitudes.

The second part of the dissertation deals with the effect of near receiver velocity structure on seismic wave amplitudes. We use the near-receiver-scattered component of teleseismic coda to calibrate site amplifications for the southern California seismic network. This required the development of a technique to separate the near-receiver-scattered component of teleseismic coda from the near-source-scattered component. We also developed and applied appropriate statistical analysis tools to permit accurate estimation of the site amplifications from the doubly censored non-Gaussian data. Specifically, we use maximum likelihood estimation to incorporate censored data, and the robust statistical technique of iteratively reweighting the inversion based on the misfit to reduce biasing of parameter estimates by outliers.

The main purpose of estimating site amplifications has been to enable isolation of propagation effects on Lg amplitudes, which is important to understand for accurate monitoring of nuclear testing. We conclude with the application of the site amplifications to Lg of regional events, demonstrating that they are successful in isolating propagation from site effects on Lg amplitudes.

Chapter 1

Introduction to the dissertation

Goals and Research Accomplished

A seismogram contains information about the source of the energy and the structure of the Earth between the source and the receiver. Increased understanding of seismic sources and earth structure is gained by studies designed to isolate information from just the source or from just one small portion of the path. There are two distinct parts to this thesis, both of which are designed to isolate the effect of structure immediately beneath the station at which seismograms are recorded. A significant portion of the work in both parts involves the development of processing and analysis tools, a useful end in itself.

The first part of the thesis deals with the inference of velocity structure beneath a single broadband 3-component seismic station by receiver function analysis. Complexity in teleseismic P waveforms due to the source and to path effects distant from the station are exclusively associated with P-wave energy, due to the much slower propagation velocity, and so later arrival, of S-waves. The P-waves are recorded well on both vertical and horizontal seismograms. The only shear waves in the early part of teleseismic records must have been generated by P-to-S conversion just beneath the station, and are recorded effectively only on the horizontal components. The receiver functions are computed by the deconvolution of the horizontal seismograms by the corresponding vertical seismogram. This removes the source and distant path complexity from the records, leaving a time series that represents the P-to-S converted phases generated beneath a recording station. The receiver function is then interpreted in terms of velocity structure beneath the station.

Our initial contribution to this area is the improvement of the deconvolution itself, by the development of a time domain inversion for the receiver function, discussed in appendix 1. The application of the technique to an area of complex 3-dimensional structure has had two important

results, described in chapter 2. We extended the technique's application to areas of complex structure, especially to making inferences about complex Moho topography, by incorporating other observations of the same teleseismic body waves, such as P-PmP differential times, and P-wave polarizations. We also improved understanding of the region's structure and tectonic framework through the consideration of our observations in light of other pertinent geophysical studies in the region. In chapter 3, we provide a very thorough analysis of the uncertainties in receiver function waveforms. Until now, studies of uncertainty in receiver function analysis have used only noise free synthetics, and uncertainty bounds have been invariably underestimated by consideration of only statistical error. We analyze the effect of noise on receiver function waveforms, using both synthetic and real data, and demonstrate that regularized deconvolution of noisy seismograms significantly biases receiver function amplitudes. We also examine common, yet heretofore overlooked sources of error in receiver function interpretation due to errors in commonly made physical assumptions.

The second part of the thesis also deals with the isolation of the effects of near receiver velocity structure on seismic signals, but for regional data at higher frequency. Whereas part one was driven largely by the desire to understand the earth better, this part of the thesis also has an immediate and quite important practical application. That is, understanding regional propagation is important to the verification of a global nuclear test ban treaty, which is discussed in chapter 4. We focus largely on understanding variations in amplitude of the Lg phase, so that we can predict them elsewhere. Lg is largely composed of shear-wave energy traveling in the crustal waveguide, or equivalently higher mode surface waves, and figures prominently in many regional seismic discriminants. The problem is complicated, and the work presented here lays the foundation for answering some fundamental questions. The basic scientific goal is to understand better the physics of blockage and attenuation of Lg, which can occur over just 15 to 20 km of propagation. The long term practical goal of the work is to enable prediction of variations in regional phases important to discrimination. Ideally, such prediction would be based on other globally available geophysical parameters, such as topography and gravity, from which crustal thickness may be inferred.

Improved understanding of Lg propagation has been held back by two limitations in the data available. One is that Lg amplitude varies dramatically over very short length scales along paths traversing various types of structure, but dense spatial coverage along a variety of structures is rarely available. That limitation is overcome by using data from the southern California seismic network (SCSN) which consists of hundreds of stations over a large area of tremendously variable velocity structure. The second limitation is that site amplifications are rarely known at any recording sites, so it is impossible to compare absolute amplitudes of seismic energy from one station to the next and attribute the difference to path effects between the sites. Much of the rest of the thesis deals with overcoming this limitation. So although the purpose of this work is to understand regional propagation by isolating the effects of short path segments on amplitudes of specific phases, it is necessary to first isolate and quantify the effect of the site structure.

The near-receiver-scattered component of teleseismic coda is used to calibrate site amplifications. The data are doubly censored, and contain significant large errors and non-Gaussian noise, so it is necessary to first develop appropriate statistical analysis tools, which we discuss in chapter 5. In chapter 6 we present the development, application, and testing of a technique to separate the near-receiver-scattered component of teleseismic coda from the near-source-scattered component. We then examine the suitability of near-receiver-scattered coda as an isotropic source of Lg-like energy.. Finally, in Chapter 7 we demonstrate an application of the site amplifications to Lg of regional events, and discuss the continuation of this work.

Chapter 2

Constraints on crustal structure and complex Moho topography beneath Piñon Flat, California, from teleseismic receiver functions

Abstract

We use teleseismic P-waves recorded at Piñon Flat Observatory (PFO) to constrain the 3-dimensional crustal and upper-mantle velocity structure beneath the station. By forward modeling radial receiver function waveforms we construct a 1-dimensional crustal model which includes a significant shear-velocity inversion at 9 km depth. Arrivals on the tangential components indicate dip of at least the uppermost discontinuity. Complicated Moho topography, deepening to the northwest of PFO, is suggested by azimuthal dependence of travel-times and amplitudes of the receiver functions and travel times of crustal P-wave reverberations. Although fine details cannot be resolved, each of those sets of observations plus mislocation vectors provide strong indications of abrupt Moho topography, possibly including step offsets of several kilometers. This is not only consistent with gravity data in implying Airy isostasy with compensation at Moho depth, but extends that model to a much finer length scale than had been resolved.

Introduction

Piñon Flat Observatory (PFO) is located in the tectonically active, structurally complex transitional area between the high elevation San Jacinto Mountains and the below sea-level Salton Trough (figure 1). The trough, characterized by high heat flow and thin crust associated with active rifting (e.g., Elders et al, 1972; Fuis et al., 1984), is the northern continental extent of the spreading center extending throughout the Gulf of California. PFO, at 1288 m elevation on the southeast edge of the San Jacinto massif, is 30 km southeast of the 3302 m San Jacinto Peak, and 10 km southwest of the near sea level edge of the trough.

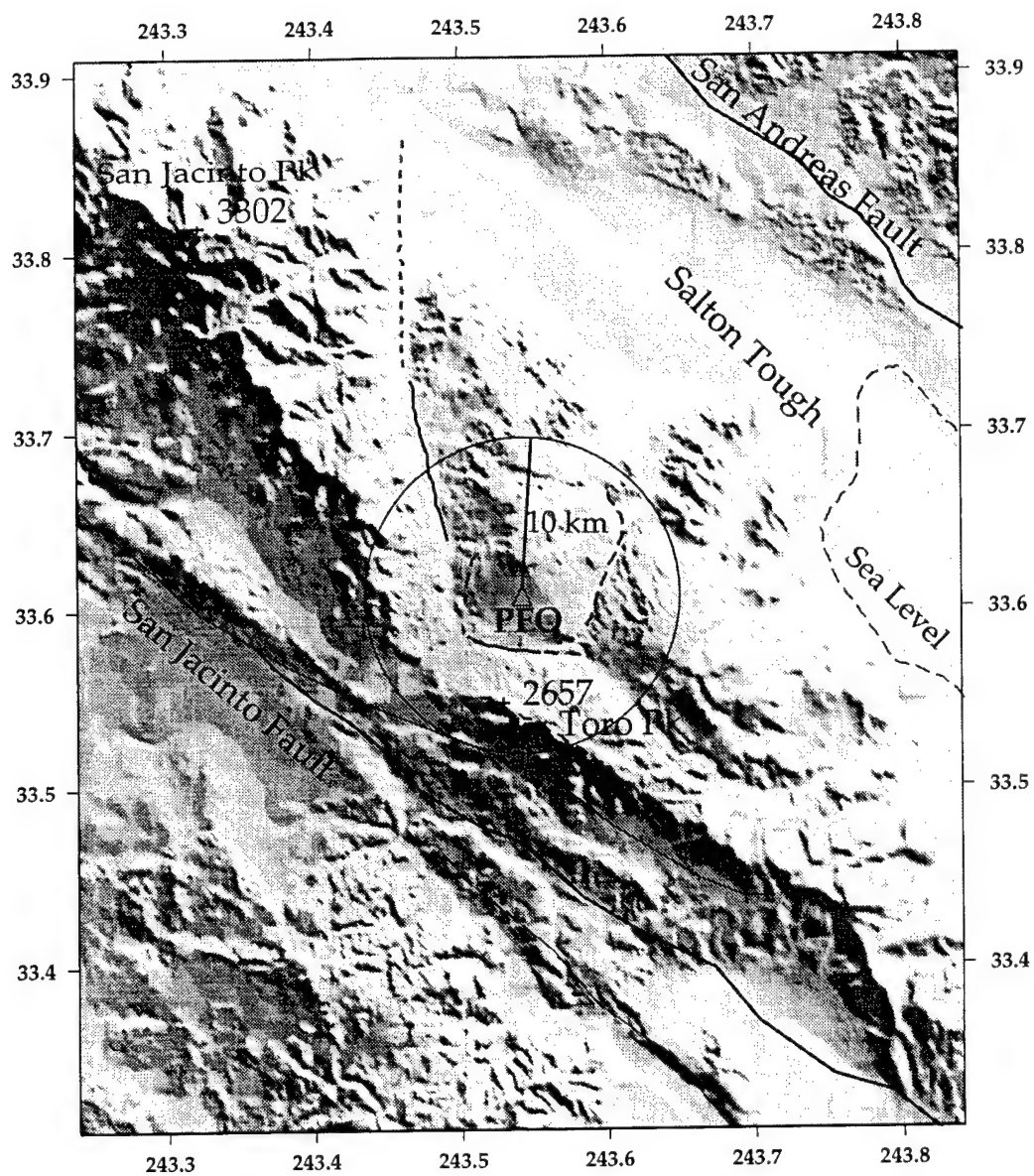


Figure 2.1: Shaded relief map of the area around PFO, CA. The San Jacinto and San Andreas faults are shown to the southwest and northeast of PFO respectively. Some smaller cross-faults near PFO, referred to in the text, are included (from Rogers, 1965). The circle about PFO is of 10 km radius. The sea level contour is indicated by a dashed line.

Resting on a broad flat area of the Mesozoic granitic rock that forms the bulk of the Peninsular Ranges, PFO is surrounded by fault-controlled contacts with older metamorphic rocks (Rogers, 1965) and is located between the San Jacinto fault zone 12 km to the southeast and the San Andreas fault zone 25 km to the northwest. Teleseismic waves of events arriving at this single broad-band station from a range of azimuths sample the varying crust and upper mantle of this complex region. We find that with data from a range of azimuths, the information in receiver functions can provide strong constraints on the structure of such a complex region.

Tectonic and Geological Setting

We review briefly the area's geology, from the surface downward. Granitic bedrock overlain by a thin layer of weathered granite forms the surface at PFO. Near surface P and S velocities of 5.4 and 3.0 km/sec respectively were obtained at this site from a 300 meter deep borehole log (Fletcher, et al., 1990). The base of the granitic portion of the batholith is estimated, based on aeromagnetic data, to be at 10 to 12 km depth (Jachens, 1991). A travel time tomography study over a local network, with its easternmost station at PFO, finds simple, smoothly varying velocity structure with no need for velocity inversions or changes in the Poisson ratio (Scott, 1992, Scott et al., 1994). Its best resolution is between 9 and 16 km depth, where the P/S velocity ratio averages 1.71, significantly less than the surface value of 1.8.

A pervasive zone of low resistivity with its top at 10 km depth was imaged by a magnetotelluric traverse of the southern Peninsular range, passing about 90 kilometers south of PFO (Park et al., 1992). It is attributed to saline fluids trapped in their upward migration at an impermeable boundary.

Gravity data (Jachens and Griscom, 1985) indicate that the region is roughly in isostatic equilibrium for an Airy model. For compensation at the Moho, Moho topography would roughly mirror surface topography multiplied by some scale factor. That and the region's precipitous surface topography (figure 1), predict extreme Moho topography. For example, for such isostasy to hold, San Jacinto Peak, 30 km northwest of PFO would require a crustal root 9 km thicker than that beneath PFO (equivalent to a 17°

Moho dip). That seems to present a contradiction with an apparently strong elastic crust. Seismicity of magnitude greater than 2 on the San Jacinto and San Andreas Faults near PFO, to depths of 20 and 22 km respectively (Sanders, 1990), suggests that the lithosphere has some strength to at least those depths. The flexural rigidity of 20 km thick, unbroken elastic lithosphere should virtually fully support topography that is much less than 1000 km wavelength (e.g., Turcotte and Schubert, 1982), and so San Jacinto Peak should be supported flexurally. To understand this apparent contradiction requires consideration of the region's tectonic history.

PFO is located within the eastern margin of the Cenozoic Great Basin extension, where much of the extension, occurring between 6 and 13 m.y. ago (Ekren et al., 1968, Anderson et al., 1972, Eberly and Stanley, 1978) was concentrated (Proffett, 1977). It is also near the San Andreas fault, which formed between 5.5 and 7 million years ago, when the transform boundary between the Pacific Plate and the North American Plate "jumped" inland, to meet the north end of the spreading Gulf of California (Atwater, 1970, Curran and Moore, 1984). The transform boundary may have even jumped to its present position due to the weakness of the lithosphere there relative to that at its previous position outside the range of extension. There is general agreement that prior to the uplift of the Peninsular Ranges there was a flexurally repressed crustal root (e.g., O'Connor and Chase, 1989). Uplift may have been initiated when the San Andreas fault shifted to its current position, fracturing the crust and releasing the restrained buoyancy forces (O'Connor and Chase, 1989), or earlier during the late Cenozoic extension, (Dokka and Merriam, 1982; Stock and Hodges, 1990). Regardless of timing, initiation of uplift depended on the crust being fractured throughout its elastic portion, permitting offsets at the Moho. The stress regime at that time, that permitted isostatic balance to be reached, was not necessarily the same as today's.

We have mentioned a simple model of Airy isostasy with compensation at the Moho, which is not necessarily the only possible explanation for the gravity data. Pratt isostasy may be indicated by variations in upper mantle velocities (e.g., Hearn and Clayton, 1986, Sung and Jackson, 1992), although those heterogeneities were observed on much greater scale lengths than considered here. High density crustal

basement, suggested for the southern Salton trough based on gravity data (Fuis et al., 1984), is another possible alternate explanation.

Deeper structure was probed by a refraction experiment (Benz and McCarthy, 1994), from which was inferred an upper mantle LVZ at 40 to 55 km depth throughout the Basin and Range - Colorado Plateau transition. Walck (1984) used array mislocations to infer the existence of an east-west trending antiform with axial depth of 100 km, 70 km north of PFO.

Data

We have analyzed 117 high signal-to-noise ratio recordings of teleseismic P-waves recorded at PFO over a thirty month period. These events are well distributed in azimuth and distance (figure 2). We analyzed these data using the receiver function technique (e.g. Langston, 1979; Owens et al., 1984). For horizontally layered structure, receiver functions are ideally a series of spikes in which each arrival represents a P-to-S converted phase or some multiply reflected phase beneath the receiver that ends in an S-wave leg. In the case of dipping interfaces, receiver function arrivals may also represent P multiples. The receiver functions are estimated by deconvolution of the radial and transverse components of the seismogram by the vertical. The advantage of using receiver functions instead of original seismograms is that source and path complexities, which are present in all components of the seismograms, are in principle removed by the deconvolution, isolating the local earth response in the receiver functions. From receiver functions, the existence of discontinuities beneath a station, and their approximate depths and velocity contrasts may be inferred. The receiver functions used here for waveform modeling and analysis of Moho topography were calculated using a simultaneous time domain deconvolution of records from multiple events from the same source region (Gurrola et al., 1995).

We interpret the waveforms of the receiver functions using a simple forward modeling approach, the result of which is then modified based on independent information regarding the local structure. For further insight into the apparently complicated Moho topography, we have incorporated other

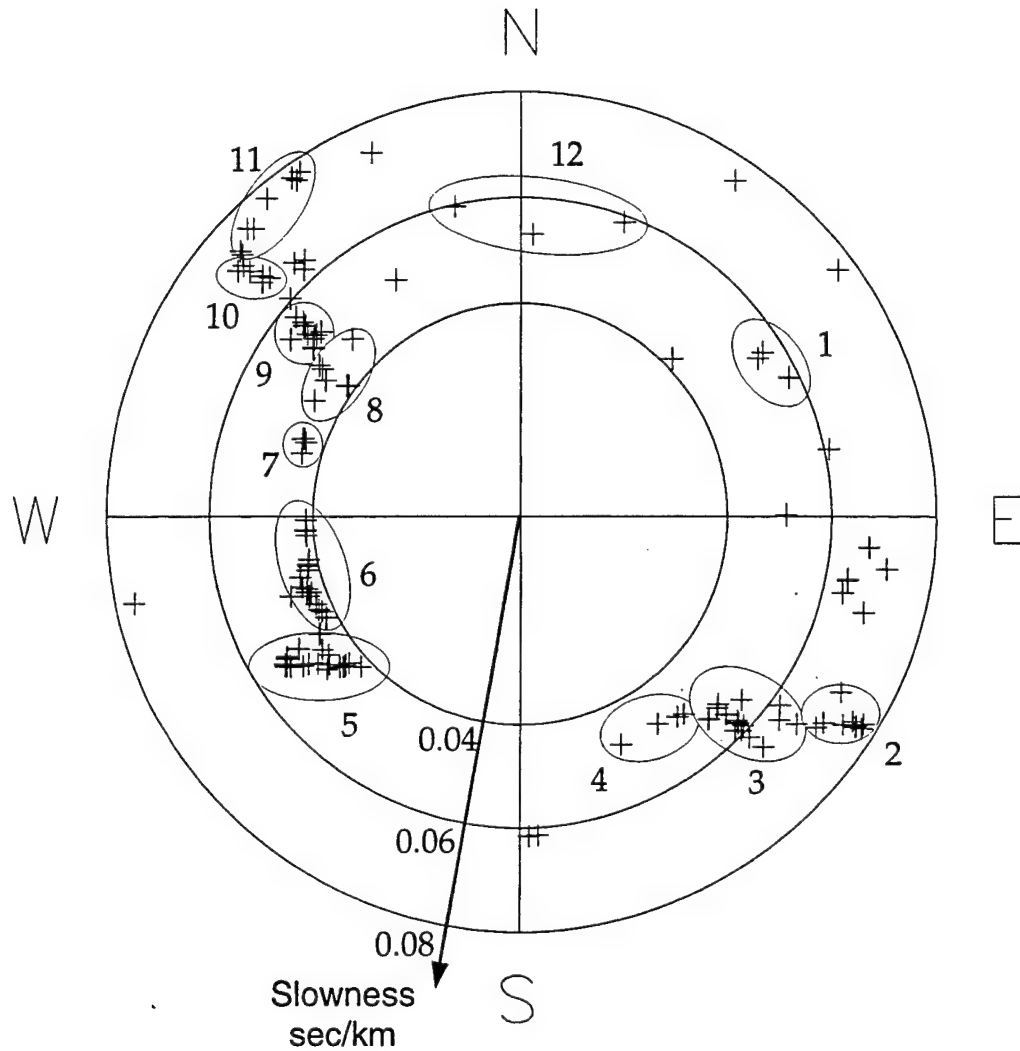


Figure 2.2: Station-centered plot of 117 events at PFO by ray parameter and backazimuth. Circles, from the outermost inward, are at 0.08, 0.06, and 0.04 sec/km. Nearby events have been grouped according to ray parameter and backazimuth (the events in each group are encircled). The numbers correspond to the receiver functions in figure 8. Isolated events are used in the individual analyses discussed in the text.

observations, specifically, the azimuthal dependence of teleseismic P-wave mislocation vectors and crustal P-wave reverberation travel times.

Forward Modeling

Radial PFO receiver functions do not vary with backazimuth for the first 3.4 seconds and can therefore be modeled using homogeneous horizontal layers, but the timing of the arrival interpreted as the Moho Ps phase does vary systematically with backazimuth, from 3.4 to 4.2 seconds after the initial arrival (for simplicity, we will refer to the initial peak as P). We have used events from all azimuths, binned only by ray parameter, to calculate the receiver functions used for plane-layered crustal modeling. Receiver functions calculated for the two smallest ray parameter bins are the least complicated (figure 3). Presumably this is because the ray paths for these waves are steepest and so least sensitive to lateral heterogeneities in the crust. We model these two traces to obtain a one dimensional crustal model.

Receiver functions contain information about the existence of discrete velocity discontinuities but are relatively insensitive to smooth velocity variations between these discontinuities. To minimize complexity in our forward modeling in a manner consistent with the type of information available in the data, we attempt to construct a model with as few discontinuities as possible. This contrasts with a common approach in recent receiver function inversion studies (e.g., Ammon et al., 1990), which have focussed on constructing the smoothest model with many thin layers. Since the features we are trying to fit are few and simple, fitting them by forward modeling proves to be straightforward and provides some insight into the trade-offs involved.

Our systematic approach is as follows. We choose P and S velocities for the uppermost layer and maintain the same P-to-S velocity ratio throughout the crust. The first arrival after P is modeled as the Ps converted phase from a velocity discontinuity. The depth of the discontinuity is chosen to match the timing and the magnitude of the velocity jump is chosen to match the amplitude. Comparisons are made using ray synthetics (Langston, 1977) convolved with a 0.2 second half-width Gaussian function to

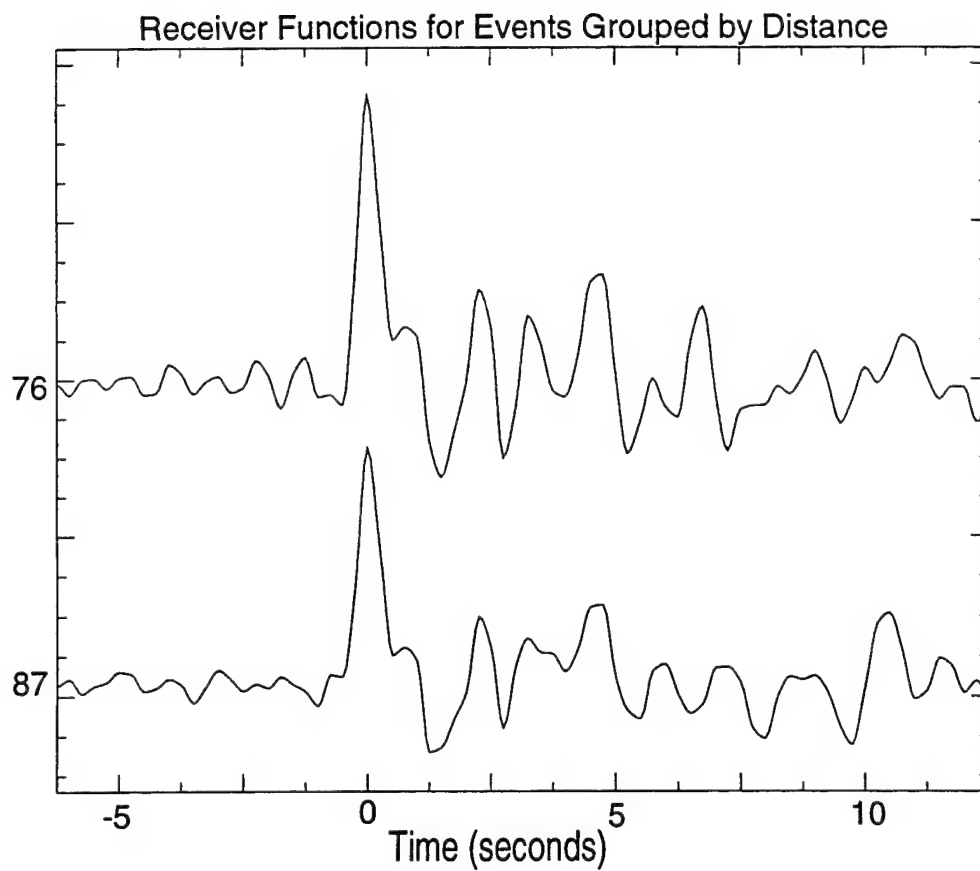


Figure 2.3: Receiver functions calculated for events binned by ray parameter only. The average distance in degrees for each set of events is to the left of each trace.

approximate the frequency content of the data. The next arrival in the data that cannot be interpreted as a reverberation off the first discontinuity is modeled as the Ps phase from a second discontinuity. The timing of receiver function arrivals is a robust measurement, and so depth, given some velocity, will be well constrained. Receiver function amplitudes, on the other hand, are very sensitive to noise, errors in physical assumptions (e.g. direction of arrival of rays, dip of layers), and the specifics of the deconvolution technique (Baker, et al., 1996), and so the amplitude of velocity jumps are very poorly constrained.

We start with the P and S velocities of 5.4 and 3.0 km/sec respectively for the uppermost layer, obtained from the 300 meter deep borehole PFO (Fletcher, et al., 1990). The first arrival after P appears as a shoulder on the right side of the main peak at 0.6 seconds. It is modeled as the Ps phase of a discontinuity at 3.4 km depth. The model and fit to the data are shown in the top row of figure 4. The data shown is from the steepest incidence group of figure 3. The PpP_is and PpS_is phases (labeled in figure 4, top) in the synthetics also match arrivals in the data, supporting both our initial assumption that the first arrival after P is a Ps phase and our choice of Poisson's ratio. PpP_is describes the ray that reflects as P-wave off the free surface and then is converted to S upon reflection upward at the *i*'th discontinuity. PpS_is is similar, but with the conversion occurring at the free surface reflection. The arrivals in the data would not have been matched as reverberations off a single discontinuity if we had assumed a Poisson solid. Although reverberations within a low-velocity surface layer could provide an alternative explanation of the early arrivals, the high velocities in the borehole and the granitic geology of the site virtually rule out the existence of such a layer.

The first feature in the data not accounted for by the first interface (figure 4, row 1) is the large negative trough at 1.0 seconds, which we interpret as the Ps arrival from the top of a low-velocity zone (LVZ). A low-velocity surface layer would again have been the only simple structure that could provide an alternative explanation for the arrival. We add a velocity inversion with a 0.7 km/sec drop in S-wave velocity in the second model (figure 4, row 2) at 9.2 km depth. A velocity increase at 17.2 km depth produces a Ps arrival at 2.6 seconds to match the peak in the data at that time (figure 4, row 3). The Moho

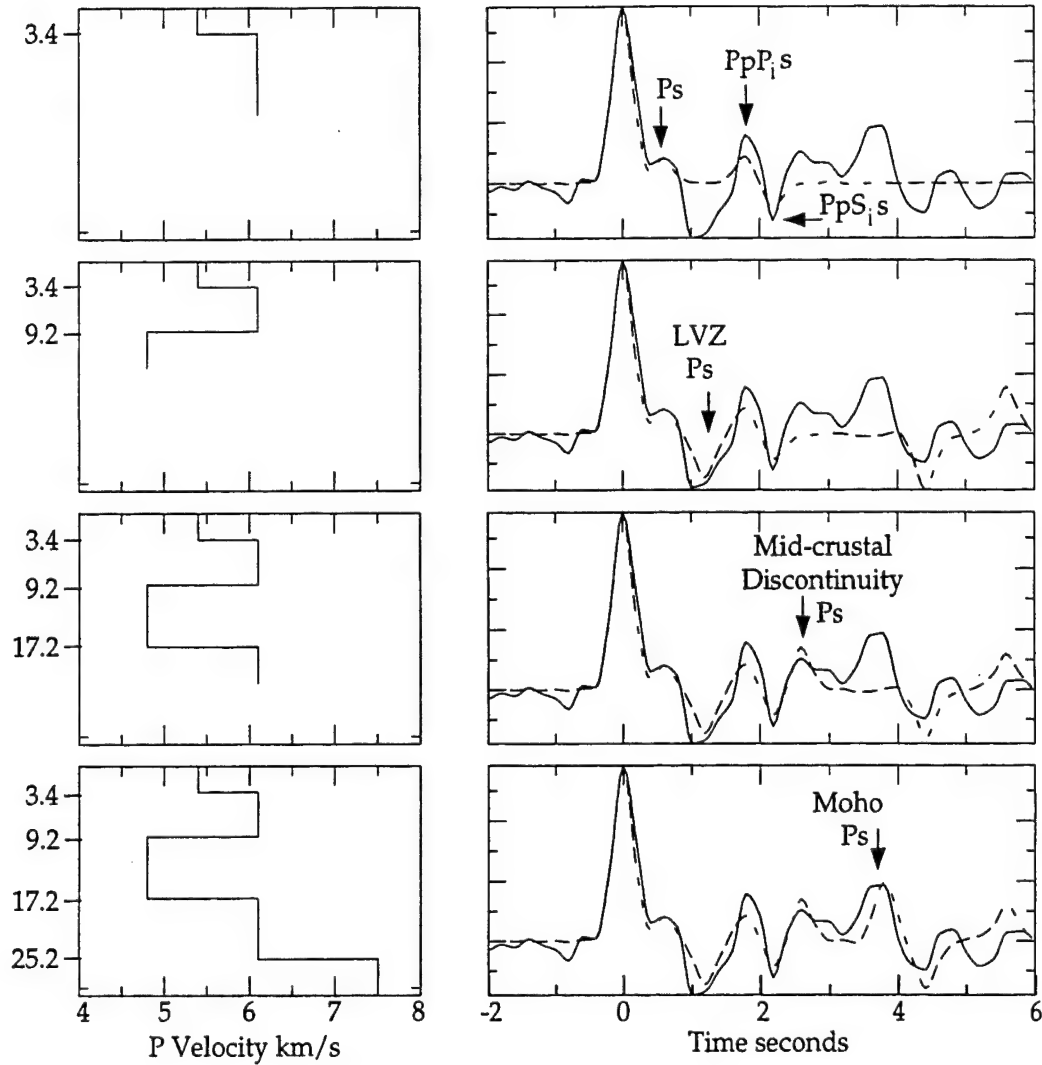


Figure 2.4: Incremental development of a simple velocity model. On the right side, the receiver function from the steepest incidence angle group of figure 3 is plotted as a solid line and the synthetic receiver function corresponding to the velocity model shown to the left is plotted as a dashed line. Phases indicated in the synthetics are due to the newest feature of each successive model.

Ps arrivals in these "all azimuth" receiver functions are broad, a result of simultaneously deconvolving events from various backazimuths, whose Moho Ps phase varies in time. For now we put the fourth and final discontinuity into our simple model at 25.2 km (figure 4, row 4). For the earlier arrivals, variations between the synthetic receiver functions and the data are less than those between different groupings of events (figures 3, 9), suggesting that we have fit the data as well as the noise allows.

This simple modeling illustrates just what we can learn from receiver functions alone (nearly alone, *a priori* knowledge of the uppermost velocity was helpful). That is, we can identify 3 crustal discontinuities, one being a velocity inversion, and the Moho, and place them accurately on a depth-velocity curve, and we are confident of the Poisson ratio in the uppermost crust because of the identification of the crustal multiples. We can now combine this new knowledge with previous, independently determined constraints to produce a better image of earth structure.

Because of significant uncertainty in receiver function amplitudes (Baker, et al., 1996), and concomitant uncertainty in the magnitude of the velocity jumps and layer velocities, as well as our lack of constraint on smooth velocity gradients between discontinuities and variation of Poisson's ratio, we do not expect the thicknesses of the simple model layers to be accurate. We incorporate independent information regarding average slownesses from the travel time tomography to help to constrain layer thicknesses (Scott, 1992, Scott, et al., 1994). Near surface velocities are poorly constrained by the tomography study, due to minimal ray coverage. Resolution of velocities is best between 9 and 16 km depth, where the P/S velocity ratio averages 1.708 ($V_p=6.12$, $V_s=3.58$) compared to the surface value of 1.8 we have retained throughout. We modify the model by using the average P/S velocity ratio from the local travel time tomography study throughout the crust, except in the topmost layer where we retain the borehole value of 1.8, and in the narrow LVZ from 9 to 12 km depth. We also adopt the absolute P and S-wave velocities found in the tomographic study for the best constrained depth section covered (9 to 16 km), again with the exception of the LVZ. With these changes, the Moho depth of the model drops to nearly 30 km, bringing it in line with results of previous investigations, albeit, of a more regional scale

(Hearn and Clayton, 1986; Sung and Jackson, 1992). An 8 km thick LVZ would have been resolved in the travel-time tomography (Scott, 1992, Scott et al., 1994). For consistency with the tomography, the LVZ is thinned and given a gradational base (so it produces no large Ps phase). A shear-wave velocity discontinuity alone can produce the trough at 1.2 seconds to match the data. We show (figure 5, right) the extreme case of no P wave LVZ. In figure 6 we see that synthetic receiver functions based on this modified model fit the data as well as the simple one.

Because of the refined model's better agreement with the results of travel time tomography, with regard to P and S velocities and the thickness of the LVZ, and its better agreement with the Moho depth of more regional studies, we consider it a better approximation of true earth structure.

Complex Moho Topography near the San Jacinto Mt/Salton Trough Transition

There is significant azimuthal variation of both travel times and amplitudes of the Moho Ps phase relative to P on the receiver functions computed for PFO. Unfortunately, the trade-offs between parameters that affect receiver function amplitudes, discussed in the previous section, become even more complicated as many combinations of parameters varying with azimuth might explain the observations. In addition, our implicit assumption that observed variations are due to lateral fluctuations of properties at the interface where the phase is generated may not hold. For example, surface scattered energy from a particular azimuth could arrive simultaneously with the Moho Ps phase, changing the apparent timing and amplitude. To reduce these ambiguities, we have also examined the azimuthal variation of event mislocation vectors and crustal P-wave reverberation travel times.

Each type of observation we make samples different portions of the crust and is sensitive to parameters in different ways. The travel time and amplitude of the Moho Ps phase relative to P are sensitive to the amount and direction of dip where the direct P and the Ps phases cross the Moho. The travel time is also sensitive to velocity variations above the Moho. The amplitude is sensitive to variations in the velocity jump. Which portion of the crust is sampled by the P and Ps phases is strongly dependent on

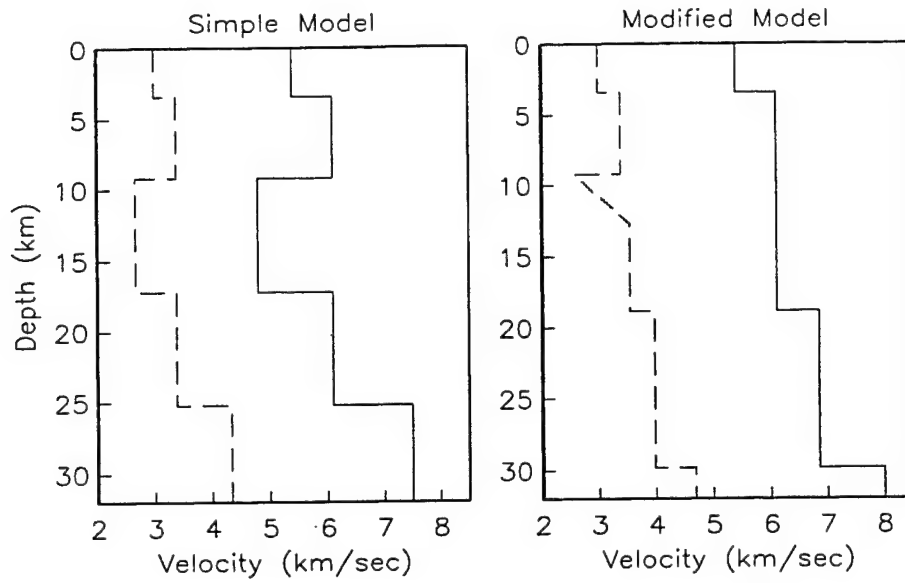


Figure 2.5: Two velocity models which fit the data equally well based on forward modeling.

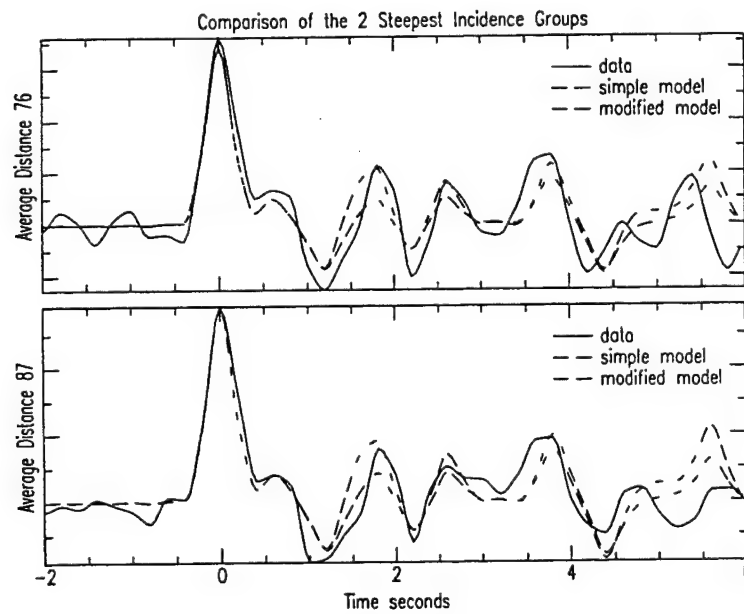


Figure 2.6: Synthetic receiver functions for the simple (dotted) and modified (dashed) models compared to the data (solid). Comparisons are made for the steepest (bottom) and second steepest incidence (top) group receiver functions of figure 3.

Moho dip (figure 7). In contrast, mislocation vectors are sensitive to lateral velocity variations along the entire ray path, although a steeply dipping Moho would cause significant mislocation. The region affecting direct P-waves extends further from the station than that affecting P-to-S converted phases from the Moho. The multiply reverberating PpPmp phase samples an even greater lateral segment of the crust (figure 7). When we compare inferences we make from each type of observation, we are assuming that, whatever the character of Moho variations, they will be somewhat consistent in their nature over the length scales we are sampling. Gross inconsistencies between the inferences made from observations of different phases would suggest rapid variations in Moho depth and dip.

Figure 8 shows the receiver functions for the individual back azimuth and ray parameter groups identified in figure 2. They are lowpass filtered below 1 hertz to demonstrate that timing and amplitude differences observed are not simply due to varying frequency content of the receiver functions. The Moho Ps varies significantly in amplitude and time, from 3.4 to 4.2 seconds after P. The pattern of Moho Ps-P times measured for individual receiver functions (i.e. calculated for individual events, not the groups) is shown in slowness-azimuth space in figure 9 (left). The largest peak between 2.5 and 4.5 seconds was taken to be the Moho Ps converted phase. We attempt to model it with a dipping planar Moho. The pattern is matched well for a 32 km deep 6.3 km/sec layer over a half space dipping 20° to the northwest (figure 9, right). Varying the strike by 20° degrades the fit significantly. To quantify better the strike and dip that provide the best fit to the data, we calculated the observed-minus-predicted Moho Ps-P times for models covering a range of values for strike and dip of the interface. To avoid biasing results by high density data clusters we average the data over bins of 0.0045 sec/km in ray parameter and 10° in backazimuth. We then calculated the standard deviation of the residuals for all models with 5° incremental variations in dip angle (from 0° to 30°) and direction and find a well-defined minimum at 15° to 20° dip to the northwest (figure 10). The demeaned residual pattern is shown for 20° dip at 225° (fig 11, left), the same rms error as 15° dip at 220° . The point where the residual is plotted represents the horizontal distance and backazimuth to the point where the ray for the Ps phase intersects the Moho. For comparison, we plot the demeaned Ps-P residuals relative to a 30 km thick 6.3 km/s flat lying layer over a half space (figure 11,

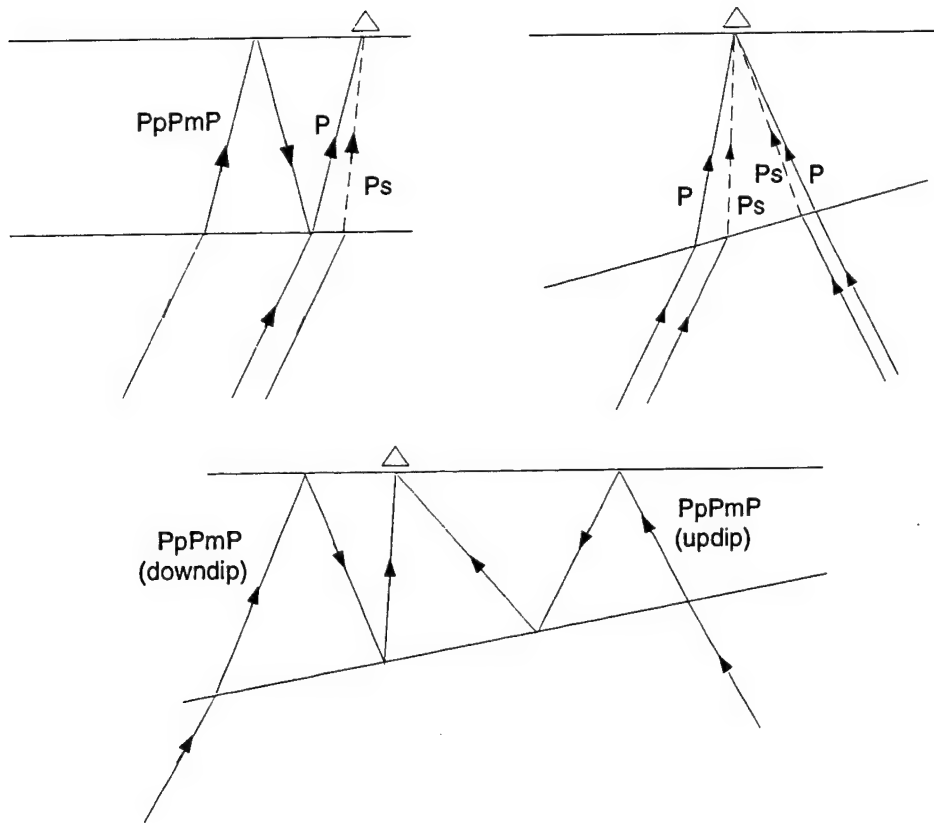


Figure 2.7: Ray paths of converted and reverberated phases for horizontal and dipping interfaces. Note the difference in horizontal distance from the station sampled by similar phases updip relative to down dip.

Receiver Functions Grouped by Distance and Backazimuth

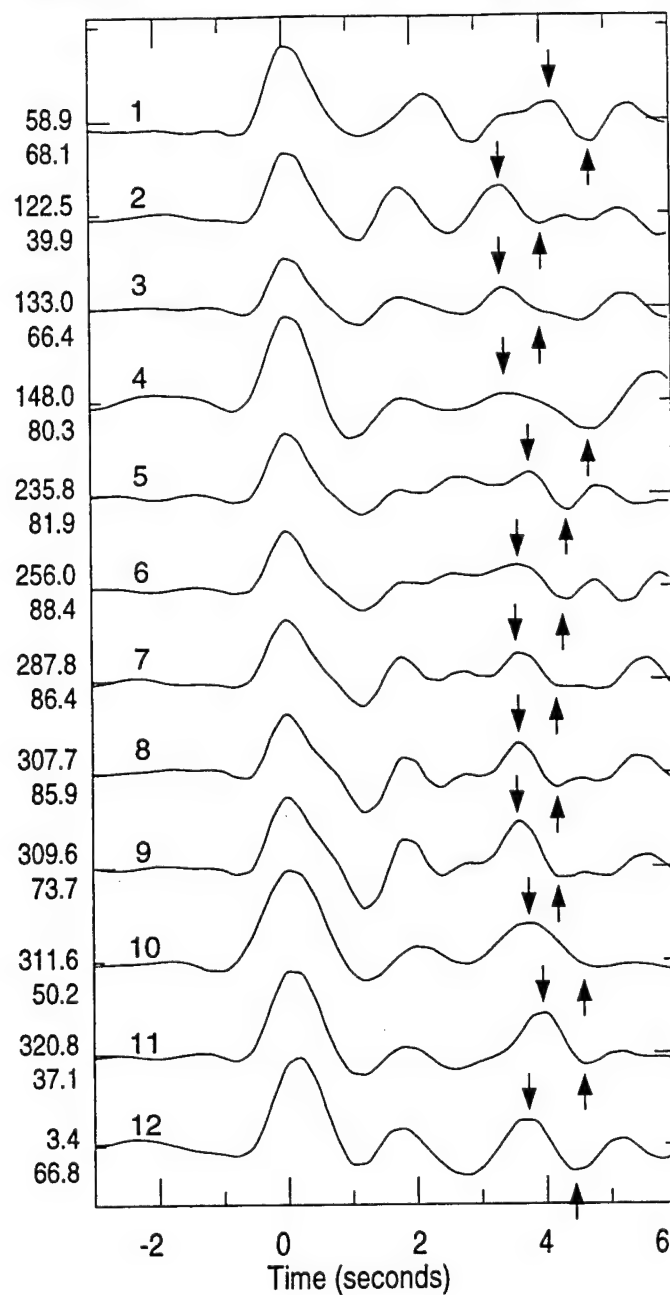


Figure 2.8: Receiver functions, low-pass filtered below 1 hertz, for the event groups pictured in figure 2, with group numbers of figure 2 above each trace. Average backazimuth and distance for each group is to the left of the traces. Note the variability of the Moho Ps-P time at about 4 seconds (downward arrow). Upward arrow indicates negative peak after Moho Ps.

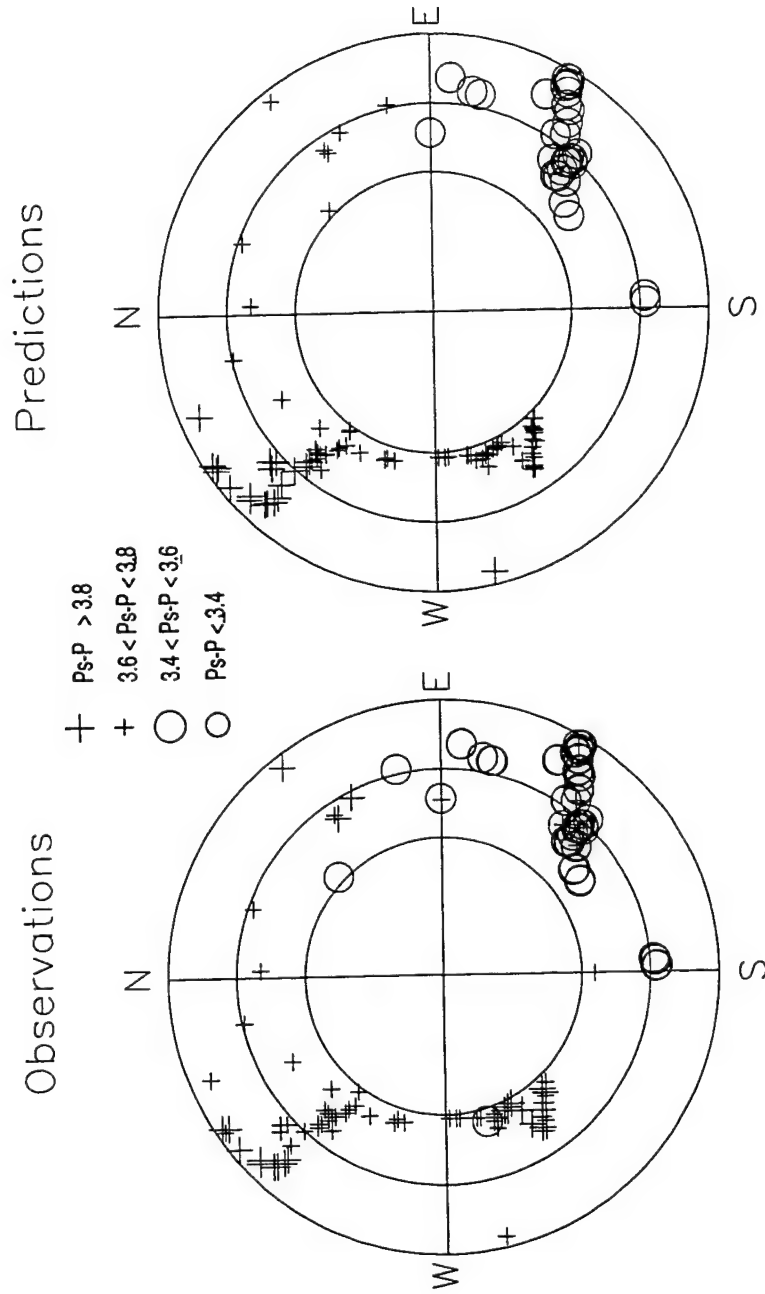


Figure 2.9: Moho P_s-P times for individual events, plotted on the same station centered plot as in figure 2. The distinctive pattern of longer times to the northwest and shorter times to the southeast in the data (top plot) is well matched by synthetics calculated for a 32 km deep 6.3 km/sec layer over a half space dipping 20 degrees to the northwest.

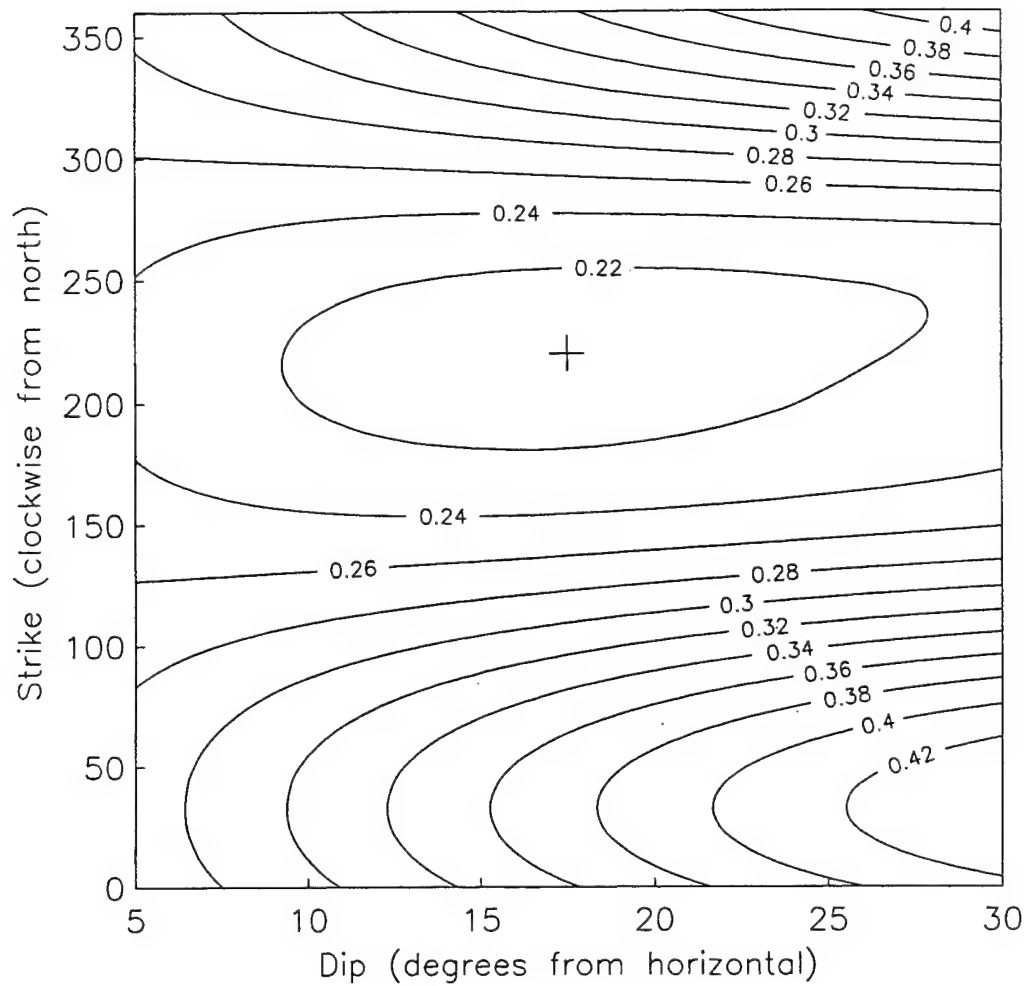


Figure 2.10: Contour plot of the demeaned one norm of observed-minus-predicted Moho Ps-P times in seconds, for dipping planar layer over a half space models ranging over all strikes and dips up to 300 in 50 increments. The minimum is at 15 to 20 degrees northwest dip.

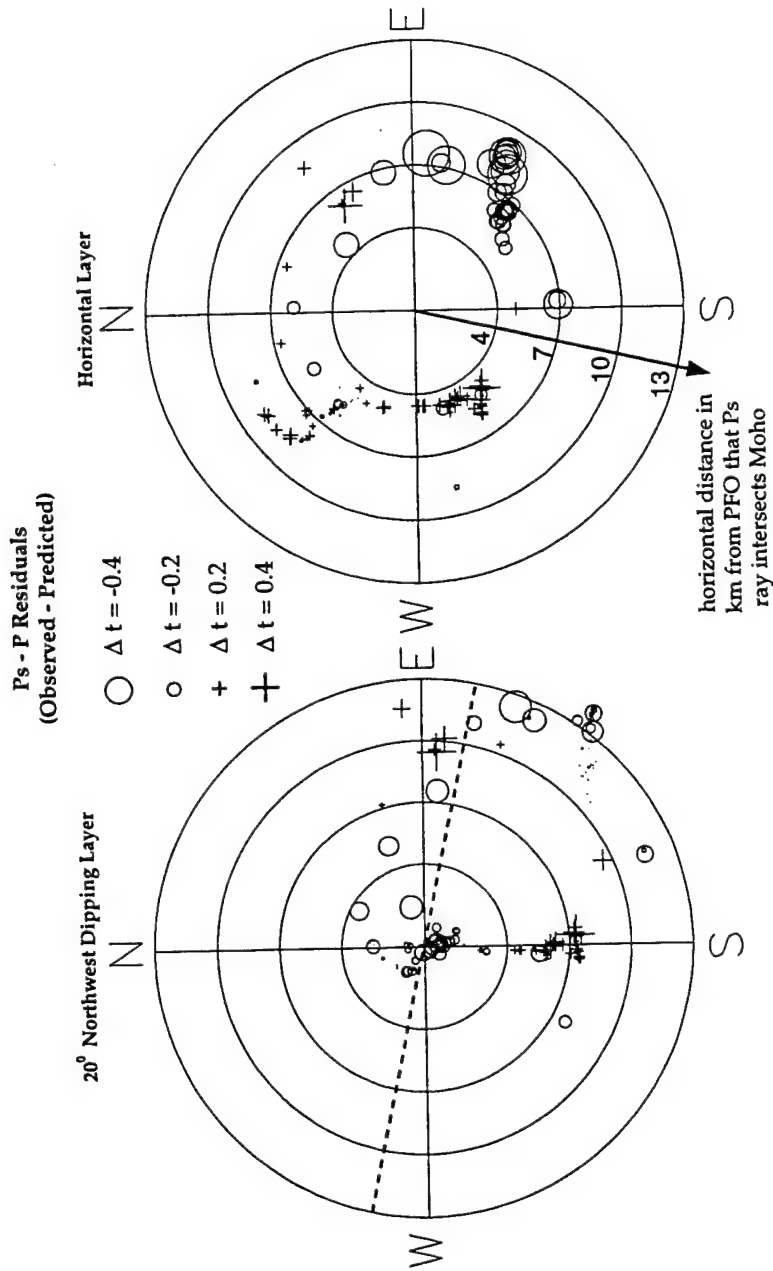


Figure 2.11: Demeaned Moho Ps-P time residuals for a 6.3 km/sec 32 km deep layer over a half space dipping 20 degrees northwest (left). Points are plotted at the horizontal distance and backazimuth from the station that the Ps converted phase would be generated at the Moho and are scaled by the size of the residual. Note that for this model, all rays cross the Moho directly beneath or to the southeast of the station. The dashed line running 120° south of east indicates the position of one of the cross sections of figure 17. Demeaned Moho Ps-P time residuals relative to a 6.3 km/sec 30 km deep horizontal layer over a half space (right). Note not only the greater consistency in residual times for the dipping model, but what different areas of the Moho are sampled in each model.

right). Note that because of refraction at the dipping interface, the Ps rays on the left of figure 11 intersect the Moho "updip" of where they would intersect a horizontal Moho (right side of figure 11). The standard deviation of the residuals is 0.25 s for the flat model and 0.20 s for the dipping model.

There are indications of deviations from planar structure. Data at steep incidence in the southwest and northeast quadrants show a juxtaposition of very different Ps-P times over very short distances (figure 11). Although there are few data from the northeast, there is a small consistent group of events at shallow incidence, all with large positive residuals (greater Ps-P times than predicted). Events at steeper incidence and events at 20° - 30° more southerly backazimuths have large negative residuals. Another possible juxtaposition of large and small residual times is seen due south of PFO (in figure 11, left side) about the 7 km radius circle. These rapid spatial variations of times may indicate a sharp change in depth and/or dip of the Moho. Comparing the 13 km radius (outer) circle of figure 11 (left side) with that in figure 1, we see that the apparent discontinuity to the east of PFO is near the surface expression of the San Jacinto Mountains - Salton Trough boundary (see also figure 17). Although this does not indicate the position of the batholith contact at depth, the mass above the Moho on either side of this boundary is likely to vary strongly. The apparently anomalous points to the south of PFO (figure 11) coincide with the steep 1400 meter north slope of Toro Peak (figure 1). The Ps-P time differences there would be equivalent to variations of Moho depth of 4 to 5 kilometers for flat-lying models with no lateral P velocity variations. Further, iterating through the same set of models as above for just the steeply incident events from the southwest through the northwest, for which there is very dense data coverage, we find that the minimum Ps-P time residual is for a model dipping nearly due west. Given the density of coverage and the consistency of the times, we think this indicates a real deviation from planar structure.

The positions at which the residuals for the dipping planar model are plotted vary greatly from those of the flat lying model (figure 11). This points to a serious problem with our approach thus far. Some of these rays have been refracted past the vertical, so as to appear to arrive from the opposite backazimuth. This would lead to negative Ps arrivals, which we do not observe. This suggests that deeper Moho to the

northwest, still the simplest explanation for the observed Ps-P time pattern (figures 8-11), cannot be accomplished entirely by planar dip of the Moho. We suggest that it is more likely to be accomplished with step offsets, as was also indicated by the juxtaposition of different residuals, or by some combination of dip and step offsets. An alternate explanation, lateral velocity variations, seem less plausible. If P and S velocities varied together as is usual, large changes in both would be necessary to make significant changes in relative S and P travel times through the crust. Even in the improbable case of lateral heterogeneities occurring only in P velocities, an average velocity variation of 10 percent over the entire crust would be required to produce the same Ps-P time variation as a 4 km increase in crustal thickness.

Whereas the Ps-P times depend on both depth and dip of an interface, the amplitudes of P and Ps phases are most sensitive to dip. The Ps/P amplitude ratio can be a more powerful measure of dip than the amplitudes are separately, as the P and Ps amplitudes vary oppositely with dip (Owens et al., 1988). Because of the trade-off between dip and size of the velocity discontinuity in predicting Ps/P amplitude ratios, as well as the sensitivity of receiver function amplitudes to noise and to small changes in dip as seen in synthetic tests, we can use amplitudes only to predict the general direction and not the steepness of the dip, and then only where we have dense data coverage.

Figure 12 shows the observed Moho Ps/P amplitude ratios. As amplitude ratios of individual receiver functions vary significantly, we plot the amplitude ratios of the receiver functions computed for events binned by ray parameter and backazimuth and low-pass filtered (shown in figure 8). In figure 12 we compare the observed to synthetic ratios for a 20° northwest dipping model. The overall pattern of amplitude variation is similar to that of the observations. The major deviation between predicted and observed amplitudes is for events from the southeast, where we see that, for 20° dip, there should be almost no predicted Ps, as the incident rays would be nearly perpendicular to the plane of the discontinuity. A deviation from the northwest dipping planar model with a gentler slope in the southeast than in other quadrants would explain the observations. Further, in contradiction with the above results in which the Ps-P travel times for the subset of events coming in at steep incidence from the west indicated

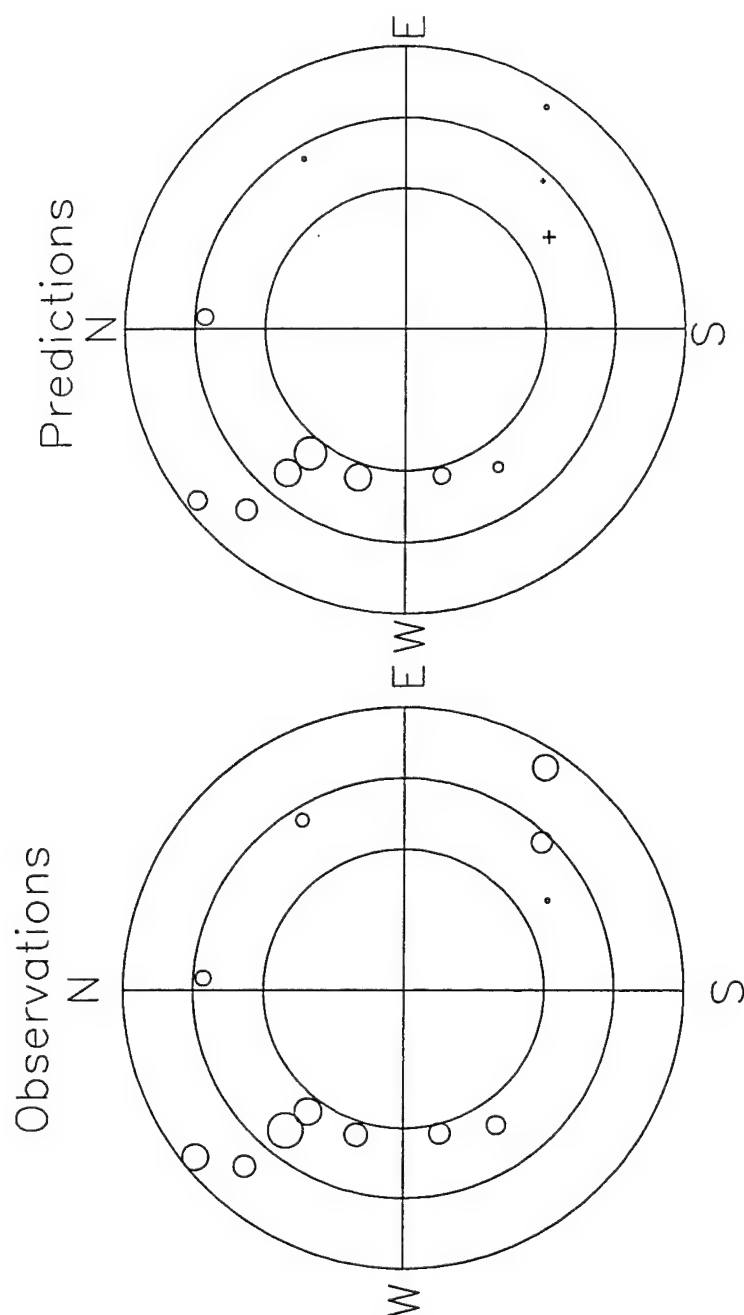


Figure 2.12: Moho Ps/P amplitude ratios for receiver functions of groups of figure 2, on the same station centered plot. Azimuthal variation observed in the data (left) is roughly matched by synthetics for the same 6.3 km/sec 32 km deep layer over a half space dipping 20 degrees northwest. Absolute values of the amplitudes are not important (see the discussion regarding uncertainty). Only relative amplitudes at different azimuths are used to infer dip direction. Plus symbols indicate reversed polarity of the Ps arrival.

a westerly dip, the very distinct increase in the Ps/P amplitude ratio from southwest to northwest indicates a northwest dip. An explanation of both the travel time and amplitude variations requires more complicated structure than a planar dipping interface - for example, downward step offsets in the Moho from the west to the northwest, while maintaining northwest dip in the individual segments. To sum up thus far, the Moho deviates significantly from planar structure over length scales on the order of 10 km or less. The specifics of those deviations cannot be resolved with present data. Regardless of the second order structure, the best fitting plane to the Moho Ps data dips steeply to the northwest. The Ps-P time difference is equivalent to flat-lying models of 7 km difference in thickness.

The PpPmp phase can also be used to constrain depth and dip of the Moho. To reduce the complexity of the original seismograms due to source and distant path effects, we stacked the seismograms of the impulsive events within each ray parameter and backazimuth grouping of figure 2, after aligning and normalizing the largest arrival of each event. Figure 13 shows the individual vertical component records (top five traces) for one of the bins and the stack of the five records (bottom trace). We identify the only remaining distinct secondary arrival in the stack as PpPmp. Similar processing of the radial components confirms that the arrival has the same polarity on the radial component and so is not likely a Ps converted phase. Unfortunately, the only impulsive events are from the west. Events with eastern backazimuth are generally smaller, mid-Atlantic ridge events with emergent arrivals. Figure 14 shows the stacked arrivals for each of four bins, and their respective PpPmp-P times. We see that the differential time increases from southwest to northwest, consistent with deeper Moho to the northwest. The differences between PpPmp-P times at different azimuths cannot be modeled using a dipping layer alone regardless of the degree of dip without severe revision of the crustal velocities we have been using. The reason for this is illustrated in figure 7. Although an increase in dip increases the vertical distance the down-dip rays must travel, the horizontal ray path distances decrease. The result is less time variation than we might at first expect, although the sense of time variation is what we expect, with longer PpPmp travel times down-dip. An alternate explanation of the data is, again, to call on Moho step offsets as a means of thickening the crust to the northwest. If the Moho were everywhere horizontal, with 6.3 km/sec average crustal velocity, the

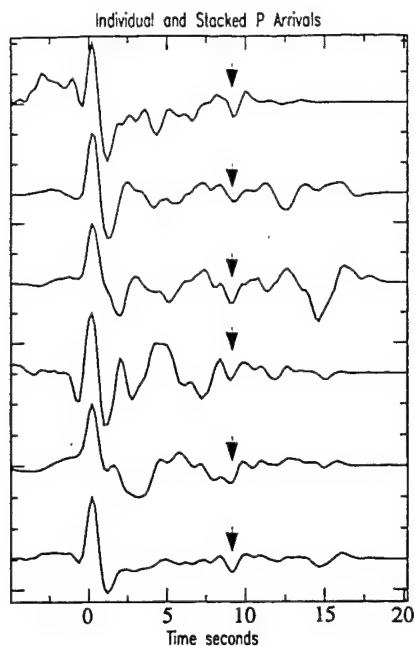


Figure 2.13: Normalized P waves (vertical recordings) of impulsive events from group 5 of figure 2 (top five traces), aligned by arrival time, and their stack (bottom trace).

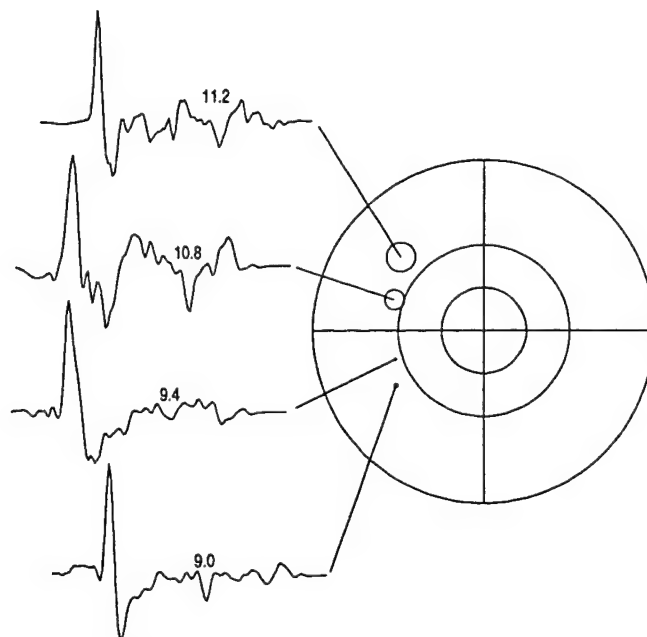


Figure 2.14: Stacks for the 4 groups containing impulsive events. PpPmp-P times are listed above the presumed PpPmp arrival of each trace. The position of each group is indicated, with the circle scaled by the residual relative to the flat-lying 6.3 km/sec 30 km deep layer over a half space of figure 11 (so as to account for the effect of variations in ray parameter between groups).

PpPmp-P times would indicate crustal thicknesses of 29, 31, 35, and 37 km from southwest to northwest.

Mislocation vectors are the difference between the predicted and observed directions of arrival at a station, plotted on a focal sphere (e.g. Davies, 1973). The tangential components of the mislocation vectors are shown in figure 15. We used the data variance tensor decomposition (Aster et al., 1990) to measure the 3-dimensional particle motion. A horizontal Moho would cause no mislocation, but dipping structure will bend the rays so they come in from further updip than predicted. To avoid biasing the results we used an objective criterion based on the linearity of particle motion to determine whether to include a measurement and made no modifications (e.g. to the data window used) once the mislocation was calculated. We observe a consistent pattern of mislocation vectors. These observations are matched by a layer over a half space model dipping to the southwest (figure 15, bottom), perpendicular to the overall direction of Moho dip we inferred from interpretation of the receiver functions. The radial components of the mislocation vectors are much noisier, but are consistent with the southwest dipping model. The receiver function Moho Ps, the PpPmp, and the mislocation vector observations are each internally consistent. All observations indicate deviations from planar Moho topography. Using a planar dipping interface model, the mislocation vectors suggest dip of some layer to the southwest, whereas the others suggest deeper Moho to the northwest. The pattern we observe in the mislocation vectors could be due to bending of the ray paths anywhere between the sources and receiver. The radial receiver function waveforms indicated no significant planar dipping crustal interfaces, although there is poor resolution of dip at the uppermost interface. A study of array mislocations (Burdick and Powell, 1980; Walck, 1984) indicates that across southern California there is no average regional mislocation observed, suggesting that the pattern at PFO is not global, but must have been produced locally. Walck explains mislocations she observes in the area near PFO as being due to a combination of both crustal and deeper (50-200 km) variations in velocity structure. She infers the existence of an east-west trending antiform with axial depth of 100 km, 70 km north of PFO. Rays from the northwest, but not the southwest, reaching stations at the latitude of PFO are affected by that antiform. She suggests that rays from the southeast are affected by low-velocity below the Salton Trough. We cannot distinguish as she does between the shallow and deep

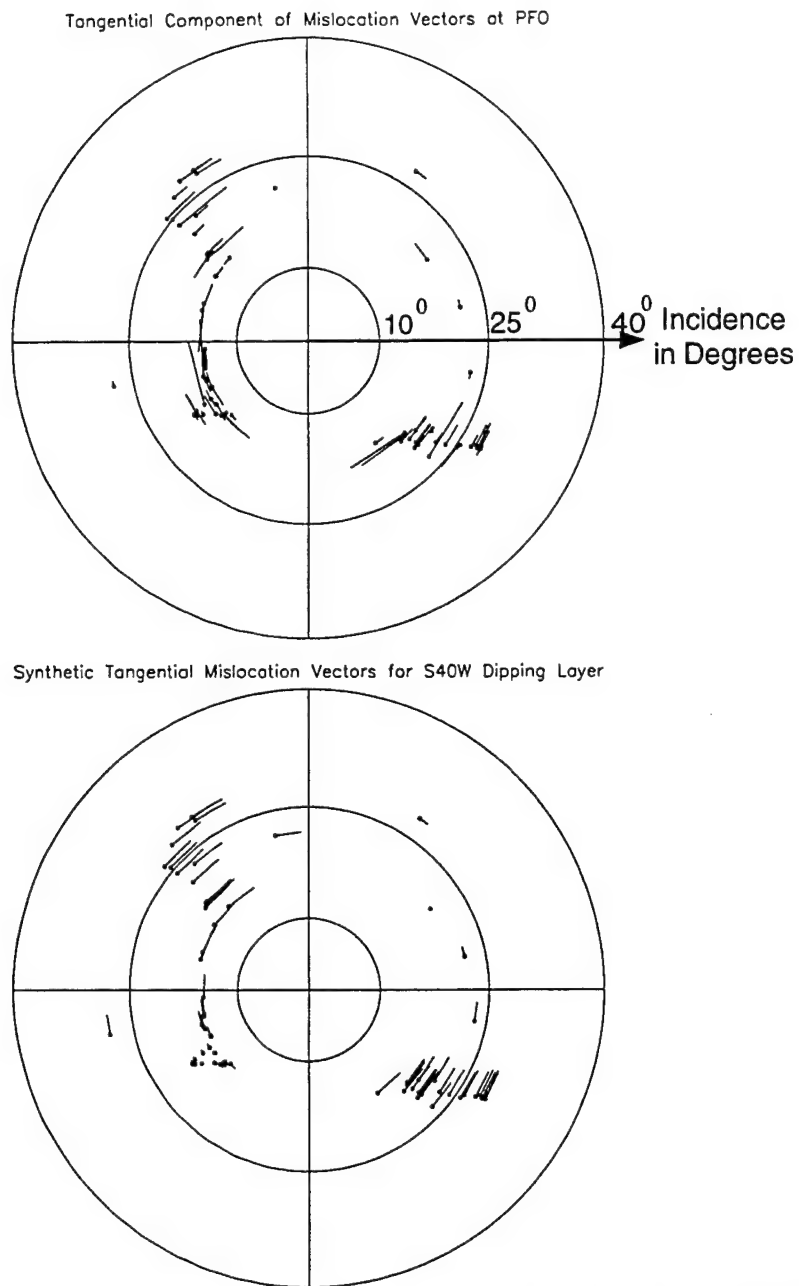


Figure 2.15: Tangential component of mislocation vectors for initial P waves at PFO (top) and for a layer over a half space dipping 20 degrees towards S40W (bottom). Circles are at 10° , 25° , and 40° incidence. Predicted positions of the events are plotted as disks. Arrows point to the measured positions of the events. Eighteen of twenty one mislocation vectors in the northwest quadrant are pointing clockwise, with a mean of nearly 5 degrees, the southeast quadrant has a mean tangential mislocation of 2.5 degrees counterclockwise with sixteen of twenty one events consistent in direction, while the southwest quadrant mislocation vectors are much less consistent and have a mean of 1.5 degrees clockwise.

effects, but it is reasonable to suggest that much of the pattern of mislocation vectors observed at PFO is a result of some combination of such structures. The pressing question is not what causes the pattern observed at PFO, but why there is no signature in the mislocation vectors at PFO from a northwest dipping Moho. For such a structure, the greatest tangential mislocation should be observed in the northeast (where we have almost no data) and southwest quadrants. The signal in the northwest and southeast quadrants should be small, and so could be overwhelmed by the signal from the antiform to the northwest and low-velocity in the rift to the southeast. The data in the southwest quadrant, however, are inconsistent with the mislocations expected from a planar northwest dipping Moho, and so imply non-planar Moho topography.

There is a negative arrival immediately following the Moho Ps arrival, peaking at 3.8 to 4.4 seconds after P (figure 8). For some of the receiver functions this phase is matched by the PpPs from the LVZ of the synthetics (Figures 4 and 6). However, it also tracks the azimuthal variation of the Moho Ps phase (figure 8). Its synchronization with the Moho Ps phase suggests that the arrival may be the Ps phase from the base of a high-velocity lid at the top of the mantle. Both phases could be interfering there, making interpretation problematic. Beyond that arrival, consistency between receiver functions decreases, probably because of decreasing signal amplitude for the later arrivals, interference between later arrivals and reverberations of early arrivals, greater sensitivity of later arrivals to dip and laterally varying structure, and the effect of complicated Moho topography on later crustal reverberations.

Tangential Component Receiver Functions and Dipping Structure

Arrivals on the tangential components of receiver functions represent energy coming in off the predicted backazimuth. We can attempt to model them deterministically only if for some azimuths, they have a counterpart on the radial component receiver functions and if there is continuity between receiver functions from similar backazimuths and ray parameters. The extent of variation in Moho topography inferred from the radial components encourages us to expect a Moho Ps signal on the tangential compo-

nents at PFO. Somewhat surprisingly, only a couple of the groups' tangential receiver functions have arrivals at the same time as the Moho Ps on the radials, and even in those cases, there is no consistency between adjacent groups. This does not imply that there is no Moho dip, but simply reflects the difficulty in interpreting this component. The lack of a strong Moho signal on the tangential components is consistent with the Moho depth change being accomplished by step offsets rather than by a smooth surface.

There are early tangential component arrivals with sufficient continuity between adjacent groups to warrant further scrutiny. Those arrivals appear to correspond to the converted and reflected phases from the uppermost discontinuity (figures 4 and 5). We note however that interpretation of the radial receiver functions becomes much more ambiguous if we consider models with dipping interfaces. In these cases, the receiver function arrivals no longer are restricted to representing phases that arrive at the seismometer as S-waves. In fact, the largest receiver function arrival after P for a simple dipping layer over a half space can be the first P multiple, PpPip. Which phase is largest depends on the angle between the ray azimuth and the interface strike. We concentrate our attention on the tangential component receiver function of group 5 of figure 1, both because it has the most events and so has very high signal-to-noise ratio, and because the tangential mislocation vectors at that distance and backazimuth are nearly zero (figure 15). Receiver function arrivals from dipping interfaces are very sensitive to the angle through which the seismograms are rotated. Rotation errors of the size observed could cause significant tangential component arrivals to disappear, or even change polarity. Thus the mislocation vectors we discussed earlier make interpretation of the other groups' arrivals more ambiguous. Such a mislocation study should always be performed if tangential components are going to be modeled, to ensure that arrivals due to energy refracted out of the sagittal plane below the depth of interest are not misinterpreted in terms of shallower dipping structure. That being done, the sensitivity to rotation can actually be used to infer both the existence and direction of dip.

The radial and tangential receiver functions of group 5 (of figure 1), and their point-by-point product, indicating the correlation at each time point, are shown in figure 16. For this group, there is good

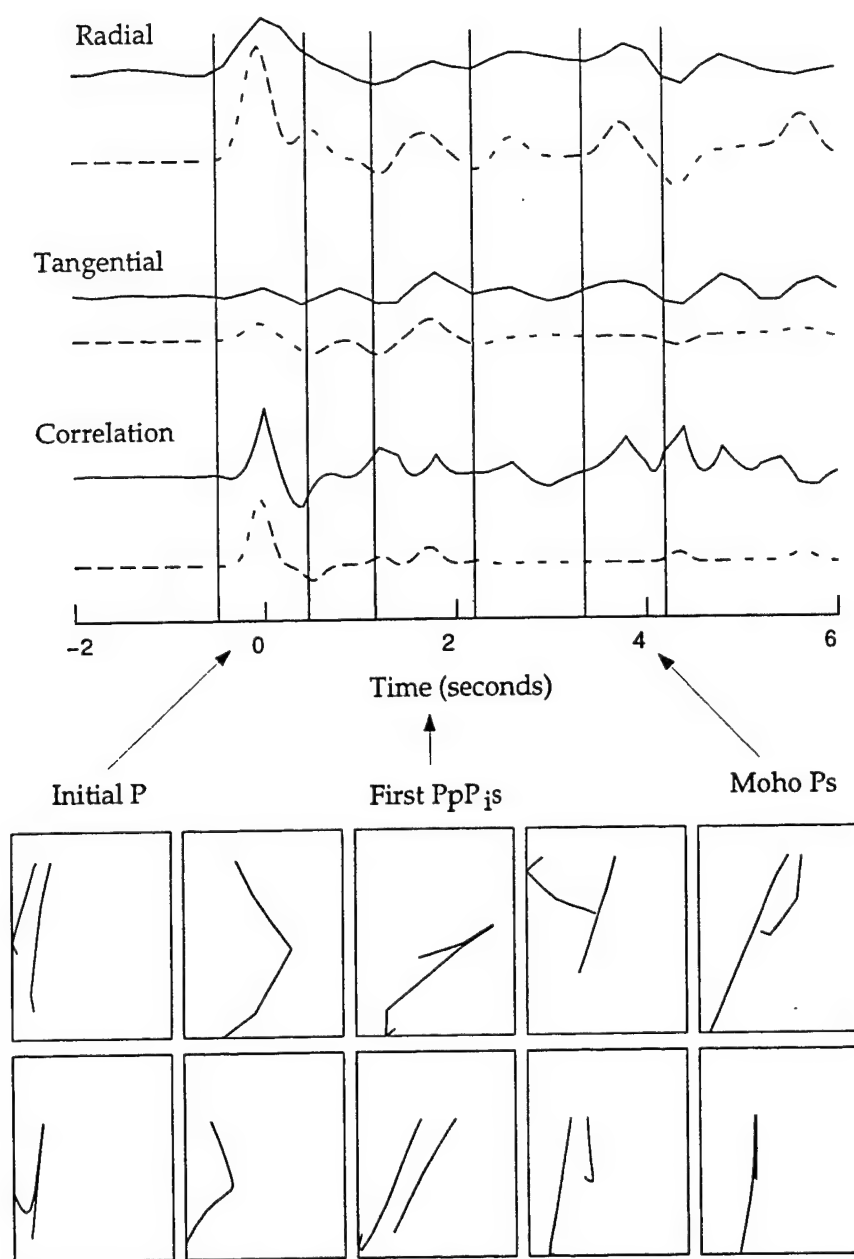


Figure 2.16: Radial (solid line, upper trace) and tangential (solid line, second trace) receiver functions of group 5 (from figure 2), and their point-by-point product, indicating their coherence (solid line, lower trace). Synthetic receiver functions and their coherence (dashed lines) are shown below the data traces, for the refined model of figure 5 in which the shallowest discontinuity dips 150 southward. Vertical lines through the traces delineate the windows for which particle motion is plotted below (the upper row is for the data and the lower row is for the synthetics).

correlation for the earliest crustal phases as well as the Moho Ps, but only the early arrivals appear consistently in nearby groups, and we will concentrate on those phases. The dashed curves are the corresponding synthetic traces for the preferred model (figure 5), in which the uppermost discontinuity is permitted to dip southward 15° (striking 100°). That direction was chosen by comparison with synthetics of the polarities and sensitivities of initial arrival and the PpP_s phase to misrotation.

Another piece of information we can utilize is the polarization direction of receiver function arrivals (Langston, 1989). The columns through the traces in the upper part of figure 16 delineate the windows for which particle motions are shown in the lower part of the figure. Note that for the data, the polarization directions of the initial arrival and the Moho Ps (columns 1 and 5) are both somewhat out of the radial direction expected for horizontal layers, but for PpP_s of the first interface (column 3), the polarization direction is pointing roughly 60° away from the radial direction, while the other crustal arrivals are mixed (less linear and possibly oriented between those extremes). The absolute values of polarization directions are not robust measurements, subject as they are to the uncertainties in receiver function amplitudes (Baker, et al., 1996), and to the additional uncertainty in interface strike and dip angles and incoming ray backazimuth and incidence. The relative values may however carry useful information. The initial P and Moho Ps have roughly similar polarization directions, and the first PpP_s phase polarization direction is much further from the radial direction. That fundamental difference between the phases is reproduced well by the synthetics (lower set of particle motion plots, figure 16).

While predictions for the simple case fit the data for some other groups, there are significant deviations as well. The data do not distinguish whether the deviations are due to greater complexity in the structure (e.g. variation of dip with azimuth or strong discontinuous scatterers in the crust), or to misrotation of the seismograms due to other deeper dipping structures. Overlap of the much larger initial arrival with the first Ps phase prevents us from using azimuthal dependence of the timing on the radial component as was done for the Moho Ps, so we are limited in what we can confidently interpret in tangential components of these data.

To summarize our investigation of the tangential component receiver functions, the available *interpretable* evidence indicates that the 3.4 km deep interface dips southward, although that conclusion is admittedly nonunique. We also conclude that consideration of mislocation vectors is important for avoiding misinterpretation of tangential receiver functions. Their use will enhance the credibility of interpretations made by controlling for misrotation of the horizontal component seismograms, a major source of error in tangential arrivals.

Tectonic Implications:

Crustal Low-Velocity Zone, Rheology or Lithology?

We next consider the contributions of the above analysis to our understanding of the tectonics of the study area.

The shear-wave LVZ has a sharp top at 9 km depth. The lack of a clearly identifiable arrival from the base of the LVZ leaves its thickness unconstrained, and suggests that its base may be gradational. We model it as being quite thin, as it was not resolved in local travel time tomography (Scott, 1992). A possible mechanism for a zone of shear-wave low-velocity is a layer of saline fluid, like that inferred by Park et al. (1992). We consider carefully the mechanism that would provide an impermeable boundary. Park et al. attribute it to the brittle-ductile transition, estimated by Doser and Kanamori (1986) to be at 11-12 km depth in the eastern Peninsular Ranges, because 80% of the seismicity occurs above that depth. The seismicity deepens and heat flow decreases in the northern Peninsular Ranges (Doser and Kanamori, 1986), leading to estimates of a deeper transition zone. Doser and Kanamori (1986) use a rheological model with granite to 14 km depth, and diabase beneath, for the area around PFO, and while they do not make an exact estimate of depth to the brittle-ductile transition, they place it in the diabase. However, Bailey (1990) cautions that the arguments for trapping of saline fluid at the brittle-ductile transition are "intended to apply to stable continental crust, not to tectonically active regions". A requirement for trapping fluids is that the least principal stress be vertical, so as to permit horizontal fracturing. The T axes of

earthquake mechanisms throughout the northern Peninsular Range and eastern Transverse Range are however, horizontal (Seeber and Armbruster, 1995), suggesting that any fluids migrating upward would not stop at the transition, but only at some other boundary. Beneath PFO, that boundary could be the 10 to 12 km deep base of the granitic portion of the batholith (Jachens et al., 1991). Given the uncertainties in depth estimations from both receiver functions and aeromagnetic data, the LVZ and base of the batholith could coincide. From the measured surface heat flow in the vicinity of PFO of $\sim 60 \text{ mW/m}^2$ (Lachenbruch, 1985), granite should remain brittle well below 14 km depth (Doser and Kanamori, 1986), and be impermeable to fluids (Bailey, 1990). From the above discussion, we find saline fluids trapped at the base of the granitic portion of the batholith to be the most likely tectonic explanation of the inferred crustal LVZ. The interpretation is however nonunique.

An alternate explanation is supplied by Min and Wu (1987), who demonstrate that granitic rock in a region of high heat flow will develop a pronounced LVZ. This provided a mechanism for a low V_p/V_s ratio observed for reflection-refraction data from the Tibetan Plateau, where the heat flow measured in 2 lakes was 91 mW/m^2 and 146 mW/m^2 (Francheteau et al., 1984). High thermal expansion of quartz relative to neighboring grain boundaries is hypothesized to cause microcracking at pressures corresponding to depths from 10 to 20 km, increasing until the temperature reaches 650°C when hardening associated with a phase change to beta-structure occurs (Kern, 1982). If this mechanism were responsible for the LVZ at PFO, we would expect a LVZ up to 10 km thick, with P velocities dropping even more than S velocities. As we discussed in the crustal modeling section, we have no constraints from receiver functions to distinguish the P velocity contrast. Scott (1992) however, in her travel time tomography study of the area, resolved no changes in Poisson ratio throughout the depth range that we have modeled as having the LVZ, and resolved no LVZ in P or S velocities. Thus, the base of the granitic portion of the batholith would have to be reached at least within a couple of kilometers depth beneath the top of the LVZ, for this mechanism to be invoked and produce a LVZ sufficiently thin to remain unresolved in the travel time tomography. While not impossible, that seems to require more fortuity than the first explanation. The low heat flow measured at the surface also would seem to argue against this mechanism,

but, as pointed out by Park et al. (1992), the surface heat flow of 60 mW/m^2 reflects temperatures at 10 km 3 m.y. ago. The opening of the Salton Trough in this region between 4 and 5 m.y. ago (Lachenbruch et al. 1985) has possibly influenced temperatures in the deep crust and mid-crust, although those changes would not yet be apparent at the surface.

Three-component recordings of teleseismic data in the same area as the magnetotelluric traverse would be helpful by permitting determination of whether a low resistivity zone and a seismic LVZ are coincident there. A seismic reflection profile to determine whether there is a bright reflector at the same depth would also be useful independent information, particularly as there is some correlation between low resistivity and crustal reflectors (e.g. Hyndman and Shearer, 1989).

Moho Topography

Our results relate to Moho topography on two length scales, the larger scale being the average over 15 to 20 km diameter beneath PFO of thicker crust northwest of PFO (figures 9 and 10) and the smaller scale being the inference of irregularity of the Moho with significant depth variation over just kilometers of horizontal distance (figure 17, inferred from figures 11-15). The larger scale result - the Moho model dipping 15° to 20° to the northwest that best fits receiver function Ps-P times (figure 11, left side) and is corroborated by Ps/P amplitude variations (figure 12) and PpPmp-P times (figure 14) - is consistent with the dominant topography being in isostatic balance, that is, with San Jacinto Peak having a thick crustal root.

The non-planar Moho topography and very steep Moho offsets over quite short horizontal length scales are more difficult to interpret, but potentially more interesting. The gravity data does not resolve whether Airy isostasy can be extended to those length scales. Nonetheless, the agreement of Airy isostasy and our larger scale observations, and their disagreement with elastic support, suggest an extension of Airy isostasy to the shorter scale observations. That is, the fracturing of the crust and subsequent uplift of the mountains due to unleashed buoyancy forces could account for topography on a smaller horizontal

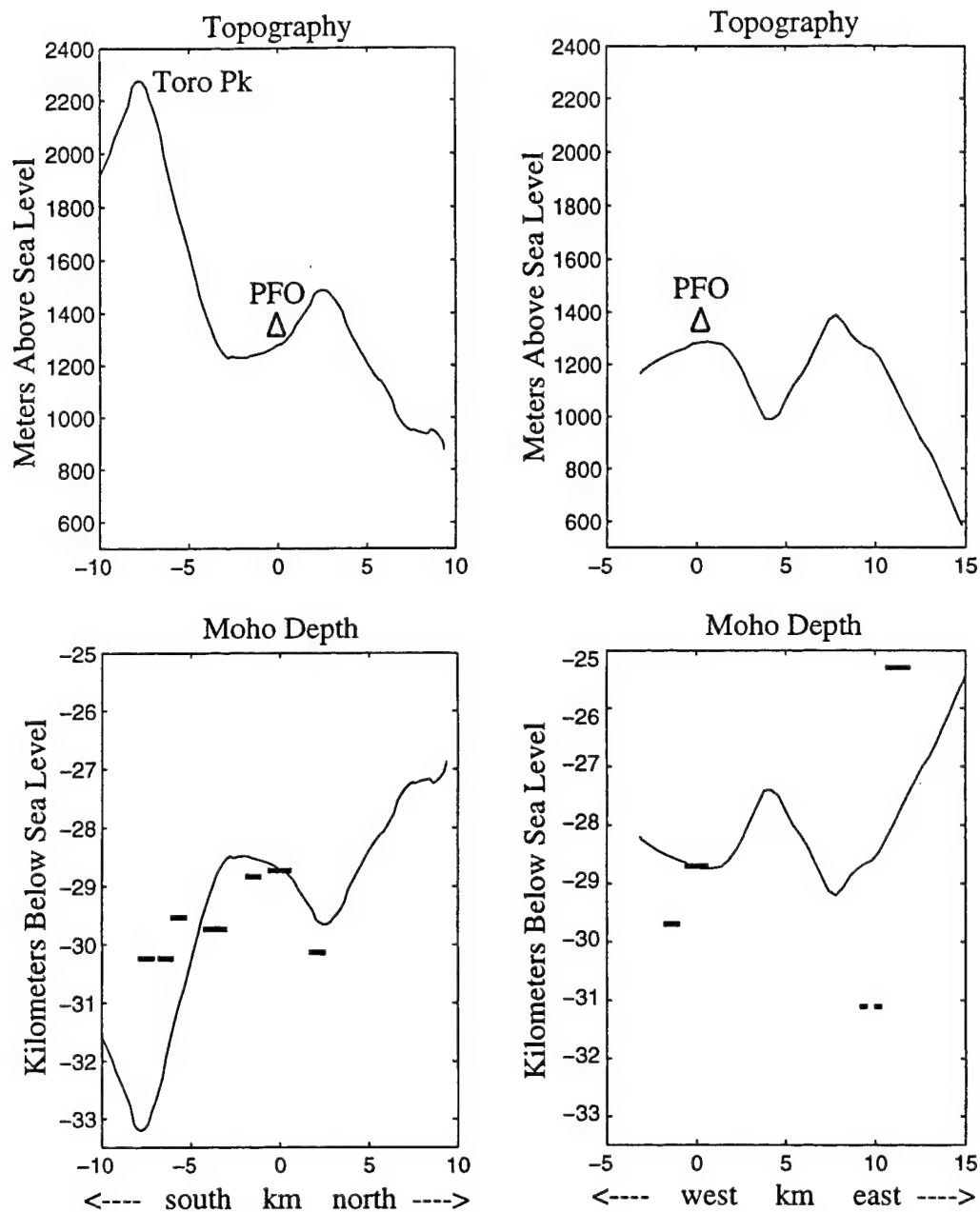


Figure 2.17: North-south (upper left) and nearly east-west (upper right) topographic cross-sections through PFO. The position of the second cross-section is indicated by a dashed line through the center of the circle in the left side of figure 11. PFO's position is indicated by the triangle. The lower plots indicate Moho depth for each cross-section inferred by assuming Airy isostasy with the depth of compensation at the Moho. The short horizontal bars are estimates of Moho depth based on receiver functions.

scale than San Jacinto Peak. Support for this speculation is given in Figure 17. There we have plotted the topography along north-south (left) and nearly east-west (right) cross-sections (the dashed line 12° south of east in the left side of figure 11). Beneath the topographic profiles are the predicted Moho depth profiles, based on Airy isostasy with compensation at Moho depth. The horizontal bars represent estimates of Moho depth along the profiles. Most estimates are based on the average Ps-P times of well over 10 events. The estimates are based on the depth of flat lying Moho. Estimates based on dipping layers would give similar relative results, but given the uncertainty in absolute measurements we chose to use the simplest model possible for depth estimates. Positions are based on the intersection of the Ps phase with the northwest dipping model of the left side of figure 11. While this is the best estimate available to us, based on minimization of the rms error in Ps-P times, it is clearly subject to large errors, and so correlating fine details of the depth estimates and predicted topography would be speculative. To first order however, the receiver function depth estimates match the predicted Moho depth variations well. The only exception is the bar at 31 km depth, plotted with a dashed line, at 10 km east of PFO. That estimate involved just 5 records, but they were all consistent. The bar at 11 to 12 km east of PFO at 25 km depth involved 4 records. Those two estimates were made from clusters of events centered approximately 4 km south and north respectively of the cross-section (the large pluses and large circles north and south of the cross-section line of the left side of figure 11). All other estimates were made using events whose Ps phases crossed the Moho within approximately a kilometer of one of the cross-sections. We originally identified the Moho Ps as the largest phase between 2.5 and 4.5 seconds after P, and interpret the cluster of anomalously large Ps-P times east of PFO as due to misidentification of a later phase as a Moho Ps. From the anomalous data then, which sample the Moho closer to the Salton Trough than any other data, we infer that the Moho becomes more gradational there due higher temperature, and so produces a much smaller converted phase.

We also note that other abrupt Moho offsets have been observed in the Pyrenees (a 15-20 km vertical offset has been inferred from refraction data (Daignieres, et al., 1989)), and in the Catalina Mountains, Arizona, (4 km of Moho depth variation has been inferred from receiver function modeling (Myers and

Beck, 1994)).

A final feature noted in the receiver functions is the large negative phase that follows the Moho Ps. Its interpretation as the Ps phase from an upper mantle low-velocity zone is consistent with results of the PACE refraction line (Benz and McCarthy, 1994). As this phase tracks the Moho Ps phase regardless of the Moho phase's timing, the above interpretation would require that the high-velocity upper mantle lid be of fairly uniform thickness and be offset with the crust. This does not seriously affect the assumption of compensation depth at the Moho, as density variations between the upper mantle lid and LVZ are thought to be very small. They are less than one percent in PREM.

Conclusions

Receiver function modeling has yielded a one dimensional velocity model beneath PFO which includes a high contrast shear-wave velocity inversion at 9 km depth (figure 6). Travel time tomography results have proven to be a useful complement to receiver function studies. Where receiver functions tell us of the existence of discontinuities and place them on a velocity-depth curve, tomography tends to smear out discontinuities but provides us with average slownesses which allow us to determine the depths of discontinuities with greater confidence. Inclusion of results from travel time tomography near PFO (Scott, 1992, Scott et al., 1994) has provided useful constraints in this study on both P and S velocities. Further, tomography results have constrained the LVZ imaged in receiver functions, but apparently smoothed over in the tomography, to be a very thin layer.

The overall tendency toward thicker crust to the northwest of PFO and the non-planar Moho topography and rapid spatial variation of Moho depth inferred from the spatial variations of receiver function Ps-P times, Ps/P amplitudes, and PpPmp-P times, is consistent with a model of Airy isostasy with depth of compensation at the Moho, operating over length scales of only kilometers. This agrees with gravity data, to the extent of its resolution. The extension of Airy isostasy compensated at Moho depth to such a fine scale suggests that fracturing of the crust at the time of uplift of the San Jacinto Mountains was not

limited to the major transform faults. Rather, the crust was fractured everywhere, and the current topography is due to the extreme apparent weakness of the crust at that time.

References

- Ammon, C.J., G.E. Randall, and G. Zandt, On the nonuniqueness of receiver function inversions, *J. Geophys. Res.*, 95, 15,303-15318, 1990
- Anderson, R.E., C.R. Longwell, R.L. Armstrong, and R.F. Marvin, Significance of K-Ar ages of Tertiary rocks from the Lake Mead region, Nevada-Arizona: *Geol. Soc. Am. Bull.*, 83, 273-288, 1972
- Aster R., P.M. Shearer, and J. Berger, Quantitative measurements of shear wave polarizations at the Anza seismic network, southern California: Implications for shear wave splitting and earthquake prediction, *J. Geophys. Res.*, 95, 12,449-12473, 1990
- Atwater, T., Implications of plate tectonics for the Cenozoic tectonic evolution of western North America, *Geol. Soc. Am. Bull.*, 81, 3513-3536, 1970
- Baker, G.E., H. Gurrola, J.B. Minster, and G. Zandt, Uncertainty estimates for receiver function waveforms and implications for resultant velocity models, submitted to *Bull. Seismol. Soc. Am.*, 1996
- Bailey, R., Trapping of aqueous fluids in the deep crust, *Geophys. Res. Lett.*, 8, 1129-1132, 1990
- Benz, H.M. and J. McCarthy, Evidence for an upper mantle low velocity zone beneath the southern Basin and Range-Colorado Plateau transition zone, *Geophys. Res. L.*, 21, 509-512, 1994
- Burdick L.J., and C.A. Powell, Apparent velocity measurements for the lower mantle from a wide-aperture array, *J. Geophys. Res.*, 85, 3845-3856, 1980
- Curry, J.R. and D.G. Moore, Geologic history of the mouth of the Gulf of California, in *Tectonics and Sedimentation Along the California Margin*, V. 38, Pacific Section SEPM, 17-35, Crouch, J.K. and S.B. Bachman, Eds., 1984
- Daignieres, M., B. de Cabissole, J. Gallart, A. Hirn, E. Surinach, and M. Torne, Geophysical constraints on the deep structure along the Ecore Pyrenees, *Tectonics*, V 8, 5, 1051-1058, 1989
- Davies, D., Seismology with large arrays, *Rep. Progr. Phys.*, 36, 1233-1283, 1973
- Dokka, R.K., and R.H. Merriam, Late Cenozoic extension of northeastern Baja California, Mexico, *Geol. Soc. Am. Bull.*, 93, 371-378, 1982
- Doser, D., and H. Kanamori, Depth of seismicity in the Imperial Valley region (1977-1983) and its relationship to heat flow, crustal structure, and the October 15, 1979, earthquake, *J. Geophys. Res.*, 91, 675-688, 1986
- Eberly, L.D., and T.B. Stanley, Cenozoic stratigraphy and geologic history of southwestern Arizona: *Geol. Soc. Am. Bull.*, 89, 921-940, 1978
- Ekren, L.D., C.L. Rodgers, R.E. Anderson, and P.P. Orkild, Age of Basin and Range normal faults in

- Nevada Test Site and Nellis Air Force Range, Nevada, in Eckel, E.B., Nevada Test Site: Geol. Soc. Am. Memoir 110, 247-250, 1968
- Elders, W.A., R.W. Rex, T. Meidav, P.T. Robinson, and S. Biehler, Crustal spreading in southern California, *Science*, 178, 15-24, 1972
- Fletcher, J., T. Fumal, H. Liu, and R. Porcella, Near-surface velocities and attenuation at two boreholes near Anza, California from logging data, *Bull. Seismol. Soc. Am.*, 80, 807-831, 1990
- Francheteau, J., C. Jaupart, S.X. Jie, K. Wen-Hua, L. De-Lu, B. Jia-Chi, W. Hung-Pin, and D. Hsia-Yeu, High heat flow in southern Tibet, *Nature*, 307, 32-36, 1984
- Fuis G.S., W.D. Mooney, J.H. Healey, G.A. McMechan, and W.J. Lutter, A Seismic Refraction Survey of the Imperial Valley Region, California, *J. Geophys. Res.*, 89, 1165-1189, 1984
- Gurrola H.G., G.E. Baker, and J.B. Minster, Simultaneous time domain deconvolution with application to receiver functions, *Geophys. J. Intl.*, 120, 537-543, 1995
- Hearn T.M. and R.W. Clayton, Lateral velocity variations in southern California, 2. Results for the lower crust from Pn-waves, *Bull. Seismol. Soc. Am.*, 76, 1986
- Hyndman, R. and P. Shearer, Water in the lower continental crust: modelling magnetotelluric and seismic reflection results, *Geophys. J. Intl.*, 98, 343-365, 1989
- Jachens, R.C., and A. Griscom, An isostatic residual gravity map of California. In: *The utility of regional gravity and magnetic anomaly maps*, Ed. W.J. Hinze, Seg, Tulsa, Oklahoma, 347-360, 1985
- Jachens, R.C., V. Todd, D. Morton, and A. Griscom, Constraints on the structural evolution of the Peninsular Ranges batholith, California, from a new aeromagnetic map: *GSA Abstracts with Programs*, v. 23, 38, 1991
- Kern, H., P- and S-wave velocities in crustal and upper mantle rocks under the simultaneous action of high confining pressure and high temperature and the effect of the rock microstructure. In: *High pressure researches in geosciences*, W. Schreyer, ed., 15-45, Schweizerbart'sche Verlagbuchhandlung, Stuttgart, 1982
- Lachenbruch, A., J. Sass, and S. Galanis, Jr., Heat flow in southernmost California and the origin of the Salton trough, *J. Geophys. Res.*, 90, 6709-6736, 1985
- Langston C.A., Structure under Mount Rainier, Washington, inferred from teleseismic body waves, *J. Geophys. Res.*, 84, 4749-4762, 1979
- Langston C.A. The effect of planar dipping structure on source and receiver responses for constant ray parameter, *Bull. Seismol. Soc. Am.*, 67, 1029-1050, 1977
- Myers, S.C. and S.L. Beck, Evidence for a local crustal root beneath the Santa Catalina Metamorphic

- Core Complex, Arizona, *Geology*, 22, 223-226, 1994
- Min Z., and F.T. Wu, Nature of the upper crust beneath central Tibet, *Earth and Planetary Science Letters*, 84, 204-211, 1987
- O'Connor, J.E., and C.G. Chase, Uplift of the Sierra San Pedro Mártir, Baja California, Mexico, *Tectonics*, 8, 833-844, 1989
- Owens, T.J., G. Zandt, and S.R. Taylor. Seismic evidence for an ancient rift beneath the Cumberland Plateau, Tennessee: a detailed analysis of broadband teleseismic P waveforms, *J. Geophys. Res.*, 89, 7783-7795, 1984
- Owens, T.J., R.S. Crosson, and M.A. Hendreckson, Constraints on the subduction geometry beneath western Washington from broadband teleseismic waveform modeling, *Bull. Seismol. Soc. Am.*, 78, 1319-1334, 1988
- Park, S., G. Jiracek, and K. Johnson, Magnetotelluric evidence from a brittle-ductile transition, Peninsular Ranges batholith, southern California, *Geophys. Res. Lett.*, 19, 2143-2146, 1992
- Proffett, J.M., Cenozoic Geology of the Yerington district, Nevada, and implications for the nature and origin of Basin and Range faulting: *Geol. Soc. Am. Bull.*, 88, 247-266, 1977
- Rogers, T.H., Geologic map of California, Santa Ana sheet, California Division of Mines and Geology, 1965
- Sanders, C.O., Earthquake depths and the relation to strain accumulation and stress near strike-slip faults in southern California, *J. Geophys. Res.*, 95, 4751-4762, 1990
- Scott, J., Microearthquake studies in the Anza seismic gap, Ph.D. Thesis, 277 pp., Univ. of Calif. San Diego, 1992
- Scott, J., T.G. Masters, and F.L. Vernon, 3-D Velocity structure of the San Jacinto Fault Zone near Anza, California, *Geophys. J. Intl.*, 119, 611-626, 1994
- Seeber, L. and J. Armbruster, The San Andreas fault system through the eastern Transverse Ranges as illuminated by earthquakes, *J. Geophys. Res.*, 100, 8285-8310, 1995
- Stock, J. M. and K. V. Hodges, Miocene to Recent structural development of an extensional accommodation zone, northeastern Baja California, Mexico, *J. Struc. Geol.*, 12, pp 315-328, 1990
- Sung, L. and D.D. Jackson, Crustal and uppermost mantle structure under southern California, *Bull. Seismol. Soc. Am.*, 82, 934-961, 1992
- Turcotte, D. and G. Schubert, *Geodynamics, Applications of Continuum Physics to Geological Problems*, pp 122-123, Pub. John Wiley and Sons, 1982

Walck, M. Teleseismic array analysis of upper mantle compressional velocity structure, Ph.D. Thesis, Calif. Inst. of Technology, 1984

Chapter 3

Uncertainty of Receiver Function Waveforms and Implications for Modeling

Abstract

This paper provides a thorough examination of the uncertainty and bias in the computation and interpretation of receiver functions. Real data are used to quantify uncertainty in receiver function waveforms and the resulting limitations in their interpretation are explored. A set of realistic synthetic seismograms are used to investigate the effects of additive noise and regularization on receiver function amplitudes. The synthetics are computed by raytracing through a simple earth model, convolution of the resulting seismogram with different observed P-wave signals, and the addition of different samples of real vertical and horizontal seismic noise.

We make a bootstrap estimate of the standard deviation of receiver functions for a high quality real data set and map this uncertainty into the velocity contrasts determined at model interfaces. Bias in the regularized deconvolution of noisy data is found to be comparable to, or greater than, the uncertainty indicated by the standard deviations of the mean receiver function.

We examine the effectiveness of averaging functions applied to receiver functions to correct the amplitudes of the initial peak. We find that normalization by averaging functions can restore the initial P amplitudes of individual synthetics even for high noise levels. The initial P amplitudes may be underestimated in stacks of many receiver functions if the normalization is performed using the maximum rather than zero lag amplitude of the receiver functions. The averaging functions greatly underestimate the extent of waveform distortion introduced by regularized deconvolution.

We use the velocity spectrum stacking technique, applied to data recorded from a broad range of ray parameters at a shield site, to investigate the trade-off between depth and velocity for models derived from receiver functions studies.

Finally, we consider the effects of inadequacy in the physical assumptions commonly made for receiver function interpretation. We show how inaccuracy in the assumed backazimuth and incidence of the signal can lead to significant errors in the interpretation of absolute, but not relative, receiver function amplitudes.

We conclude that:

- 1) Arrival times of identifiable receiver function phases are robust for what we consider the usable range of signal-to-noise ratio levels and are the primary source of information derived from receiver functions. They indicate the presence of discontinuities and their depths, given reasonable independent estimates of slowness.
- 2) Receiver function amplitudes provide poor constraints on the absolute magnitudes of the velocity contrasts and the dips of interfaces. Relative receiver function amplitudes can, however, be used to infer relative velocity contrasts at different interfaces and approximate orientations of dipping interfaces.

Introduction

Receiver function analysis is a more recently popularized but not as widely accepted technique as refraction and reflection profiling or tomography. Skepticism of the results from receiver function studies may be due to incomplete understanding of the strengths and limitations of the technique which occasionally results in optimistic over-interpretation of receiver functions. This paper is an attempt to improve the credibility of receiver functions by carefully discussing the limitations of their interpretation and to outlining those aspects of Earth structure that can most effectively be modeled using this technique.

Receiver functions represent P-to-S converted phases generated at interfaces beneath seismic stations, isolated from other complexities in teleseismic waveforms by deconvolution of the vertical component of a seismogram from its horizontal components (Burdick and Langston, 1977; Vinnik, 1977; Langston, 1979). This technique has been used to infer crustal structure (e.g. Langston, 1979;

Owens, 1984), subducting slab geometry (e.g. Cassidy, 1993), and upper mantle discontinuities (e.g. Gurrrola, et al, 1995; Vinnik, 1977, Kind and Vinnik, 1983, Bostock, 1996). The utility of receiver function waveforms in constraining Earth structure have been addressed largely via noise free synthetic studies (Ammon, et al., 1990, Cassidy, 1992). We extend that work by considering the uncertainty in receiver function waveforms, using real data, and by using realistic noisy synthetic seismograms to examine some causes of that uncertainty.

Ammon et. al. (1990) addressed resolution and uniqueness of one-dimensional velocity structures using noise-free synthetic data and automatic waveform inversions, and concluded that large, sharp velocity discontinuities can be identified and placed on a depth-velocity curve, while gradational velocity variations (with ~10% change) are not well resolved. They also demonstrated by varying layer thicknesses, P-wave velocities (V_p), S-wave velocities (V_s), and densities, that a wide range of models can produce identical receiver functions. Cassidy (1992) examined the importance of absolute amplitudes to the inference of dip angle of an interface and discussed a potential pitfall of modeling Ps/P amplitude ratios. Ammon (1991) introduced a technique to correct receiver function amplitudes by normalizing by averaging functions and discussed its importance in constraining near surface velocities.

We extend that work in several ways. We estimate the statistical uncertainty in receiver functions computed from real data and consider how that maps into inferred structure. We use "noisy" synthetics to isolate the effects of additive noise and degree of regularization on receiver functions waveforms. We also demonstrate that the regularized deconvolution of noisy data can introduce a large bias into receiver function amplitudes. We also investigate an important potential pitfall in modeling absolute amplitudes which may result from the error in assuming that the teleseismic P wave always arrives at the backazimuth and incidence predicted from the relative event-receiver positions.

We use velocity spectrum stacks (VSS) to place bounds on the range of depths and velocities that can produce similar phase delays across the range of teleseismic ray parameters.

Bootstrap Estimate of the Standard Deviation

For most of the examples in this section we use records from 29 teleseismic events, within a small range of ray parameters from the recording station, that were used to infer a one-dimensional velocity model (Baker et al., 1996). A bootstrap estimate of the standard deviation of the receiver function from those seismograms is determined (Efron, 1979, 1982). This is done by randomly selecting, with replacement (i.e. a seismogram may be chosen multiple times), 29 seismograms from the original set of 29, and calculating their receiver function. This is repeated 100 times, and the standard deviation of the resulting 100 receiver functions is an estimate of the standard deviation of the receiver function calculated from the original 29 seismograms. In our first example we complete this procedure using the simultaneous time-domain deconvolution technique of Gurrola et. al (1995). Figure 1 (right side) shows 2 standard deviation error bounds about the mean of these 100 receiver functions. The Kolmogorov-Smirnov test indicates that the amplitude distribution at any fixed time of these receiver functions is Gaussian. If the errors are also uncorrelated, 2 standard deviations represent the 95% confidence interval.

Confidence Intervals on Velocity Jump Amplitudes

We use the forward modeling approach of Baker et al. (1996) to map the 95 percent confidence interval of the receiver function amplitudes into minimum confidence intervals for the size of the velocity contrasts in their model by:

- 1) adopting the same independently determined surface P and S wave velocities as Baker et al. (1996).
- 2) choosing the depth of the first (next) discontinuity to fit the peak arrival time of the first (next) Ps phase.
- 3) determining the range of velocities in the second layer that produce synthetic receiver functions whose Ps phase spans the two standard deviation amplitude range of the corresponding observed Ps phase. For example, the velocity contrast at the shallowest discontinuity in the model can range from 0.8 to 1.5 km/s.

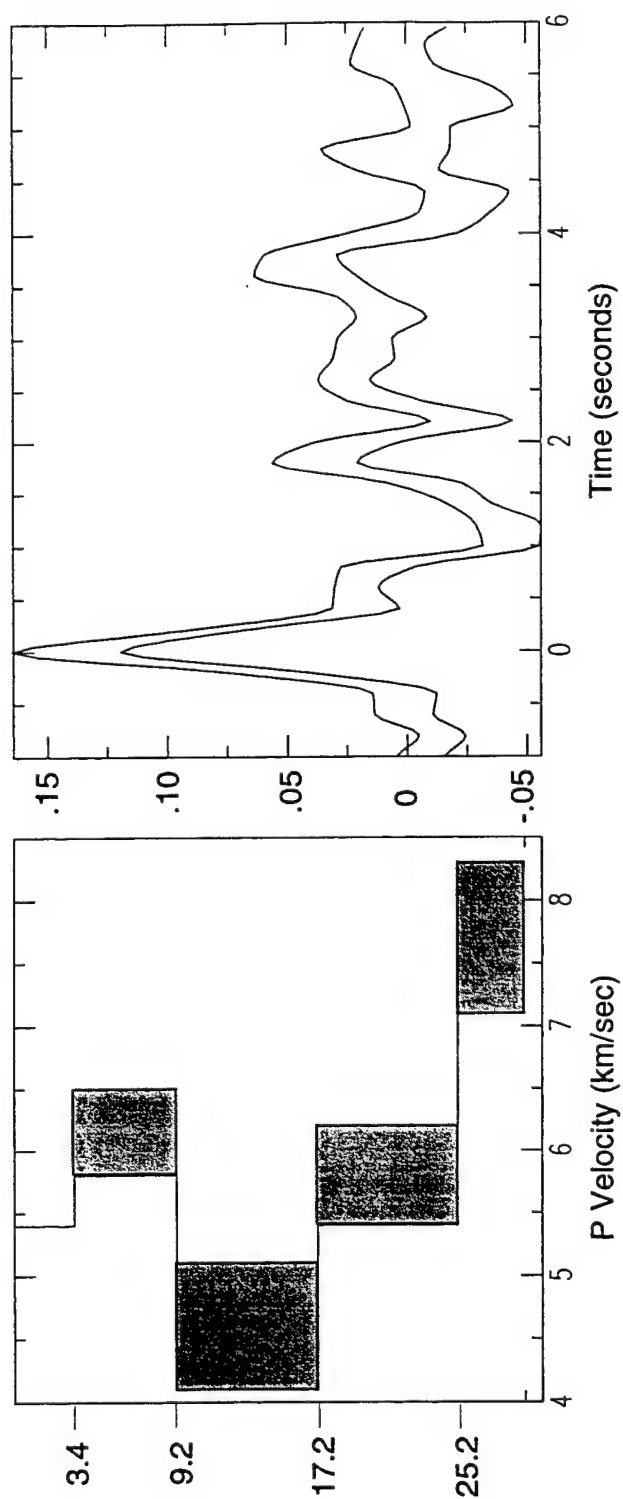


Figure 3.1: The receiver function modeled for crustal structure in Baker et al. (1996), *2 standard deviations from bootstrap estimates (right). Corresponding error bounds on the size of velocity discontinuities of the model found in Baker et al. (1996) (not on absolute velocities), ignoring the effects errors in velocity would have on depth (left).

To estimate confidence intervals for deeper discontinuities, we assume velocities for the shallower layers that precisely fit the mean amplitudes of the bootstrapped receiver functions and then repeat steps (2) and (3).

By assuming the values of velocity and thickness of the shallower layers that provide an exact fit to the earlier receiver function phases, we have optimistically estimated a "best case" uncertainty in the velocity contrast at each discontinuity (figure 1, left side). These are not estimates of uncertainty in the absolute values of the velocities, and represent minimum confidence intervals for two reasons. First, we have ignored errors in depth, V_p , and V_s of shallower layers that can increase the absolute error in velocities of deeper layers. We note that even without including the effects of errors propagated from shallower layers, the uncertainty in the inferred velocity contrast increases at each successive interface, which reflects the increased error in receiver function amplitudes as a function of time delay (figure 1, right side). Second, so far we have only considered the limitation on the resolution of velocity structure due to statistical uncertainty in receiver function amplitudes. We next discuss the bias introduced by deconvolution.

Amplitude Bias due to the Deconvolution

Receiver function amplitudes are usually presented as unbiased estimates of the true amplitude. That is, it is assumed that the true amplitude has a high probability of being within some uncertainty bounds about the estimated amplitude. In fact, the error in receiver function amplitudes due to bias introduced by low signal-to-noise level or by the deconvolution itself may be even greater than that indicated by the statistical uncertainty.

We explore two related possible sources of error, that due to the type of deconvolution we employ and that induced by the extent of regularization applied to the deconvolution. The simultaneous time domain deconvolution is set up as a regularized inverse problem using the method of Lagrange multipliers (Gurrola et al, 1995). Specifically, we write $Ax=b$, where A is the convolution matrix of a vertical seismogram, b is the horizontal seismogram, and x is the receiver function. The regularized

solution is $x=(A^T A+\lambda I)^{-1} A^T b$. The Lagrange multiplier, λ , balances the trade-off between misfit and the L_2 norm of the model. In choosing λ we attempt to balance what qualitatively appear to be excessive high frequency noise and excessive ringing. The choice of λ can be made consistent by automating its selection, often based on the curve of misfit versus model norm, or even based on some a priori knowledge of noise in the system. We find that within the range of acceptable values of λ , receiver function amplitudes vary significantly (figure 2).

Regularization is required because the data are contaminated by noise. In the formulation chosen, we are ignoring the presence of noise in the vertical records that are used to construct the A matrix. In teleseismic body wave recordings, the vertical seismograms have higher signal-to-noise ratios than those of the horizontal seismograms. Synthetic tests we have performed, in which we compare the results of deconvolution of noisy and noise-free vertical seismograms from noisy horizontal seismograms at typical signal-to-noise levels for both, indicate that ignoring the effects of noise on the vertical seismograms is not a dominant source of uncertainty in receiver functions.

In the frequency domain deconvolution for receiver functions, regularization is accomplished by the 'water level' technique in which all values of the power spectrum of the vertical component of the seismogram below a specified minimum value are replaced by that value (Oldenburg, 1981; Langston, 1979, Owens et al, 1984). High frequency noise introduced in the frequency domain deconvolution is usually eliminated by low pass filtering (usually with a Gaussian filter) after deconvolution. In figure 2 we show four different receiver functions, each calculated from the same 25 seismograms of events from a single source region (Baker et al., 1996). The top and second traces were computed using Lagrange multipliers of 1000 and 5000, applied to the simultaneous time domain deconvolution of these 25 seismograms. The third and fourth traces were computed in the frequency domain using water levels of 10^{-5} and 10^{-4} and Gaussian filters of half-width 5. These four receiver functions appear to be equally good candidates for modeling.

In interpreting receiver functions, we usually rely on the amplitude ratio of secondary arrivals to the initial peak more than we rely on absolute amplitudes. We therefore consider the variation in that

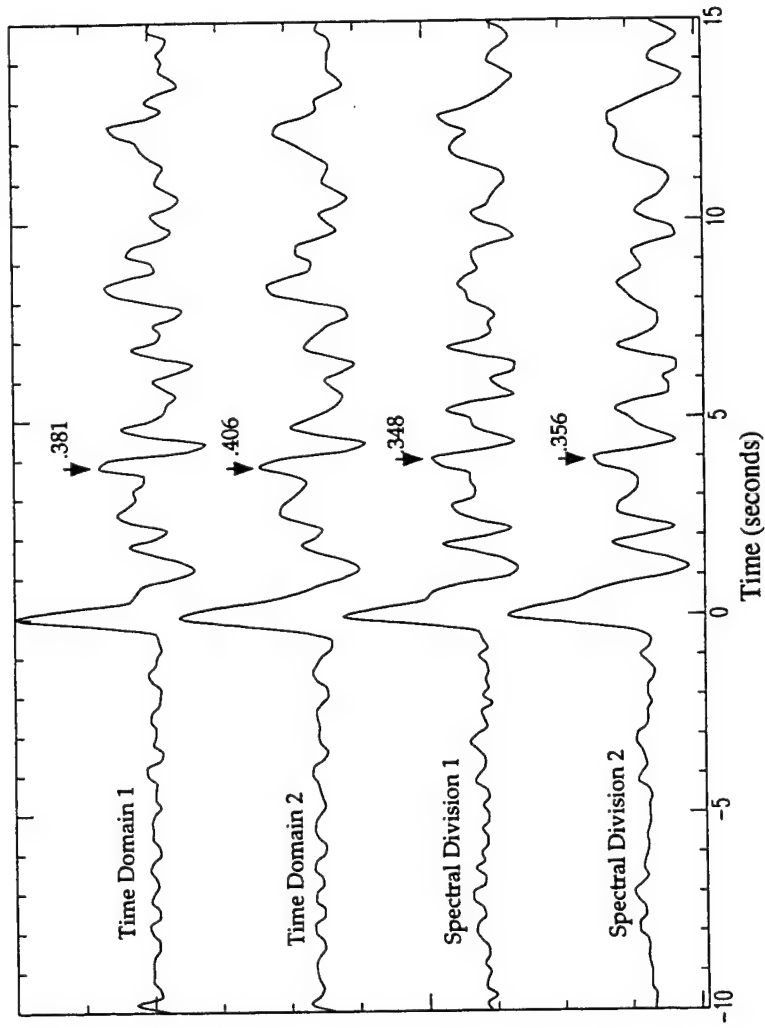


Figure 3.2. Receiver functions calculated from 25 events in one source region, recorded at Piñon Flat Observatory, California. The deconvolution was performed using both time and frequency domain methods, each with 2 different but very similar degrees of regularization applied. The time domain deconvolution receiver functions (top 2 traces) have Lagrange multipliers of 1000 and 5000 (from the top down). The spectral division receiver functions with comparable degrees of regularization from the water level pre-whitening technique (water level values of 0.00001 and 0.00001 of the maximum amplitude, last 2 traces respectively).

amplitude ratio. Each trace is labeled with that receiver function's Moho Ps/P amplitude ratio. The Ps/P ratio of the second trace is 17% larger than that of the third trace, and we do not know which of these more closely represents the "correct" amplitude ratio. From this we conclude that significant systematic error, in addition to the statistical uncertainty estimated in the previous section, is likely present in receiver function amplitudes. We also observe that estimated amplitudes of smaller arrivals are even less stable than the Moho Ps amplitude.

The Effect of Additive Noise

To investigate the error due to additive noise and the regularization required in the deconvolution operation, we use realistic synthetic seismograms computed for a layer over a half space model.

To produce the noisy synthetic seismograms

- 1) We first compute generalized ray theory synthetic seismograms (Langston and Helmberger, 1975) through a simple one layer model;
- 2) We convolve this synthetic with 25 different source functions (generated by windowing the first 6 seconds of teleseismic P-arrivals and tapering the trailing end), to produce 25 different synthetic seismograms.
- 3) We then add 25 different segments of real horizontal and vertical seismic noise to the appropriate synthetics (figure 3).

We perform the simultaneous time-domain deconvolution for the 25 synthetic seismograms for a range of noise levels. For each successively lower level of signal to noise ratio, a larger Lagrange multiplier was used to reduce the successively higher levels of high frequency oscillations in the solutions. Figure 4 shows the effect of the higher noise level and degree of regularization on Ps/P amplitude ratios. The uncertainty bounds are ± 2 standard deviations, estimated by bootstrap as was done for figure 1. The number above each datum is the Lagrange multiplier. The receiver functions calculated from the 25 events at each noise level are shown below each datum. The horizontal dotted line at 0.380 indicates the expected value of the Ps/P amplitude ratio. As the S/N decreases, the Ps/P

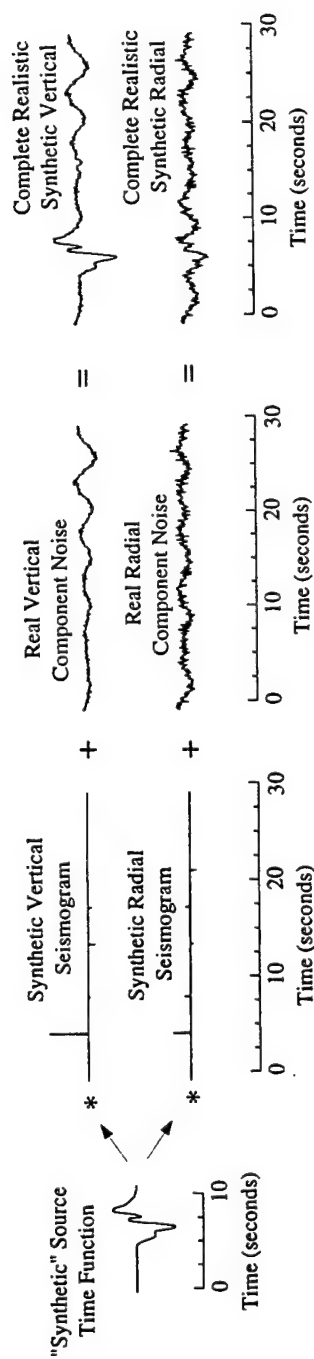


Figure 3.3: Construction of synthetic seismograms. We use the first 6 seconds of real vertical component P arrivals, tapered at the trailing edge, as source functions (e.g. leftmost trace), convolved with the appropriate component synthetic seismograms for a simple 30 km thick, 6 km/sec layer over an 8 km/sec half space (second set of traces from the left). Segments of real vertical and radial component seismic noise scaled to some particular noise level (third set of traces), are added to the appropriate convolution products to produce realistic noisy synthetic seismograms (fourth set of traces).

amplitude ratios also decrease, to the point that the bias becomes a greater source of error than the statistical uncertainty. In fact, the error bounds due to statistical uncertainty do not even increase significantly until the lowest S/N is reached. That is partly because the successively higher levels of regularization needed to damp out high frequency oscillations in the receiver functions at higher noise levels, help to keep the variation in amplitudes small, even as the mean amplitude shifts further and further from the true solution. From this we can see that error bounds based on the statistical uncertainty are not indicative of the accuracy of the estimate. This is troubling when we consider that for S/N=10 (figure 4), the large individual receiver function arrivals stand out much further above the background noise level than do arrivals in real receiver functions. The frequency domain deconvolution produces a very similar result.

The effects of noise level and regularization are not independent. A given level of regularization will produce different results depending on the level and character of noise in the data. Even so, we can observe something of the relative effects of noise and regularization level in figure 5. There we see the receiver functions calculated from the 25 synthetic seismograms at a range of S/N levels and levels of regularization (each column is a constant S/N, each row is a constant λ). One striking effect is the difference between over- and under-damped receiver functions. Receiver functions with no damping (bottom row) all have excessive high frequency noise, which decreases with an increase in λ . Receiver functions with increasingly larger λ are much smoother, but arrivals begin to exhibit large sidelobes. Also, for a "good" receiver function, increased regularization decreases the Ps/P amplitude ratio. For example, at virtually no noise (the right column), the receiver function with no regularization has the correct amplitude. One might however prefer the receiver function at $\lambda=10^3$, as it has much less high frequency noise, so the significant arrivals are more prominent, but the Ps/P amplitude ratio is much less accurate. One reason for that is that increasing the regularization level increasingly minimizes the norm of x , in addition to satisfying the data, i.e., minimizing $Ax=b$. This does not mean that under-regularized receiver functions will provide more accurate amplitudes for real receiver functions. In our simulations we can not obtain much more accurate amplitudes for higher noise level receiver functions

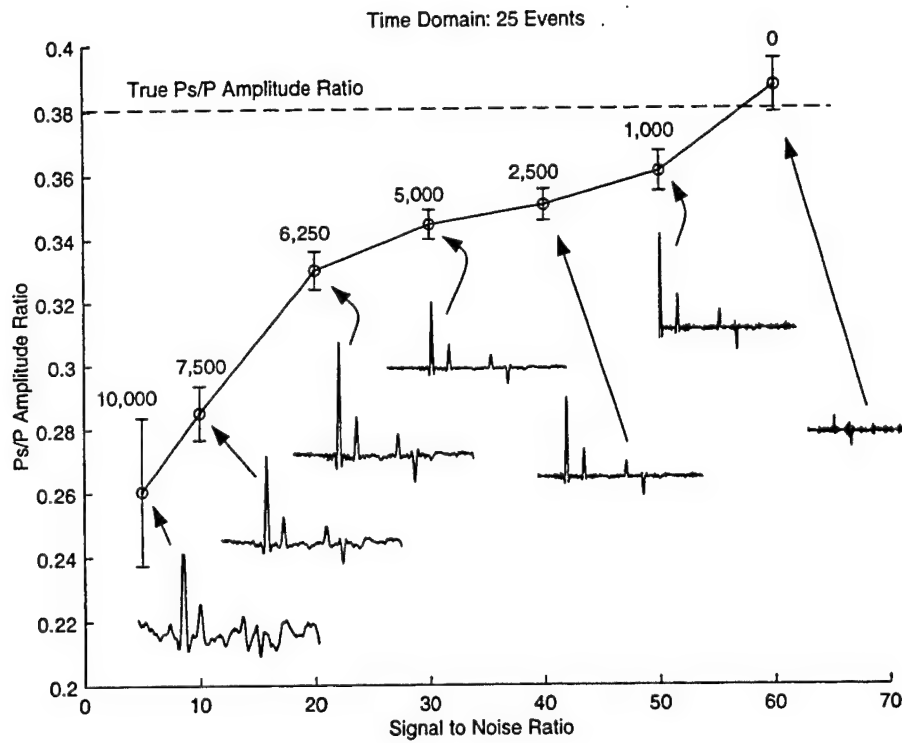


Figure 3.4: Ps/P amplitude ratios for the receiver functions calculated from 25 synthetics of the type illustrated in figure 3, at various signal to noise levels. The true Ps/P amplitude ratio of 0.380 is indicated by the dashed line. The uncertainty bounds are bootstrap estimates of 1 standard deviation of the distribution. The value of the Lagrange multiplier is shown above each datum, and the receiver function for each is shown below. The Ps/P amplitude ratio decreases with increasing noise and regularization.

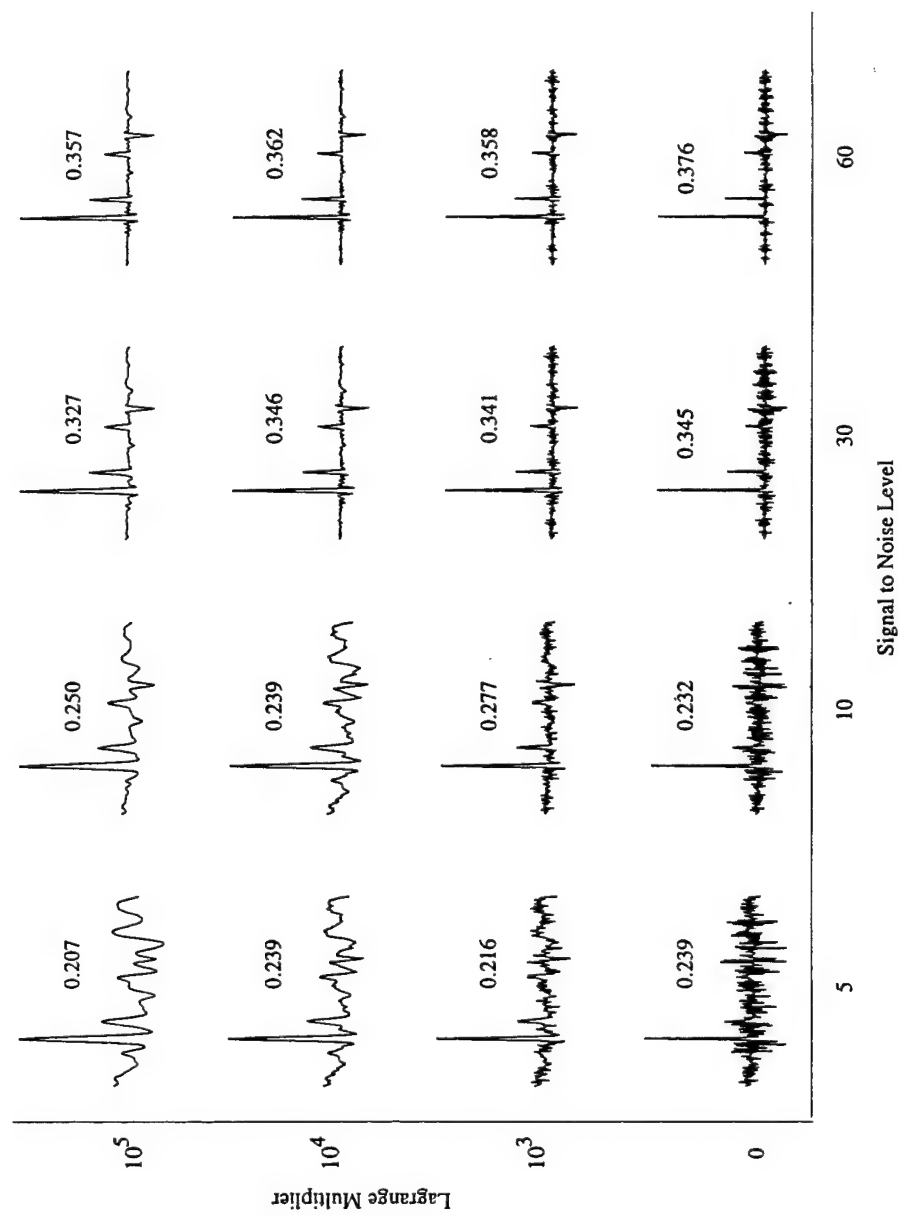


Figure 3.5: This figure illustrates the effect of varying noise level (horizontal axis) and level of regularization (vertical axis) on receiver function waveforms. The receiver functions are calculated with the simultaneous time domain method from 25 noisy synthetic seismograms. The numbers above each receiver function are the P_s/P amplitude ratios.

by applying less regularization. At too low a regularization level, the true arrivals are overwhelmed by the high frequency noise (figure 5). Also, these experiments are idealistic in that they only address one source of error, namely additive noise.

The effects of increasing regularization at higher noise levels are also more complicated. For example, at $S/N=10$ and $\lambda=0$ (second column, bottom row, figure 5), the later arrivals are indistinguishable in the high frequency noise. As λ increases to 10^3 (second row up), the major arrivals become more distinct and the Ps/P amplitude ratio becomes somewhat more accurate. At $\lambda=10^4$ (third row up), the receiver function has a great deal of long period noise, and the Ps/P amplitude ratio has decreased again. At $\lambda=10^5$ (top row), the receiver function actually looks quite good. It is very smooth, and although there are significant sidelobes, especially around the initial peak, the messy erratic look has improved. The Ps/P amplitude ratio has also increased again. This improvement is misleading however, and clearly illustrates a danger in overdamping. It is commonly thought that if roughness is heavily penalized, then any arrivals still in the model must be necessary to fit the data. Here we see a nice looking receiver function, with a clear negative arrival, which is completely spurious, between the first and second legitimate secondary arrivals. Such features can be produced in overdamped models to provide the next best fit to the data when the true model features are penalized.

Figure 5 also indicates the fallibility of the argument that one should damp all receiver function calculations similarly, in the mistaken belief that this will treat all the data similarly so the results will be comparable. The effect of a given level of damping varies greatly depending on the structure of the noise relative to the forward model.

To further illustrate the effects of varying noise level on waveforms, each of the 25 individual receiver functions for each S/N level are shown in the right hand column of figure 6. These receiver functions were calculated using the frequency domain deconvolution of Ammon (1991) which attempts to preserve absolute amplitudes. As the signal to noise level decreases, the amplitudes of recognizable phases begin to vary. The initial P and Ps amplitudes given in figure 6 are the averages of the 25 receiver functions at each S/N level. The 2 standard deviations errors listed indicate the statistical

uncertainty of the measurements. For receiver functions with no noise (top row, right side), the amplitudes are essentially correct - the expected P and Ps amplitudes are 0.445 and 0.169 respectively. Note however the variation in the waveforms. The set of receiver functions (on the top left of figure 6) are computed from synthetic seismograms with no noise added. The only difference between the seismograms used is the shape of the synthetic source function convolved with each.

As was observed for the time domain receiver functions, the accuracy of Ps arrival amplitudes deteriorates as S/N decreases (S/N are given to the right of each set of traces), even though the receiver functions still look acceptable. For example, in the case where S/N equals 10 (bottom right, figure 7), the stack of all of the individual receiver functions looks as good or better than typical real receiver functions but precise matching of amplitudes would lead to extremely inaccurate estimates of Earth structure.

The Effects of Regularization on Receiver Function Waveforms

We consider what causes some of the effects observed in figures 4, 5, and 6. For simplicity we will confine the remainder of our discussion of the effects of regularization in the framework of the time domain deconvolution. Similar effects and explanations exist for the frequency domain deconvolution. We observed that if too little regularization is applied, the receiver function is plagued by high frequency noise, and if too much regularization is applied, the receiver function is plagued by ringing about each arrival. The reasons for those effects are straightforward. In any inverse problem, which we can write as $Ax=b$, high frequency error in the solution x is due to the excessive prominence in x of the eigenvectors associated with small eigenvalues of the A matrix. Even though we do not solve the matrix inversion with singular value decomposition, or regularize by singular value truncation, it is appropriate to discuss these effects in terms of the eigenvectors of matrix, as regularization works by directly affecting the influence of eigenvectors.

Because the regularized problem is written $(A^T A + \lambda I)x = A^T b$ (Gurrola, et. al., 1995), we examine the eigenvalues and eigenvectors of $A^T A$, rather than A . Figure 8 shows some of the eigenvectors

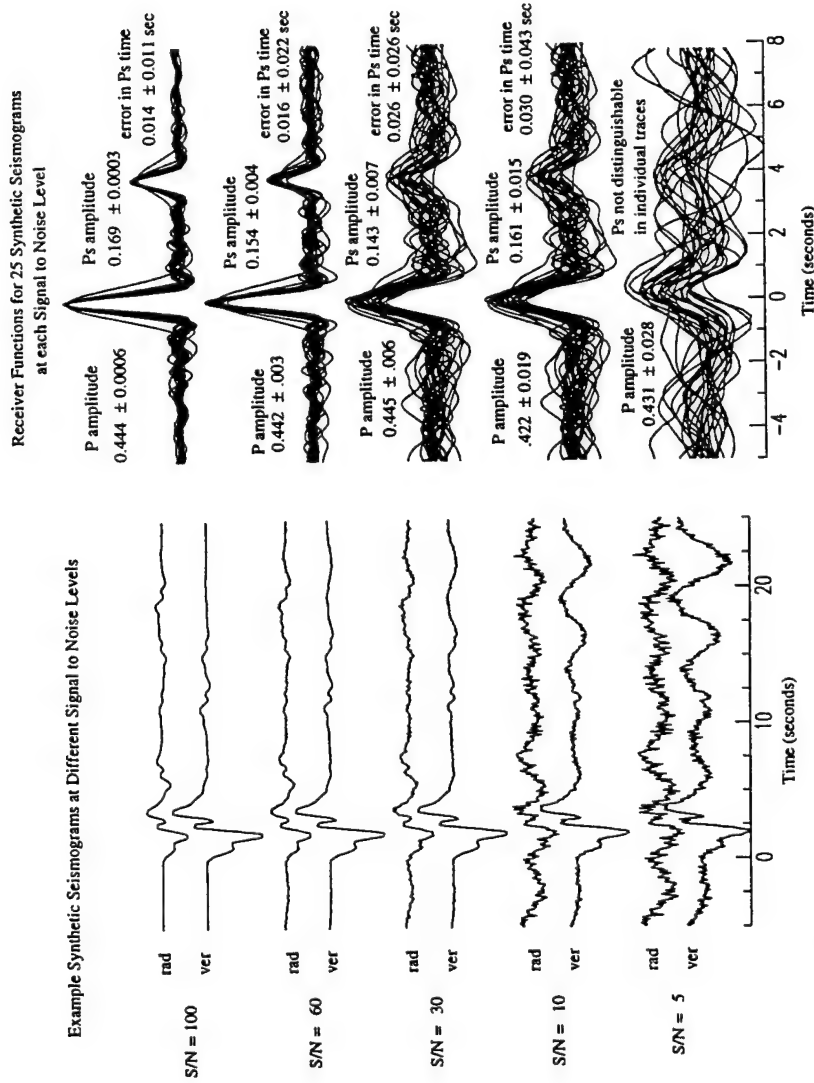


Figure 3.6: This figure illustrates the effect of varying noise level on individual receiver function waveforms. In the left column are typical synthetic seismograms at each signal to noise level (the maximum signal peak to rms pre-event noise levels, S/N, are listed to the left of each set of traces). The receiver functions for 25 such synthetic seismograms (with different source functions and noise windows, but the same S/N levels), are shown on the right, with the mean and 2 standard deviations uncertainty listed for the P and Ps amplitudes and the Ps-P timing error of each set.

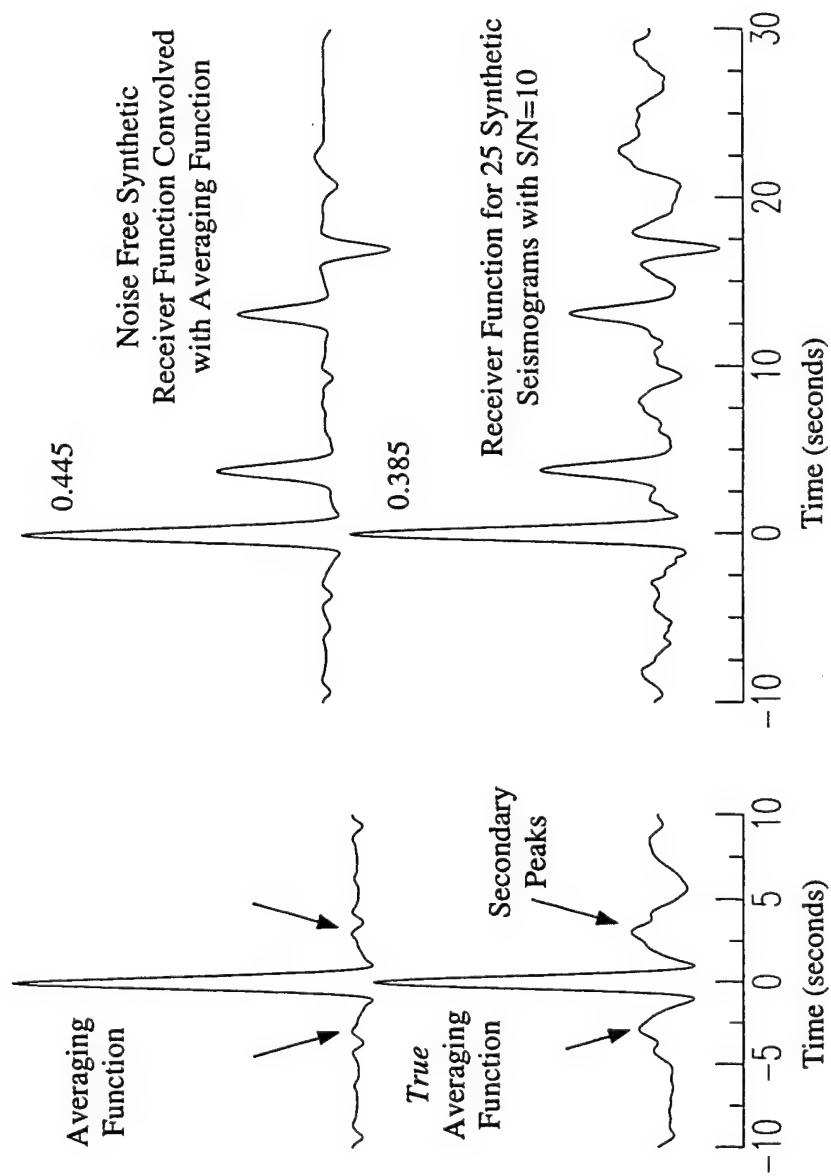


Figure 3.7: Comparison of a stack of 25, $S/N=10$, receiver functions (bottom right) with a synthetic receiver function for the same layer over a half space model after convolution with the averaging function (averaging function is upper left and convolution with synthetic is upper right). The sidelobes of the averaging function are very much smaller than those of the receiver function. A more accurate estimate of the effects of deconvolution on the receiver function is shown on the lower left (discussed in text).

associated with the largest and smallest eigenvalues of ATA, for the real receiver function of figure 1. We confirm that the smallest eigenvalues are associated with very high frequency eigenvectors. With a condition number of 106, the smallest eigenvalues ATA will be overemphasized in the inverse. By applying a higher degree of regularization (i.e. increasing λ), the smallest eigenvectors lose their significance in the inversion and so the high frequency noise is damped and the fit to the data is compromised. When the model size is penalized to effect regularization, the amplitudes of peaks in the model are decreased, and in the case of receiver functions, sidelobes and prominent secondary peaks adjacent to the true peaks provide the next best fit to the data. This is observed in figures 4, 5, and 6.,

We have found that significant variation of amplitudes (e.g. figure 2) occurs for different reasonable choices of λ . Further, there is no possible choice of λ that will let us avoid all the negative consequences of deconvolution of noisy data. We can attempt however to estimate the effect of regularization on the waveforms. To that end we investigate the use of averaging functions.

Averaging Functions - Preserving Absolute Amplitudes

Averaging functions are calculated by deconvolving vertical component seismograms from themselves, with the same level of regularization as applied to the corresponding receiver function calculation (Ammon, 1991). Accurate initial peak amplitudes are important in constraining near surface velocities, so to restore absolute amplitudes, receiver functions are normalized by the maximum amplitude of their averaging functions (Ammon, 1991). Initial P amplitudes are accurately restored by the application of averaging functions to the noisy synthetics, throughout the given range of noise levels. In the worst case, $S/N=10$, the mean amplitude of the initial P-arrivals is 95% of the true amplitude and nearly within two standard deviations of the true value.

We note, however, that the initial peak amplitude is underestimated when the receiver functions are stacked. This holds true even at long period (i.e. even for receiver functions smoothed with a Gaussian of half-width of unity). This error occurs because of what appear to be timing errors at high noise levels. At all noise levels, in stacks of receiver functions, the peak arrival times of major phases

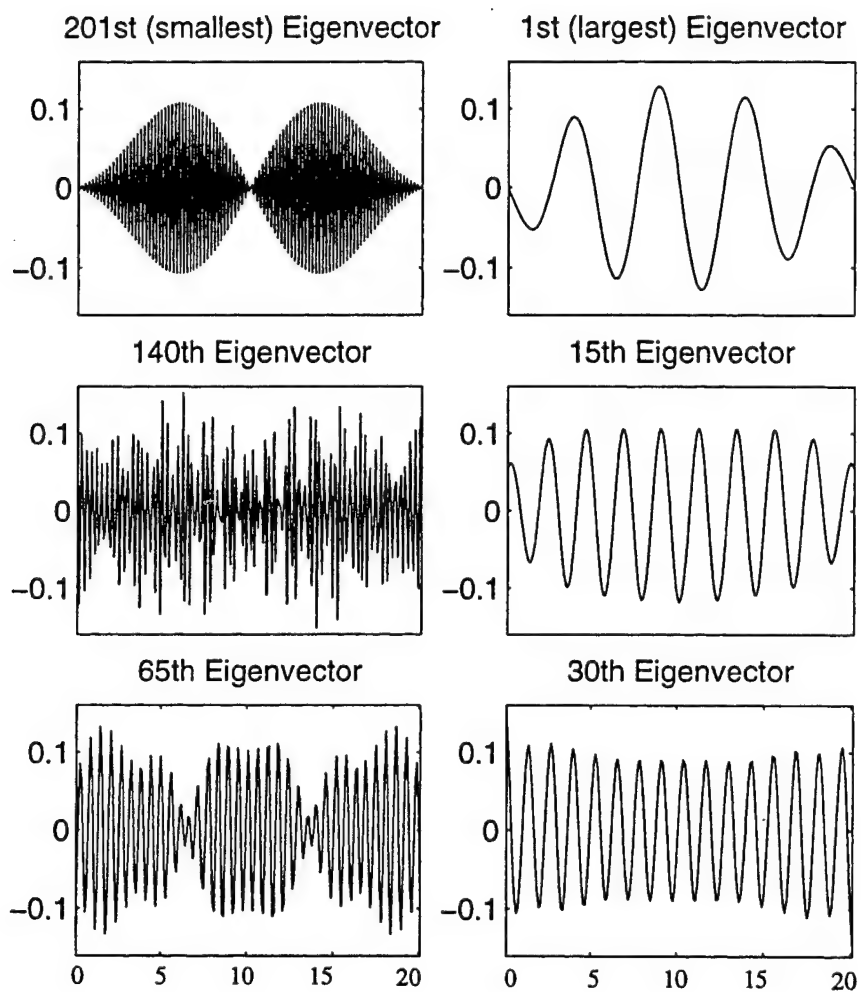


Figure 3.8: Eigenvectors of the ATA matrix (where A is the convolution matrix of the vertical seismograms) for the receiver function shown in figure 1. The smallest eigenvalues are associated with high frequency oscillations.

are correct, but the arrival times of these phases can be off by several time steps in individual receiver functions (we used $\Delta t = 0.05$ seconds). For example, for the $S/N=10$ synthetics, the mean maximum amplitude for all 25 receiver functions (figure 6) is 0.422, 95% of the true amplitude, but for a stack of the 25 receiver functions, the peak amplitude is 0.385, 87% of the true amplitude (figure 7). The reason is that the individual receiver function peaks don't quite line up in time. For the $S/N = 10$ receiver functions, 12 are aligned, 5 each are 0.05 seconds late and early, 1 is 0.1 second early and 2 are 0.15 seconds late.

This problem can be avoided with a minor change in how the normalization is done. Typically, the maximum receiver function amplitude is normalized. When the maximum peak position does not coincide with the expected initial peak position, the maximum value ends up with the correct normalized value and the value at the expected initial peak position is too small. That results in smaller amplitudes than expected when receiver functions are stacked. If receiver function amplitude at the expected initial peak position were normalized, then the value of the stack's initial peak would be correct. We note that the receiver functions should not be shifted in time to align the initial peaks before stacking, as the root cause of the apparent timing errors are actually amplitude errors. That is, the additive noise causes random errors in the initial peak and near-initial peak amplitudes, occasionally causing the near-initial peak values to be greater.

Averaging Functions - Estimating the Effects of Deconvolution on the Waveform

Cassidy (1992) suggests that if sidelobes are present in the averaging functions, they could be incorporated into the synthetics when modeling receiver functions. There is a fundamental difference however, between the deconvolutions for receiver functions and averaging functions. How the radial seismogram is mapped into the receiver function by the inverse of vertical seismogram's convolution matrix depends on the structure of the data in terms of the eigenvectors of the forward modeling matrix. That relationship will be very different, and more complicated, for data that do not fit the model (i.e. receiver functions) than for data that identically fit the model (i.e. averaging functions).

That leads us to question how good of an estimate of the effects of regularization the averaging function may be. Therefore we use the noisy synthetics to test how well averaging functions estimate the effects of deconvolution on the waveform.

We calculate and stack the receiver functions and averaging functions for the 25 synthetic seismograms with $S/N = 10$. We use the frequency domain deconvolution with the modification for preserving amplitudes (Ammon, 1991). We compare the receiver function (bottom right, figure 6) with an ideal synthetic convolved with the averaging function (top right, figure 6), and find that the sidelobes are much larger for the receiver function than predicted by the averaging function.

We do one further experiment with these synthetics to more accurately quantify the effect of regularized deconvolution on producing sidelobes. When we calculate averaging functions, we deconvolve the vertical component synthetic seismograms with noise added (figure 3), from themselves. We now calculate what we label as a true averaging function (lower left, figure 6), by doing a slightly different version of the same thing. We make two similar vertical seismograms using the same source function, but using two different segments of vertical seismic noise, and deconvolve one from the other. We do this 25 times and stack the results. Because the additive noise is different for each pair of seismograms being deconvolved, there is not a precise fit to the data as there was in the case of the averaging function, and so the situation of the true averaging function is closer to that of the receiver function. The sidelobes about the initial peak of the true averaging function are twice as large as they are in the standard averaging function, and the secondary positive peaks (arrows on figure 7) are an order of magnitude larger than for the standard averaging function. From this we conclude that averaging functions provide a very optimistic, minimum estimate of the waveform distortion due to regularization. This is strongly related to the point made in conjunction with figure 6, that a single level of regularization will not have the same effect on two different sets of data with different noise characteristics.

We consider one final aspect of averaging functions. The averaging function is nominally only valid for the initial receiver function peak. We test the validity of the estimate for other points of a

receiver function by considering the operation in the time domain. The resolution about any point in a receiver function is shown by the corresponding row of the resolution matrix, $R=(A^T A+\lambda I)^{-1} A^T A$ (e.g. Menke, 1989). That is, each point of a receiver function may be thought of as having a different averaging function. There is no general guarantee that the averaging functions for different points of a receiver function will be the same. Nonetheless, for the deconvolutions performed for both the receiver function modeled in Baker et al. (1996) and the more highly regularized noisy synthetics of figure 4, the greatest difference in amplitudes of averaging functions about different points of the receiver functions was less than 1 percent and the shape of averaging functions about different points is nearly indistinguishable. This confirms the assumption of Ammon (1991) that simply deconvolving the vertical components from themselves, which in the time domain corresponds to finding the row of the resolution matrix corresponding to the initial peak of the receiver function, is as appropriate for each point of the receiver function as it is for the initial peak.

This has no bearing on the effects of regularized deconvolution of noisy data in diminishing the amplitudes of secondary peaks. The resolution matrix, and averaging functions, are only affected by the assumed Green's functions (the vertical seismograms) and ignore how well the data are fit, which is what will control the amplitudes of secondary peaks.

Relationship between receiver function amplitude, model velocity, and estimated depths

Gurrola and Minster (1996) stack receiver functions from all azimuths using a modification of the velocity spectrum stacking technique (VSS) commonly used in reflection seismology (Taner and Koehler, 1969). We use that technique here to examine the range of models that can explain the full range of teleseismic data. We use data from a shield location with a simple crustal model in order to focus on the trade-off between velocity and depth in arrival times and minimize possible complications due to complex crustal structure.

We computed receiver functions from the same 199 teleseismic events (from 300 to 900 distance range) recorded at Obninsk, Russia (OBN) used by Gurrola et al. (1996). After low-pass filtering at 0.3

Hz, these receiver functions were effectively modeled with two layers over a half space (figure 9). The large number of events, distribution of source regions, and simplicity of the model make this an ideal station for a discussion of the trade-off between velocity and depth in modeling receiver structure. Figure 10 is a VSS produced from the OBN receiver functions. Each point in a VSS is produced by applying moveout corrections appropriate for a particular phase to each receiver function, and stacking them. The goal is to identify the velocity models that produce the largest stacked amplitude for the target phase. The points in the VSS in figure 10 represent the combinations of V_p , V_s , and depth that produce similar "largest" amplitudes (within 95% confidence levels determined by a bootstrap estimate) when events from the entire teleseismic range are stacked after correction for moveout (Gurrola and Minster, 1996). The plot on the upper left is a 3-D view of the models that fit the arrival times equally well. The other three images in figure 10 are the same VSS, but viewed along each coordinate axis. Velocities are represented as a percentage of PREM, and are allowed to vary up to 10% from that model, which is more than twice the range found by virtually all regional and global velocity models (Nolet et al., 1994). Such a range of V_p and V_s provide a 20 km range of equally acceptable model depths (figure 10, upper left).

We examine the relationship between perturbations in model parameters to clarify the basis of the variations observed in figure 10. The moveout correction is given by

$$t = z \left(\sqrt{\frac{1}{V_s^2} - p^2} - \sqrt{\frac{1}{V_p^2} - p^2} \right) \quad (1)$$

where t is the time delay of the P_s phase relative to the direct P wave (moveout correction), z is depth, V_s is the S -velocity, V_p is the P -velocity, and p is the ray parameter. By differentiating equation 1 with respect to z , V_s , and V_p , we arrive at an expression describing the relationship between small perturbations in these parameters that produce similar moveout corrections.

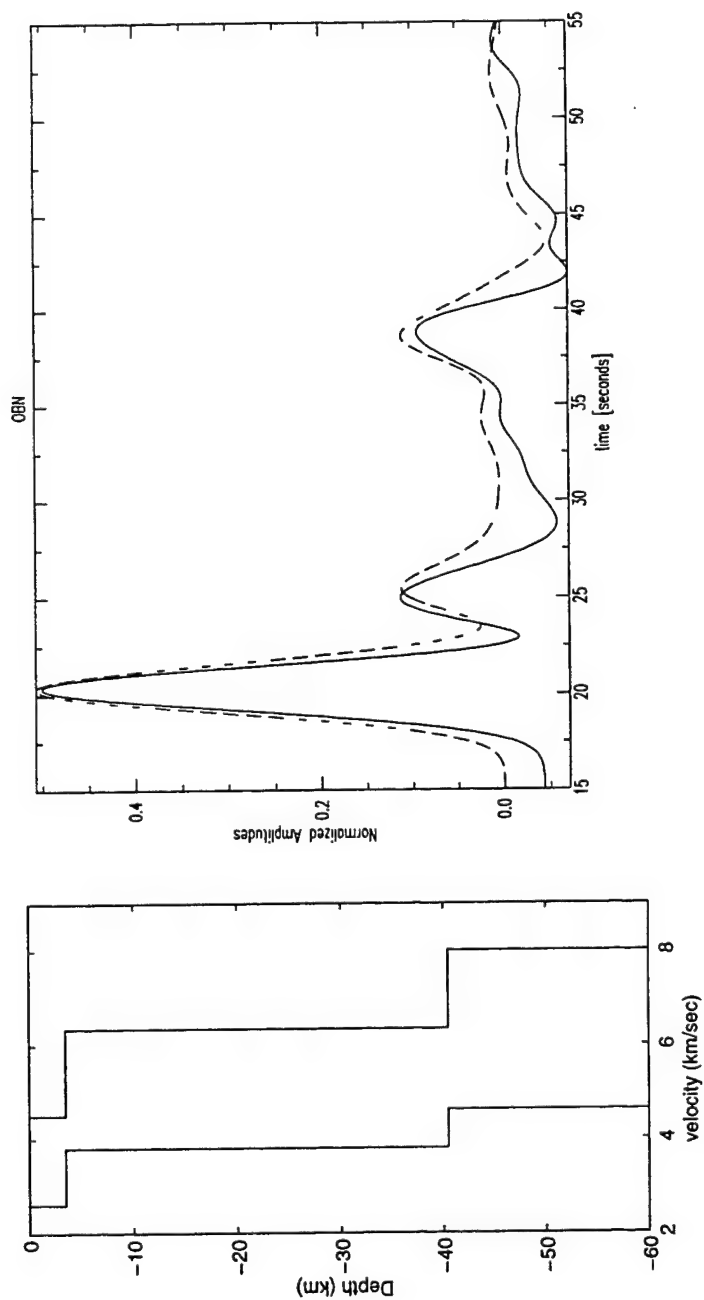


Figure 3.9: Velocity model used for OBN data (left) and fit of the synthetic from the model (dashed line) to the OBN data (solid line).

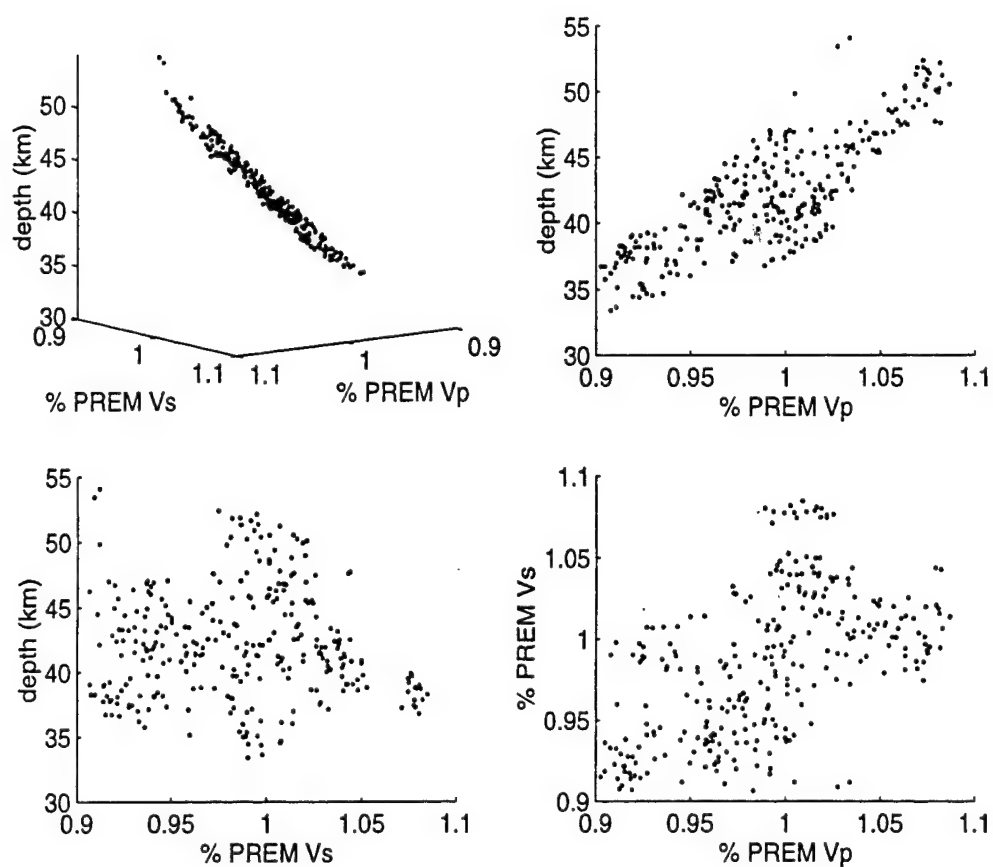


Figure 3.10: VSS for data recorded at OBN. Upper left, view in 3-space. Upper right, view in V_p -depth space. Lower left, view in V_s -depth space. Lower right, view in V_p - V_s space.

$$dt = -\frac{z}{V_s^2} dV_s + \frac{z}{V_p^2} dV_p + \left(\frac{1}{V_s} - \frac{1}{V_p} \right) dz \quad (2)$$

For convenience Gurrola and Minster (1996) represent perturbations in these model parameters as a ratio of the perturbation in the model parameters and a fixed value of each, resulting in

$$-1.73dM_s + dM_p + 0.73 dM_z = 0, \text{ or}$$

$$dM_z = \frac{(1.73dM_s + dM_p)}{0.73} \quad (3)$$

where $dM_p = dV_p/V_p$, $dM_s = dV_s/V_s$ and $dM_z = dz/z$ and assuming a Poisson solid ($V_p/V_s = \sqrt{3}$). From equation 3 we see that a correlated 10% spread of possible values for V_p and V_s about the expected value will result in a 10% change in depth (4.4 km) about the expected depth, which is smaller than the 10 km spread of depth estimates about the mean value of 44 km seen in figure 10. Equation 3 indicates that a 10 km spread in depth estimates would require a 6% spread in anti-correlated P and S velocities, which is consistent with the distribution of plausible velocity models in figure 10.

For near vertical ray paths, this trade-off between depth and velocity in computing arrival times can not be overcome by simultaneously fitting the Ps, P2p1s and P1p2s phases. We use the notation of Gurrola and Minster (1996), in which P2p1s indicates a reverberating phase with two P-wave path segments between the discontinuity and the free surface and one S-wave leg. Similarly, P1p2s has one P-wave leg and two S-wave legs. Figure 11 shows the receiver functions computed from the models given in that figure, at ray parameters of 0.04, 0.06, and 0.08. For this example we return to a simplified version of the model used in the discussion of uncertainty in receiver function amplitudes and time delays. The model is shown by the solid line in figure 11 (upper left), and includes a 30 km thick layer ($V_p = 6.5$ km/sec and $V_s = 3.8$ km/sec) over a half space (with $V_p = 8.0$ km/sec and

$V_s = 4.6$ km/sec). The two models shown by dashed lines were computed for velocities and thicknesses in the top layer $\pm 10\%$ of those given by the solid line. We can see that the delay times for the Ps, P2p1s and P1p2s are nearly unaffected by a uniform change in model parameters. For vertical incidence the travel time of each of these phases is given by

$$\begin{aligned}
 T_{Ps} &= \frac{z}{V_s} - \frac{z}{V_p}, \\
 T_{P2p1s} &= \frac{z}{V_s} + \frac{z}{V_p}, \text{ and} \\
 T_{P1p2s} &= 2 \frac{z}{V_s}
 \end{aligned} \tag{4}$$

where T_P , T_{P2p1s} and T_{P1p2s} are the respective arrival times of the Ps, P2p1s, and P1p2s phases relative to the initial arrival. The ray path for a vertically incident wave will be the same for a P- and an S-wave, in which case we can see that a correlated increase or decrease in V_p , V_s , and z will result in no change in each of these arrival times. From figure 11 (upper right and lower left), we see that the arrival times behave very much like those of a vertically incident wave for the 0.04 sec/km and 0.06 sec/km ray parameters (which covers half the teleseismic band). For the 0.08 sec/km ray parameter (figure 11, lower right), there is a small difference in the P2p1s arrival times which is perceptible in noise free-delta function synthetics, but would be less than the perceptible limits discussed above for realistic synthetics and observed data. Figure 12 illustrates that just a 2% change in S-wave velocity is sufficient to remove the difference observed between those synthetics. The dashed line model of figure 12 has a 2% lower S-wave velocity than the corresponding model of figure 11 (4.123 km/sec vs. 4.223). That difference is less than the expected resolution of any receiver function study. Figure 12 (right side) shows that the P2p1s arrival times are indistinguishable between those two models.

Clarke and Silver (1993) also discuss the problems in determining a unique velocity-depth model from near vertically incident phases. They point out that we at best can find a likely model defined by

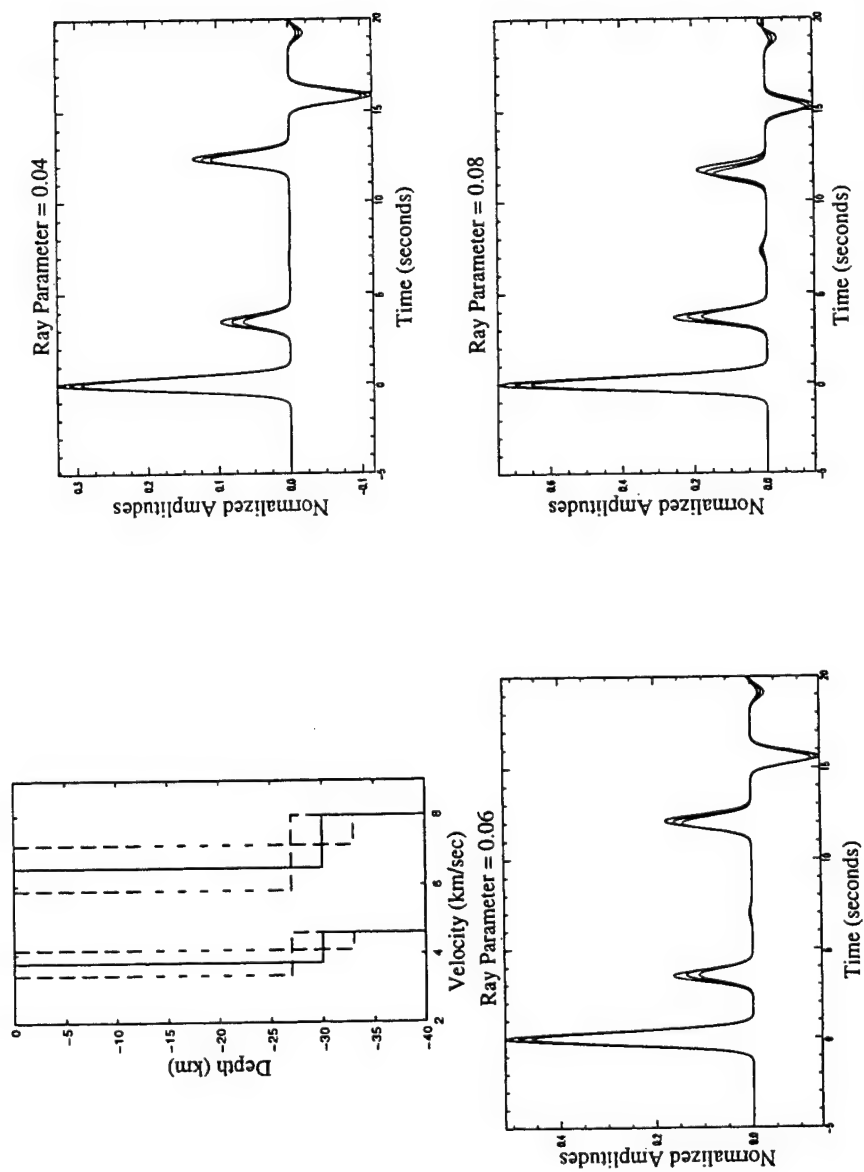


Figure 3.11: The simple velocity model (upper left) adopted for demonstration of the effects of moveout with ray parameter (solid line) and $\pm 10\%$ perturbations to that model (dashed lines). Receiver functions calculated for the models for ray parameters of 0.04 (upper right), 0.06 (lower left), and 0.08 (lower right)..

Poisson's ratio and depth. To do so accurately, it is necessary to use more primary phases than typically used in a receiver function study. Specifically, they used P-to-S phases, S-to-P precursors and reverberations (converted and direct) of several different teleseismic phases (e.g. P, S, ScS, PcP and SkS), thereby enriching the available distribution of ray parameter.

Other Sources of Uncertainty

As large as the Ps/P amplitude ratio variation is for receiver functions of synthetic seismograms with realistic signal to noise ratios, it is even greater for the receiver functions calculated from observed data. This indicates that additive noise is not the only important source of uncertainty in receiver function amplitudes. Greater sources of error than additive noise are likely signal-generated noise and inadequacies in our physical assumptions (e.g. topographic effects, anisotropy, 3-D structure, small scale scatterers in the crust). Imprecision in the assumption that the energy follows the great circle path can lead to errors in amplitudes as a result of misrotation of the seismograms before deconvolution. Baker et al. (1996) demonstrate that this is a significant problem in regions of tectonic complexity such as PFO. Anisotropy observed beneath shield regions (Silver et al., 1988) can also cause raypath bending away from the great circle path.

Error in Receiver Function Amplitudes due to Scattering along the Paths of Different Phases

Ps and P waves sample different segments of the crust, and array studies suggest that amplitudes of similar steep arrivals are extremely sensitive to small variations in their different lithospheric paths. For example, Haddon and Husebye (1978) observed significant spatial variations of teleseismic P amplitudes recorded at the NORSAR array, which they attributed to small lithospheric lateral velocity heterogeneities. The amplitudes fluctuated much more rapidly across the array than did the travel times. We have seen that receiver function peak arrival times are much less sensitive than amplitudes to error introduced by additive noise and the processing. This indicates that the receiver function peak

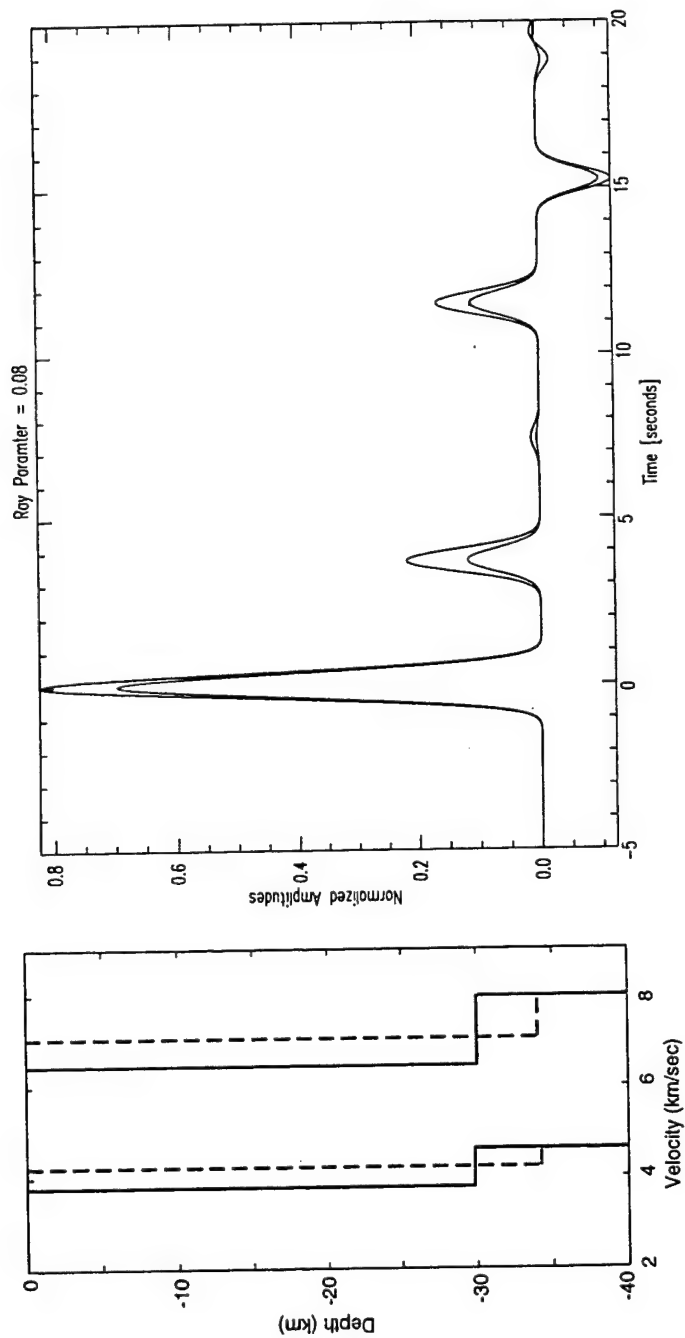


Figure 3.12: The velocity model of figure 11 (solid line), and a velocity model (dashed line) with 2% lower S-wave velocity than the dashed line model of figure 11 (left). Synthetic receiver functions for the two velocity models, showing no difference in arrival times.

arrival times are also more robust to small scale velocity heterogeneities in the Earth, and so are more appropriate for making inferences about major discontinuities.

At the LASA array, PcP and P amplitudes were observed to be uncorrelated for the same events, even though P amplitude variations for different events several degrees apart are highly correlated. The PcP variations for the same sets of events several degrees apart are also highly correlated (Frasier and Chowdhury, 1974). The authors determined that the lack of correlation between P and PcP is due to near receiver scattering by complex crustal and upper mantle structure. This is especially relevant to the interpretation of receiver function amplitudes, because the difference in incidence angle, and so crustal raypaths, between P and PcP for events recorded at LASA is the same as the difference between P and Ps phases seen in receiver functions. For example, for a 600 distant surface source recorded at LASA, assuming a 6 km/sec P-wave velocity and a Poisson solid near the receiver, the P-wave incidence angle is 21.90, and both the PcP and Ps incidence angles are 12.40. Because the Ps and PcP paths vary in the same way from the P-wave path, we should expect to see similar disparate effects on Ps and P amplitudes to those seen in PcP and P amplitudes, providing another indication that inference of precise interface dips or velocity jumps from relative Ps and P amplitudes would be dubious.

Errors in Model Parameters due to Inappropriate Assumptions of Incidence or Backazimuth

In areas of complex structure there is often a difference, called the mislocation vector (Davies and Sheppard, 1972), between measured and predicted incidence angles and backazimuths. In fact, mislocation vectors may be significant enough to be used for inferring lateral velocity variations (e.g. Walck and Minster, 1982, Powell and Mitchell, 1994). We consider the sensitivity of receiver function amplitudes to such mislocation vectors. For the optimistic case of a difference between predicted and observed incidence angles of 3 degrees, for the very simple layer over a half space model used earlier, there is an approximately 16% percent difference in the initial P amplitude and a 19% difference in the Moho Ps amplitude (figure 13). On the other hand, there is only a 3% difference in the Moho Ps/P amplitude ratio. This suggests that the mislocation vectors should be examined for events from which

receiver functions are calculated, and especially if they are large, that modeling Ps/P amplitude ratios will lead to much smaller errors than modeling absolute amplitudes.

If structure in the region modeled is not horizontally layered, the difference between expected and predicted backazimuth (the tangential component of mislocation vectors) can be large and can cause further misinterpretations of receiver functions. Rotation of the horizontal component seismograms to a predicted backazimuth that differs from the true backazimuth of energy incident on a dipping interface produces only negligible errors in the absolute P amplitude of the radial receiver functions, but can cause much larger errors in converted phases, and even larger errors in amplitudes of reverberations (e.g. Cassidy, 1992). On the tangential receiver functions, such misrotation can cause polarity reversals of some phases.

Conclusions

Analysis of the uncertainties in receiver functions using both real data and synthetics indicates that peak arrival times are a reliable source of information about the Earth. Peak arrival times do not vary significantly with noise level or with the method of deconvolution or the level of regularization. Amplitudes are, however, very sensitive to the effects of both noise and the deconvolution. Noise not only contributes to the very large statistical uncertainty of receiver function amplitudes, but can bias the regularized deconvolution toward smaller amplitudes. The bias can be the source of much larger error than that indicated by the statistical uncertainty.

The interpretation of receiver function amplitudes is also very sensitive to errors in the assumed ray parameter and backazimuth, and is likely sensitive to small differences in velocity structure between the P and Ps ray paths. These observations all indicate that the most reliable value of receiver functions lies in the identification of discontinuities and the appropriate depth-velocity curve. Without outside constraints on velocities, depths cannot be constrained. We have shown that the errors in depth are of the same order as the errors in velocity, so accurate a priori velocity information will make it possible to accurately constrain depths.

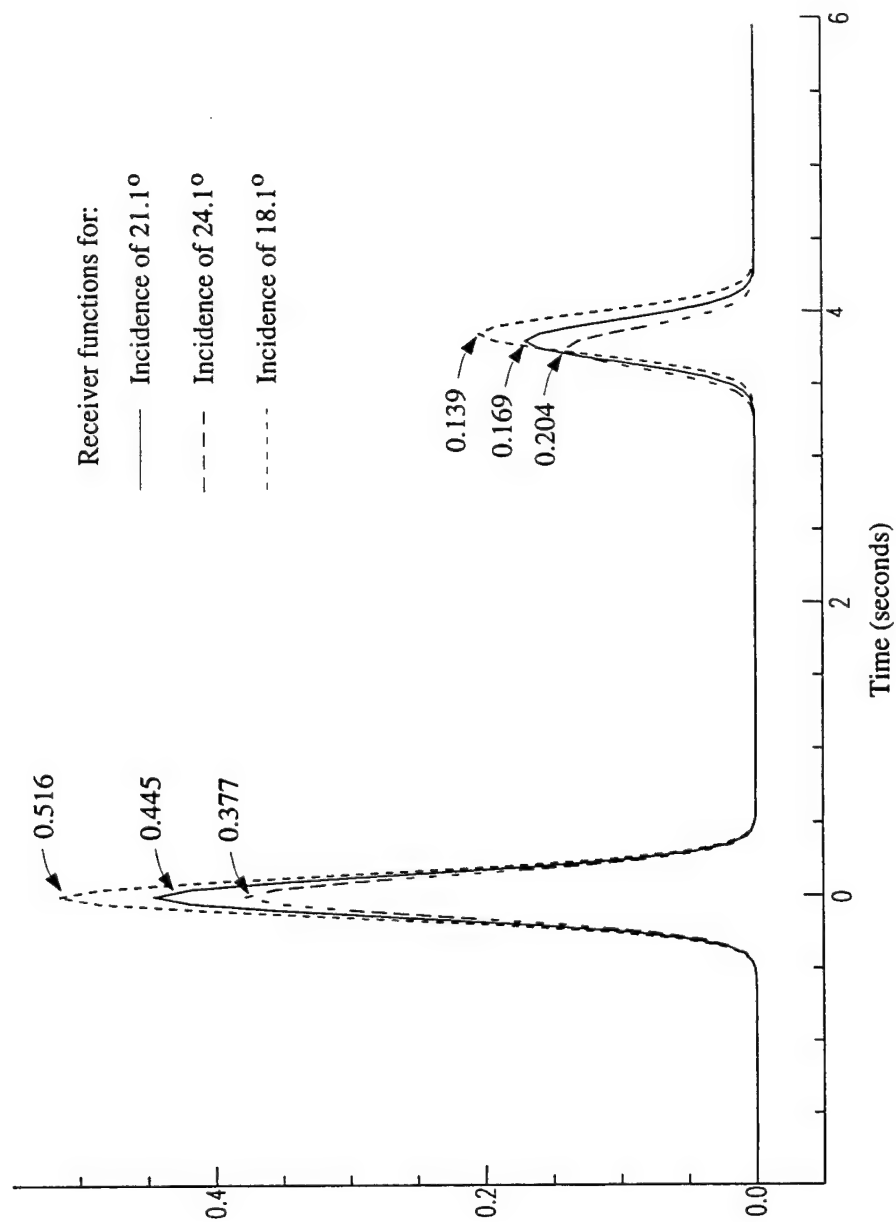


Figure 3.13: Receiver functions for the same layer over a half space model used for all synthetics in this paper. The solid line shows the ideal receiver function. The long and short dashed lines respectively show receiver functions for which the ray arrives with plus and minus 3 degrees difference in incidence angle from that expected. The P and Ps amplitudes for each are shown.

The large error associated with receiver function amplitudes renders dubious the precise estimation of a velocity contrast, or the precise dip of a discontinuity. That lack of precision is exacerbated by the large number of parameters to which the amplitude is sensitive, including the velocities and densities above and below the interface (Ammon, 1990), the degree and direction of the dip of the interface, and the incidence angle and backazimuth of energy arriving at the interface (Baker et al. 1996). Amplitudes should therefore only be used to corroborate inferences of approximate dip directions, relative dips of interfaces, or relative magnitudes of velocity contrasts.

It might seem that our criticism of the technique that we have relied on so heavily in Baker et al. (1996) is unduly pessimistic. On the contrary, it is this careful examination of the pitfalls of receiver function waveform modeling that gives us a high degree of confidence in the interpretations made. The knowledge that peak arrival times are more robust than amplitudes legitimizes the approach that focuses on modeling arrival times. In Baker et al. (1996), it was the careful, critical analysis of mislocation vectors that indicated the one quadrant for which we could at least speculate regarding the tangential component receiver functions, confident that they were not an artifact of misrotation of the horizontal seismograms.

Receiver functions are a powerful technique, which provide information about the existence, relative strengths, and position in depth-velocity space, of shear wave discontinuities beneath a 3-component seismic station.

References

- Ammon, C.J., G. Randall, and G. Zandt (1990), On the nonuniqueness of receiver function inversions, *J. Geophys. Res.*, **95**, 15,303-15,318
- Ammon, C.J. (1991), The isolation of receiver effects from teleseismic P waveforms, *Bull. Seism. Soc. Am.* **81**, 2504-2510
- Baker, G.E., J.B. Minster, G. Zandt, and H. Gurrola (1996), Constraints on crustal structure and complex Moho topography beneath Piñon Flat, California, from teleseismic receiver functions, *Bull. Seism. Soc. Am.*, **96**, (in press)
- Bostock, M. G. (1996), Ps conversions from the upper mantle transition zone beneath the Canadian landmass, *J. Geophys. Res.*, **101**, 8383-8402
- Burdick, L. J., and C. A. Langston (1977), Modeling crustal structure through the use of converted phases in the teleseismic body waveforms, *Bull. Seism. Soc. Amer.*, **67**, 677-692
- Cassidy, J.F. (1992), Numerical experiments in broadband receiver function analysis (1992), *Bull. Seism. Soc. Am.* **82**, 1453-1474
- Cassidy, John F. and R.M. Ellis (1994), S wave velocity structure of the northern Cascadia subduction zone, *J. Geophys. Res.*, **98**, 4407-4421
- Clarke, T. J., and P. G. Silver (1993), Estimation of crustal Poisson ratios from broad band teleseismic data, *Geophys. Res. Lett.*, **20**, 241-244
- Davies, D., and R.M. Sheppard (1972), Lateral heterogeneities in the Earth's mantle, *Nature*, **239**, 318
- Efron, B.E. (1982), The jackknife, the bootstrap and other resampling plans, pub. Society for Industrial and Applied Mathematics
- Efron, B.E. (1979), Bootstrap methods: another look at the jackknife, *Ann. Statist.*, **7**, 1-26
- Frasier, C.W. and D.K. Chowdhury (1974), Effect of scattering on PcP/P amplitude ratios at Lasa from 400 to 840 distance, *J. Geophys. Res.*, **79**, 5469-5477
- Gurrola H.G., G.E.Baker, and J.B.Minster (1995), Simultaneous time domain deconvolution with application to receiver functions, *Geophys. J. Intl.*, **120**, 537-543
- Gurrola, H., and B. Minster, Thickness estimates of the upper mantle transition zone from bootstrapped velocity spectrum stacks of receiver functions, submitted to *Geophys. J. Intl.*, Sept., 1996
- Haddon, R.A.W. and E.S. Husebye (1978), Joint interpretation of P-wave time and amplitude anomalies in terms of lithospheric heterogeneities, **55**, 19-43
- Kind, R. and L. P. Vinnik (1988), The upper-mantle discontinuities underneath the GRF array from P-to-S converted phases, *J. Geophys.*, **62**, 138-147
- Langston, C.A., and D. Helmberger (1975), A procedure for modeling shallow dislocation sources, *Geophys. J. Intl.*, **42**, 117-130
- Langston C.A. (1979), Structure under Mount Rainier, Washington, inferred from teleseismic body waves, *J. Geophys. Res.*, **84**, 4749-4762

- Menke, W. (1989), *Geophysical data analysis: Discrete Inverse Theory*, Academic Press Inc.
- Nolet, G., S. P. Grand, and B. L. N. Kennet (1994), Seismic heterogeneity in the upper mantle, *J. Geophys. Res.*, **99**, 23,753-23,766
- Oldenburg, D.W. (1981), A comprehensive solution to the linear deconvolution problem, *Geophys. J.R. Astr. Soc.*, **65**, 331-357
- Owens, T.J., G. Zandt, and S.R. Taylor (1984), Seismic evidence for an ancient rift beneath the Cumberland Plateau, Tennessee: a detailed analysis of broadband teleseismic P waveforms, *J. Geophys. Res.*, **89**, 7783-7795
- Powell, C., and B. Mitchell (1994), Relative array analysis of the southern California lithosphere, *J. Geophys. Res.*, **99**, 15,257-15,275
- Silver, P.G. and W.W. Chan (1988), Implications for continental structure and evolution from seismic anisotropy, *Nature*, **335**, 34-39
- Taner, M. T. and F. Koehler (1969), Velocity spectra: digital computer derivation and applications of velocity functions, *Geophys.*, **34**, 859-881
- Vinnik, L. P. (1977), Detection of waves converted from P-to-SV in the mantle, *Phys. Earth Planet. Inter.*, **15**, 294-303
- Walck, M. and J.B. Minster (1982), Relative array analysis of upper mantle lateral velocity variations in southern California, *J. Geophys. Res.*, **87**, 1757-1772

Chapter 4

The role of seismology in monitoring nuclear testing

Introduction

Nuclear weapons constitute one of the most obvious threats to the continuation of human society, and since their development, efforts have been made to curb their proliferation. Early tests of nuclear weapons by the United States and the Soviet Union were conducted in the atmosphere until the Partial Test Ban Treaty was signed by the U.S. and the U.S.S.R. in 1963, prohibiting nuclear weapons testing anywhere but underground. Seismology then became the critical tool for monitoring nuclear explosions, and annual funding for seismology increased 25-fold from the 1950's to the 1960's, driving rapid development of the field. The early focus was on establishing a global network for the detection of nuclear explosions, their discrimination from earthquakes, and determination of their locations. Discrimination began simply with an examination of P-wave first motions, and advanced with the recognition that seismograms from nuclear explosion sources were deficient in S-wave energy compared to earthquakes, and deficient in surface wave energy relative to shallow earthquakes.

The Threshold Test Ban Treaty, signed in 1974, limited the yield of nuclear explosions to 150 kt, and the size the explosions became a focus of attention. It was recognized that where continental paths are available, the regional phase Lg provides an accurate magnitude and, therefore, yield estimate (e.g., Nuttli, 1973, Baumgardt, 1984, Ringdal and Hokland, 1987).

Since 1992, the U.S., most other western nuclear powers, and Russia have adhered to a moratorium on nuclear testing, and France has joined after completing a series of tests this year. All are involved in negotiating a Comprehensive Test Ban Treaty (CTBT), which would ban all nuclear testing. China has also declared its interest in signing a CTBT, once it completes an ongoing series of tests. All the while that efforts to limit the development of weapons among declared nuclear powers

were continuing, a parallel effort was underway to limit the spread of such weapons. The Non-Proliferation Treaty, (NPT) signed in 1968, prohibited nuclear weapon possession by all signatories except the declared nuclear weapons states. Discussions on extension of the NPT are ongoing, with their resolution being dependent on the outcome of CTBT talks. Seismology will remain one of the most powerful tools available for monitoring both a CTBT and the NPT, with the focus on reducing the levels at which detection, location, and discrimination are feasible. This will be achieved by the expansion of global seismic coverage (e.g. Simpson et al., 1996; Harjes, 1996). This effort will involve analyzing regional seismograms from areas of the globe for which seismicity and seismic propagation have not previously been characterized. Thus, improving the effectiveness of regional seismic monitoring has become an important goal.

The second half of this thesis deals with one of the technical issues important to this global effort; that is, improving the performance of nuclear discriminants at the regional level. Specifically, the research focuses on improved understanding of the effects of path properties, such as waveguide thickness, slope, and roughness, on Lg propagation. Quantifying such effects is the essential first step toward understanding them, and eventually, to producing path corrections for regional seismic discriminants that are transportable (i.e. that may be applied in a region other than where they were derived).

Errors in regional nuclear discriminants due to path effects

Earthquakes and nuclear explosions are very different types of seismic sources (e.g. Mueller and Murphy, 1971; Stevens and Day, 1985), and discrimination between them would be much simpler, almost foolproof, if there were seismic instruments very near all seismic sources. That being impractical, we must use seismograms recorded anywhere from hundreds to thousands of kilometers from source epicenters. The discriminants measure the differences between energy of different types, or between energy in different frequency bands, that should reflect corresponding differences at the source. Intrinsic and scattering attenuation, and conversion of energy from one type to another occur

during propagation and can cause significant errors in regional seismic discriminants. The most effective discriminants are those that are in some way "path-proof". For example, the Lg/Pg amplitude ratio is a more accurate measure of source parameters than Lg/Pn amplitude ratios, because the energy in Lg and Pg phases travels in the crustal waveguide and so is subject to similar changes in the path of propagation. Pn, on the other hand, travels mostly in the upper mantle where it is subject to completely different path variations. In fact, in a test of all single regional high frequency discriminants, the Lg/Pg amplitude ratio was found to be the most effective (Taylor et al., 1989). There is, however, still significant error associated with the Lg/Pg amplitude ratio discriminant (e.g. Taylor, et al., 1989).

Discrimination can be improved in a number of ways. Denser coverage by better instruments in better sites is always desirable. More accurate discriminants may still be developed. If the errors in the current regional discriminants are in any way systematic, they may also be reduced. It is this last option that we will pursue.

To improve discrimination, we would like to know whether misclassified events have anything in common. Previous research (e.g. Baumgardt, 1985; Zhang et al., 1994) has shown correlations of Lg amplitude variation with features along the propagation path. Thus, it is reasonable to expect some systematic geographic variation in the amplitude ratios. We test this idea using data from the southern California seismic network (SCSN). For reasons detailed below, the southern California seismic network provides an ideal laboratory for improving regional discrimination. To test the spatial correlation of misclassified events, we plot the $\log(Lg/Pg)$ amplitude ratio discriminant at each SCSN station recording a set of regional events, both earthquakes and nuclear explosions from the Nevada Test Site (NTS) (figure 1). For consistency with previous studies the data are filtered to match the WWSSN short-period instrument response and the peak amplitudes of Lg and Pg are measured. Later, to ensure somewhat greater robustness of measurements, we use rms measurements of Lg and Pg amplitudes. The data then are filtered from 0.6 to 3 Hz to maximize observation of Lg by avoiding most longer period fundamental mode Rayleigh wave energy and the sometimes overwhelming level of higher frequency noise. We find, however, that discrimination results are virtually identical for the

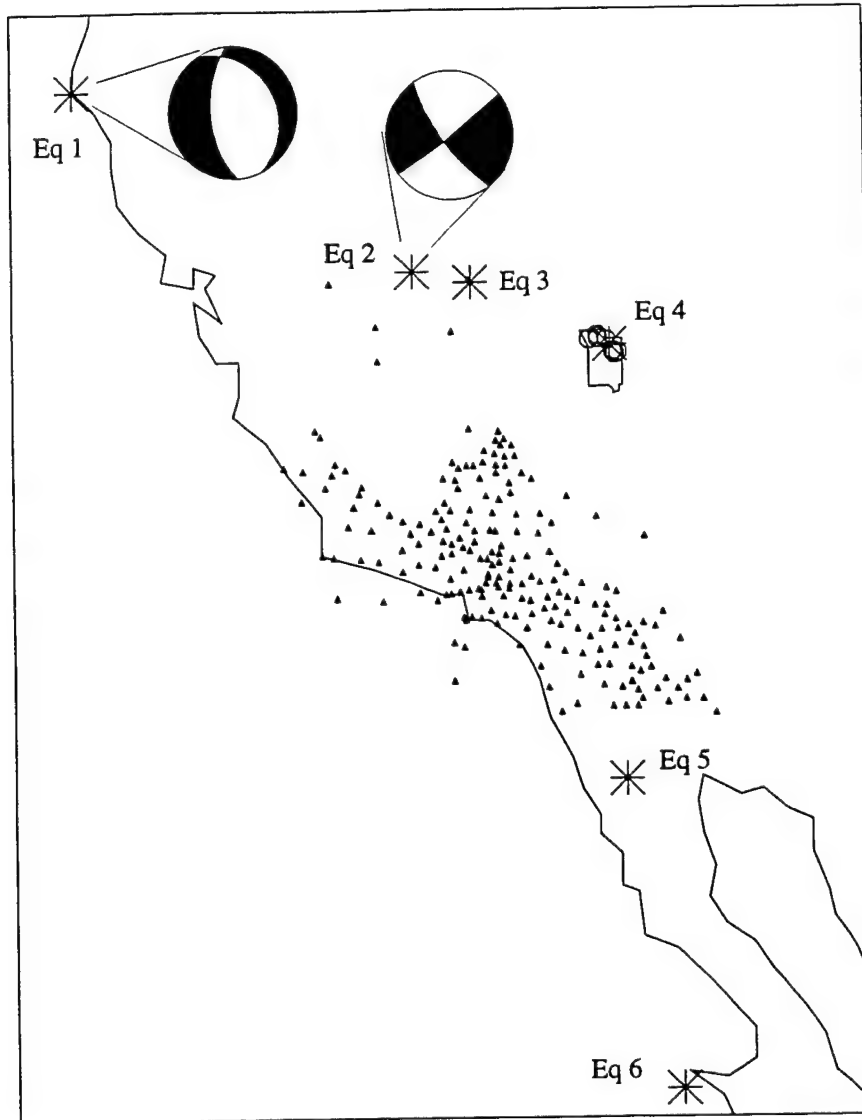


Figure 4.1: Peak $\log(Lg/Pg)$ amplitude ratios for a subset of SCSN data, corrected to the WWSSN response. Earthquake records are plotted as crosses and explosion records are plotted as circles. The discrimination line separating earthquakes and explosions matches that found by Taylor et. al. (1986) for the western U.S. We will address whether the scatter and misidentification (i.e. symbols on the "wrong side" of the line) is due to identifiable propagation effects.

peak and rms amplitude measurements. The events and SCSN stations are shown in figure 2. Indeed, a strong geographic pattern is observed across the SCSN for NTS events and several earthquakes at different locations (figures 3-13). The problem now becomes a search for the cause of the patterns of variations observed.

The pattern of variation in Lg/Pg amplitude ratios is similar for 10 NTS events whose records we have examined (figures 3, 4, and 5). The sources span 50 km in epicentral distance, indicating that very near source scattering is not responsible for the Lg/Pg variation. A similar pattern is even observed for a shallow earthquake that occurred within NTS (figures 6 and 7), indicating that the source radiation pattern is also not likely a significant factor. Figures 8, 9, and 10 indicate that distance, near receiver scattering, and site effects are not primary causes of the variation. We also see no correlation between nodes in the P radiation pattern (either predicted by known mechanisms or observed in first arrival polarizations) and maxima in Lg/Pg ratios (figures 11-13), strengthening the previous indication (figures 6 and 7) that the source radiation pattern does not dominate the observed geographical distribution. By elimination of other possibilities, we conclude that geographic variations in Lg/Pg amplitude ratios result from differences in structure to which the regional phases are sensitive. Next we consider what may cause the variations along the propagation paths.

To determine what propagation effects cause Lg/Pg amplitude ratios to vary, it would be helpful to have two types of information that are rarely available. One is seismic data from a very densely spaced network that spans the type of structures thought to cause Lg attenuation and blockage. The second is knowledge of the amplification at all station sites. We discuss the reasons for wanting both of these in the following sections.

The importance of fine scale observations

Lg blockage by oceanic crust was recognized by the first researchers to describe Lg (Press and Ewing, 1952). Insight into the physical processes behind seismic observations has been gained by synthetic modeling, despite the many simplifying assumptions required to make the analytical and

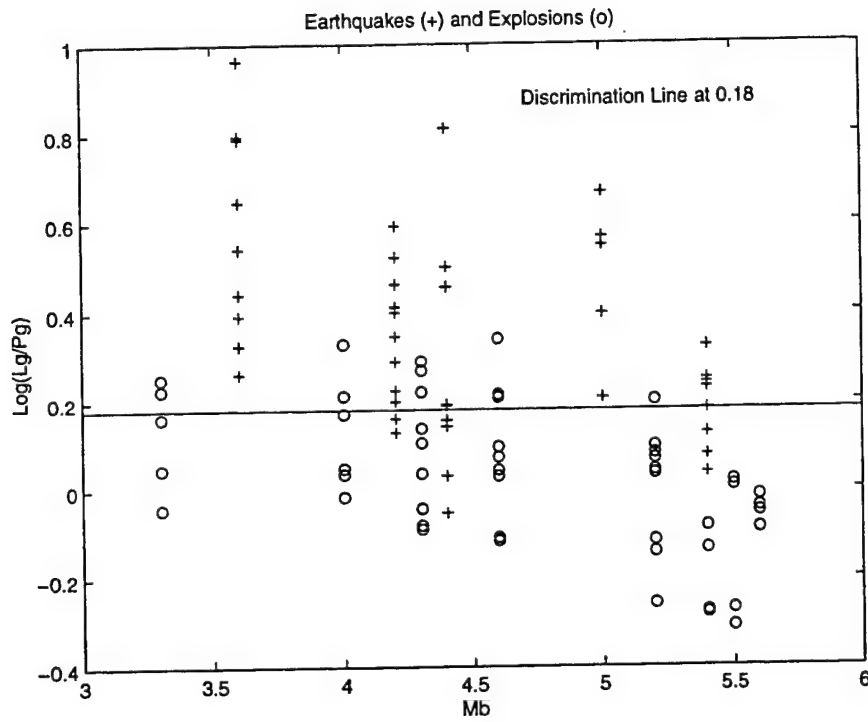


Figure 4.2: Map of southern California seismic network stations (triangles) with regional earthquakes (asterisks) and explosions (circles) that are discussed in the chapter.

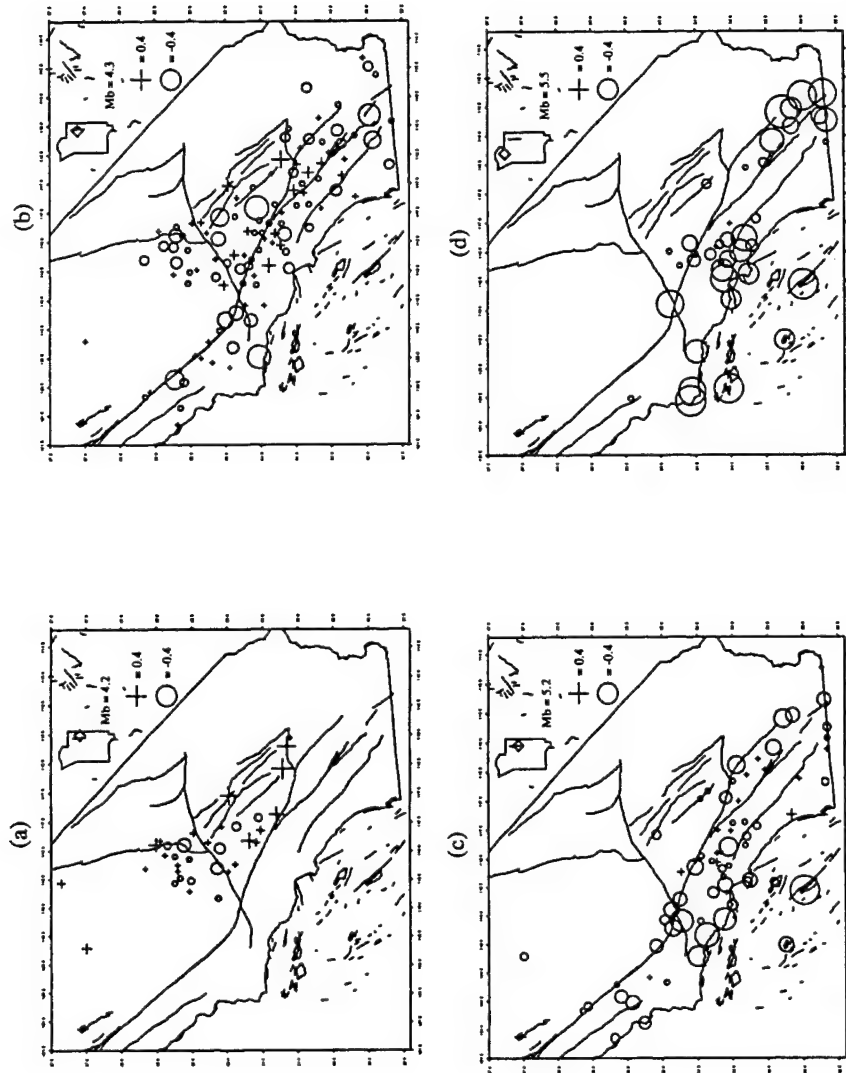


Figure 4.3: Results of $\log(Lg/Pg)$ discrimination using southern California network recordings for 4 nuclear explosions. Crosses indicate identification of the source as an earthquake. Circles indicate identification as an explosion. Symbols are scaled by their distance from the discrimination line of figure 1. The smaller explosions, Floydada (1991, day 227, upper left) and Coso (1991, day 67, upper right), are misclassified more frequently than the larger explosions, Lubbock (1991, day 291, lower left) and Hoya (1991, day 257, lower right). The sampling is biased because of the limited dynamic range of the instruments, leading to clipped records at short distances for large events, and low signal to noise level records at long distances for small events.

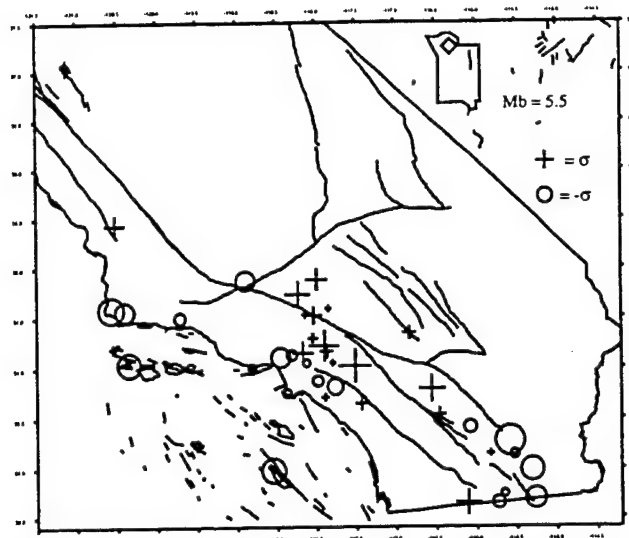


Figure 4.4: To examine possible geographic variation in the pattern of $\log(Lg/Pg)$ amplitudes, we standardize the distribution of each event's discriminant values (i.e. remove the mean and normalize so that one standard deviation equals 1.0). The result above is for Hoya (figure 3d). Here, symbol size is scaled by proximity to the mean, with crosses positive and circles negative. Note that the crosses appear to be in the same region in which misclassifications occurred for the smaller explosions.

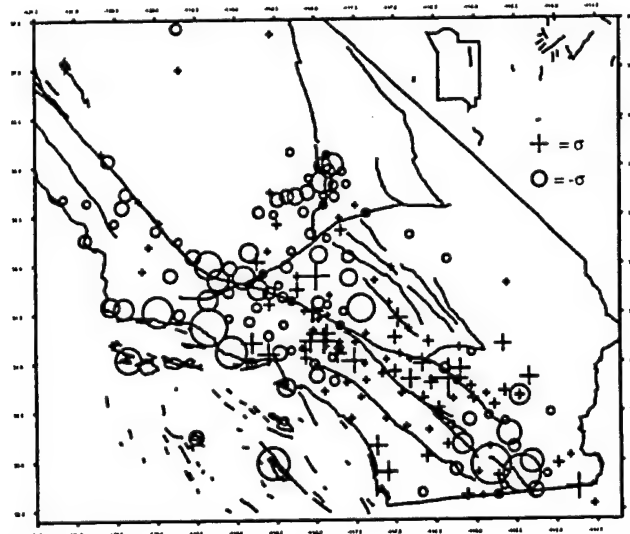


Figure 4.5: The normalization described in figure 4 was performed for 10 nuclear explosions. The mean for each station, for all the events it recorded, was then plotted above, revealing a distinct geographic pattern. Although we have ignored the possible effects of the bias in sampling (nearer stations recording more small events and more distant stations recording larger events), inspection of results for individual events suggests that the pattern is robust. That the pattern appears to be common to all events, whose sources span 50 km within NTS, argues against near source scattering strongly affecting the discriminant values.

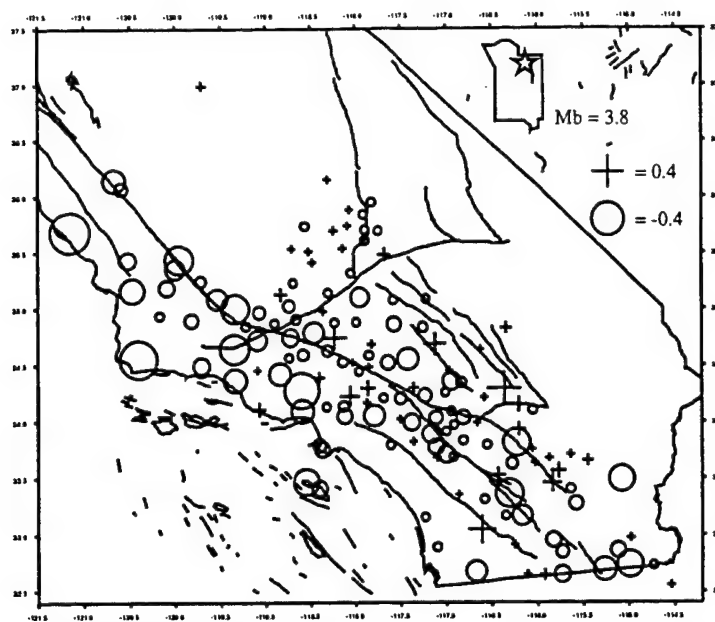


Figure 4.6: Log(Lg/Pg) amplitude ratios for earthquake no. 4 ($M_b = 3.8$) of figure 2. As in figure 3, crosses are "earthquake-like" values scaled by distance above the discrimination line of figure 1, and circles represent "explosion-like" values scaled by distance below the line. For this shallow earthquake (~ 2 km depth), 100 out of 150 recordings misclassify the event as an explosion. This serves as a warning that, even if we develop perfect path corrections, there will be anomalous events.

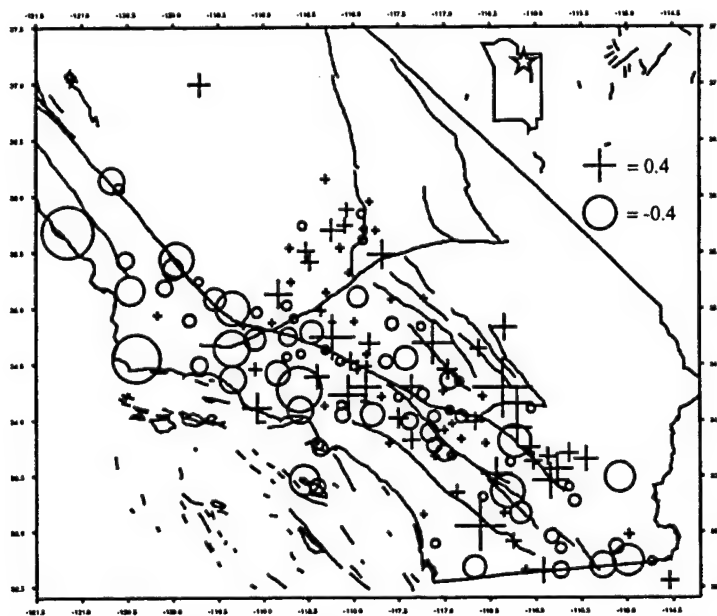


Figure 4.7: Normalized log(Lg/Pg) amplitude ratios, as in figure 4, for earthquake number 4 (figures 2 and 6). The relative pattern of large and small Lg to Pg amplitude ratios is quite similar to that observed for the nuclear explosions (figure 5), further indicating that neither source radiation or near source scattering is important to the pattern of Lg/Pg amplitude ratio variations.

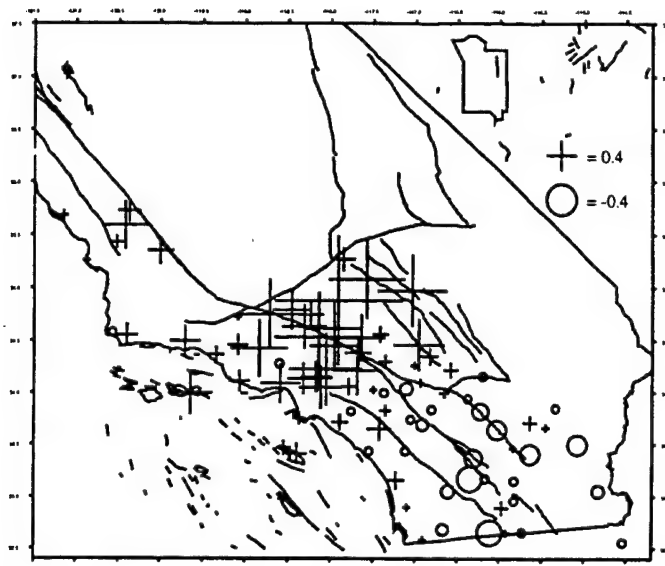


Figure 4.8: Event classification as in figure 6, for earthquake no. 3 ($M_b = 4.4$) of figure 2. All of the stations at which the event is misclassified are clustered at the greatest distance from the source. Although this alone might suggest a potential distance, or near-receiver scattering, or receiver site effect, we find a very different pattern for earthquake no. 1 (figure 9).

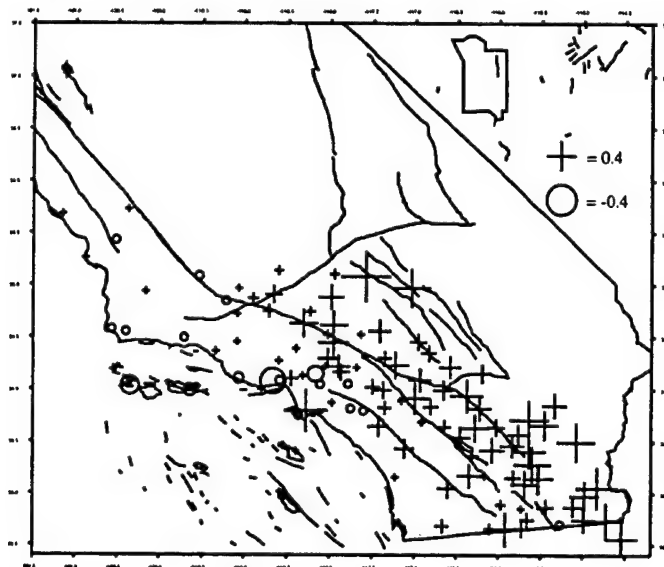


Figure 4.9: Event classification as in figures 6 and 8 for earthquake no. 1 ($M_b = 4.2$) of figure 2. In contrast to figure 8, the distinct area of misclassifications is nearest the source, and at a completely different set of stations. Taken together, this figure and figure 8 indicate that neither distance, near-receiver scattering, or site effects control the pattern of relative Lg to Pg amplitudes in any simple way.

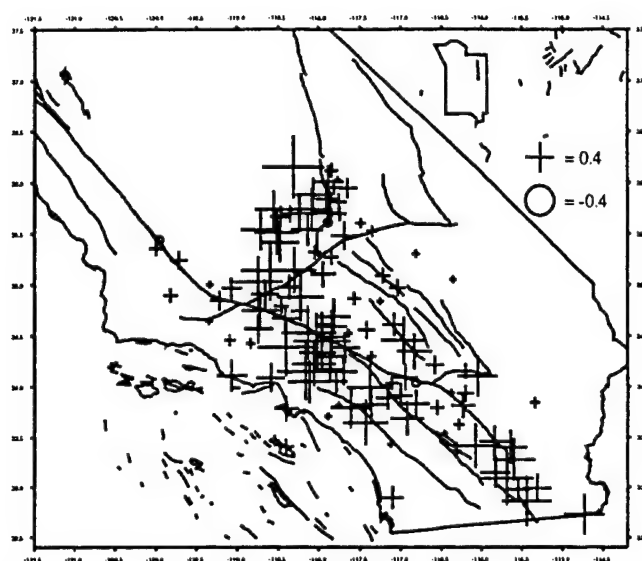


Figure 4.10: Event classification as in figures 6, 8, and 9, for earthquake no. 6 ($M_b = 4.2$) of figure 2. There are almost no misclassifications for this event. The two areas in which the smaller amplitude ratios cluster (in the center and at the northwest edge of the network), are distinct from the areas of smaller amplitude ratio for the events from different azimuths (figures 6, 8, and 9), strengthening the argument against any influence of distance, near-receiver scattering, or site effects.

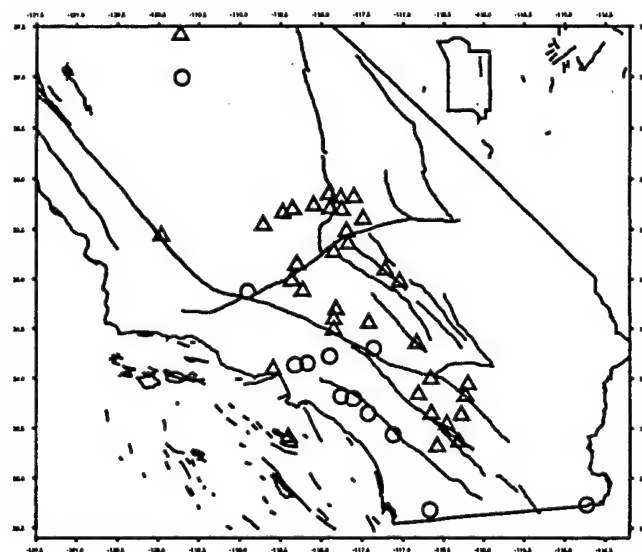


Figure 4.11: Pn first motion polarity for earthquake number 1 (figures 2 and 9). Triangles indicate positive first motion, and circles, negative. If the source radiation controlled the pattern of Lg/Pg amplitude ratio variation observed, we might expect higher Lg/Pg amplitude ratios to be recorded along P-nodal lines. Here, the polarities suggest a possible P-nodal plane running roughly northwest-southeast, correlating in no way with the amplitude ratio pattern observed.

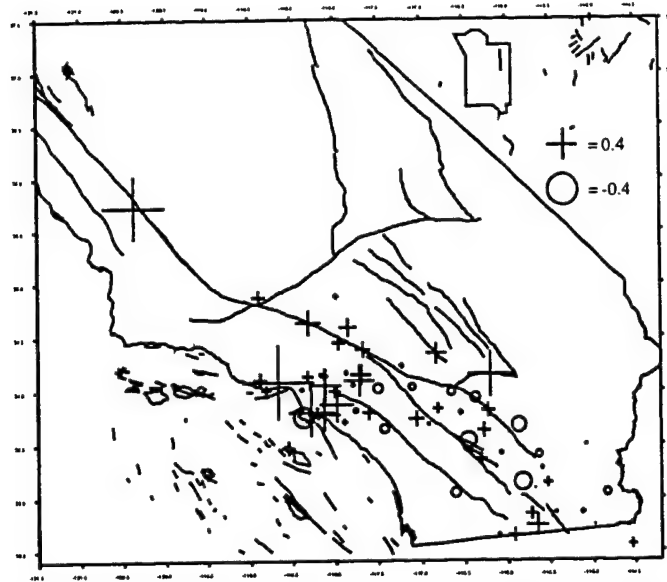


Figure 4.12: Event classification as in figures 6, 8, 9, and 10, for earthquake no. 2. There were relatively fewer observations for this $M_b = 5.4$ event, due to clipping, than were available for the nearby earthquake no. 3 (figure 8), but the pattern of misclassifications is similar. We can compare this result to one predicted by the known source focal mechanism (figure 13).

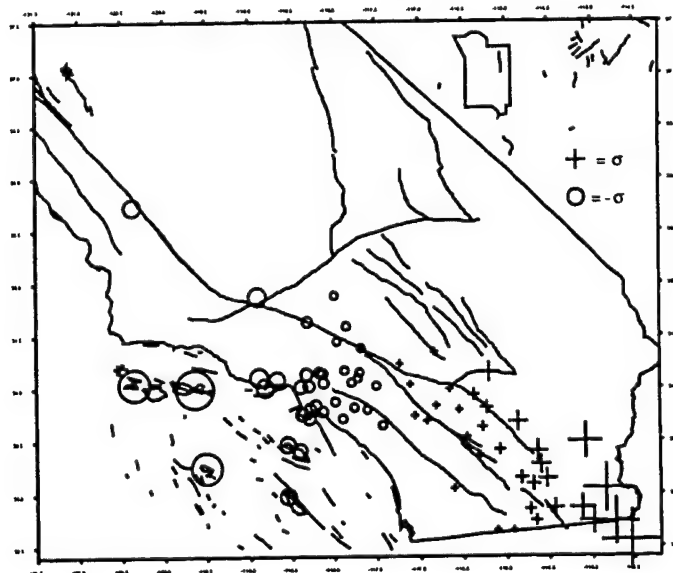


Figure 4.13: Ratio of predicted S to P amplitudes radiated from the source of earthquake no. 2. The relative amplitudes have been normalized as in figure 4. The largest crosses are in the vicinity of the P-node, just the opposite of the observed pattern (figure 12). This suggests that at approximately 1 Hz, and in this distance range, the focal mechanism has little effect on the observed Lg and Pg amplitudes.

computational aspects of modeling wave propagation tractable. Attempts to explain Lg blockage by synthetic modeling have limited value, however, for two reasons. One is simply that Lg is a high frequency phase and modeling assumptions about the homogeneity of the earth begin to break down at higher frequency (Gibson and Campillo, 1994). The second problem is a lack of appropriate observations for comparison. The feasibility of several different, sometimes conflicting mechanisms has been demonstrated in different synthetic modeling-based studies. For example, Cao and Muirhead (1993) used finite difference simulations of P-SV waves across thinning crust overlain by sediments and water, and concluded that the water column is critically important for Lg blockage. Zhang and Lay (1995) modeled propagation through very similar structure, also using finite-difference simulations as well as normal mode analysis, to argue that the water column is unnecessary. They conclude that Lg does not propagate in oceanic crust because an insufficient number of higher surface wave modes can exist in crust only 6 km thick. Other approaches indicate the feasibility of other, contradictory, blockage mechanisms. Kennett (1986) uses ray diagrams to argue for the predominance of back-scattering by dramatically thinning crust at the continental-oceanic crust interface, with what little energy is transmitted into the oceanic crust rapidly leaking into the mantle. Maupin (1989) finds that coupled mode synthetics predict insufficient backscattering of energy, or leakage into the mantle, to explain the extent of blockage observed. She concludes that low Q, due to scattering by small scale lower crustal heterogeneity, likely controls Lg blockage.

The difficulty is that while synthetic studies can indicate a variety of feasible mechanisms, they cannot unequivocally determine which mechanism is actually operating in the earth. Further constraints on the models, based on better observations than are currently available, are necessary to distinguish between the proposed mechanisms. Baumgardt (1990), using array analysis, demonstrated the possibility that Lg was scattered to Sn at a continent-ocean transition, providing a further constraint on synthetic studies. A recent study, more conclusive due to the density of spatial sampling (Shapiro, et al., 1996), may resolve more of the differences between synthetic studies, but has also pointed out a major problem with all approaches thus far. Most studies reporting Lg blockage have depended on very

widely spaced stations and events, and so some ambiguity over the rate of Lg blockage has existed. It is widely quoted in the modeling literature (e.g. Kennett, 1986, Cao and Muirhead, 1993, Zhang and Lay, 1995) that 100 to 200 km of oceanic crust blocks all Lg propagation, and modelers have used this number as a minimum constraint on their models. In fact, in the experiment of Shapiro et al. (1996), 7 ocean bottom seismometers covered 100 km that spanned the continent-ocean transition. That dense coverage revealed that Lg scatters effectively to Sn and to slow S waves in the ocean bottom sediments, disappearing within just 20 km. None of the mechanisms proposed in the previously discussed studies predict such a rapid loss of Lg energy. On the contrary, it is challenging to identify a mechanism that will completely attenuate Lg within even 100 km in such models. Thus while the mechanisms proposed may be valid, they may not be relevant.

It was also recognized very early that in addition to blockage by oceanic crust, other interruptions of "normal" continental structure could block Lg transmission. Båth (1954) reported that Lg did not propagate across the Tibetan Plateau or the Caucasus. Sedimentary basins have also been observed to attenuate Lg significantly (e.g. Baumgardt, 1990, Ibañez et al., 1991). However, continental blockage is more equivocal than oceanic. Some mountain ranges, such as the Tien Shan, appear to attenuate Lg, but don't completely extinguish it (Ruzaikan, et al., 1977). The Norwegian-Danish basin, with 8 to 10 km deep sediments, has no apparent effect on Lg propagation (Gregerson, 1984). Attempts at modeling continental blockage have been even less successful than those aimed at explaining oceanic blockage, although they have been useful in paring the list of feasible mechanisms. For example, Gibson and Campillo (1994) argue that because neither boundary-integral-equation or dynamic ray tracing synthetics can predict the Lg blockage observed in propagation across the Pyrenees, the basic large-scale structure of the mountain range is not the cause. They suggest, as did Maupin (1989), small scale heterogeneity in the lower crust.

As in the case where Shapiro et al (1996) made substantial progress in understanding Lg blockage by oceanic crust, by making appropriate observations, understanding of continental Lg blockage will advance with better observations. Regional events from many azimuths recorded at the SCSN, with its

20 km station spacing over a 300 by 500 km region spanning mountain ranges (with and without crustal roots), deep and shallow sedimentary basins, an active rift zone, and areas of both rapidly and gradually varying crustal thickness, can handily meet this need.

The need for site amplifications

To make it clear why knowledge of the amplification at all recording sites is desirable, it is useful to recapitulate our assessment to this point.

- 1) Errors in the Lg/Pg amplitude ratio discriminant can be attributed to propagation effects.
- 2) To improve discrimination it is our goal to be able to predict, and thus correct for, those propagation effects.
- 3) At least one of the phases involved, Lg, is greatly affected by changes in crustal waveguide properties, although the mechanisms behind those changes are not well understood.

In fact, Pg, although less thoroughly studied, is also known to be sensitive to variations in waveguide properties. In synthetic studies, efficient Pg propagation is shown to depend on the existence of a low velocity surface layer (e.g. Haskell, 1966; Olsen, et al., 1983). It is not clear that Lg and Pg are sensitive to the same parameters, at least in the same way. Thus, while we could develop empirical relationships based on the correlations between changes in Lg/Pg amplitude ratios and waveguide properties, their predictive value elsewhere would be dubious without an understanding of their physical basis. To understand the basis for the changes in the amplitude ratios, an understanding of the propagation of each phase is necessary. That understanding will be based on correlations between changes in path properties and the amplitudes of individual phases. To make such correlations, it will be necessary to separate site effects from path effects, for which knowledge of site amplifications is necessary.

As we are concentrating first on understanding Lg propagation, we will attempt to calibrate the SCSN sites for Lg propagation. Note that when amplitude ratio discriminants are used, it is assumed implicitly that site amplifications are the same for both phases used, a possible source of error if

differences exist and are mapped into path corrections. Barker et al. (1980), however, found that for recordings of events with very similar paths to adjacent stations on very different geological structures, the Lg to Pg amplitude ratios were the same. Eventually, we must examine carefully the question of how sensitive site amplifications are to wavetype. If the Lg site amplifications prove to be appropriate for Pg as well, gaining understanding of that phase's variations will be much simpler.

The rest of this thesis is devoted to enabling the observation of variations in absolute Lg amplitudes along all types of propagation paths. To do so, we must calibrate all possible SCSN sites for Lg amplification, which we do using the near receiver scattered (*diffuse*) component of teleseismic coda as an isotropic source of Lg-like energy. The coda measurements are noisy, with the possibility of many large errors, and the data are censored, so in chapter 5 we present the development and application of appropriate statistical techniques for obtaining the best site amplification estimates possible from the data. In chapter 6, we examine the nature of diffuse coda and Lg, both through a review of the literature and through array analysis. We also develop and apply a method for separating the near receiver from the near source scattered coda. In chapter 7 we present a preliminary application of the site amplifications to Lg, and discuss the steps necessary to quantify the relationship between structure and Lg amplitude variation.

References

- Barker, B.W., Z.A. Der, and C.P. Mrazek (1981), The effect of crustal structure on the regional phases Pg and Lg at the Nevada Test Site, *J. Geophys. Res.*, **86**, 1686-1700
- Bath, M. (1954), The elastic waves Lg and Rg along Euroasiatic paths, *Arkiv for Geofysik*, **2**, 295-325
- Baumgardt, D.R. (1984), Relative Lg and P-coda magnitude analysis of the Shagan River Explosions, *Final Report to AFOSR, SAS-TR-84-03*, ENSCO, Inc., Springfield Virginia
- Baumgardt, D.R. (1985), Attenuation, blockage, and scattering of teleseismic Lg from underground nuclear explosions in Eurasia, ENSCO, Inc., *Scientific Report, No. 1, AFGL-TR-85-0332*
- Baumgardt, D.R. (1990), Investigation of teleseismic Lg blockage and scattering using regional arrays, *Bull. Seis. Soc. Am.*, **80**, 2261-2281
- Cao, S. and K.J. Muirhead (1993), Finite difference modeling of Lg blockage, *Geophys. J. Intl.*, **115**, 85-96
- Gibson R.L. Jr. and M. Campillo (1994), Numerical simulation of high- and low-frequency Lg-wave propagation, *Geophys. J. Intl.*, **118**, 47-56
- Gregerson, S. (1984), Lg-wave propagation and crustal structure differences near Denmark and the North Sea, *Geophys. J. R. Astr. Soc.*, **79**, 217-234
- Harjes, H.-P., (1996) Towards a global seismic monitoring system - lessons learned from Geneva experiments, in *Monitoring a Comprehensive Test Ban Treaty*, Kluwer Academic Publishers
- Haskell, N.A. (1966), The leakage attenuation of continental crustal P waves, *J. Geophys. Res.*, **71**, 3955-3967
- Ibañez, J.M., J. Morales, F. de Miguel, F. Vidal, G. Alguacil, and A.M. Posadas (1991), Effect of a sedimentary basin on estimations of Q_C and Q_{Lg} , *Phys. Earth Plan. Int.*, **66**, 244-252
- Kennett, B.L.N. (1986), Lg waves and structural boundaries, *Bull. Seis. Soc. Am.*, **76**, 1133-1141
- Maupin, V. (1989) Numerical modeling of Lg wave propagation across the North Sea Central Graben, *Geophys. J. Intl.*, **99**, 273-283
- Mueller, R.A. and J.R. Murphy (1971), Seismic characteristics of underground nuclear detonations, *Bull. Seis. Soc. Am.*, **61**, 1675-1692
- Nuttli, O.W. (1973), Seismic wave attenuation and magnitude relations for eastern North America, *J. Geophys. Res.*, **78**, 5212-5218
- Olsen, K.H., L.W. Braile, and J.N. Stewart (1983), Modeling short-period crustal phases (P, Lg) for long-range refraction profiles, *Phys. Earth Plan. Int.*, **31**, 334-347
- Press F. and M. Ewing (1952), Two slow surface waves across North America, *Bull. Seis. Soc. Am.*, **42**, 219-228
- Ringdal, F., and B.K. Hokland (1987), Magnitudes of large Semipalatinsk explosions using P coda and Lg measurements at NORSAR, *NORSAR Sci. Rept. No. 1-88/89*, Kjeller, Norway

- Ruzaikin, A.I., I.L. Nersesov, and V.I. Khalturin (1977) Propagation of Lg and lateral variations in crustal structure in Asia, *J. Geophys. Res.*, **82**, 307-316
- Shapiro, N., N. Béthoux, M. Campillo, and A. Paul (1996), Regional seismic phases across the Ligurian Sea: Lg blockage and oceanic propagation, *Phys. Earth Plan. Int.*, **93**, 257-268
- Simpson, D., R. Butler, T. Ahern, and T. Wallace, (1996) Expanding the global seismographic network, in *Monitoring a Comprehensive Test Ban Treaty*, Kluwer Academic Publishers
- Taylor, S.R., M. Denny, E. Vergino, and R. Glaser (1989), Regional discrimination between NTS explosions and western U.S. earthquakes, *Bull. Seis. Soc. Am.*, **79** 1142-1176
- Stevens, J.L. and S.M. Day (1985), The physical basis of $m_b:M_s$ and variable frequency magnitude methods of earthquake/explosion discrimination, *J. Geophys. Res.*, **90**, 3009-3020
- Zhang, T., S. Schwartz, and T. Lay (1994), Multivariate analysis of waveguide effects on short-period regional wave propagation in Eurasia and its application in seismic discrimination, *J. Geophys. Res.*, **99**, 21929-21945
- Zhang T. and T. Lay (1995), Why the Lg phase does not traverse oceanic crust, *Bull. Seis. Soc. Am.*, **85**, 1665-1678

Chapter 5

Iterative reweighting for estimation of magnitude and site amplifications from doubly censored and corrupted data

Abstract

Geophysical data are commonly drawn from heavy tailed distributions and are often censored. We present the use of two techniques that improve parameter estimation from such data. The first, the technique of robust reweighting of data based on misfit, limits bias in parameter estimates either from outliers or non-Gaussian distributed errors and improves accuracy of error analysis. The second technique permits the incorporation of censored data into parameter estimates through maximum likelihood estimation.

We use the example of event magnitude and site amplification estimation from censored seismic network data, with both synthetic examples and real data, to illustrate the implementation and effectiveness of these techniques. For the second technique, we derive the likelihood function for the problem and make a linear approximation to find its maximum with an iterative algorithm.

Problems addressed

We address some problems common to geophysical data that can cause significant errors in estimated parameters.

The first problem is that of non-normally distributed errors. Least squares is probably the most common method used to estimate parameters from geophysical data. Its popularity is due to the efficiency of its calculation and its ease of implementation. The least squares solution, however, is the optimal solution only if the errors are normal. The assumption of normality is often not even made explicitly or tested, although in reality, data are commonly drawn from heavy-tailed distributions and

have significantly more outliers than predicted by the normal distribution (e.g. Huber, 1972). This can bias the least squares solution significantly through the square in the error term. The term *outliers* refers to measurements that appear to fall well outside the distribution of the great majority of the data, whatever that distribution is. By *heavy-tailed*, we refer to any distribution with heavier tails than the normal distribution. Both terms will be useful in the discussion that follows, although we note that whether a particular datum is an outlier or is drawn from a heavy -tailed distribution may be mostly a matter of one's outlook.

For perspective on the ubiquity of the assumption of normality, we mention an interesting historical note. That is, that the normal distribution was introduced by Gauss, in 1821, *not* because of its omnipresence in nature, but because it is the distribution for which the easily calculated arithmetic mean is the best estimate (Huber, 1972).

The other problem we address is the censoring of data. By censoring, we mean that large signals are clipped at some recording instruments, while small signals remain below background noise levels at some other instruments. That a signal is above or below some threshold is useful information and its exclusion can significantly bias parameter estimates (e.g. Ringdal, 1977, Blandford and Schumway, 1982).

The problem of site amplification and magnitude estimation from SCSN data

To facilitate the presentation of the techniques that deal with the above problems, we use the calculation of site amplifications from the near-receiver scattered component of teleseismic coda for southern California seismic network (SCSN) stations. A thorough discussion of the SCSN site amplifications can be found in Baker, et. al. (1996).

To estimate the site amplifications, we must also estimate event magnitudes. The problem is very straightforward: we measure rms amplitudes of near source scattered teleseismic coda from many events at all stations within a network. We write each measured amplitude as

$$A_{i,j} = E_j \cdot S_i \cdot \Gamma_{i,j} \quad (1)$$

where S_i is the site amplification at station i , E_j is the rms amplitude of the coda over some time window for event j (for unit site amplification), and $\Gamma_{i,j}$ is a factor that accounts for random error from all possible sources. We take the natural logarithm of (1), to obtain

$$a_{i,j} = e_j + s_i + \gamma_{i,j}. \quad (2)$$

We use a multiplicative factor to describe the noise in (1), as the errors in the magnitudes and logarithms of the site amplifications are assumed to be additive. If $\gamma_{i,j}$ were assumed to be independent zero mean Gaussian errors with standard deviations $\sigma_{i,j}$, the least squares solution to the matrix equation below would be the best solution we could find (e.g. Press, et. al., 1988). The assumption that $\gamma_{i,j}$ are normal is equivalent to taking $\Gamma_{i,j}$ to be lognormal, a distribution commonly held to result from the multiplicative combination of independent random variables (e.g. Priestley, 1981).

$$\begin{array}{c} \uparrow \\ (p \cdot q + 1) \\ \downarrow \end{array} \left| \begin{array}{cccccccccccc} \frac{1}{\sigma_{1,1}} & 0 & 0 & . & . & . & \frac{1}{\sigma_{1,1}} & 0 & 0 & . & . & . \\ \frac{1}{\sigma_{1,2}} & 0 & 0 & . & . & . & 0 & \frac{1}{\sigma_{1,2}} & 0 & . & . & . \\ \frac{1}{\sigma_{1,3}} & 0 & 0 & . & . & . & 0 & 0 & \frac{1}{\sigma_{1,3}} & . & . & . \\ . & . & . & . & . & . & . & . & . & . & . & . \\ . & . & . & . & . & . & . & . & . & . & . & . \\ . & . & . & . & . & . & . & . & . & . & . & . \\ 0 & \frac{1}{\sigma_{2,1}} & 0 & . & . & . & \frac{1}{\sigma_{2,1}} & 0 & 0 & . & . & . \\ 0 & \frac{1}{\sigma_{2,2}} & 0 & . & . & . & 0 & \frac{1}{\sigma_{2,2}} & 0 & . & . & . \\ 0 & \frac{1}{\sigma_{2,3}} & 0 & . & . & . & 0 & 0 & \frac{1}{\sigma_{2,3}} & . & . & . \\ . & . & . & . & . & . & . & . & . & . & . & . \\ . & . & . & . & 0 & \frac{1}{\sigma_{q-1,p}} & . & . & . & \frac{1}{\sigma_{q-1,p}} & 0 & . \\ . & . & . & . & 0 & \frac{1}{\sigma_{q,p}} & . & . & . & 0 & \frac{1}{\sigma_{q,p}} & . \\ . & . & . & . & 0 & \frac{1}{\sigma_{q,p}} & . & . & . & 0 & \frac{1}{\sigma_{q,p}} & . \\ & & & 0 & 0 & 0 & 0 & 1 & 1 & 1 & 1 & 1 \end{array} \right| \cdot \begin{array}{c} e_1 \\ e_2 \\ . \\ . \\ . \\ e_p \\ s_1 \\ s_2 \\ . \\ . \\ s_q \end{array} = \begin{array}{c} \frac{a_{1,1}}{\sigma_{1,1}} \\ \frac{a_{2,1}}{\sigma_{2,1}} \\ . \\ . \\ \frac{a_{1,2}}{\sigma_{1,2}} \\ \frac{a_{2,2}}{\sigma_{2,2}} \\ . \\ . \\ \frac{a_{q-1,p}}{\sigma_{q-1,p}} \\ \frac{a_{q,p}}{\sigma_{q,p}} \\ 0 \end{array} \quad (3)$$

$\leftarrow (p+q) \rightarrow$

The last row of the matrix constrains the network to have no mean amplification and prevents event and station parameters from trading off. The matrix would only reach its full height of $p+q+1$ if there were no missing data. Expressing (3) as $\mathbf{M}\mathbf{e}=\mathbf{a}$, we can write the least squares solution in matrix form as $\hat{\mathbf{e}} = (\mathbf{M}^T\mathbf{M})^{-1}\mathbf{M}^T\mathbf{a}$ (e.g. Lawson and Hanson, 1974).

We have reason, however, to doubt that $\gamma_{i,j}$ are independent zero mean Gaussian errors. The model we use requires a large number of assumptions (e.g. we assume that near-receiver scattering is isotropic, that the incoming teleseismic P-wave has constant amplitude over southern California, and that instrument calibrations do not drift over time). It is easy to see that major violations of any assumptions could lead to large outliers. Further, SCSN seismograms are often mislabeled, so some measurements may be attributed to the wrong stations, causing occasional very large errors (we estimate that as much as 1% of the data that we have used may be mislabeled in this way). A statistical test of the error distribution, presented in a later section, confirms this skepticism. In the following sections we will address the consequences of using the least squares estimate when the errors are not normal and will use the site amplification problem to illustrate a method of estimation that is robust to such difficulties with the data.

Size is one further important factor in this problem. We have recordings of 41 events on 211 stations, for a total of 4,397 on-scale amplitude measurements, 110 upper threshold measurements, and 703 lower threshold measurements. Despite the large number of measurements, some individual parameters depend on few data, so if one datum is in some way *bad*, we need a way of identifying it. Because the entire set of data in this case is so large, our means of recognizing dubious data must be automatic.

Additionally, because seismometers have limited dynamic range, the data are censored. Ignoring the censored data may result in biased site amplification estimates and event magnitudes. We illustrate a method for incorporating censored data into the parameter estimates in later sections.

Robust reweighting

The first set of problems we introduced, heavy-tailed distributions and egregious blunders contaminating the data, are dealt with by robust statistics techniques. The simplest robust statistics technique is probably that of truncating the data, that is, discarding some number of the largest and smallest measurements, and computing the least squares solution with the remaining data. The simplest *a posteriori* technique is to compute a least squares solution, discard any data considered to be outliers, for example, anything with greater than 3 standard deviations of misfit, and then re-compute the least squares solution with the remaining data. Any such technique is driven by the consideration that some data are likely to be *bad*. This may also be viewed as insufficiency of the model, in which case unmodeled parameters are mapped into the modeled parameters. Either way, outlying data must be identified and discarded or downweighted, or they may severely bias the least squares solution, specifically because that solution seeks to minimize the squared error.

We use the technique of robust reweighting, which has distinct advantages over the simpler robust techniques mentioned above. The advantages derive from its ability to downweight data, rather than simply keep or discard them. By just discarding outliers, the assumption is made that those data are bad, that is, that some error must have been made in their collection. In that way, potentially useful data that are simply drawn from a heavy-tailed distribution are likely to be discarded. In contrast, reducing the weights applied to outlying data, which can be viewed as increasing the estimate of $\sigma_{i,j}$ in (3), permits application of a milder penalty than would normally be applied to such data by the least squares penalty function. Thus, such data can influence the solution without dominating it. Similarly, if the data are drawn from a heavy-tailed distribution, the least squares solution is likely to be biased by even moderately outlying data that are not discarded. By downweighting moderately outlying data, the penalty applied to them can be reduced, for example to something like the penalty applied by the L_1 -norm estimate. The L_1 -norm estimate is more appropriate for data from a heavy-tailed distribution, but it is much more cumbersome to implement and slower to calculate than the least squares estimate, which robust reweighting lets us continue to use. Versions of robust reweighting of data have been

applied in geophysics for some time (e.g. Jeffreys, 1932), although the practice is not as widespread as may be warranted.

The identification and downweighting of outliers is an iterative procedure. A set of weights is determined by a reweighting function that is dependent on the misfit. The misfit is

$$\mathbf{z}_n = \mathbf{W}_n \cdot \mathbf{M} \cdot \hat{\mathbf{e}}_n - \mathbf{W}_n \cdot \mathbf{a}, \quad (4)$$

where \mathbf{M} is the forward model matrix in any linear inverse or parameter estimation problem written as $\mathbf{M} \cdot \mathbf{e} = \mathbf{a}$, such as (3), \mathbf{a} is the data vector, $\hat{\mathbf{e}}_n$ is the estimate of the vector of parameters at the n 'th iteration, and \mathbf{W}_n is the diagonal weight matrix that was applied at the n 'th iteration. A new set of weights is calculated based on the misfit, and the least squares solution of the newly reweighted problem,

$$\mathbf{W}_{n+1} \cdot \mathbf{M} \cdot \hat{\mathbf{e}}_{n+1} = \mathbf{W}_{n+1} \cdot \mathbf{a}, \quad (5)$$

is found. The process continues until some criterion is met.

The values of the robust weights are calculated from a reweighting function. The integral of reweighting functions, called influence functions, are more commonly discussed in the statistics literature. The integrals of the influence functions are the penalty functions associated with the reweighted least squares inversions. A common robust reweighting penalty function and the least squares and L_1 -norm penalty functions are shown in figure 1, along with their associated influence and reweighting functions (note: the L_1 -norm penalty function is shown only for comparison with the others, but has no true influence function as the weights approach infinity near zero misfit). In the upper left panel we can see the overwhelming penalty applied by the least squares criterion to data that cause moderate to large misfits. It is through that large penalty that outliers can significantly bias the least squares estimate. The L_1 -norm penalty is more appropriate for data from a heavy tailed

distribution (the L_1 -norm solution is the maximum likelihood estimator for exponentially distributed data), although it is still very large for egregious errors. An influence function such as the Hampel 17a function (e.g. Montgomery and Peck, 1982), in which the influence of large outliers decreases until they are eventually completely ignored is more appropriate for data sets where occasional egregious errors are expected. Such influence functions, that is, those with a negative slope, are called *redescenders*. Convergence is guaranteed only when the influence function is convex, which redescenders are not. In practice however, convergence is usually rapid and convergence problems are rare (e.g. Montgomery and Peck, 1982).

The Hampel 17a influence function is linear, like the least squares solution, for data with little misfit, constant, like the L_1 -norm solution, for data with moderate misfit, and reduces the influence of data, eventually to zero, outside of that range. The robust weights for the Hampel 17a function are determined as follows:

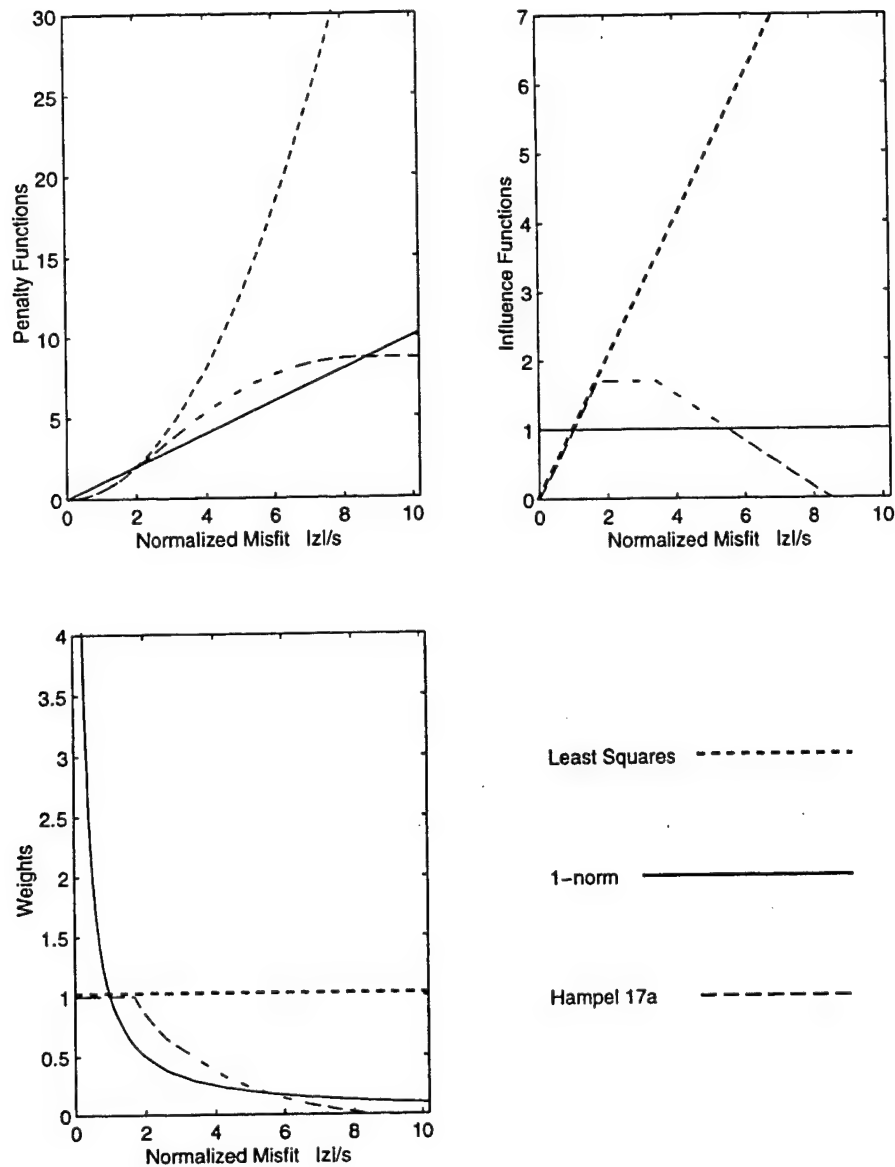


Figure 5.1: Penalty functions (upper left) for misfit of least squares, L1-norm, and Hampel 17a solutions and their 1st and 2nd derivatives, i.e., influence functions (upper right) and the values for robust weights (lower left). Note that the L1-norm does not have a true influence function, as its robust weights would approach infinity near zero misfit. It is included here for comparison with the other solutions.

$$\begin{aligned}
w(z) &= 1, & \text{for } |z| \leq a \\
w(z) &= \frac{a}{|z|}, & \text{for } a < |z| \leq b \\
w(z) &= \frac{a(c-|z|)}{|z|(c-b)}, & \text{for } b < |z| \leq c \\
w(z) &= 0, & \text{for } |z| > c
\end{aligned} \tag{6}$$

where z is the misfit from (4), normalized by some robust estimate of the standard deviation, such as the scaled median absolute deviation,

$$s = \frac{\text{median}(|z - \text{median}(z)|)}{z_m} \tag{7}$$

(e.g. Montgomery and Peck, 1982). $z_m = 0.6745$ is obtained from

$$\int_0^{z_m} \frac{1}{\sqrt{2\pi}} e^{-\frac{z^2}{2}} dz = 0.25. \tag{8}$$

so that when z is standard normal (i.e. $\mu=0$ and $\sigma=1.0$), half of the points will be between $-z_m$ and $+z_m$, and s will equal 1.0.

Because reweighting functions downweight data on the tails of the distribution, they effectively “reshape” the distribution to appear more Gaussian. That is not to suggest that it is important to perturb reweighting function parameters (a , b , and c of (6) in the case of the Hampel 17a function) to exactly reshape the errors to be Gaussian. There is nothing that suggests that would be meaningful. What is important is that the final parameter estimates be robust with respect to the choice of both influence function and influence function parameters. We used $a=1.7$, $b=3.4$, and $c=8.5$ for our final estimates, as suggested by Montgomery and Peck (1982). Those estimates were robust to large variations in influence function parameter values. For example, we varied a from 1.1 to 2.3. and used other

influence functions, without significantly affecting the values of the magnitude and site amplification estimates.

We have described the robust reweighting as a way of improving parameter estimates by reducing the undue influence outliers have on a least squares solution. It could also be viewed, more basically, as a way of determining the most accurate estimates of the data's standard deviations. We attempt to achieve that by updating the standard deviation estimates for each datum based on how closely that datum corresponds to other data for the same event or station.

In addition to better parameter estimates, another distinct advantage of robust reweighting is that the covariance matrix becomes a much more accurate estimate of the uncertainties in the parameters. That is so, because the diagonal elements of the covariance matrix, $C=[(WM)^T(WM)]^{-1}$ (where W is the final weighting matrix and M is the forward modeling matrix as above) are estimates of the variance when scaled by the total misfit

$$\hat{\sigma}^2 = \frac{1}{u-v} \sum_i \sum_j [a_{i,j} - (\hat{e}_j + \hat{s}_i)]^2 \quad (9)$$

(e.g. Lawson and Hanson, 1974). The accuracy of those estimates, however, depends on the weights being proportional to the inverses of the standard deviations.

Trade-offs between the standard least squares and the robust solutions

We've suggested that if errors are not normally distributed or the data include some large outliers, the least squares solution could provide a poor estimate of some parameter values. If on the other hand, the errors are normally distributed, the least squares solution is the maximum likelihood solution. Any other solution, including the robust reweighted solution, would be worse, so there is a price to be paid for using robust reweighting. We illustrate with a simple synthetic example the relative extent of error we risk from using each approach.

We constructed an exact synthetic data set assuming 10 stations with various site amplifications recording 20 events of various magnitude. We then added normally distributed random noise scaled to have a standard deviation equal to 10% of the expected log amplitude for each measurement, and found the least squares and robust estimates. We repeated the experiment 100 times to determine accurately the typical error of each type of solution (Table 1). The average error of the robust estimates of magnitude are only 3% worse than those of the least squares estimates (2.65% vs. 2.57%), and the site amplification estimates are only 3.5% worse (9.96% vs. 9.623%). However, when the added noise is taken from the heavier-tailed exponential distribution, the least squares magnitude estimates are 12% worse than the robust estimates (3.6% Vs 3.22%) and the site amplification estimates are 17% worse (13.15% vs. 11.23%). The difference is even greater if there are some large outliers in the data. For a data set as above, but with a couple of measurements significantly off (one measurement is ~ 2.5 times too large, and one is ~ 2 times too small), the least squares estimates are much worse than the robust reweighted estimates. Those 2 *bad* measurements affect the estimates of 4 parameters, the 2 events involved and the 2 stations. Over 100 runs (adding different random exponential noise, but the same 2 blunders), the mean least squares estimates for those parameters were significantly worse than the robust estimates (Table 1). The difference is due to the robust weights assigned to the those parameters. In the least squares solution, all measurements are assigned equal weight. In the robust estimates, the 2 dubious data are recognized and assigned weights of about 0.36 (the mean weight for all other measurements in the final robust iteration was 0.965).

Table 5.1: Differences in mean errors between the least squares (second and third columns) and robust (rightmost two columns) solutions to synthetic data with normal (top row) and exponential (second row) noise, and large outliers (bottom rows).

Type of noise added	Mean least squares error		Mean robust solution error	
	Magnitudes	Amplifications	Magnitudes	Amplifications
Gaussian	2.57%	9.62%	2.65%	9.96%
Exponential	3.60%	13.15%	3.22%	11.23%

	Magnitudes	Amplifications	Magnitudes	Amplifications
	L.S. (true)	L.S. (true)	robust (true)	robust (true)
Exponential +2	6.74 (6.5)	0.342 (0.300)	6.55 (6.5)	0.309 (0.300)
blunders	6.33 (6.5)	0.341 (0.375)	6.52 (6.5)	0.380 (0.375)

The effect of robust reweighting on real data

In considering whether to use a particular technique, one wishes to know whether the improvement in resolution will be sufficient to justify the time and effort required to implement it. This section demonstrates the considerable advantages of robust reweighting over standard least squares for a real geophysical problem. As one would expect from the earlier technique description, the additional programming required to implement robust reweighting, once the least squares estimate has been accomplished, is almost negligible.

For the SCSN problem, we do not have to simply guess what the error distribution is. Once we have a solution, we can test whether the errors fit the assumed distribution. Although the L_1 -norm solution is generally preferred as an initial solution for robust techniques as it is not nearly as sensitive to outliers as the least squares solution, it is unwieldy to calculate for such a large system. Hence we

begin with a standard least squares solution weighted only by signal-to-pre-event-noise ratios (the validity of that *a priori* estimate of the standard deviation is discussed in Appendix 1). We perform a Kolmogorov-Smirnov test on the misfits, and find that the distribution is normal with probability zero. We can see that the actual error distribution has much heavier tails than the normal distribution, and has some very large errors (Figure 2). The heavier-than-Gaussian tails and very large errors indicate that robust reweighting is warranted. The robust weights are determined based on the Hampel 17a influence function with equation (6) parameters set to values of $a=1.7$, $b=3.5$, and $c=8$. Although these are typical suggested values (e.g. Montgomery and Peck, 1982), we re-iterate that it is most important that the final parameter estimates be robust to a wide range of choices of a , b , and c .

Even limiting consideration to those recording at least 10 events on-scale, we found dramatic changes in site amplifications due to robust reweighting. 28 sites (out of 189 recording 10 or more events) had changes of 10% or greater. 13 changed by more than 20%. Examining the data that were downweighted at sites with large estimates of variance reveals the power of the robust reweighting to identify dubious data that would otherwise almost certainly go unnoticed.

We begin with a simple example, station SBK, which had the 4th largest variance and a change in site amplification from 0.51 to 0.83. Figure 3 (top left panel) shows that 7 recordings out of 29 were given nearly zero weight, and all 7 are from the same continuous time interval (the beginning of 1992 through to the beginning of 1994). Clearly, something was different about the station during that interval. We suppose that an indication of the station's magnification can be obtained by background noise levels, and so compare the pre-event noise vs. the date (second row, left column) and the robust weights vs. pre-event noise (bottom row, left column). Pre-event noise levels much lower than were typical for SBK were recorded for the downweighted events. We conclude that the instrument's magnification was reduced during this time period, without the change in instrument parameters being recorded. In this case robust re-weighting has greatly improved a parameter estimate by removing dubious data. For this station, the same end might have been achieved via a careful, and lengthy, examination of pre-event noise levels vs. time for all stations (although it is only through the robust

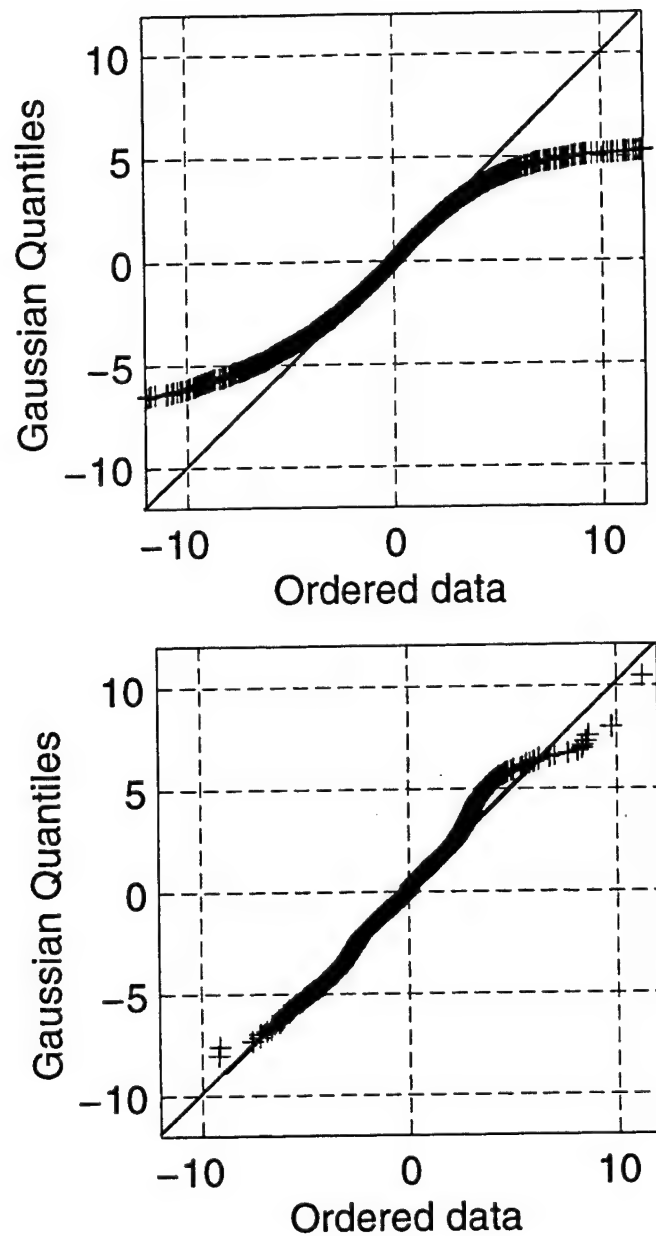


Figure 5.2: Quantile-quantile plots for the misfits from the least squares (top), and robustly reweighted solution (bottom). If the misfits were normally distributed, the points would lie along the diagonal. The large deviation from the diagonal beginning at approximately 2 standard deviations, in the least squares case, indicates that the distribution of the error is much heavier-tailed than normal. The very large outliers most likely indicate outright blunders in the data.

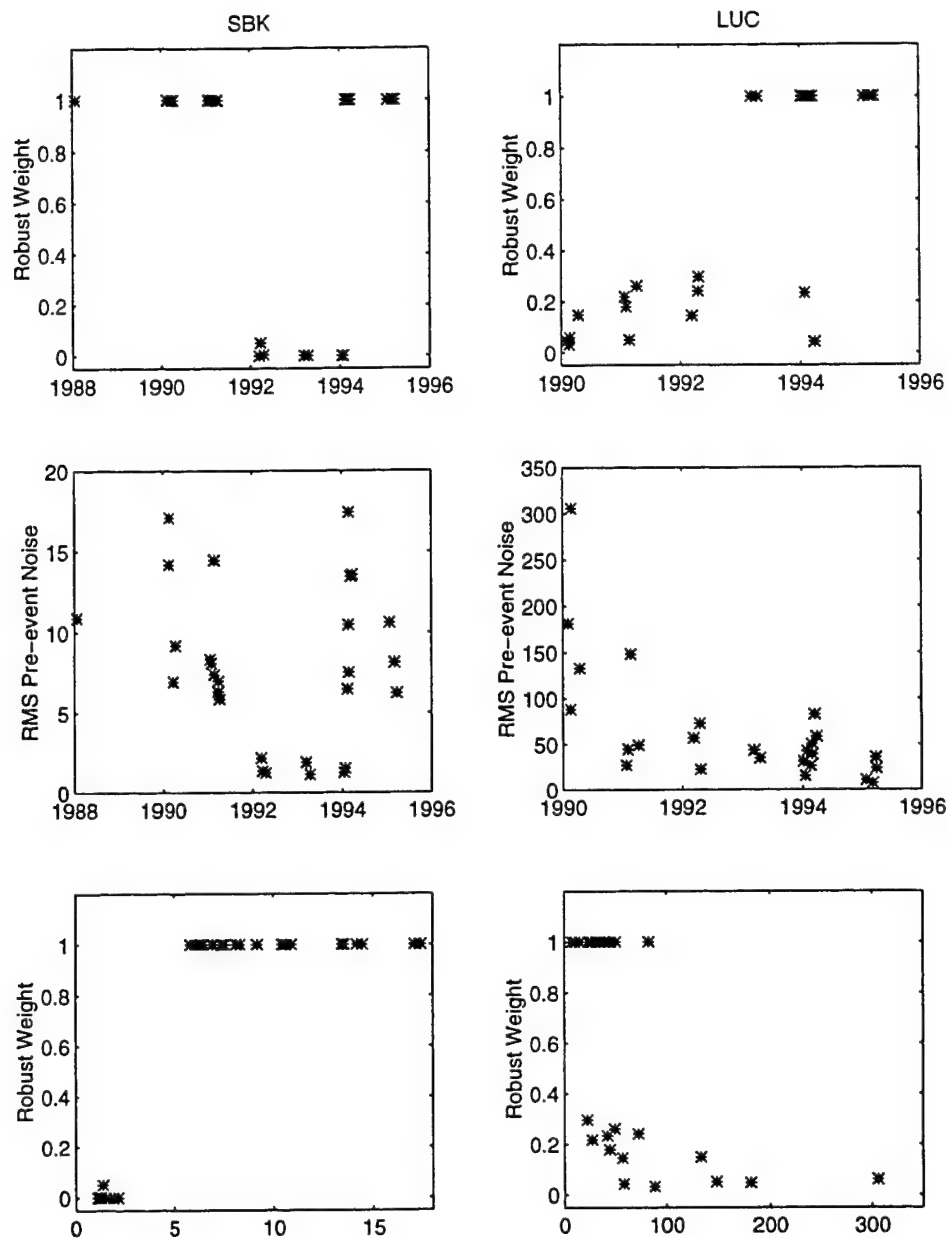


Figure 5.3: Plots of robust weights vs. event dates (top row) for two of the stations most affected by the robust reweighting, showing a distinct grouping of low weights within specific time periods. Pre-event noise levels vs. event dates (middle row) indicate that magnification was likely significantly lower than was recorded in instrument parameter logs for station SBK (left column) during that time period. The robust weights are plotted vs. the pre-event noise levels in the bottom row. The correlation is perfect for SBK, but more muddled for LUC (right column)

reweighting that it occurred to us to perform such a test), or by simply throwing out very large outliers. The next example is not as straightforward, and could not have been resolved by other such means.

The site amplification at LUC had by far the largest variance and the greatest change, from 0.51 to 1.02. 13 out of the 26 recordings were given robust weights of 0.3 or less, and 11 of them are from the same continuous time period (figure 3, upper right). As with SBK, it appears likely that something about the instrument response was different during that time period, but just what is less clear. The pre-event noise level was higher for the 4 events in 1990, but from then on the level remained within a roughly constant range. Something else, perhaps a change in the seismometer's response to velocities much higher than background noise levels, appears to have changed. Although we cannot identify the exact cause, the suspicious grouping of low weights with time indicates a problem with the instrument response that the robust reweighting has effectively alerted us to. Similar problems with incorrect instrument response information appear to be at the root of the changes in most other stations with high variances. In no case did low robust weights clearly correlate with event azimuth, depth, or size. For a small number of stations with high variances, a clear cause is not evident. It may be that multiple causes obscure the explanation (e.g. incorrect instrument parameters for multiple time periods, mislabeling of some seismograms resulting in their attribution to the wrong stations). We cannot be certain in such cases, as we are for most, that the parameter estimate has been improved by the robust reweighting, but the technique has clearly alerted us that those site amplifications are poorly constrained.

The magnitude estimates were not as strongly affected, with the greatest change between least squares and robust solutions being 2.7%, or 0.2 magnitude units. Upon re-examining the records for that event, we see that 5 of the 107 recordings were given robust weights of zero, and all 5 were at stations recognized as having incorrect instrument response parameters on the event date. All other recordings of that event had robust weights of 1.0. The small changes in other event magnitudes also appear attributable to errors in instrument responses.

As mentioned in the description of robust reweighting, for such a solution to be meaningful, it must be consistent in the face of changes to the influence function parameters (i.e. a , b , and c of (6)) and to the use of alternate influence functions. The SCSN robust solutions remained consistent throughout both types of changes.

To summarize, scrutiny of the data behind the parameters most affected by the robust reweighting indicates that the technique has correctly singled out and downweighted problematic data and so improved parameter estimates, and has alerted us to poorly constrained parameter values. We conclude that, just as in the synthetic experiments, robust reweighting has improved the estimates of site amplifications for the SCSN.

Incorporating censored data into parameter estimates: Previous work in magnitude estimation

Ringdal (1977) incorporated low signal level information into magnitude estimation using maximum likelihood estimation. Estimating only magnitude and variance, he was able to simply examine a range of parameter values to maximize the likelihood function. He found that magnitude biases of 0.5 magnitude units due to censoring were probable for teleseismic events recorded on a small network, and were correctable by incorporation of the censored data. He anticipated further improvement for larger networks. Blandford and Shumway (1982) extended that work to include clipping information and the estimation of individual station biases and distance corrections. They maximized the likelihood function using the expectation maximization approach. Our approach expands on both of these studies. We also consider doubly censored data, although we use an inverse approach to solve iteratively a linearized version of the set of equations obtained by setting the derivatives of the likelihood function equal to zero.

Derivation of the Likelihood Function

The problem is to determine the set of site amplifications and event magnitudes that is most likely, given the set of amplitudes we have measured. To do so, we assume that the noise in the data is

normally distributed so that we can determine functions that describe the probability of having obtained each type of measurement (upper thresholds for clipped data, amplitude measurements for on-scale data, and lower thresholds for below noise level data) in terms of the parameters we wish to estimate, namely site amplifications and event magnitudes. As the inaccuracy of the assumption of normality has been amply demonstrated, we use robust reweighting to solve the censored problem, but for clarity we do not discuss it further in this section. The likelihood function is the product of the probabilities for each individual measurement and so represents the probability of having obtained a particular entire set of measurements, in terms of a set of parameter values (e.g. Montgomery and Peck, 1982). The *most likely* set of parameter values is that set which maximizes the probability of having obtained the actual measurements, and so is found by maximizing the likelihood function.

As each $a_{i,j}$ is a random variable drawn from a normal distribution with mean $(e_j + s_i)$ and standard deviation $\sigma_{i,j}$, according to the assumptions made in writing (2), the probability of obtaining a particular value $a_{i,j}$, that is, the probability density function of $a_{i,j}$, is

$$P(a_{i,j}) = \phi\left(\frac{a_{i,j} - e_j - s_i}{\sigma_{i,j}}\right) \quad (10)$$

where ϕ is the standard normal distribution function. For noisy records, the probability of the amplitude being below the measured noise level is the integral of the distribution (10) over the range of values below the noise level, that is,

$$\begin{aligned} P(a_{i,j} \leq t_{i,j}) &= \int_{-\infty}^{\left(\frac{t_{i,j} - e_j - s_i}{\sigma_{i,j}}\right)} \phi\left(\frac{a_{i,j} - e_j - s_i}{\sigma_{i,j}}\right) d\left(\frac{a_{i,j} - e_j - s_i}{\sigma_{i,j}}\right) \\ &= \Phi\left(\frac{t_{i,j} - e_j - s_i}{\sigma_{i,j}}\right) \end{aligned}$$

$$= \int_{-\infty}^{t_{i,j}} \phi\left(\frac{a_{i,j} - e_j - s_i}{\sigma_{i,j}}\right) \frac{da_{i,j}}{\sigma_{i,j}} \quad (11)$$

where $t_{i,j}$ is the estimated amplitude threshold, obtained by measuring the noise level over the appropriate time window, and $\Phi(x)$ is the cumulative distribution function of a standardized random variable, i.e. $\Phi(x) = \int_{-\infty}^x e^{-\frac{t^2}{2}} dt$. Similarly, for clipped records, we estimate $t_{i,j}$, a maximum threshold. Then, the equation,

$$\begin{aligned} P(a_{i,j} \geq t_{i,j}) &= \int_{\left(\frac{t_{i,j} - e_j - s_i}{\sigma_{i,j}}\right)}^{\infty} \phi\left(\frac{a_{i,j} - e_j - s_i}{\sigma_{i,j}}\right) d\left(\frac{a_{i,j} - e_j - s_i}{\sigma_{i,j}}\right) \\ &= \Phi\left(\frac{-t_{i,j} + e_j + s_i}{\sigma_{i,j}}\right) \\ &= \int_{-\infty}^{-t_{i,j} + e_j + s_i} \phi\left(\frac{a_{i,j} - e_j - s_i}{\sigma_{i,j}}\right) \frac{da_{i,j}}{\sigma_{i,j}} \end{aligned} \quad (12)$$

describes the probability that the amplitude is above the threshold.

The likelihood function is

$$L(a_{1,1}, a_{1,2}, \dots, a_{i,j}, t_{1,1}, t_{1,2}, \dots, t_{k,l}, t_{1,2}, \dots, t_{n,m} | e_1, e_2, \dots, e_p, s_1, s_2, \dots, s_q) =$$

$$\prod_{i,j \in \mathcal{D}} P(a_{i,j}) \prod_{k,l \in \mathcal{N}} P(a_{i,j} \leq t_{k,l}) \prod_{m,n \in \mathcal{C}} P(a_{i,j} \geq t_{m,n}) \quad (13)$$

where D is the set of measured amplitudes, N is the set of observations in which the signal was below the noise level, and C is the set of clipped records.

Maximizing the likelihood function by iteratively solving a linearized equation

We substitute (10), (11), and (12) into (13), separate the products into sums by taking the natural logarithm of the likelihood function, and then maximize the likelihood function by setting the derivatives with respect to e_j and s_i , equal to 0. The derivatives with respect to e_j are

$$\begin{aligned} \frac{\partial}{\partial e_j} \log(L) = & \sum_{i \in D} \left(\frac{a_{i,j} - e_j - s_i}{\sigma_{i,j}^2} \right) - \sum_{k \in N} \frac{1}{\sigma_{k,j}} \frac{\phi \left(\frac{t_{k,j} - e_j - s_k}{\sigma_{k,j}} \right)}{\Phi \left(\frac{t_{k,j} - e_j - s_k}{\sigma_{k,j}} \right)} \\ & + \sum_{m \in C} \frac{1}{\sigma_{m,j}} \frac{\phi \left(\frac{-t_{m,j} + e_j + s_m}{\sigma_{m,j}} \right)}{\Phi \left(\frac{-t_{m,j} + e_j + s_m}{\sigma_{m,j}} \right)} \end{aligned} \quad (14)$$

where the summations are over all stations that recorded the event j on-scale (first term on the right side), stations where the signal was below the noise level (second term), and stations that clipped (third term). The equations for derivatives with respect to the station amplification parameters are similar (the terms are identical, but the summations are over all events recorded at the station). In the second and third terms, the data are nonlinear functions of the parameters. To maximize the likelihood function, we linearize (14) and use a starting model based on just the on-scale recordings (robustly reweighted) to find iteratively the parameter values where (14) is closest to zero.

For convenience, we call the derivative of the log of the likelihood function, (14), $Z(\mathbf{e})$, where \mathbf{e} is the set of all parameters, $(e_1, e_2, \dots, e_p, s_1, s_2, \dots, s_q)$. The Taylor series expansion of one element of $Z(\mathbf{e})$, for example the derivative with respect to e_j in (14), is

$$Z_j(\mathbf{e}) = Z_j(\mathbf{e}_0) + \sum_h \left. \frac{dZ_j}{de_h} \right|_{e_h=e_{h_0}} (e_h - e_{h_0}). \quad (15)$$

The summation is over all parameters \mathbf{e} . The only non-zero derivatives of $Z_j(\mathbf{e})$ are those with respect to site amplifications at the stations that recorded the event and with respect to e_j .

(15) equals zero when L is maximized, so

$$Z_j(\mathbf{e}_0) = - \sum_h \left. \frac{dZ_j}{de_h} \right|_{e_h=e_{h_0}} (e_h - e_{h_0}), \quad (16)$$

is the equation we need to satisfy.

The derivative of Z_j , the second derivative of the likelihood function (14), with respect to the event e_j , is

$$\begin{aligned} \frac{\partial^2}{\partial e_j^2} \log(L) = & \sum_{i \in \mathcal{D}} \frac{-1}{\sigma_{i,j}^2} - \frac{1}{\sigma_{k,j}^2} \sum_{k \in \mathcal{N}} \left\{ G\left(\frac{t_{k,j} - e_j - s_k}{\sigma_{k,j}}\right) + H\left(\frac{t_{k,j} - e_j - s_k}{\sigma_{k,j}}\right) \right\} \\ & - \frac{1}{\sigma_{m,j}^2} \sum_{m \in \mathcal{C}} \left\{ G\left(\frac{-2t_{m,j} + e_j + s_m}{\sigma_{m,j}}\right) + H\left(\frac{-2t_{m,j} + e_j + s_m}{\sigma_{m,j}}\right) \right\} \quad (17) \end{aligned}$$

where

$$G(x) = x \frac{\phi(x)}{\Phi(x)}, \text{ and } H(x) = \frac{\phi^2(x)}{\Phi^2(x)}. \quad (18)$$

The summations in (17) are over all stations recording the event, on- and off-scale.

The second derivatives with respect to station amplifications are again similar, with the difference being that the summations are over all events recorded at the station. The derivatives with respect to

both an event and station parameter consist of just the single term in (17) containing both parameters e_y and s_x . Whether $a_{x,y}$ is an on-scale or threshold measurement only effects which summation of (17) the term is drawn from. Successive estimates of \mathbf{e}_0 are calculated from (15), until they don't vary significantly from the previous estimate. (15), expressed in matrix form is

$$\begin{bmatrix} \frac{\partial \mathcal{L}(\mathbf{e}_0)}{\partial e_1} \\ \frac{\partial \mathcal{L}(\mathbf{e}_0)}{\partial e_2} \\ \vdots \\ \frac{\partial \mathcal{L}(\mathbf{e}_0)}{\partial e_p} \\ \frac{\partial \mathcal{L}(\mathbf{e}_0)}{\partial s_1} \\ \frac{\partial \mathcal{L}(\mathbf{e}_0)}{\partial s_2} \\ \vdots \\ \frac{\partial \mathcal{L}(\mathbf{e}_0)}{\partial s_q} \\ 0 \end{bmatrix} = \begin{bmatrix} \frac{\partial^2 \mathcal{L}(\mathbf{e}_0)}{\partial e_1^2} & 0 & \dots & 0 & \frac{\partial^2 \mathcal{L}(\mathbf{e}_0)}{\partial e_1 \partial s_1} & \frac{\partial^2 \mathcal{L}(\mathbf{e}_0)}{\partial e_1 \partial s_2} & \dots & \dots & \frac{\partial^2 \mathcal{L}(\mathbf{e}_0)}{\partial e_1 \partial s_q} \\ 0 & \frac{\partial^2 \mathcal{L}(\mathbf{e}_0)}{\partial e_2^2} & \dots & 0 & \frac{\partial^2 \mathcal{L}(\mathbf{e}_0)}{\partial e_2 \partial s_1} & \frac{\partial^2 \mathcal{L}(\mathbf{e}_0)}{\partial e_2 \partial s_2} & \dots & \dots & \frac{\partial^2 \mathcal{L}(\mathbf{e}_0)}{\partial e_2 \partial s_q} \\ \vdots & \vdots & \ddots & 0 & \vdots & \vdots & & & \vdots \\ 0 & 0 & 0 & \frac{\partial^2 \mathcal{L}(\mathbf{e}_0)}{\partial e_p^2} & \frac{\partial^2 \mathcal{L}(\mathbf{e}_0)}{\partial e_p \partial s_1} & \frac{\partial^2 \mathcal{L}(\mathbf{e}_0)}{\partial e_p \partial s_2} & \dots & \dots & \frac{\partial^2 \mathcal{L}(\mathbf{e}_0)}{\partial e_p \partial s_q} \\ \frac{\partial^2 \mathcal{L}(\mathbf{e}_0)}{\partial e_1 \partial s_1} & \frac{\partial^2 \mathcal{L}(\mathbf{e}_0)}{\partial e_2 \partial s_1} & \dots & \frac{\partial^2 \mathcal{L}(\mathbf{e}_0)}{\partial e_p \partial s_1} & \frac{\partial^2 \mathcal{L}(\mathbf{e}_0)}{\partial s_1^2} & 0 & \dots & \dots & 0 \\ \frac{\partial^2 \mathcal{L}(\mathbf{e}_0)}{\partial e_1 \partial s_2} & \frac{\partial^2 \mathcal{L}(\mathbf{e}_0)}{\partial e_2 \partial s_2} & \dots & \frac{\partial^2 \mathcal{L}(\mathbf{e}_0)}{\partial e_p \partial s_2} & 0 & \frac{\partial^2 \mathcal{L}(\mathbf{e}_0)}{\partial s_2^2} & \dots & \dots & 0 \\ \vdots & \vdots & & \vdots & \vdots & \vdots & \ddots & & \vdots \\ \vdots & \vdots & & \vdots & \vdots & \vdots & & \ddots & \vdots \\ \frac{\partial^2 \mathcal{L}(\mathbf{e}_0)}{\partial e_1 \partial s_q} & \frac{\partial^2 \mathcal{L}(\mathbf{e}_0)}{\partial e_2 \partial s_q} & \dots & \frac{\partial^2 \mathcal{L}(\mathbf{e}_0)}{\partial e_p \partial s_q} & 0 & 0 & \dots & \dots & \frac{\partial^2 \mathcal{L}(\mathbf{e}_0)}{\partial s_q^2} \\ 0 & 0 & \dots & 0 & 1 & 1 & \dots & \dots & 1 \end{bmatrix} \begin{bmatrix} e_1 - e_{1_0} \\ e_2 - e_{2_0} \\ \vdots \\ e_p - e_{p_0} \\ s_1 - s_{1_0} \\ s_2 - s_{2_0} \\ \vdots \\ s_q - s_{q_0} \end{bmatrix} \quad (19)$$

where $\mathcal{L}(\mathbf{e}_0)$ represents the log of the likelihood function, evaluated at \mathbf{e}_0 .

In implementing the iterative calculations by inversion of (19), it is necessary to normalize the standard deviation estimates of all data. For the least squares estimate from just the on-scale data, it was sufficient that the weights be proportional to the inverse standard deviations, but the arguments of functions in (17) depend on the absolute value of the standard deviations. Hence, all standard deviation estimates should be scaled, either by s of (4), or σ of (9).

The practical effects of iterative reweighting to incorporate censored data

For a set of data with events recorded on overlapping sets of stations, simultaneously calculating site amplifications and event magnitudes serves the same purpose as iterative reweighting for censoring. This was noted by Ringdal (1977), who demonstrated the effect of censoring on small data sets where the type of measurement precluded estimating station corrections (he measured teleseismic

peak amplitudes, which are sensitive to backazimuth at the station and source radiation patterns). In tests for the case of single censoring, both for synthetic data from a 10 station network and 100 events, and with data from 13 WWSSN stations and 61 events, Ringdal showed that a bias of 0.5 Mb units was a realistic effect of estimating magnitudes of teleseismic events from censored data without estimating station corrections. In the SCSN problem we are able to simultaneously calculate magnitudes and site amplifications, as rms amplitude measurements of near-source scattered coda are insensitive, or at least much less sensitive, to event azimuth. This does not mean that the censored data are entirely redundant, as the data are both limited and noisy.

For the SCSN study, there proved to be sufficient overlapping data that the iterations for censoring had little first order effect on most parameter values. Changes in magnitude estimates were on the order of 1% or less. There were some greater changes in site amplification values (table 2). For application of site amplifications, we use only those sites with at least 10 on-scale recordings (Baker, et. al., 1996), but to illustrate the importance of censored data on parameters dependent on fewer data, we present all site amplifications with more than a 5% change in their values due to the incorporation of censored data (only one had more than 10 on-scale recordings). Note that one site amplification (the first listed) increased by 5.8%, despite having no censored data. The magnitude of each event that station recorded was reduced in magnitude by the incorporation of censored data. This indicates the surprising importance of the very small changes in magnitude estimates to site amplification estimates when few data are available. While the effect of censored data proved to be small for this problem, we consider the changes to be an improvement in the accuracy of the site amplifications calculated. This exercise also provides some insight into the extent of the effect of censoring in a problem with many data and many parameters. Although the noise level of the data and appropriateness of the model are important and will make prediction of the effect of censoring difficult, this result indicates that for any problem with parameters dependent on few data, especially if the extent of overlap of parameter values is small, ignoring censoring could lead to significant error.

Table 5.2: Differences between site amplifications for the SCSN with and without incorporating censored data.

Number of on-scale recordings	Number of below-noise recordings	Number of clipped recordings	Censored estimate	Uncensored estimate	Difference between estimates
6	0	0	0.54	0.57	5.8%
16	2	0	1.13	1.05	7.2%
2	6	1	1.23	1.11	10.3%
3	2	0	0.98	0.87	11.3%
1	1	0	0.47	0.54	14.2%
4	4	0	0.61	0.72	16.8%
3	8	11	0.74	0.86	17.2%

Conclusions

We have demonstrated with both synthetic and real data examples how robust statistics significantly improve the accuracy of magnitude and site amplification estimation. This works by reducing the influence of outliers in data drawn from heavy tailed distributions, and so should be applicable to a wide variety of geophysical problems. The robust reweighting not only automatically *throws out* very large outliers from data sets too large to permit more than spot-checking of outliers, but downweights moderate outliers so that the least squares criterion does not allow a single datum or a few data to bias a solution significantly. It also greatly increases the accuracy of uncertainty estimates for a least squares problem. Its efficiency and ease of implementation make it an attractive and sensible choice for improving geophysical parameter estimates.

We also find that parameter estimates are improved through the incorporation of censored data via maximum likelihood estimation. This was previously demonstrated, and our contributions are 1) to

derive and present all equations necessary to incorporate censored data into estimates of magnitude and station amplifications, and 2), to confirm its usefulness on a very large data set, where overlapping events and stations might have lead us to suspect that the censored data would not be important. Again, we expect this technique could be applied with profit to other areas of geophysics where signals are often outside the range of the recording instruments.

References

- Baker, G. E., G. Wagner, and J. B. Minster (1996), Site amplifications of southern California network stations from diffuse teleseismic coda, manuscript in preparation
- Blandford R., and R. Shumway (1982), Magnitude:yield for nuclear explosions in granite at the Nevada Test Site and Algeria: joint determination with station effects and with data containing clipped and low-amplitude signals, *Teledyne Geotech Report*, VSC-TR-82-12
- Huber, Peter J. (1972), Robust statistics: a review, *Annals of Math. Stats.*, V **42**, no. 4, 1041-1067
- Jeffreys, H. (1932), An alternative to the rejection of observations, *Proc. Roy. Soc. A*, **137**, 78-87
- Lawson, C. and R. Hanson (1974), Solving least squares problems, Prentice-Hall Inc.
- Montgomery, P. and E. Peck (1982), Introduction to linear regression analysis, Pub. John Wiley and Sons.
- Press, W.H., B.P. Flannery, S.A. Teukolsky, and W.T. Vetterling (1988), Numerical recipes in C, the art of scientific computing, Cambridge Univ. Press
- Priestley, M.B. (1981), Spectral analysis and time series, Academic Press
- Ringdal, F. (1977), Maximum likelihood estimation of seismic event magnitude, *Bull. Seism. Soc. Am.*, **67**, 789-802

Appendix 5.1

Validity of *a priori* weighting by ratios of signal to pre-event noise

For the SCSN problem, we made an initial estimate of each $\sigma_{i,j}$ based on the signal to pre-event noise ratio. Pre-event noise may be a major source of error in the measurements of amplitudes, but statistical variability is likely due to more than additive background noise. For example, as mentioned earlier, scattering into the coda may be distinctly azimuthally dependent at some stations or a radiation pattern nodal line for some event might cross the network so that incoming energy varies significantly. Since we don't know *a priori* which amplitude measurements will be affected, the best we can do for an initial estimate of the standard deviation is to use the ratio of signal amplitude to pre-event noise, but recognizing that there will be other contributions to the overall error process, we should place a minimum on the permissible estimate of $\sigma_{i,j}$. We note that although seismic pre-event noise is additive, we expressed the uncertainty in the amplitude as a multiplicative factor in (1). This expression, which permits separation of all the factors in (1) by taking the logarithm, could prove difficult to justify theoretically, but may provide an adequate empirical model of the noise. We relate the effect of the ratio of the signal to pre-event noise, to Γ of (1), as follows. As the signal and noise are assumed to be independent, the mean squared sum of their amplitudes should be additive, and so we can write

$$\begin{aligned} A_t^2 &= A_s^2 + A_n^2 \\ &= A_s^2 \left(1 + \frac{A_n^2}{A_s^2} \right) \end{aligned} \quad (A1)$$

Hence,

$$\Gamma = \sqrt{1 + \frac{A_n^2}{A_s^2}}. \quad (A2)$$

We set the minimum permissible value of $\sigma_{i,j}$ at $\log(1.2)$, which is done in practice by taking $\hat{\sigma}_{i,j} = \log(1.2 \cdot \Gamma_{i,j})$. When the signal and noise levels are equal, we have a minimum weight of $[\log(1.2 \cdot \sqrt{2})]^{-1}$. The effective maximum weight of $[\log(1.2)]^{-1}$ is approached when the signal to noise ratio becomes very large (at a signal to noise amplitude ratio of about 8 to 10, the differences between weights become fairly small).

The robust reweighting provides us with the opportunity to examine the validity of this signal to pre-event noise ratio based *a priori* weighting. We cannot generally do this for real data, as we don't know the true solution. It turns out however, that the robust solution is nearly independent of whether we initiate the robust iterations with the weighted or unweighted least squares solution. The difference between magnitude estimates starting with the weighted vs. the unweighted least squares estimates was less than 0.3% for all events. One site amplification varied by nearly 4%, one by 2%, 15 varied between 1% and 2%, and the remaining 194 varied by less than 1%. If we accept that the robust solution is closer to the true solution, it is worth asking whether the *a priori* weights we chose brought us closer to that solution. We can see from Table A1 that they did. For every site amplification for which the *a priori* weighted and unweighted least squares solutions varied by more than 5%, the weighted solution was closer to the robust solution (Table A1).

Table 5A.1: Differences between unweighted and *a priori* weighted least squares site amplification estimates. The robust estimates are effectively the same whether we begin with or without *a priori* weighting, and we see that the *a priori* weighted values are always closer to the presumably more accurate, robustly weighted values.

Difference between estimates	Number of events recorded at each station	Unweighted least squares estimate	Weighted least squares estimate	Robustly weighted least squares estimate
5.1%	10	1.49	1.57	2.13
5.1%	24	0.72	0.76	0.81
5.5%	18	0.45	0.48	0.68
5.7%	26	0.62	0.65	0.72
8.0%	16	0.80	0.87	1.05
8.6%	34	0.59	0.65	0.68
14.5%	19	0.57	0.67	1.12
24.8%	37	0.46	0.61	0.60
28.2%	28	0.51	0.71	0.68
28.5%	18	0.78	1.09	1.05

Diffuse coda site amplifications in southern California and the nature of Lg waves

Abstract

We use near-receiver-scattered teleseismic coda (*diffuse coda*) to calibrate the amplification of 189 southern California seismic network (SCSN) stations. This calibration is done to enable the estimation of variations in the absolute amplitude of the crustal seismic phase Lg. We investigate the basis for the assumption that diffuse coda provides an isotropic source of Lg-like energy through a review of previous research on both teleseismic coda and Lg. We also investigate which parameters influence site amplifications, and to what extent. The results of this analysis provide the basis for the design of an Lg propagation study. Specifically, we discuss how best to control factors important to site amplification so that observed Lg amplitude variations may be attributed fully to path effects.

To separate the diffuse from the *coherent* (near-source scattered) component of teleseismic coda, we remove the network beam from each individual trace. The site amplifications and signal magnitudes are simultaneously estimated using a maximum likelihood approach for doubly censored data, with robust re-weighting (Baker and Minster, 1996). The insensitivity of site amplifications to small differences in wavetype is verified by the high correlation of those calculated from deep event coda and those calculated from shallow event coda. The diffuse coda site amplifications are also well correlated with site amplifications determined from S-wave coda of local events (Su and Aki, 1995).

Introduction

We have isolated the near-receiver scattered component of teleseismic coda and used it to calibrate site amplifications at SCSN stations (figure 1). Instrument gains were calculated for all stations at the time of each event (Wald et. al., 1994), and data were not used for stations and times for which any instrument constants were not known.

There are three distinct stages to this work, which we discuss separately. We first consider the nature of teleseismic coda and Lg and discuss the implications for the design of an Lg propagation study. We then describe the processing required to separate diffuse from coherent coda. Finally, we examine the site amplifications themselves. We compare the diffuse coda site amplifications calculated from just deep event coda with those calculated from shallow event coda. We also compare the diffuse coda site amplifications calculated from all events with site amplifications from local S-wave coda, and consider implications of the differences.

Motivation - Isolating site effects from propagation effects on absolute amplitudes.

High frequency regional discriminants for nuclear verification fail quite often. That is, they classify an explosion as an earthquake or vice-versa (e.g. Taylor et. al., 1989). Some such errors may be due to truly odd sources or to near-source scattering, but much of the misclassification is a result of changes in the signal due to structure along the path of propagation (e.g. Baker and Minster, 1995). Thus, these changes may be predictable. Zhang et al. (1994) showed that some variation of Lg amplitudes, relative to other regional phases, are reasonably well correlated with measurable properties of the path, such as statistics of topography. That study was based on just 7 stations spread out across Eurasia, and the path lengths were one or two orders of magnitude greater than the scale at which Lg has been observed to disappear entirely. For example, the Lg/Pg amplitude ratio, the best single high frequency regional discriminant (Taylor, et. al., 1989), has been observed to change dramatically over just 20 km distance for regional events recorded on the SCSN (Baker and Minster, 1995). To better understand the physics of problem, we must quantify the variations in Lg amplitude with path properties, such as was done by

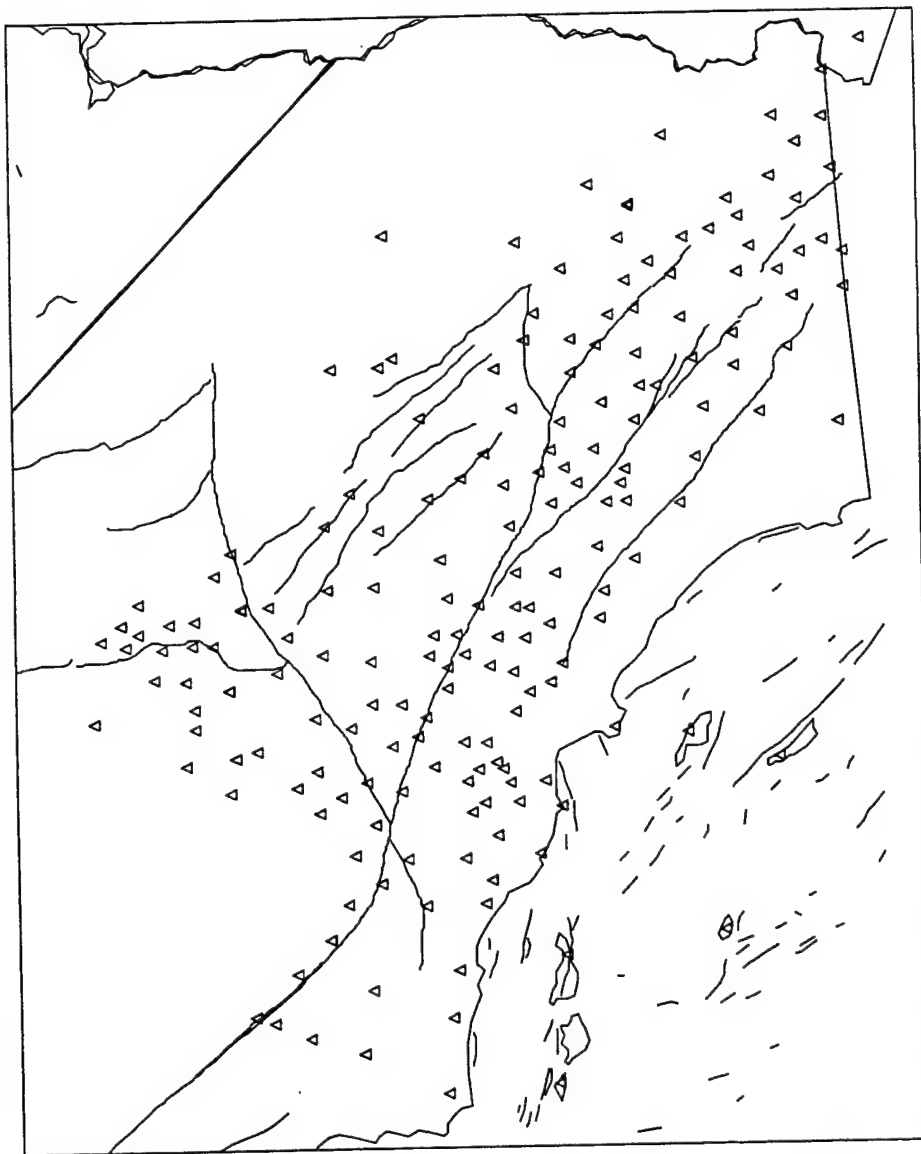


Figure 6.1: Stations of the southern California seismic network for which site amplifications were calculated.

Zhang and Lay (1994), but at a densely spaced network such as the SCSN. We must also resolve the ambiguity as to which phase varies, Lg or Pg, which is why Lg site amplifications are necessary. To calibrate each site it would be ideal to have an isotropic source of Lg of known amplitude. We use the diffuse teleseismic coda to approximate that ideal.

What controls site amplifications?

To determine whether diffuse coda is an appropriate surrogate for Lg, we first must consider what characteristics of a wave influence its amplification. Amplification has long been recognized to depend on the impedance of the uppermost layer (e.g. Gutenberg, 1957). In southern California, the mean amplification for large numbers of sites binned by sediment age correlate well with the age, which presumably correlates with impedance (Su and Aki, 1995). There is significant variation within each bin however, which suggests that there are important secondary factors influencing amplification. Those factors could be a variety of things, many of which are difficult to measure. For example, the effects on surface amplification of focusing and de-focusing of various surface topographies have been modeled and shown to be significant. Specifically, Kawase (1988) modeled the effects of canyon topography, Bouchon (1973) modeled the effects of mountain topography, and Trifunac (1971) modeled the effects of an alluvium filled valley. Benites and Aki (1989) simulated the effect of small-scale, near-surface heterogeneity on surface amplification, and found that both higher and lower impedance inclusions de-amplify the surface motion. The harder inclusions do so by scattering and de-focusing the incoming energy, whereas the softer inclusions do so by trapping energy within the inclusions, where it eventually attenuates as it resonates.

The layer thickness to which a signal is sensitive will depend on its frequency. In media whose impedance increases with depth, higher frequencies should have greater amplification. This frequency dependence has also been observed (e.g. Gutenberg, 1957).

Figure 2 illustrates that the incidence angle at the surface should also be a factor in amplification (e.g. Aki and Richards, 1980). This curve is valid for any velocity medium. In practice however, the incidence angle is likely to be highly variable, and unpredictable. For example, Vernon et al. (1991)

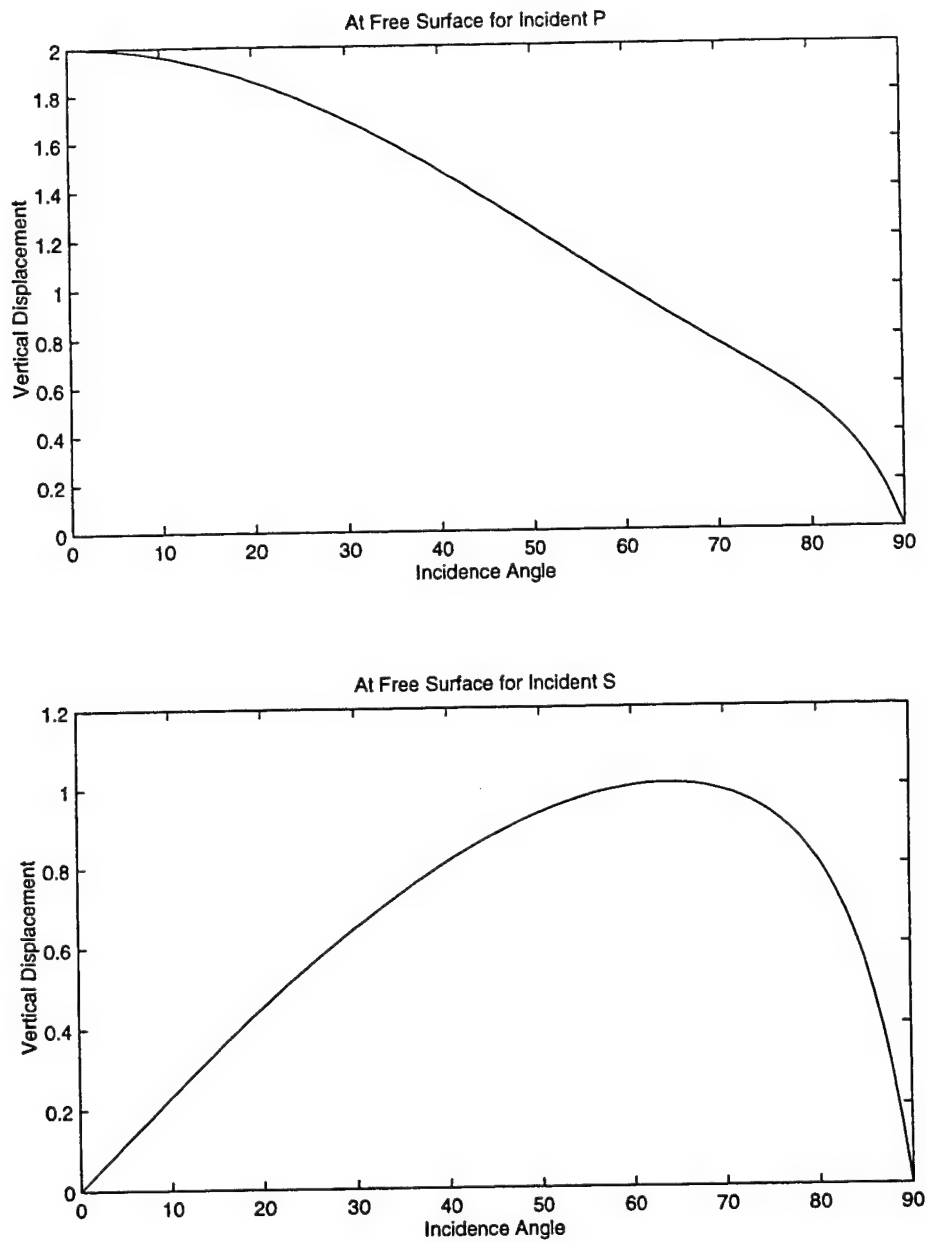


Figure 6.2: Vertical amplification at a free surface for incoming P-waves (top) and S-waves (bottom) as a function of incidence angle.

examined data from a surface array and a borehole instrument placed in a nearly ideal locale, with a planar surface a few meters above granite bedrock. Vertically incident P-waves were much more coherent between 300 and 150 meters depth (from the borehole recordings) than they were between 150 meters depth and the surface. Further, the energy in coda is especially highly scattered. Vernon et al. (1991) found surface recordings of local event S-waves to be incoherent at little more than one wavelength spacing. Another array study in the same location found that local S-wave coda is incoherent at less than one wavelength distances, and that most of the coda energy appears to have been scattered very near the array (Wagner and Owens, 1993). Although knowing the incidence precisely for any arrival is unlikely, it is probable that a statistical difference in incidence at the surface would exist between steeply incident teleseismic coda, and locally scattered, more horizontally traveling coda, and so they may have different amplifications.

Resonance is commonly observed in sedimentary basins (e.g. Hough, et al., 1992, Milana, et al., 1996) and could be a factor in site amplifications, especially for coda. Site amplifications however, for coda waves have been shown to correlate well with azimuthally averaged local S-waves (Tsujiura, 1978), which should not be subject to resonance, so resonance may not be a factor in amplifications for most sites. Also, local S-wave coda site amplifications for different frequencies correlate well, with a few notable exceptions in large sedimentary basins. We discuss this further in the section comparing diffuse and local coda site amplifications.

In addition to these considerations, the problem of site amplification estimation is inherently underdetermined, so only relative site amplifications can be determined. If site amplifications were estimated for two different types of signals at the same frequency (e.g. steeply incident P-waves, and surface waves), with both sets of signals being internally consistent in ray parameter and wave type, the relative site amplifications should be the same. In order to compute useful site amplifications, the most important factor to control is the frequency of the calibration signal and the signal of interest. The most common passband for the study of Lg is around 0.3 to 6 Hz (e.g. Zhang et al., 1994). This effectively

enhances Lg relative to lower frequency fundamental mode Rayleigh wave energy and higher frequency noise. We have calculated site amplifications from diffuse coda in the same passband.

We next consider the nature of Lg and diffuse coda. We first review previous work on both. Modeling of Lg blockage was thoroughly discussed in chapter 4 of this thesis. Here we review more general studies of Lg. We also discuss possible differences and similarities in the sources of earthquake and nuclear explosion Lg, and the source of diffuse coda.

What is Lg?

The Lg phase was recognized early in the history of modern regional seismology (Press and Ewing, 1952) as it is often the largest phase on regional high frequency seismograms. The names Lg and Rg are historical, coming from the initial guess that these were high frequency Love and Rayleigh waves traveling in a thin near surface granite layer. B  th (1954) later argued that the phases propagate in a low velocity channel within the mid-crust. Knopoff, et al. (1973) demonstrated theoretically that the entire crust provided the waveguide and no low-velocity layer was required. Oliver and Ewing (1957, 1958) first recognized that Lg and Rg are composed of higher mode surface waves. Cara et al. (1981) resolved higher mode Rayleigh waves within Lg, at two to five second period, and Wagner and Owens (1995) did so at approximately 2 Hz. In current usage, Lg refers to the energy on all three components of ground motion, typically arriving between 3.5 to 3.0 km/sec group velocity. Rg has come to refer to high frequency (< 3 second period) fundamental mode Rayleigh waves (e.g. Lay and Wallace, 1995).

Many of the distinguishing properties of Lg have to do with its indeterminate, scattered nature. Lg is usually composed of sufficiently scattered energy that it is impossible to identify any arrival that has followed a specific raypath. That same scattered nature of Lg, which makes it so useful as a stable measure of magnitude and yield within a calibrated region (e.g. Nuttli, 1986), also makes it difficult to model in a deterministic manner. The common practical definition of Lg as whatever energy arrives within some particular group velocity window, further reflects its disordered character. That is, although there is a ray description of Lg as multiple S-wave reverberations, it is not a practical

definition, as the discrete phases SmS, 2SmS, etc., are rarely observed. Vogfjörð and Langston (1996) were able to distinguish discrete S-wave multiple arrivals, but their resolution required beamforming at a large array. One of the first features of Lg that modelers attempted to duplicate with synthetics was its disordered, incoherent character. Bouchon (1982) demonstrated that one way the indeterminate nature of Lg could be reproduced was by summing sufficient rays reverberating off all layers in a simple four layer crustal model.

A related characteristic of Lg that has received attention is the long duration of its coda. Aki (1969) described local earthquake coda by single scattering off small scale crustal heterogeneities. This idea, and its successor, multiple scattering, have been useful in explaining the indeterminate nature of coda of many phases besides Lg (e.g. Wu and Aki, 1988). The importance of not just scattering, but of mode conversions, in explaining Lg coda was inferred from array observations (Der, et al., 1984). Bouchon and Coutant (1994) used synthetic seismograms to illustrate the potential importance to Lg coda duration of scattering due to Moho roughness. They also suggest that crustal heterogeneities play such an important role in scattering that the backscattered wavefield in Lg could be used to map heterogeneity.

Another long perplexing characteristic of Lg, the large amplitude of transverse Lg from explosion sources, provides further evidence of the importance of scattering to this phase. Explosions should generate largely compressional waves (e.g. Massé, 1981). When those P-waves scatter from discontinuities in a homogeneous, isotropic, plane layered structure, there should be some conversion to SV, but not SH. The amplitude increase of transverse Lg relative to the vertical and radial components, with distance from the source, continues until all three components are roughly equal in power. This suggests constant scattering and interconversion of Lg energy as it propagates (e.g. Gupta and Blandford, 1983). Velocity heterogeneities in the crust provide one possible explanation for transverse Lg (Gupta and Blandford, 1983). Maupin (1990) demonstrated that anisotropy could also be an effective means of scattering of SV to SH.

While the existence of transverse Lg from explosion sources indicates something about Lg's propagation, the very existence of Lg from explosions indicates something about Lg generation. One explanation of explosion Lg bears directly on the nature of diffuse coda and its similarity to Lg. Gupta et al. (1992) note that as nuclear explosions are buried in a low velocity surface layer, they produce a significant amount of Rg energy. They argue that Rg is short-lived, scattering to Lg off surface irregularities and shallow layer heterogeneities, as well as dissipating due to strong anelasticity in the surface layer. Another possible mechanism for explosion-generated Lg is the direct conversion of P- to S-wave energy, which is also dependent on the explosion occurring within a low velocity surface layer (Gutowski, et al., 1984).

The spectra of explosion and earthquake Lg phases are different, with more high frequency energy in the earthquake spectra, starting at approximately 2 Hz. The deficiency of high frequencies in explosion Lg may be due to both the scattering of Lg from Rg, which is lower frequency than the original source spectra, and to greater attenuation of high frequencies in the surficial layer where the generation of Lg occurs (e.g. Goldstein, 1995). The spectral content and amplitude of Lg also varies with explosion depth (e.g. Campillo, et al.; 1984, Goldstein, 1995), while earthquake source depth controls the relative excitation of different surface wave modes (e.g. Harkrider, 1970; Campillo, et al., 1984). Such depth dependence could affect the dominant phase and group velocities of Lg, although to our knowledge, no such dependence has been observed. Source spectra also vary, probably due to a combination of other source properties.

Wagner and Owens (1995) performed 3-component broadband array analysis of particle motions in conjunction with more standard array processing techniques to provide further information on the nature of Lg. They examined Lg from two nuclear explosions and one earthquake from within the Nevada Test Site (NTS), as recorded at a 6 km aperture 3-component broadband array at Piñon Flat Observatory in southern California, and made a number of observations important to the design of an Lg propagation study. The highest frequency energy arrives in the earliest part of the Lg wavetrain, at 3.6 to 3.4 km/sec group velocity. Distinct Love and Rayleigh waves at 2.5 and 1.8 Hz respectively,

were distinguished arriving simultaneously in that early, most prominent part of a nuclear explosion Lg phase, confirming the description of Lg as higher mode surface waves. The entire Lg wavetrain contained considerable forward scattered and multi-pathed energy, with significant backscattering beginning at approximately 3.0 km/sec group velocity. Much of the energy in the latter part of the Lg wavetrain could not be modeled as plane waves, indicating that it was scattered from very near the array.

What is diffuse coda and is it an isotropic source of Lg-like energy?

Teleseismic coda is generally understood to consist of the sum of near-source and near-receiver scattered energy (e.g. Langston, 1989). The *coherent* component of teleseismic coda consists of energy scattered into P-waves near the source, that travel along a path similar to that of the initial P wave (Bannister, et al., 1990, Dainty, 1990). The *diffuse* component of teleseismic coda consists of energy scattered near the receiver from the incoming P wave, and travels with much lower velocity, for example, approximately 3.5 km/sec near NORESS (e.g. Bannister et al., 1990, Dainty, 1990). The diffuse coda is composed primarily of nearly horizontally propagating shear waves trapped in the crustal waveguide, that is, fundamental and higher mode surface waves (e.g. Dainty, 1990). The teleseismic coda of deep focus earthquakes consists largely of diffuse coda (e.g. Dainty, 1990, Revenaugh, 1995a), and so may provide the multi-azimuthal source of energy appropriate for Lg site calibration. By separating the diffuse and coherent components, we are also able to utilize shallow event coda.

Literature on the nature of diffuse teleseismic coda is less extensive than that of Lg, largely because its diffuse character requires that array data, which are not nearly as common as single station data, be extensively processed for anything but trivial observations to be made. Most array studies have concentrated on the identification of discrete single scatterers of P to Rg near arrays (Key, 1967, Bannister, et al. 1990, Gupta, et al. 1990, Hedlin, et al. 1991). Dainty and Harris (1989) looked directly at the nature of teleseismic coda, and determined that the near-receiver scattered component was made

up of incoherent S-wave energy. Rg, even from single identifiable scatterers, does not dominate the coda. Individual scattered Rg phases are only infrequently distinguishable in the raw seismograms, and many records must be processed and stacked for identification of the most prominent scatterers. Revenaugh (1995a,b) notes that the identification of individual scatterers associated with topography has been limited to those with vertical scale lengths on the order of half the seismic wavelength used. The scatterers must also be extremely close to the array, as Rg is a very short-lived phase due to its dependence on the near surface velocity structure, which, especially in southern California, is heterogeneous and highly attenuative. In the first such study, Key (1967), identified a scatterer 13 km from the Eskdalemuir array in Scotland. Bannister et al. (1990), using a semblance technique, identified 2 scatterers 10 and 30 km from the NORESS array in Scandinavia. They looked for Rg scattered from the largest topographic feature in the area, a mountain range between 100 and 300 km distance from the array, but saw no such scattered energy. They were also unable to discern scattered energy from mountainous areas 60 km to the north and west of the array. Gupta et al. (1990) also imaged the scatterer 30 km distant from NORESS using f-k analysis and Hedlin et al. (1991) imaged both scatterers using a beam deconvolution technique and migration, but neither were able to resolve more distant scatterers.

The lack of Rg from anything but very near-receiver scatterers was also observed by Revenaugh (1995a), who used the SCSN to investigate the contribution from large areas of moderately efficient scattering to near-receiver scattered teleseismic coda. The contribution of any coherent sources of Rg to the energy in a particular seismogram was very small. Using migration, he obtained his best image of topographic scattering efficiency at a group velocity of 2.9 km/sec (which does not imply that most diffuse coda energy travels at that group velocity, only that the most coherent energy does).

Revenaugh (personal communication, 1996) observed that coherent Rg typically travels no more than 50 km in southern California. Rg presumably does not completely attenuate intrinsically, but scatters into other phases. This recalls the argument discussed earlier regarding the source of nuclear explosion Lg as being due to near-source, surface scattering of P to Rg, and subsequent scattering of Rg

to Lg. This suggests that diffuse coda, especially that arriving more than 10 to 15 seconds after the initial P arrival, may be largely composed of Lg-like energy. Bannister et al. (1990) examined two coda windows in their study at NORESS, and their findings confirm this suggestion. They only observed scattered Rg energy in the earlier time window, covering the first 30 seconds after the initial P arrival. This energy accounted for 10% to 30% of the signal, and the coherent coda accounted for 30% to 50%. The other approximately 40% of the signal was attributed to diffuse scattering at the receiver end. The authors also found that illumination of scatterers was somewhat dependent on the azimuth of the original signal. The second coda window, from 35 to 70 seconds after P, was dominated by energy with S-wave phase velocities, more diffusely scattered than the earlier Rg.

Bannister et al. (1990) conclude that the dominance of S-waves in later coda is due to direct P-to-S scattering at greater distance from the receiver, which persists because S attenuates so much more slowly than Rg. This is reminiscent of the mechanism of P to S surface layer scattering proposed by Gutowski et al. (1984). For our purposes, it is not important whether the coda comes from P to Rg scattering, and subsequent scattering of Rg to higher mode surface waves, or from direct P to S scattering. The important fact is the unanimity of array studies in identifying near-receiver scattered coda, much more than 10 seconds after the initial P-wave, as diffuse S-wave energy.

Revenaugh (1995b) also uses migration to image the uppermost mantle using P to P and P to S scattering beneath the SCSN. This required twice as many data as the P to Rg scattering (Revenaugh 1995a), as near-receiver upper mantle body wave to body wave scattering provides a very small percentage of the energy in teleseismic coda.

Implications for a study of Lg propagation

The foregoing discussion has brought out several points relevant to the design of an Lg propagation study in which absolute Lg amplitudes will be obtained by correction based on diffuse coda site amplifications. Such a study would be performed in order to better quantify Lg blockage, and would be accomplished by comparing changes in absolute Lg amplitude between stations with the intervening

path structure (see chapter 4). Thus we want to minimize anything else that could effect the estimation of absolute Lg amplitude.

Specifically, the preceding discussion has indicated several ways to minimize variations in incidence and frequency of the Lg observed, which will be important in minimizing differences in the amplification of different parts of the signal. The existence of significant multipathing and backscattering in later Lg alerts us to the importance of using a fairly narrow and early group velocity window for Lg measurements. Otherwise, differences in amplitude between stations could be masked by later arrivals.

Additionally, a narrow group velocity window would minimize amplification differences by limiting the range of modes examined within the dispersive Lg train. Early and late Lg, even within the 0.6 to 3 Hz passband, have distinctly different frequency contents, and so amplifications. Also, early and late Lg could have different phase velocities, even at the same frequency, and so would have different amplifications. The practical lower limit to the size of the group velocity window will depend on the extent of variations in the intrinsic velocity of the media over southern California. For our purposes it appears to be most important to cut off the window before the fundamental mode Rayleigh wave, at approximately 3.0 km/sec group velocity, as Rg will certainly have a different phase velocity. That group velocity also coincides with the arrival of more backscattered energy, which we want to avoid.

There are three important reasons for limiting the passband of Lg in a study of propagation. As mentioned earlier, Lg is dispersive. As with the use of a short group velocity window, the purpose of limiting the passband would be to minimize variation of amplification within the signal used. Also, the dependence of spectra on many source parameters also argues for the use of a narrow passband, to prevent differences between spectra of different events causing different relative amplification and so confounding interpretation of path effects. Finally, both the passband and group velocity window should be limited to minimize the variation in modes due to their different relative excitation by

different events. That is desirable because the mechanisms of blockage are poorly known (chapter 4), and it is possible that the blockage of different modes could depend on different crustal features.

The most important consideration in the use of teleseismic coda as a calibration signal will be the separation of steeply incident P-wave energy from the locally scattered surface waves. Also we wish to avoid Rg contamination of the calibration signal by the use of a late coda window. Additionally we need to minimize differences between the spectra of the calibration signals obtained from different events by using a narrow passband for all records. The moderate dependence of scattered energy azimuth on source azimuth (Bannister et al. 1990) suggests that improving azimuthal coverage of sources, by using shallow events, may improve the accuracy of SCSN site amplifications. This is balanced by the recognition that shallow events may contain some Rg, even when a late coda window is used, generated by scattering from the coherent coda. These theoretical concerns will be tested by comparison of site amplifications from deep vs. shallow event coda, and by the diffuse coda vs. local S-wave coda site amplifications. We may also increase the isotropy of the coda by the use of late and long coda windows.

Isolation of the diffuse component of teleseismic coda

We are also constrained in our choice of coda window by the desire to avoid all secondary phases, such as PP and PcP, which could supply steeply incident P-wave energy. Our choice is further constrained by the length of the trigger for a given event, and by event size. For large events there is frequently a trade-off between starting late enough that most records are on-scale, but not so late that the end of the event trigger time is reached at many stations. For one large deep event ($m_b=7.0$, depth=630km, distance=68°) with an especially long trigger time on the SCSN, we are able to use two separate coda windows. The first is from 85 to 115 seconds after the initial P-wave, and the second is 40 to 180 seconds after the sP arrival. In the first window, many records are clipped, but many stations for which the signal is commonly below the background noise level record good data. In the second window, the stations that are clipped in the earlier window are back on-scale (the clipping is a matter of

limited dynamic range of the data acquisition system, so the records are valid once the data are again on-scale).

Non-Lg-like elements in the calibration signal from deep events can be minimized by separating the diffuse and the coherent coda. This separation also permits the use of shallow events, providing more complete and even azimuthal coverage of sources (figure 3). To estimate the coherent portion of the coda, we stack the seismograms after alignment by cross-correlation of the initial P-wave (and for shallow events, on the entire train of P, pP, and sP). In this way, static station corrections are automatically incorporated. We make the assumption that all near-source scattered energy will stack coherently and near-receiver scattered energy will be incoherent. We then remove the coherent coda from each individual record by subtracting the scaled estimate of the coherent coda (the "beam") from the coda of each individual record. Before subtraction from an individual trace, the beam is scaled by its cross-correlation with that trace, which minimizes the amplitude of the remaining energy. The result is an estimate of the diffuse coda at each station.

We carefully consider and test the assumption that all near-source scattered energy will stack coherently. If scattering at several degrees distance from the source were to contribute to the coherent component of coda, the time lag between the initial P arrival and that scattered energy would not be constant over the several hundred kilometers spanned by the network and so that contribution to the coda would not stack coherently. For example, for a source 50 degrees from the network, at 600 km depth, and a scatterer 3 degrees from the source, at the same depth and in the plane of the ray (to maximize the variation in ray parameter), the difference in time lag between the direct and scattered P wave for stations 0.1 degrees apart in the plane of the ray would be 0.02 seconds. For stations 1 degree apart, the difference in time lags would be 0.19 seconds, and so the coherence of the scattered phase would be degraded, as energy in the signal peaks at approximately one Hz. For stations 3 degrees apart in the propagation direction, the difference in direct and scattered P times would be 0.6 seconds, and so when stacked, aligned on the initial P arrivals, the scattered arrivals would be nearly 180° out of phase and would largely cancel. As we want to use only energy traveling laterally in the crust to estimate Lg

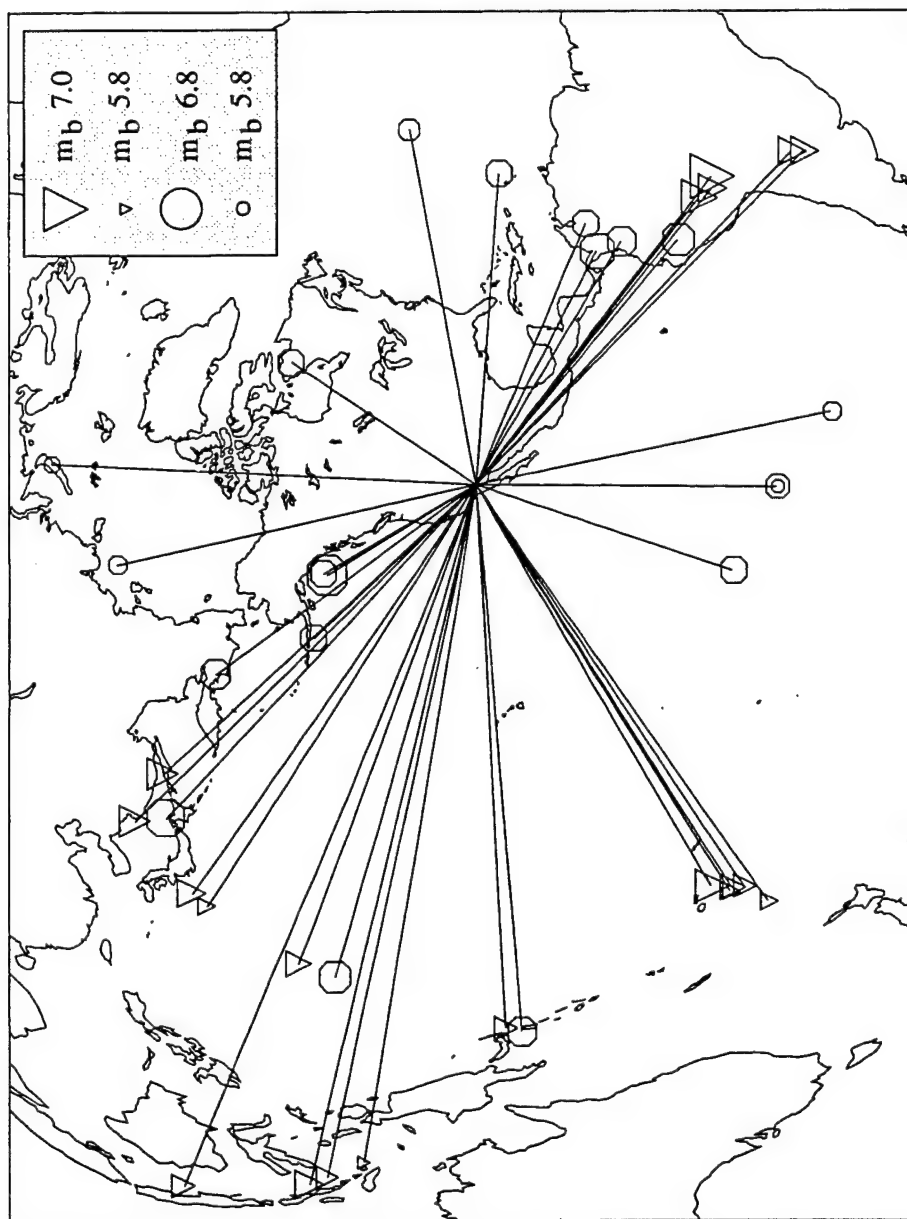


Figure 6.3: Map of teleseismic sources. Shallow source epicenters are indicated by circles, and deep source epicenters by inverted triangles. Symbols are scaled by magnitude.

amplification, we are concerned about how much steeply incident energy may exist that is not removed by subtraction of the beam. In a situation as described above, where the change in wavenumber across the network of some scattered energy in the coherent coda is significantly different from the change in the initial arrival wavenumber across the network, the correlation coefficient between coda records should vary with station spacing.

Figure 4 shows the correlation coefficients of coda windows for all SCSN station pairs plotted vs. interstation spacing, for a deep earthquake. Before beam removal (top), the least-squares fit line to the points is virtually horizontal, and the mean value is 0.0354; while some non-zero coherence is apparent, it does not vary significantly with station separation. The lower plot shows that the coherent portion of the coda is effectively removed by beam subtraction. After beam subtraction, the mean value is effectively zero. We obtained similar results for shallow earthquakes, with much larger initial values of mean coherence, but effectively zero coherence after beam removal, indicating effective separation of the coherent from the diffuse coda even for shallow earthquakes (figure 5). Our ability to perform this separation on shallow events has allowed us to improve our azimuthal coverage of teleseismic sources. In a few cases, there was a distinct slope to the line fit to the data, especially for shallow events, indicating that some steeply incident P-energy is present in the calibration signal (figure 6). Based on the difference between coherence at adjacent and distant stations, the remaining coherent coda appears to account for less than 10% of the total power of the calibration signal in even the worst case.

The mean ratio of power in coherent to diffuse coda for the 20 deep events was 0.097. That ratio for the deep events varied between 0.016 and 0.294. The maximum value was for an event at 536 km depth and 117° distance, so the large amount of coherent coda was likely due to scattering at the core-mantle boundary. Most other deep events were less than 90° distant from southern California.

For the 20 shallow events, the mean ratio of power in coherent to diffuse coda was 0.445. That ratio for the shallow events varied from 0.104 to 1.144. The depth of the event with the highest level of coherent coda was reported in the PDE catalogue to be 17 km. The event was at 75° distance, and the coda window used was chosen to start after the predicted times for the pP, sP, and PcP phases, but a

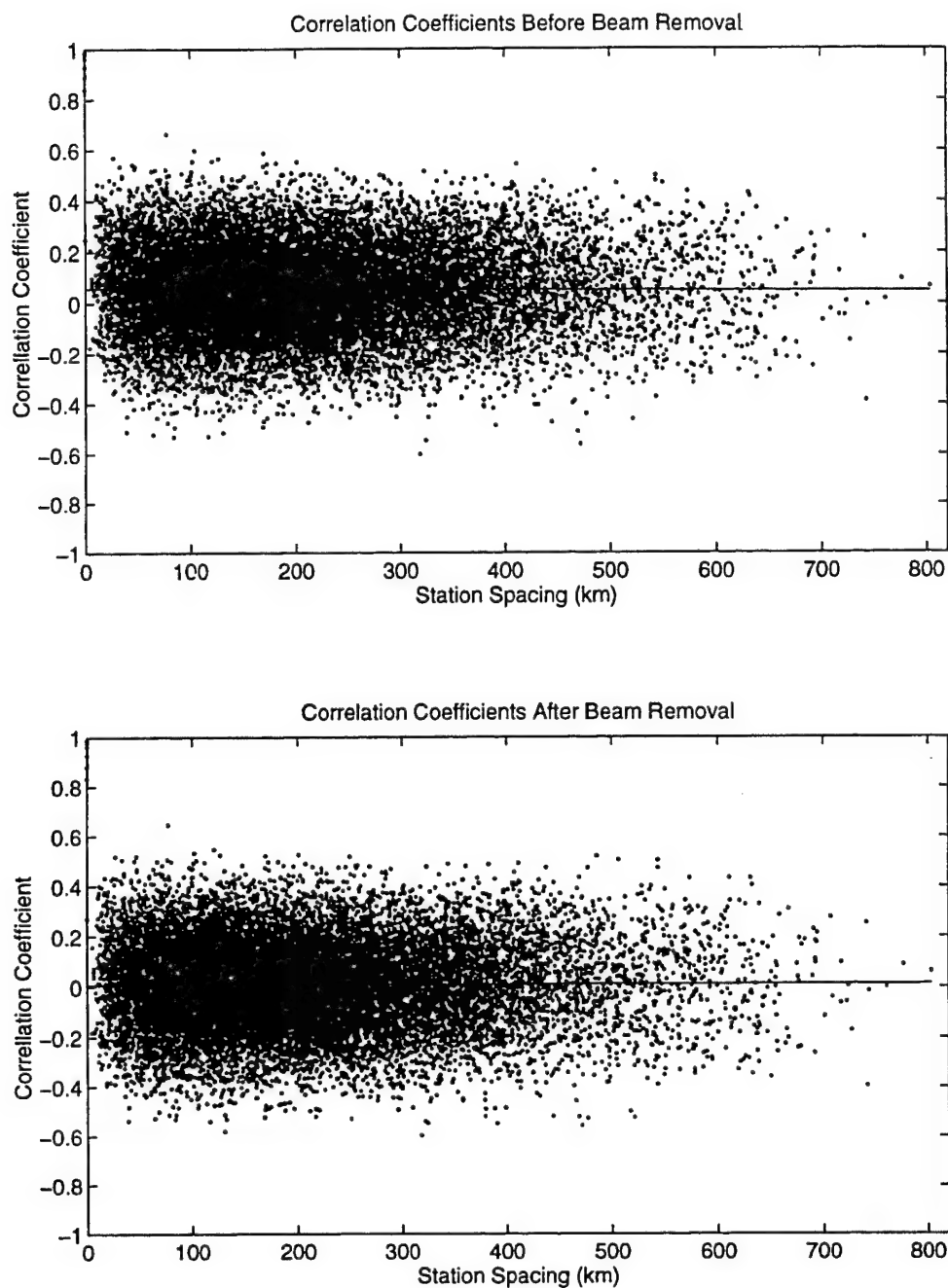


Figure 6.4: Correlation coefficients of the teleseismic coda from 21 to 61 seconds after the initial P arrival, for each pair of SCSN stations recording a deep event, vs. interstation spacing, before (top) and after beam removal (bottom). The mb 6.5, 606 km deep event was 73° from southern California. The mean correlation coefficient was 0.055 before beam removal and 0.008 after, and the slope was virtually zero, indicating complete removal of the coherent coda.

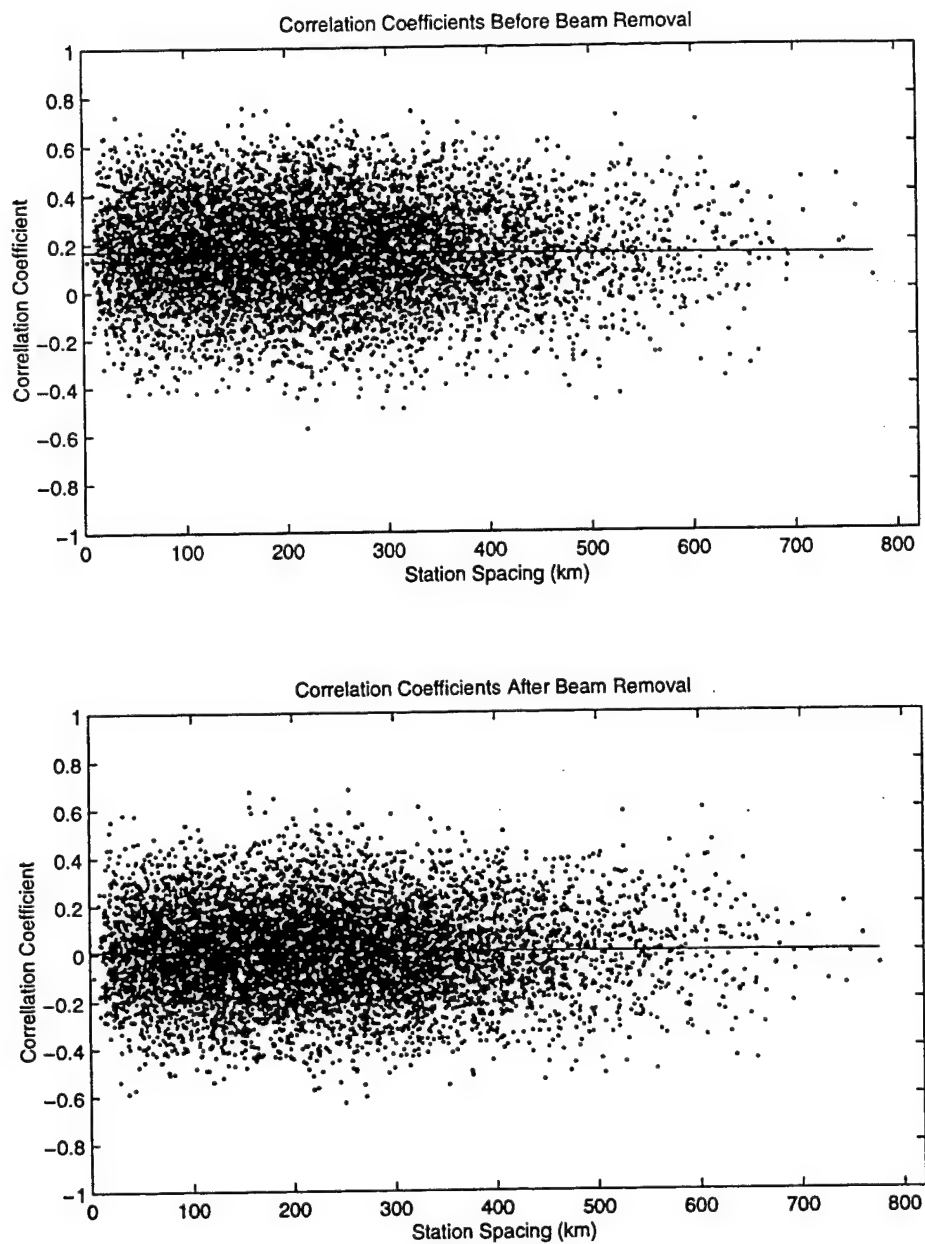


Figure 6.5: Correlation coefficients of the teleseismic coda from 20 to 45 seconds after the initial P arrival, for each pair of SCSN stations recording a shallow event, vs. interstation spacing, before (top) and after beam removal (bottom). The mb 6.2, 10 km deep event was 510 from southern California. The mean correlation coefficient was 0.162 before beam removal and 0.006 after, and the slope was virtually zero, indicating complete removal of the coherent coda.

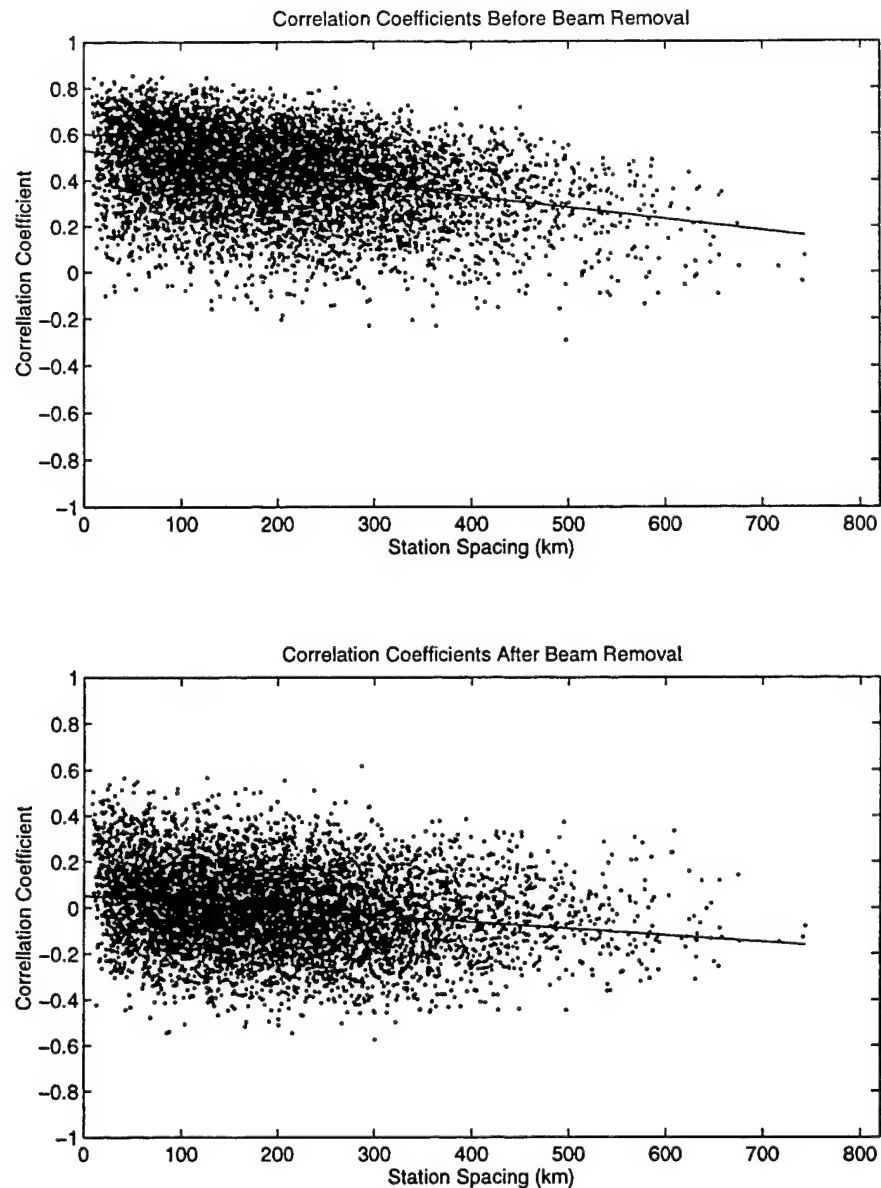


Figure 6.6: Correlation coefficients of the teleseismic coda from 40 to 95 seconds after the initial P arrival, for each pair of SCSN stations recording a shallow event, vs. interstation spacing, before beam removal (top), and after beam removal (bottom). The Mb 6.5, 19 km deep event was 53° from southern California. The mean correlation coefficient was 0.431 before beam removal and -0.005 after. There is a significant increase in the correlation coefficients with decreasing interstation spacing, indicating incomplete removal of the coherent coda. The zero distance intercept was 0.052. In this case, the coda window chosen included the PcP arrival, which is usually, but not always, insignificant, and which may have been the source of the coherent coda, although PcP was not visible in a record section. Some other shallow events had even more coherent coda, with no apparent cause. Those events usually were less distant than the average.

record section of this event shows clear arrivals well after those predicted (figure 7). The source of this coherent coda is not known. Nonetheless, it appears that the beamforming accurately estimated the coherent energy, permitting its removal (figures 8 and 9). The danger in such a situation is that high amplitude coherent coda will generate a significant amount of Rg near each station (although it is not clear whether Rg and Lg would have resolvably different amplification at the same frequencies).

How sensitive are site amplifications to differences between signal parameters?

It is difficult to accurately predict differences in amplifications due to differences in frequency, phase velocity, or wavetype, due to the complexity of the real earth. Empirical comparisons may provide a more useful test of the sensitivity of site amplifications to these parameters. To that end, we compare site amplifications for possibly different wavetypes, and consider other studies that quantify the effects of scattering near the surface.

Sensitivity to wavetype

An empirical study confirms the insensitivity of relative site amplifications to wavetype. Barker et al. (1981) observed large differences between site amplifications for Lg in three distinctly different types of strata (granite, alluvium, and tuff), using nine 3-component stations at NTS, recording 70 regional events. They found similar differences in site amplifications for Pg but were unable to discern any difference in the ratio of Lg to Pg site amplification. The authors noted that as Poisson's ratio increases significantly for the sediments, the expectation was that relative amplifications might differ there, but there was no such measurable effect.

Comparison of site amplifications from diffuse coda of deep and shallow events

To test for possible differences in amplification between the coda from deep events and that from shallow events, due to contamination of the shallow event coda by steeply incident P-wave energy or by Rayleigh wave energy generated by very near-receiver scattering from the coherent coda, we calculated

Sea of Japan Earthquake Record Section
17 km Depth, Mb 6.7

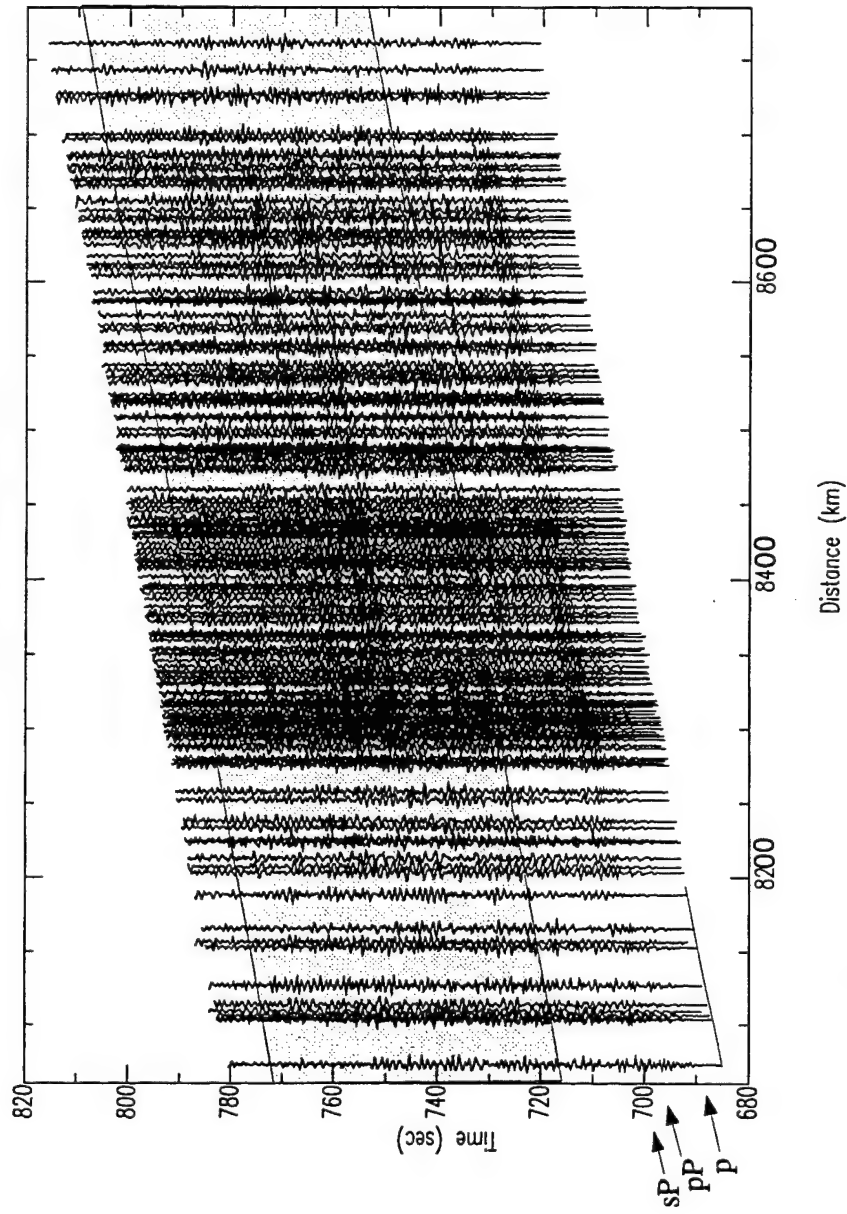


Figure 6.7: Record section for the shallow event with the largest percentage of coherent coda. The event was reported to be at 17 km depth, and we see the depth phases pP and sP as predicted for that depth, at approximately 6 and 8 seconds after the initial P arrival. Some energy is also visible at 18 seconds after P, the time predicted for PcP. The coda window used was from 25 to 80 seconds after the initial P arrival, where no major phases were predicted to arrive. However, there is a very large coherent phase with similar moveout to the initial arrival, at about 45 seconds after the initial arrival. The time window used for the calibration signal is shaded.

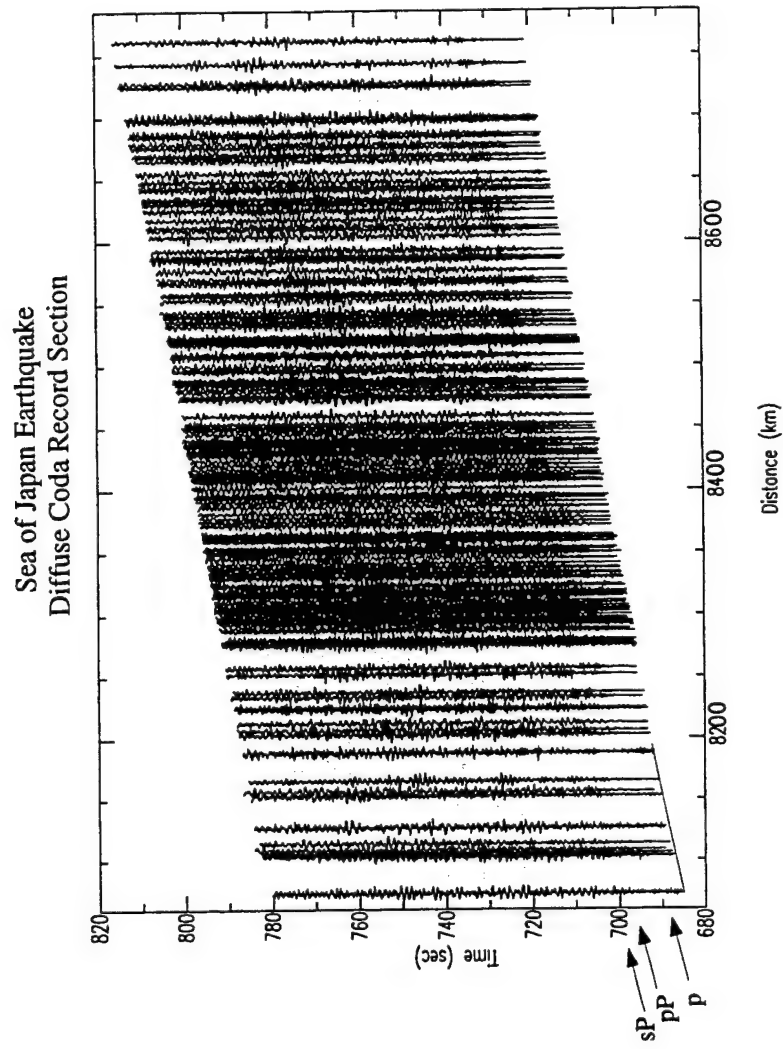


Figure 6.8: Record section for the diffuse coda of the event of figure 7. With the beam removed from each individual trace, the coherent phases that were prominent in the time window used for calibration in figure 7 are no longer apparent.

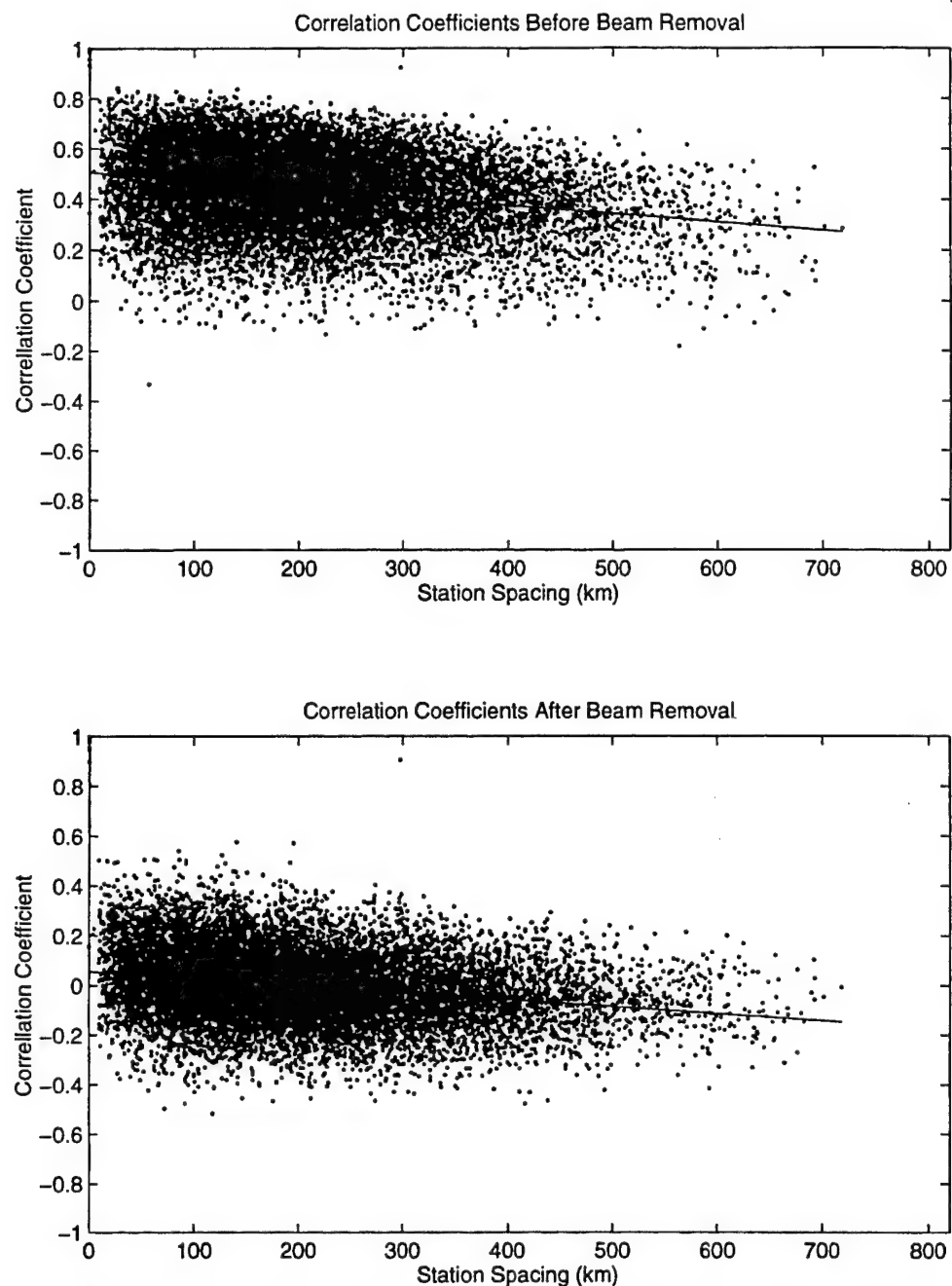


Figure 6.9: Correlation coefficients of the teleseismic coda from 25 to 80 seconds after the initial P arrival, for each pair of SCSN stations recording the shallow event of figure 7. The increase in correlation coefficient with decreasing station spacing indicates that not all of the steeply incident P-wave energy was coherent. After beam removal, the zero distance intercept was 0.056. The large decrease however, in the mean value, from 0.434 before beam removal to -0.002 after, indicates that most of the coherent coda energy was removed.

site amplifications separately from the subsets of deep and shallow events. There is no apparent difference between those results (figure 10). The slight offset of the diagonal line that the two sets of site amplifications lie along exists because the site amplifications can only be resolved to within some additive constant. In the inversion for site amplifications (Baker and Minster, 1996), the sum of the log of the amplifications is set to zero, to prevent tradeoffs with the event magnitudes. The somewhat larger deep events were recorded on a greater range of stations than were the smaller shallow events, so the stations recording more deep events had a slightly lower mean log(amplification) than the stations that recorded both deep and shallow events. Thus for stations common to both data subsets, the mean of the amplification estimates were higher for site amplifications estimated from the deep events than were those from the shallow events. What is important is that the relative amplifications are proportional for both sets of estimates (i.e. they lie along a diagonal line). The slightly larger uncertainty estimates for the shallow event amplifications reflect the typically smaller number of events recorded per station for the shallow event estimates. From this good correlation, we conclude that differences in site amplifications due to a small amount of Rg and steeply incident P-waves contaminating the Lg-like calibration signal are less than the resolution of the amplification.

Comparison of site amplifications from diffuse coda and local S-wave coda

Su and Aki (1995) calculated site amplifications for 158 stations of the SCSN using the S-wave coda of local events. Comparison of the diffuse teleseismic coda site amplifications (DTCSAs) with Su and Aki's local S-wave coda site amplifications (LSCSAs) provides a check on the accuracy and validity of both sets, as they were calculated from coda of different event types using different estimation techniques. Su and Aki estimated amplifications for specific frequencies, 1.5, 3.0, 6.0, and 12 Hz, so we expect some variation between those results and the diffuse coda results, estimated for the 0.6 to 3 Hz passband, because of the difference in frequencies and bandwidths used. Local S-wave coda is largely composed of S and/or surface wave energy (e.g. Wagner and Owens, 1993), and so should be of similar wavetype to diffuse coda.

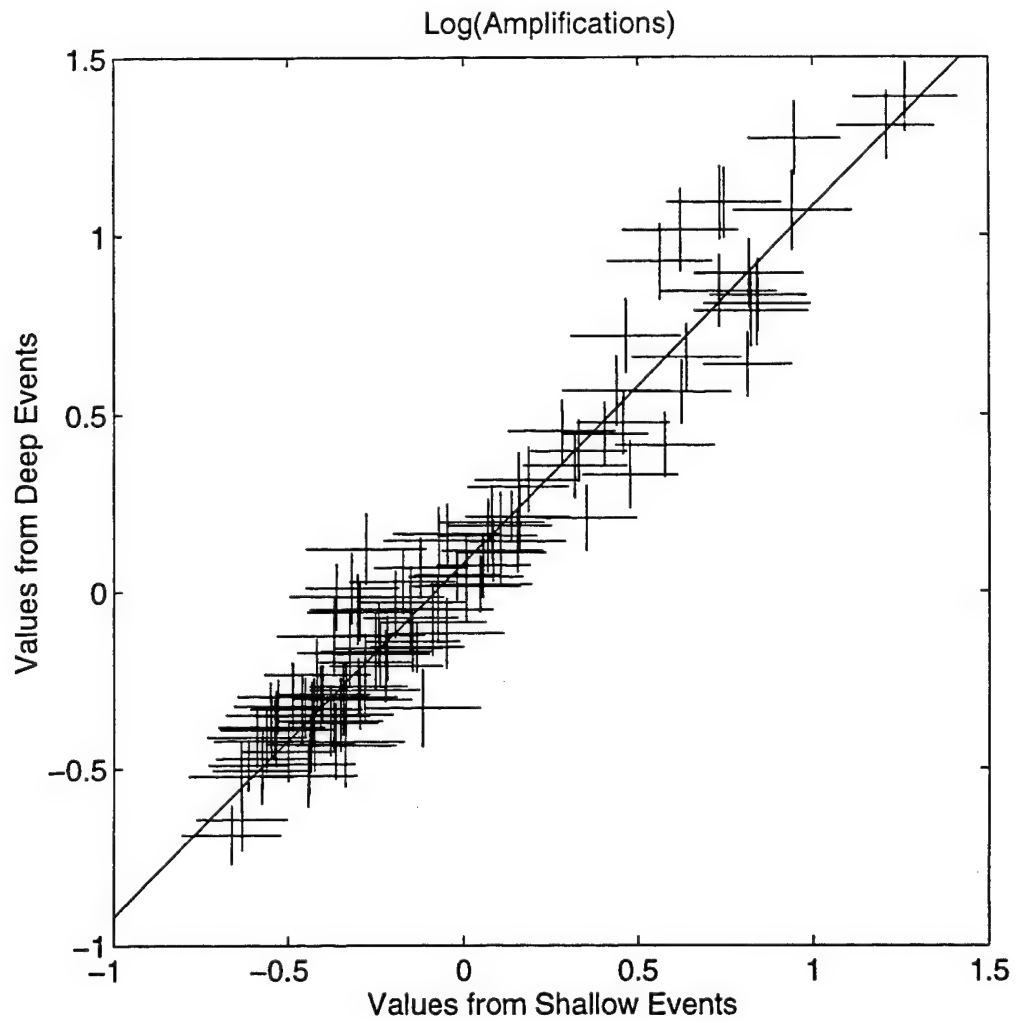


Figure 6.10: Comparison of diffuse coda site amplifications calculated from just the coda of the 20 deep events and those calculated from just the coda of the 20 shallow events. The vertical lines represent 2 standard deviations uncertainty about the deep event coda site amplifications, and the horizontal lines represent the same for the shallow event coda site amplifications.

There are 126 stations for which Su and Aki reported an amplification and for which there were a minimum 10 events recorded for the diffuse coda amplifications. The DTCSAs and LSCSAs for those stations correlate very well at all but the highest amplifications. For the 105 events with amplifications less than 3, the correlations are equally good between the DTCSAs and LSCSAs as they are between LSCSAs at different frequencies (figure 11)

The high correlations of figure 11 break down at the stations with the highest amplification (figure 12). The reasons for the breakdown of the correlations are probably different for the two sets of correlations. All of the stations with much greater local S-wave coda site amplification at lower frequency are in sediments, and most are in the Imperial Valley. The difference between the 1.5 Hz and the higher frequency LSCSAs may be due resonance at 1.5 Hz, or to greater attenuation of the higher frequency signal. Attenuation however, can not explain the differences at those stations between the DTCSAs and the 1.5 Hz LSCSAs, as the passband of 0.6 to 3 Hz used for the diffuse coda spans whatever spectral averaging was used for the 1.5 Hz S-wave. For the same reason, if resonance were the cause of the extreme differences between the highest amplification DTCSAs and LSCSAs, it could not be due to the frequency content of the signals. Resonance at 1.5 Hz for local S-wave coda but not for diffuse coda also seems unlikely, as the wavetypes are very similar, if not indistinguishable. The differences between those sets of site amplifications could be due to differences in the mechanisms that trap energy in sedimentary basins from the two sources of the respective coda waves. The source-station spacing was kept very small for the S-wave study (Su and Aki, 1995), so presumably, the hypocenters were directly beneath the basins. The diffuse coda energy would largely be S or surface waves scattered from a greater distance, mostly from outside the basin. While we cannot constrain the problem further and so speculate on details of the mechanisms, we can see that horizontally propagating surface waves entering a basin are distinctly different from S-waves entering a basin from below. Regardless of the difference between the mechanisms that trap more energy in the basin in the local S-wave case, the surface wave source is likely more appropriate for Lg.

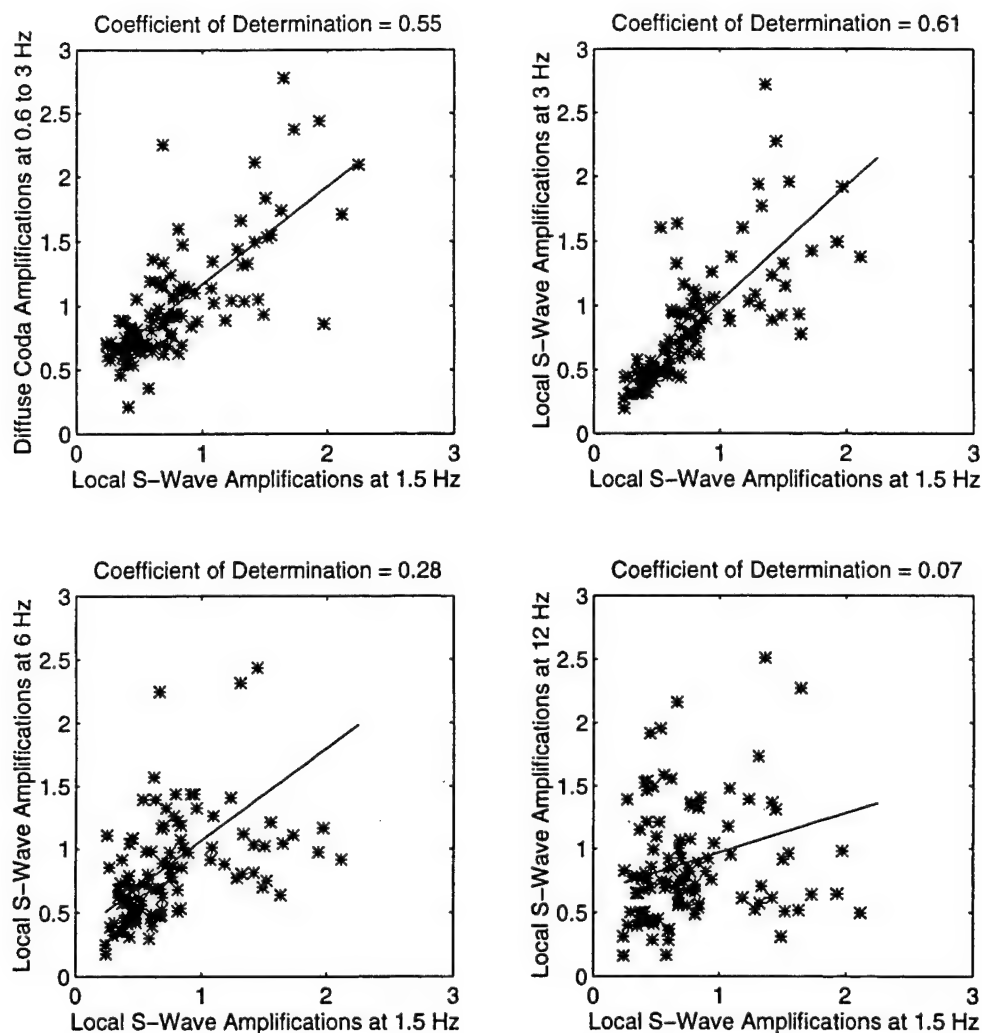


Figure 6.11: Comparison of diffuse coda site amplifications versus 1.5 Hz local S-wave coda site amplifications of Su and Aki (1995) for sites with amplifications less than 3.0 (upper left). The coefficient of determination is measure of how meaningful it is to relate two variables by a sloping line (i.e. $Y=aX+b$). Specifically, the coefficient of determination, r^2 , is given by $r^2=1-SSE/SST$, where the sum of the squared error, $SSE=\sum y_i^2-b\sum y_i-a\sum x_i y_i$, is a measure of how much variation is left unexplained by the model, and the total squared error, $SST=\sum y_i^2-(\sum y_i)^2/n$, is a measure of the total amount of variation in the observed values of the dependent variable. Thus SSE/SST is the proportion of the total variation that is not predicted by the linear model, and r^2 is the proportion of variation in the dependent variable that is predicted by the linear model. The correlation between the local S-wave coda amplifications at 1.5 Hz and the diffuse coda amplifications is about as good as between the local S-wave coda amplifications at 1.5 Hz and at 3 Hz (upper right). The correlation is much poorer for larger differences in frequency at the same site (lower plots).

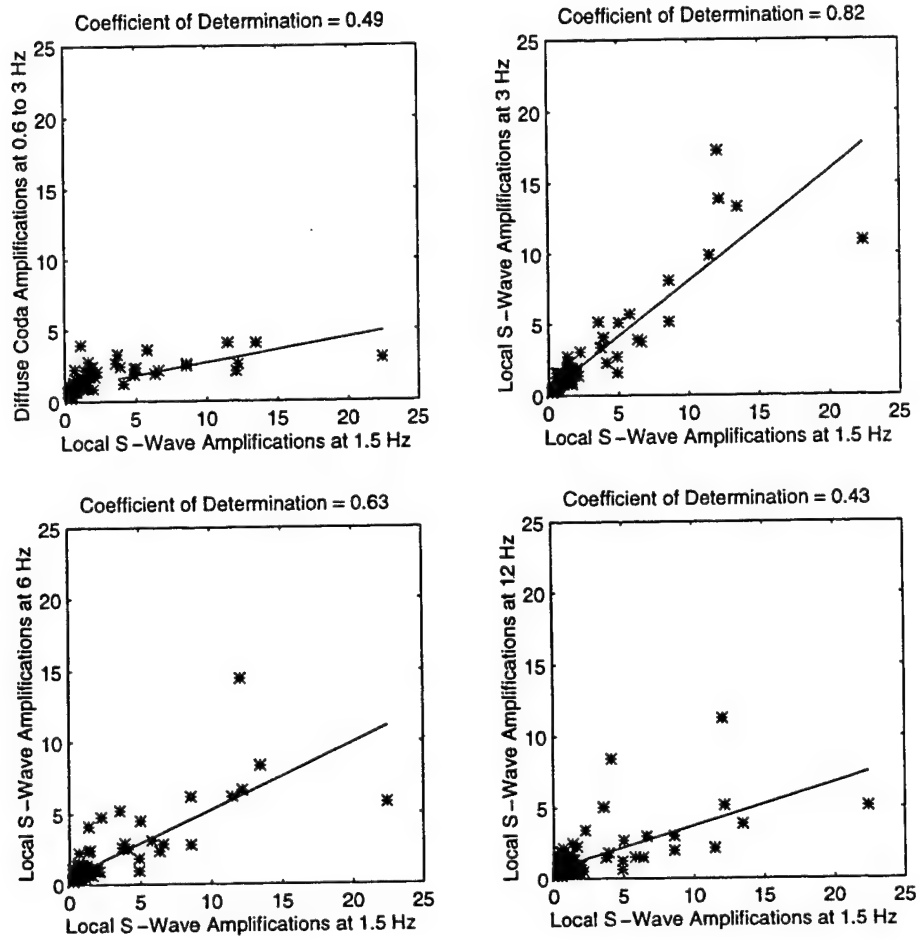


Figure 6.12: Comparison of diffuse coda site amplifications versus local 1.5 Hz S-wave coda site amplifications of Su and Aki (1995) for all amplifications (upper left). The linear relationship seen in figure 9 breaks down for the highest amplification sites, with approximately 5 times higher amplification estimated from the 1.5 Hz local S-wave coda than from the diffuse coda. The local S-wave coda site amplifications are also much greater at 1.5 and 3 Hz (upper right), than at 6 and 12 Hz (lower plots).

Conclusions

We have calculated site amplifications from the diffuse component of teleseismic coda for 189 stations of the SCSN. Reviews of previous research on site amplification and the nature of Lg and diffuse coda indicate that they are appropriate for Lg amplification.

Several pieces of evidence indicate that site amplifications are insensitive to wavetype within the resolution of studies performed. For example, relative amplifications for a range of site geologies were found to be indistinguishable for Pg and Lg phases. The diffuse coda site amplifications are the same for deep and shallow event coda, despite some known, but generally minor, contamination of the shallow event coda with Rg and steeply incident P-wave energy. Site amplifications are also similar for diffuse coda and local S-wave coda. As the local S-wave coda has been shown to correlate well with direct crustal S-wave amplifications, the higher mode and direct S wave amplifications must also be quite similar.

Even if there were some sensitivity of amplification to wavetype, diffuse coda and Lg appear to have similar source generation (scattering from Rg to higher mode surface waves, or direct P- to S-wave scattering within a shallow low velocity surface layer), and so should be composed of the same, or very similar, wavytypes. This hypothesis is confirmed by array studies, which indicate that both Lg and diffuse coda are composed of S-waves trapped in the crust, or equivalently, higher mode surface waves. Finally, we effectively remove the great majority of coherent teleseismic coda from the calibration signals.

Diffuse coda is extensively scattered, as evidenced by array studies for which most of the energy in late coda is incoherent and can not be modeled in terms of plane waves, and so is fairly isotropic.

The site amplification estimation worked well, as the diffuse coda site amplifications are well correlated with local S-wave coda site amplifications, except at the highest amplification sites. The differences between the two sets of site amplifications for the highest amplification sites, which were in sedimentary basins, may be due to resonance in the local S-wave case because the earthquake source was directly beneath the basin. This indicates that recalculating the amplifications for diffuse coda,

rather than simply using the local S-wave coda results, may have been important in avoiding later misinterpretation of propagation results in basins.

Examination of the nature of Lg and diffuse coda, and results of the amplification estimation, suggest important considerations for the design of a study that will allow observation of changes in absolute Lg amplitudes with propagation.

Site amplifications are most sensitive to frequency, and possibly also to incidence angle, so a narrow passband should be used for both Lg and diffuse coda site amplifications, to

- 1) minimize variations of frequency due to Lg dispersion,
- 2) minimize variations of frequency due to differences between sources (both Lg and diffuse coda), and
- 3) avoid possible differences in frequency content of Lg at different stations (for different events) due to different attenuation characteristics along different paths.

The sensitivity of site amplifications to frequency and incidence also suggests that Lg should be observed in an early and narrow group velocity window, to

- 1) minimize variations in frequency and wavenumber (and so incidence) due to Lg dispersion;
- 2) minimize variations in frequency and wavenumber due to the excitement of different modes by different sources;
- 3) minimize the effect multi-pathed arrivals in later Lg could have on recognizing blockage; and
- 4) avoid the inclusion of Rg, as it likely scatters differently than the higher modes. There is also a small chance that it has a different amplification than the higher modes.

The choice of Lg group velocity window will be limited by the extent of velocity variation across the region studied.

Additionally, the diffuse coda calibration signal should be taken from a late coda window to minimize the influence of very near station Rg in the calibration signal, and maximize the isotropy of scattered energy.

References

- Aki, K. (1969), Analysis of the seismic coda of local earthquakes as scattered waves, *J. Geophys. Res.*, 74, 615-631
- Aki, K. and P. Richards (1980), Quantitative Seismology: Theory and Methods, Vol. 2, 630-633, W.H. Freeman, S.F.
- Baker, G.E. and J.B. Minster (1996), Quantifying the attenuation and blockage of Lg and robust statistical estimates of site amplifications at SCSN stations, Proceedings 18th Annual Seismic Research Symposium, DARPA
- Baker, G.E. and J.B. Minster (1995), Lg site amplification calibration for isolation of Lg propagation effects, Proceedings 17th Annual Seismic Research Symposium, DARPA
- Bannister, S.C., E.S. Husebye, and B.O. Ruud (1990), Teleseismic P coda analyzed by three-component and array techniques: Deterministic location of topographic P-to-Rg scattering near the NORESS array, *Bull. Seism. Soc. Am.*, 80, 1969-1986
- Barker, B., Z. Der, and C. Mrazek, (1981), The effect of crustal structure on the regional phases Pg and Lg at the Nevada Test Site, *J. Geophys. Res.*, 86, 1686-1700
- Bäth, M., (1954), The elastic waves Lg and Rg along Eurasian paths, *Arkiv för Geofysik*, 295-325
- Benites, R. and K. Aki (1989), Boundary integral-Gaussian beam method for seismic wave scattering: SH waves in two-dimensional media, *J. Acoust. Soc. Am.*, 86, 375-386
- Bouchon, M. (1973), Effect of topography on surface motion, *Bull. Seism. Soc. Am.*, 63, 615-632
- Bouchon, M. (1982), The complete synthesis of seismic crustal phases at regional distances, *J. Geophys. Res.*, 87, 1735-1741
- Bouchon, M. and O. Coutant (1994), Calculation of synthetic seismograms in a laterally varying medium by the boundary element - discrete wavenumber method, *Bull. Seism. Soc. Am.*, 84, 1869-1181
- Campillo, M., M. Bouchon, and B. Massinon (1984) Theoretical study of the excitation, spectral characteristics, and geometrical attenuation of regional seismic phases, *Bull. Seism. Soc. Am.*, 74, 79-90
- Cara, M., J.B. Minster, and R. Le Bras (1981), Multi-mode analysis of Rayleigh-type Lg. II. Application to southern California and the northwestern Sierra Nevada, *Bull. Seism. Soc. Am.*, 71, 985-1002
- Dainty, A. and D. Harris (1989), Phase velocity estimation of diffusely scattered waves, *Bull. Seism. Soc. Am.*, 79, 1231-1250
- Dainty, A. (1990), Studies of coda using array and three-component processing, *Pure Appl. Geophys.*, 132, 221-244
- Der, Z., M. Marshall, A. O'Donnell, and T. McElfresh (1984), Spatial coherence structure and attenuation of the Lg phase, site effects, and interpretation of the Lg coda, *Bull. Seism. Soc. Am.*, 74, 1125-1147

- Goldstein, P. (1995) Slopes of P- to S-wave spectral ratios - A broadband regional seismic discriminant and a physical model, *Geophys. Res. Lett.*, 22, 3147-3150
- Gupta, I.N. and R.R. Blandford (1983), A mechanism for generation of short-period transverse motion from explosions, *Bull. Seism. Soc. Am.*, 73, 571-591
- Gupta, I.N., C.S. Lynnes, T.W. McElfresh, and R.A. Wagner (1990), F-K analysis of NORESS array and single station data to identify sources of near-receiver and near-source scattering, *Bull. Seism. Soc. Am.*, 80, 2227-2241
- Gupta, I.N., W.W. Chan, and R.A. Wagner (1992) A comparison of regional phases from underground nuclear explosions at the east Kazakh and Nevada test sites, *Bull. Seism. Soc. Am.*, 82, 352-382
- Gutenberg, B. (1957), Effects of ground on earthquake motion, *Bull. Seism. Soc. Am.*, 47, 221-250
- Gutowski, P.R., F. Hron, D. E. Wagner, and S. Treitel (1984), S*, *Bull. Seism. Soc. Am.*, 74, 61-78
- Harkrider, D. (1970) Surface waves in multilayered elastic media. Higher mode spectra and spectral ratios from point sources in plane layered earth models, *Bull. Seism. Soc. Am.*, 60, 1937-1987
- Hough, S.E., L. Seeber, A. Rovelli, L. Malagnini, A. DeCesare, G. Selveggi, and A. Lerner-Lam (1992), Ambient noise and weak motion excitation of sediment resonances; results from the Tiber Valley, Italy, *Bull. Seism. Soc. Am.*, 82, 1186-1205
- Kawase, H. (1988), Time-domain response of a semicircular canyon for incident SV, P, and Rayleigh waves calculated by the discrete wavenumber boundary element method, *Bull. Seism. Soc. Am.*, 78, 1415-1437
- Key, F.A. (1967) Signal generated noise recorded at the Eskdalemuir seismometer array station, *Bull. Seism. Soc. Am.*, 57, 27-37
- Knopoff, L., F. Schwab, and E. Kausel (1973), Interpretation of Lg, *Geophys. J. R. Astron. Soc.*, 33, 389-404
- Langston, C.A., (1989) Scattering of teleseismic body waves under Pasadena, California, *J. Geophys. Res.*, 94, 1935-1951
- Lay, T. and T. Wallace (1995) Modern Global Seismology, *San Diego Academic Press*
- Milana, G., S. Barba, E. Del Pezzo, and E. Zambonelli (1996), *Bull. Seism. Soc. Am.*, 86, 320-328
- Maupin, V. (1990) Modeling of three-component Lg waves in anisotropic crustal models, *Bull. Seism. Soc. Am.*, 80, 1311-1325
- Nuttli, O.W. (1986) Yield estimates of Nevada Test Site explosions obtained from seismic Lg waves, *J. Geophys. Res.*, 91, 2137-2151
- Oliver, J. and M. Ewing (1957) Higher modes of continental Rayleigh waves, *Bull. Seis. Soc. Am.*, 47, 187-204
- Oliver, J. and M. Ewing (1958), Normal modes of continental surface waves, *Bull. Seis. Soc. Am.*, 48, 33-50
- Press F. and M. Ewing (1952), Two slow surface waves across North America, *Bull. Seis. Soc. Am.*, 42, 219-228

- Revenaugh, J., (1995a), The contribution of topographic scattering to teleseismic coda in southern California, *Geophys. Res. Lett.*, 22, 543-546
- Revenaugh, J., (1995b), A scattered-wave image of subduction beneath the Transverse Ranges, *Science*, 268, 1888-1892
- Su F. and K. Aki, (1995), Site amplification factors in central and southern California determined from coda waves, *Bull. Seism. Soc. Am.*, 85, 452-465
- Taylor, S.R., M. Denny, E. Vergino, and R. Glaser (1989), Regional discrimination between NTS explosions and western US earthquakes, *Bull. Seism. Soc. Am.*, 79, 1142-1176
- Trifunac, M.D. (1971), Surface motion of a semi-cylindrical alluvial valley for incident plane SH waves, *Bull. Seism. Soc. Am.*, 61, 1755-1770
- Tsujiura, M. (1978), Spectral analysis of the coda waves from local earthquakes, *Bull. Earthq. Res. Inst. Univ. Tokyo*, 53, 1-48
- Vernon, F.L., J. Fletcher, L. Carroll, A. Chave, and E. Sembera (1991), Coherence of seismic body waves from local events as measured by a small-aperture array, *J. Geophys. Res.*, 96, 11,981-11,996
- Vogfjörð, K.S. and C.A. Langston (1996), Characteristics of short-period wave propagation in regions of Fennoscandia, with emphasis on Lg, *Bull. Seism. Soc. Am.*, in press
- Wagner, G. and T. Owens (1993), Broadband bearing-time records of three-component seismic array data and their application to the study of local earthquake coda, *Geophys. Res. Lett.*, 20, 1823-1826
- Wagner, G. and T. Owens (1995), Regional wavefield analysis using three-component seismic array data, *Proceedings 17th Annual Seismic Research Symposium*, DARPA
- Wald, L., S. Perry-Huston, and D. Given, (1993), The southern California network bulletin January-December 1993, *USGS Open-File Report 94-199*
- Wu R.-S., and K. Aki (1988), Introduction: Seismic wave scattering in three-dimensionally heterogeneous earth, *Pure Appl. Geophys.*, 128, 1-6
- Zhang, T., S. Schwartz, and T. Lay, (1994), Multivariate analysis of waveguide effects on short-period regional wave propagation in Eurasia and its application to seismic discrimination, *J. Geophys. Res.*, 99, 21,929-21,945
- Zhang, T. and T. Lay, (1994), Analysis of short-period regional phase path effects associated with topography in Eurasia, *Bull. Seism. Soc. Am.*, 84, 119-132

Chapter 7

Conclusion to the Dissertation

Introduction

In this chapter I review what has been accomplished. The research described in chapters 2 and 3 and in appendix 1 is complete in and of itself, and I summarize those results. Similarly, chapters 5 and 6 describe results that are important in and of themselves. In addition, those results have considerable ramifications for improving the accuracy of regional seismic discrimination. Such improvement is the long term objective which provided the motivation for the work described in the later chapters.

The chapter is organized as follows: I first briefly review the state of knowledge regarding regional propagation and blockage, and its presumed role in misclassification by regional discriminants. I also discuss what was learned by evaluating measurements of Lg/Pg amplitude ratios recorded at Southern California Seismic Network (SCSN) stations. I describe how that led to the decision that determining site amplifications at SCSN stations was one of the most important steps that could be taken towards better understanding of Lg blockage and improvement of discrimination accuracy. In the section following that, as a proof-of-concept test, I apply the site amplifications to SCSN recordings of three regional earthquakes and one nuclear explosion, and demonstrate that they perform as predicted, i.e. application of site amplification corrections permits us to separate path from receiver effects. In the penultimate section, I discuss the direction of future research that has been made possible by the results presented in chapters 5 and 6. In the concluding section, I summarize the results that have been achieved in each portion of the dissertation.

What we learned that indicated that site amplifications are important

As noted, our long term objective has been to improve the accuracy of regional seismic discrimination. The initial step toward achieving that objective was assessing the current state of

knowledge regarding regional propagation and determining how best to improve it. In doing the research necessary to making that determination, I also contributed further to that base of knowledge. I first identified gaps and possible misconceptions, or at least untested assumptions, in the current state of knowledge regarding regional propagation. It is well established that the best existing regional seismic discriminants have a high rate of error (e.g. Taylor, et al., 1989). It has been also clearly recognized that propagation effects are important in some cases and that path corrections could reduce the incidence of misclassifications (e.g. Zhang, et al., 1994). Our initial contributions to understanding the problem of reducing errors in regional event classification were the demonstrations that (1) changes in Lg/Pg amplitude ratios occur over very short spatial scales, ~20 km, often not clearly attributable to major tectonic boundaries, and that (2) areas in which the discriminant value has been affected enough to cause misclassification are spatially coherent (figures 4.3-4.10). Analysis of patterns of Lg/Pg amplitude ratios for regional sources from a wide variety of azimuths about the SCSN also let us conclude that path effects are the dominant cause of misclassification by the Lg/Pg discriminant.

In addition to indicating the direction that further research should take, the conclusions discussed above are relevant to understanding the limitations of ongoing efforts at *regionalization* (e.g. Dowla et al., 1996, Randall, et al., 1996) and of attempts at developing empirical path corrections. Regionalization is an attempt to quantify path properties, and so path effects, in politically critical regions (e.g. the Middle East, North Africa, and China). This is probably most effective in areas of simple structure with a single structural feature that disrupts regional propagation, such as the Arabian shield, which is bounded by narrow sections of oceanic crust (Vernon et al., 1996). In the area of empirically derived path corrections, Zhang et al. (1996) achieved a 22% reduction in variance for the Lg/Pg amplitude ratio using a correction based on the product of distance and topographic roughness. Path corrections that are transportable, that is, corrections that may be applied in uncalibrated regions, are the most valuable to us. How far afield from the calibration paths such topography-based corrections could be transported is not clear. The observations of abrupt changes in Lg/Pg amplitude ratios over very short paths suggest that, assuming reciprocity (as I have used many closely spaced

stations and few events), in a structurally complex area like southern California, exact knowledge of the path effect from one source position to one receiver position would have minimal predictive value for another source 30 km distant from the calibration source position. Thus, to ensure a large improvement in discriminant capability, empirical calibration of path effects may have to be performed on a much finer scale than is practical. The alternative to fine-scale calibration over much of the globe is to attempt to understand the physical basis for the fine scale variations observed in regional phase propagation. Such understanding may permit the prediction of those fine scale changes, and at the very least should make clearer the limitations of path corrections and so enable better estimation of the uncertainty in amplitude ratios.

I began this section by discussing amplitude ratios. The blockage of Lg however has long been a topic of great interest on its own. In much of the work on Lg based regional discriminants, it appears to be a common implicit assumption that variations in discriminant values are due largely to changes in Lg. Partly because of this, most of the work on regional phase propagation and blockage has focused on Lg, as discussed in chapters 4 and 6. While Lg blockage and variations in Lg/Pg amplitude ratios are related topics, it does not follow, nor has it been demonstrated, that Lg blockage alone accounts for misclassifications by the Lg/Pg discriminant. It is largely an unresolved question whether or not Lg and Pg suffer similar blockage, with second order effects on their amplitudes causing variations in their amplitude ratios. To understand the physical basis for the changes in Lg/Pg amplitude ratios, it is clear that it will be necessary to resolve the question of how each phase varies, and I return to this topic in the next section.

From our review of the literature and our observations of Lg/Pg amplitude ratios across southern California, I determined that, to significantly improve regional seismic discrimination, we would have to understand the physics of the propagation of both Lg and Pg and not just empirically quantify their relative variation. A review of the literature on blockage turned up an extensive body of theoretical studies of Lg propagation and blockage, but no observations that provided appropriate constraints for such studies. For that, it would be essential to know the instrument calibration and site amplifications at

all recording stations so that absolute amplitude measurements could be made, and site effects removed. Because I had also determined that Lg/Pg amplitude ratios varied over very short spatial scales, it was clear that observations of changes in absolute amplitudes of Lg and Pg would have to be made at the same short scale; hence the decision to estimate site amplifications appropriate for all possible SCSN stations.

I began by estimating site amplifications appropriate for Lg. This was a major undertaking which began with a thorough review of the nature of both Lg and teleseismic coda and of which parameters are important in controlling site amplification. The work also required the development of complex statistical tools for the inversion of doubly censored data from a very heavy-tailed distribution, and the development of a methodology for isolating the near-receiver-scattered component of teleseismic coda from the near-source-scattered component, to say nothing of the extensive data processing required. That is the work described in chapters 5 and 6, and summarized in the final section. The results obtained are important both for the tools developed and the results obtained.

The estimation of site amplifications concludes the research accomplished for the dissertation, but as I have presented the work in the broader context of understanding regional propagation, I will discuss how the results will be applied in the future. We have been laying the groundwork for ultimately improving the performance of the Lg/Pg regional discriminant, by permitting observation of changes in just the amplitude of Lg over short path segments and so developing the data-based constraints on modeling that are currently lacking. The first question to ask then is whether the site amplification corrections work. Do they indeed permit separation of the site effects from propagation effects on amplitude? I apply the site amplification corrections to regional data as a proof-of-concept test, and discuss the results of that test and their implications for future research.

Application of site amplifications

I apply the site amplification corrections to the records from three regional earthquakes in distinctly different source regions and one nuclear explosion from the Nevada Test Site (NTS). As discussed

above, understanding Lg blockage and understanding variations in Lg/Pg amplitude ratios are two different issues; to understand how different, I applied the site amplification corrections to both Lg and Pg amplitude measurements. In applying the corrections to both Lg and Pg, I assume that site amplifications are the same for both phases, as was found to be the case for a variety of site geologies (Barker, et al., 1981). Even if the assumption breaks down at some level of resolution, it is unlikely that differences would be great enough to affect the large-scale pattern of amplitude variations observed. I assume equal amplifications for Lg and Pg only for this step, which is largely a proof-of-concept test for our site amplification corrections. More rigorous investigation will be required before inferences can confidently be made based on fine details of variations between Lg and Pg amplitudes.

Mendocino earthquake: The first example of the correction for site amplifications is for event 1 of figures 4.2 and 4.9, a m_b 4.2 earthquake near Cape Mendocino. In figure 7.1 I show demeaned $\log(Lg/Pg)$ amplitude ratios, which makes the pattern of amplitude ratio variation more discernible. Crosses no longer represent stations specifically classifying an event as an earthquake, as they did in figure 4.9, but indicate larger than average Lg/Pg amplitude ratios, which are more earthquake-like values. Similarly, circles represent the more explosion-like smaller Lg/Pg amplitude ratios. I have used just the earliest part of the Lg window, from 3.6 to 3.3 km/sec group velocity, in order to avoid masking of blockage or attenuation of Lg by the arrival of later multi-pathed or back-scattered energy. The observed patterns of variation however are generally indistinguishable from those for a group velocity of 3.6 to 2.8 km/sec.

Figure 7.2 shows the Lg amplitudes, corrected for site amplification, from the same event. These values are also demeaned to make the variations more easily discernible. The absolute values of Lg amplitudes for this event range from zero (i.e. the pre-event noise level) to nearly 2000 nm/sec. The pattern is dominated by a decrease in Lg amplitude with distance, as expected. There is also a difference between amplitudes on either side of the San Andreas fault with smaller Lg on the southwest side. Figure 7.3, the Pg amplitudes corrected for site amplification, shows that a similar but less pronounced

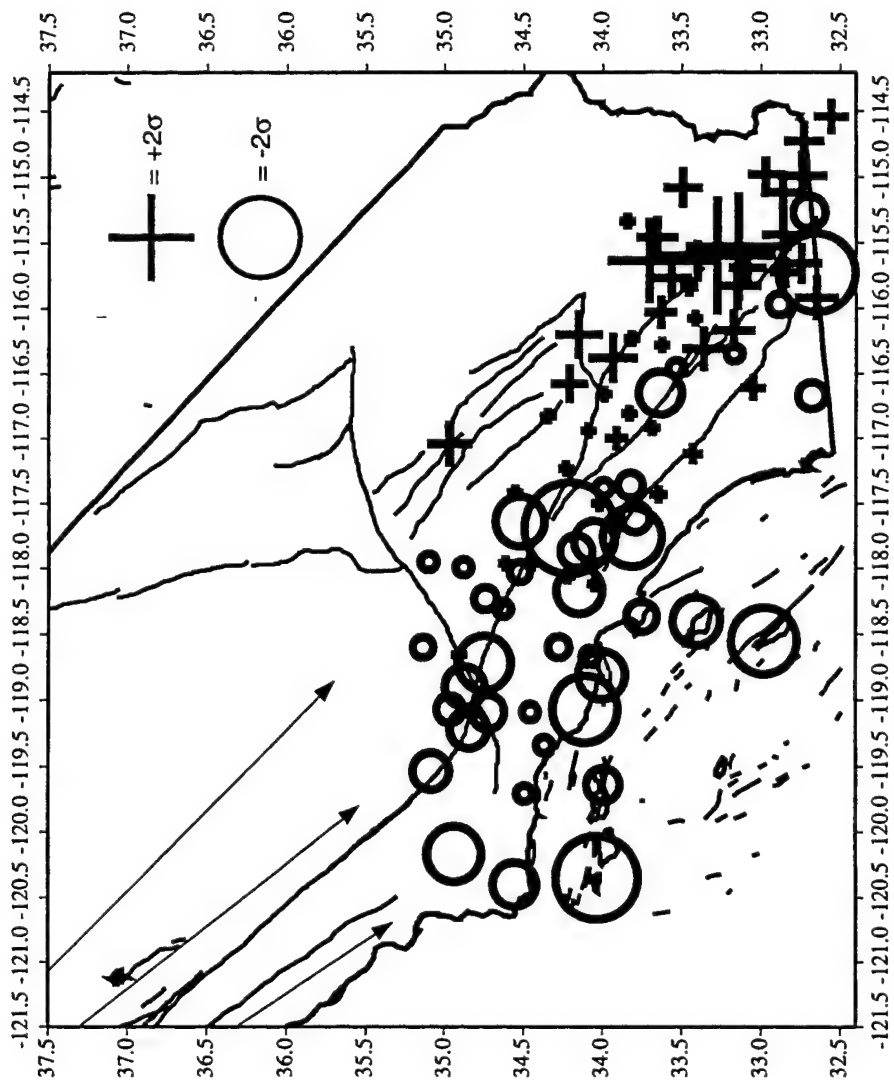


Figure 7.1: Log(Lg/Pg) amplitude ratios recorded at SCSN stations for event number one of figure 4.2. The values are demeaned, with values greater than the mean plotted as crosses and those less than the mean plotted as circles. Symbols are scaled by distance from the mean. Arrows indicate the propagation direction.

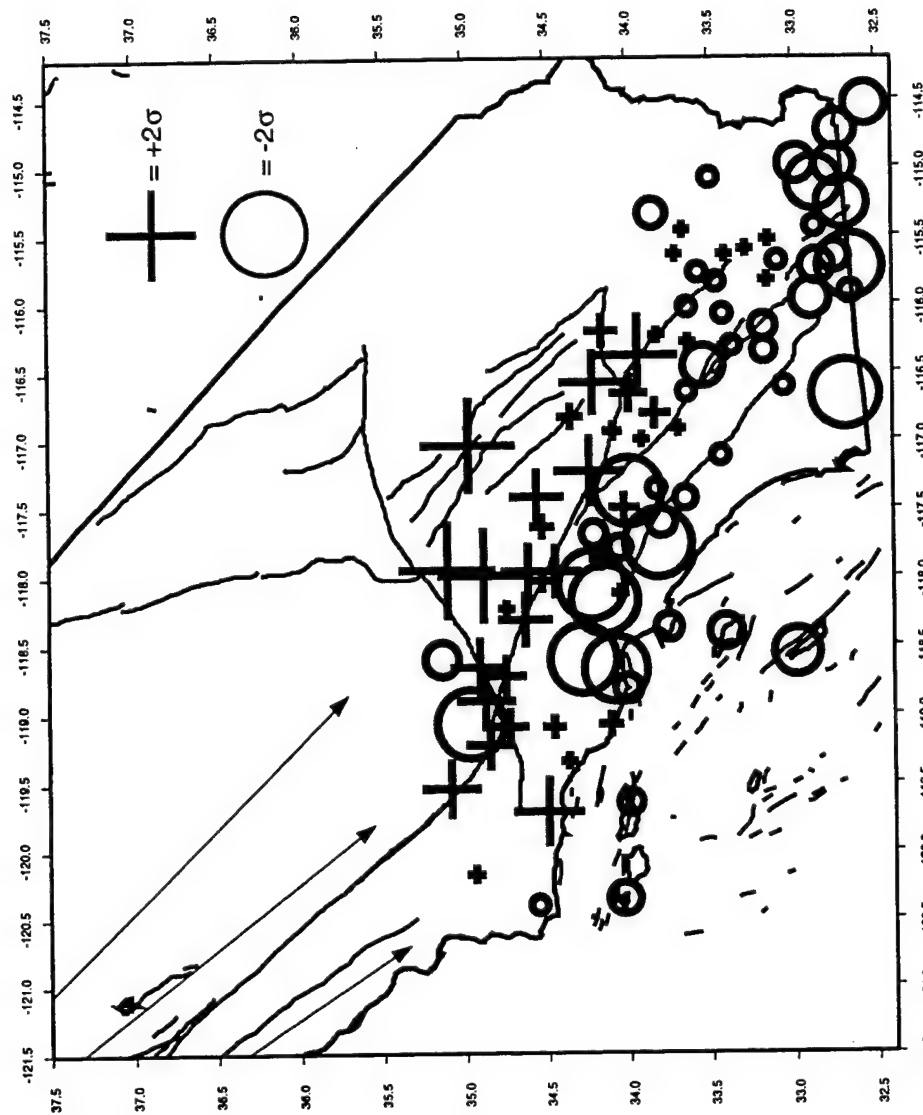


Figure 7.2: Lg amplitudes, after correction for site amplifications, for event one.

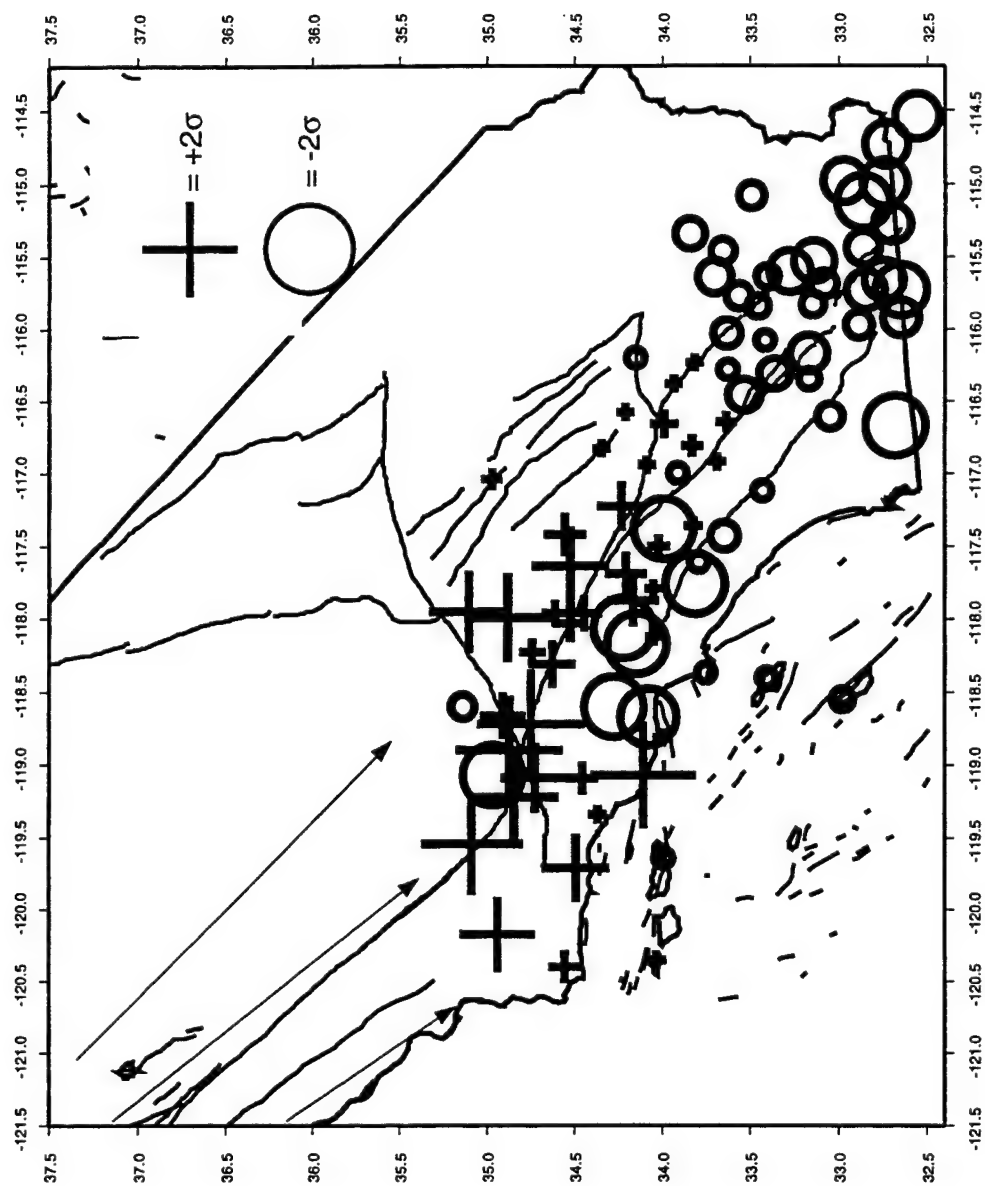


Figure 7.3: Pg amplitudes, after correction for site amplifications, for event one.

difference is apparent in the Pg amplitudes. This suggests that similar mechanisms are affecting amplitudes of both phases, but to a different extent. In the area of smallest $\log(Lg/Pg)$ in figure 7.1, the same area in which stations misclassifying the event are located (figure 4.9), the absolute Pg amplitudes are not smaller to the southwest of the San Andreas fault. Thus the misclassifications may be due to greater blockage of Lg than Pg in that area. Conversely, the area of greatest Lg/Pg amplitude ratio (figure 7.1) appears to be due to a much faster decay, or blockage, of Pg than of Lg.

Eastern Sierra Earthquake: Figure 7.4 shows the demeaned $\log(Lg/Pg)$ amplitude ratios for event 3 of figure 4.2. The smallest Lg/Pg amplitude ratios are in the southernmost part of the array, and as seen in figure 4.8, the difference in amplitude ratios is great enough there for the event to be misclassified. Although the distance effect dominates figures 7.5 and 7.6, the site-corrected Lg and Pg amplitudes, there is a significant difference between the two plots. Pg transmission appears to be much more efficient than Lg transmission throughout a north-south corridor at about 117° longitude. For this earthquake, it appears that event misclassification using the $\log(Lg/Pg)$ discriminant is attributable directly to Lg blockage.

Nuclear explosion at NTS: In contrast to the situation with earthquake records, stations misclassifying nuclear explosions have earthquake-like, large Lg/Pg ratios. The demeaned $\log(Lg/Pg)$ amplitude ratios (figure 7.7) for this explosion (the same explosion as in figure 4.3c) vary approximately inversely to those of the eastern Sierra earthquake (cf. figure 7.4). The large Lg/Pg amplitude ratios are in a corridor running south from NTS through the eastern Mojave block and on down through the Peninsular Range. The plots of site-corrected Lg and Pg (figure 7.8 and 7.9 respectively) indicate that the difference is due to especially good Lg transmission. Lg amplitudes are quite high (figure 7.8), while Pg amplitudes (figure 7.9) are average. These figures also indicate that Lg and Pg both suffer an abrupt change in amplitude along the most northerly paths recorded, which cross the southern Sierra, the Great Basin, and eventually, the San Andreas fault. For those paths, both phases were equally affected and the discriminant values remained accurate.

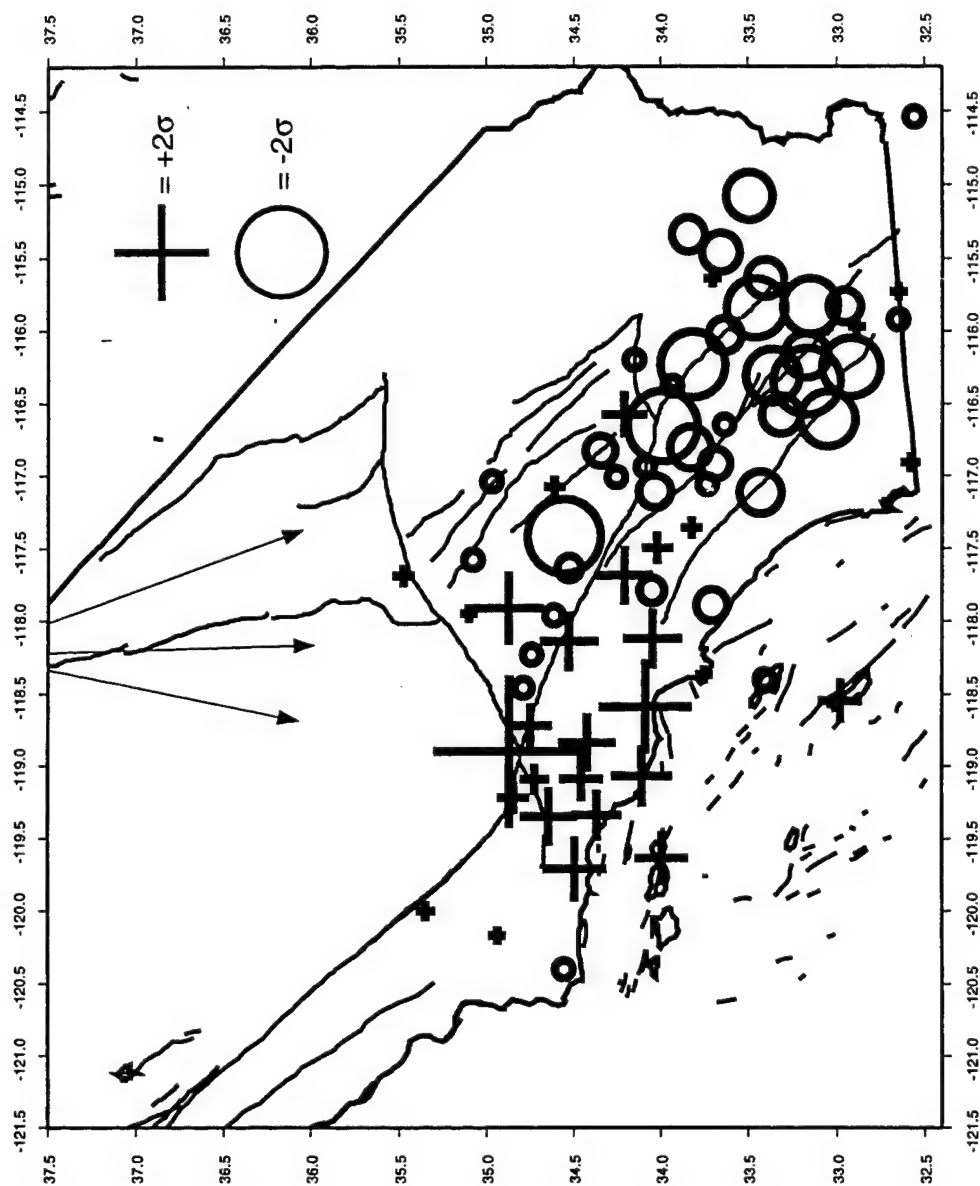


Figure 7.4: Log(Lg/Pg) amplitude ratios for event number three of figure 4.2

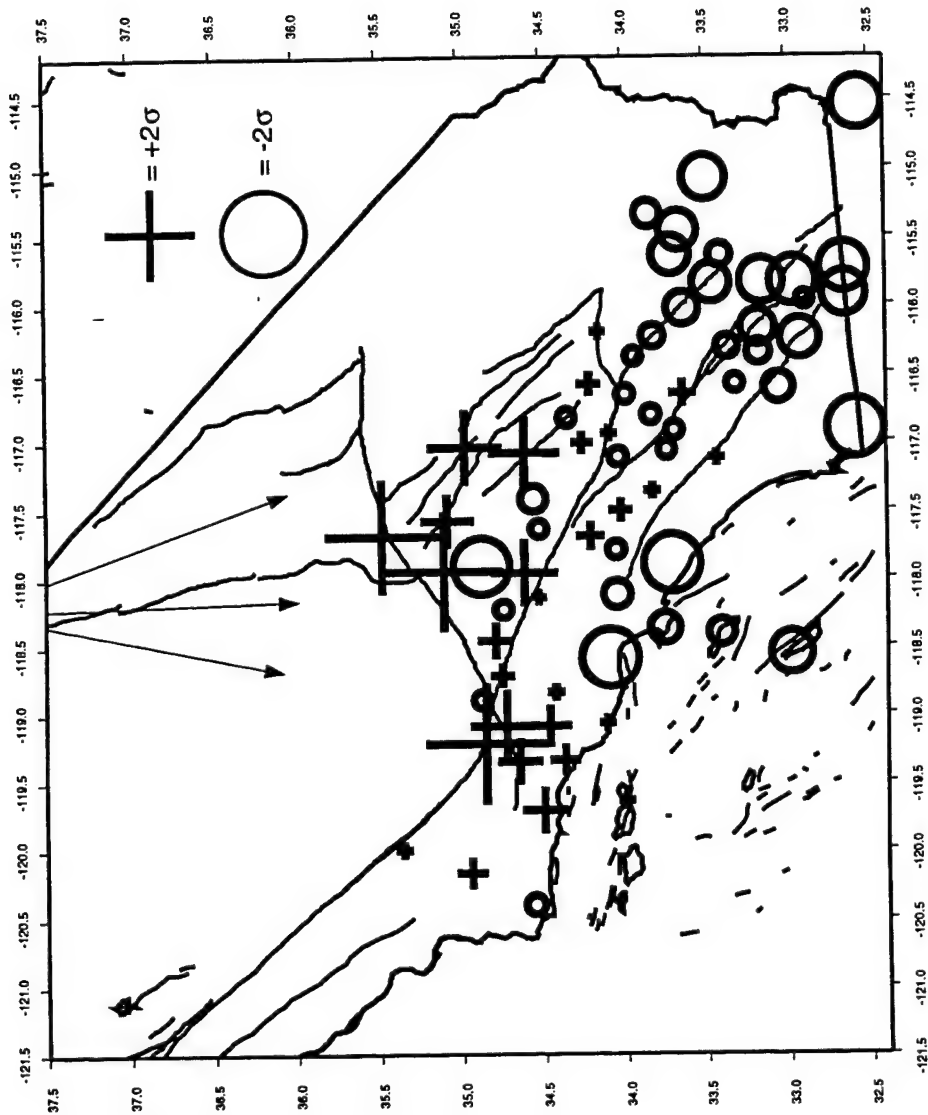


Figure 7.5: Lg amplitudes, after correction for site amplifications, for event three.

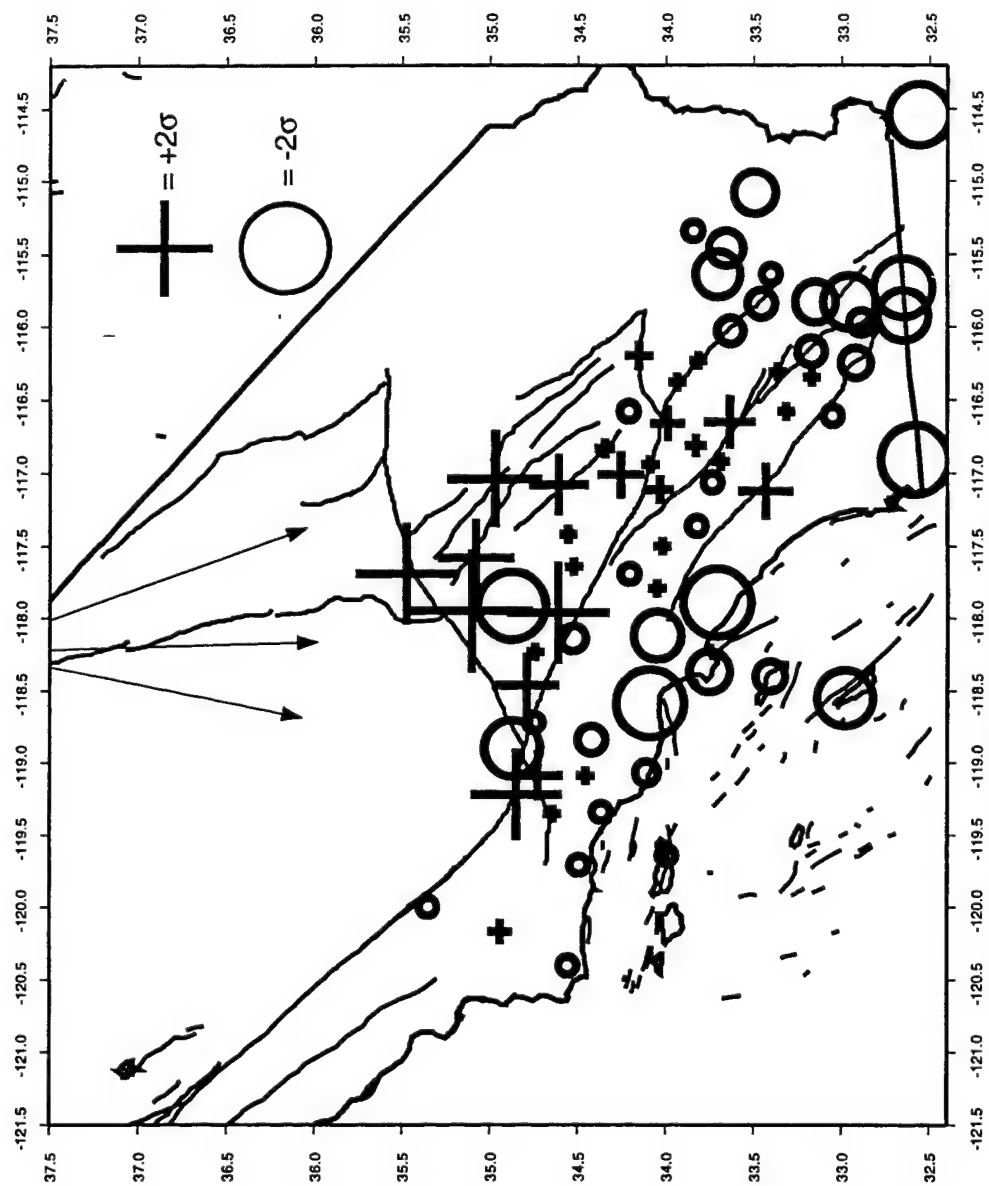


Figure 7.6: Pg amplitudes, after correction for site amplifications, for event three.

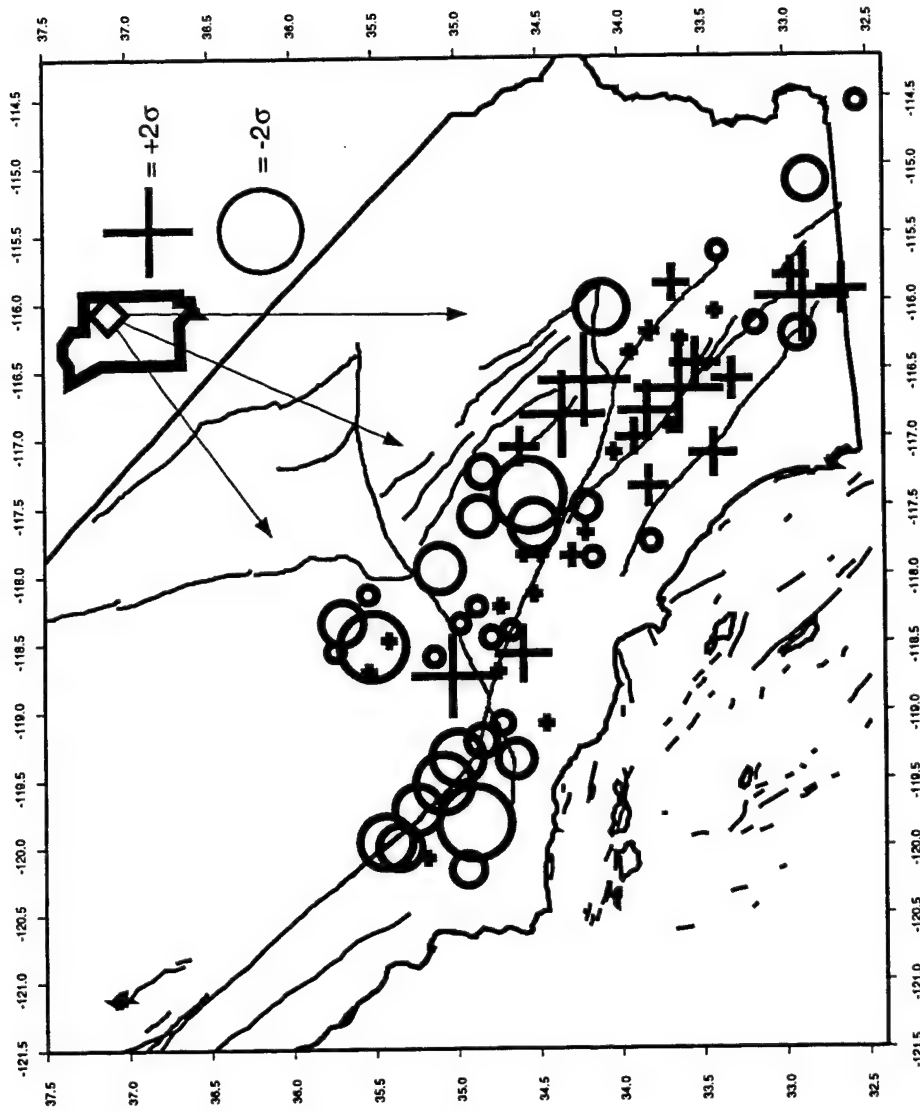


Figure 7.7: Log(Lg/Pg) amplitude ratios for a nuclear explosion at NTS.

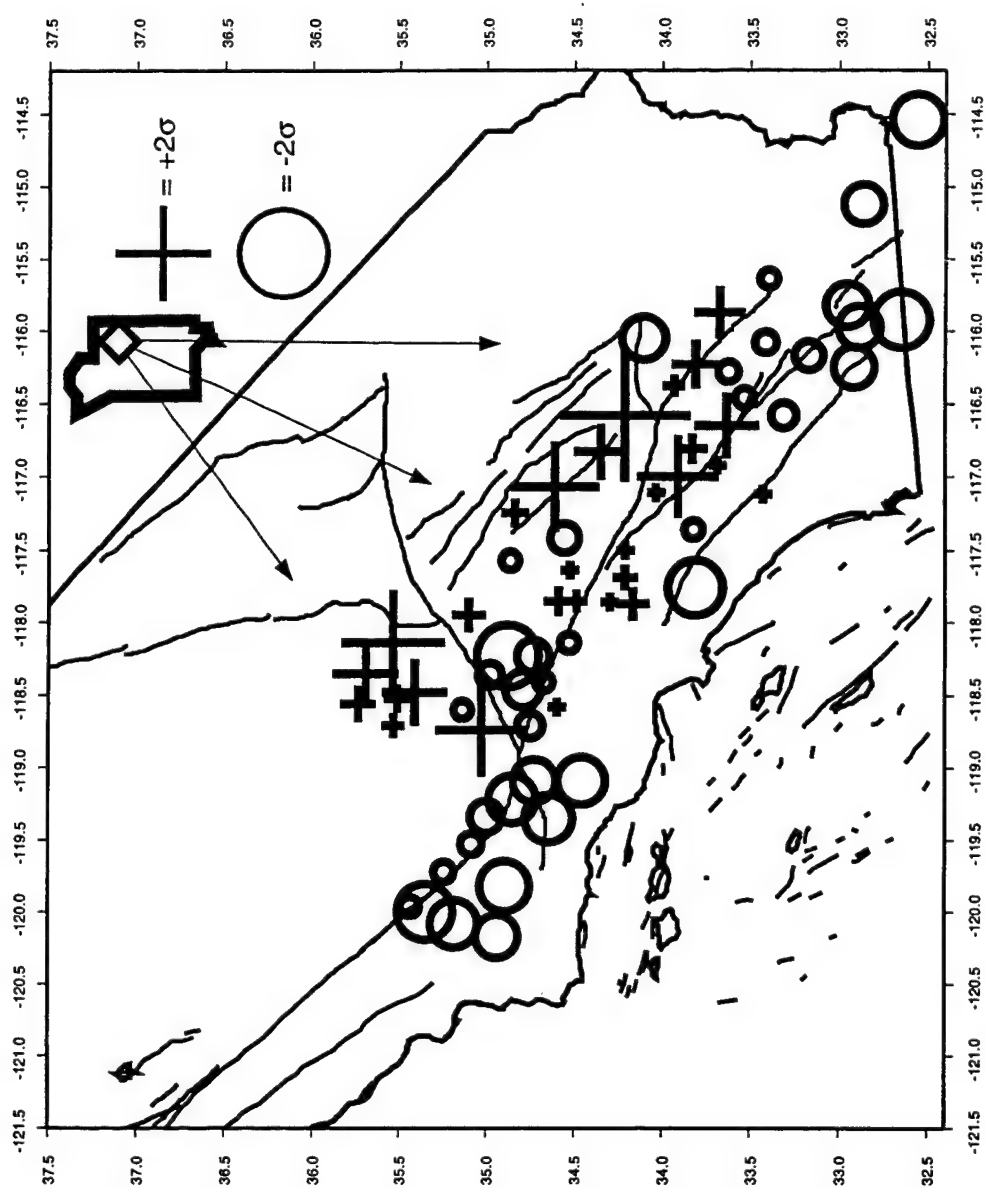


Figure 7.8: Lg amplitudes, after correction for site amplifications, for the NTS event.

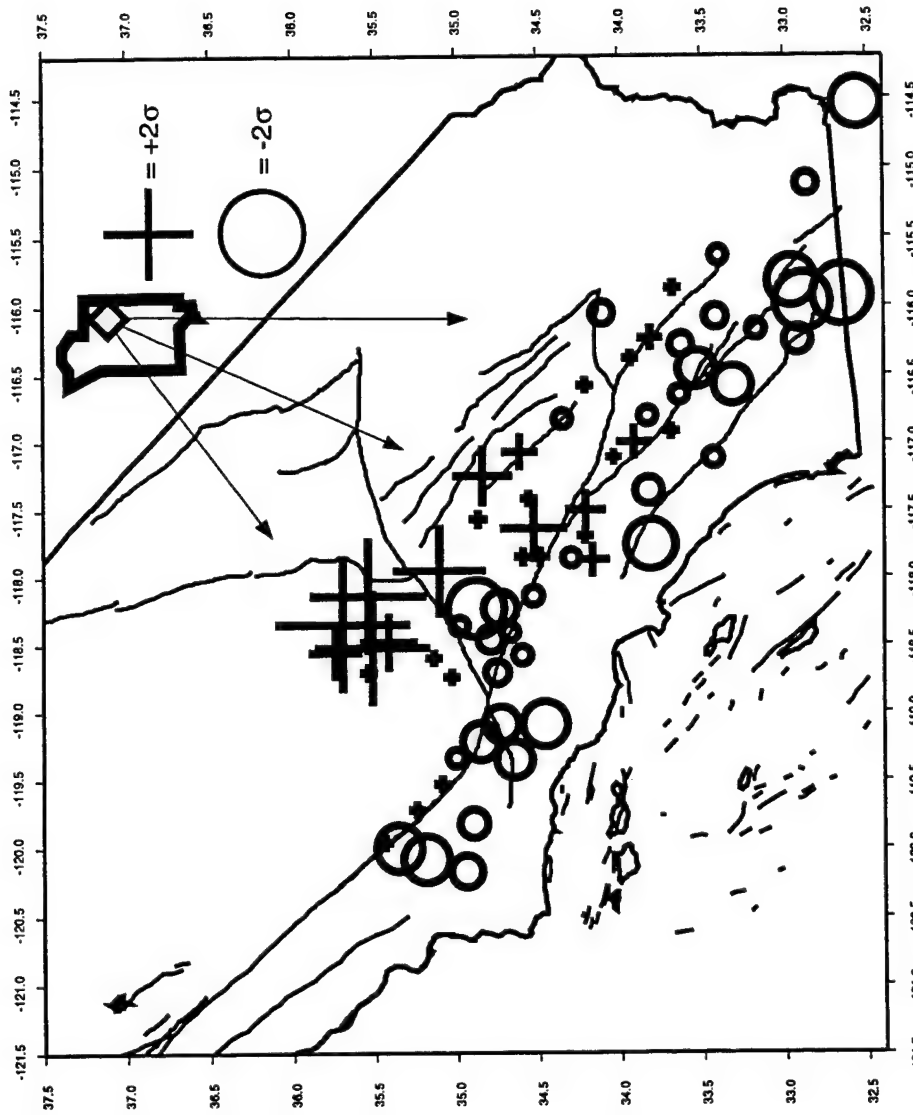


Figure 7.9: Pg amplitudes, after correction for site amplifications, for the NTS event.

Baja earthquake: As was observed in the records for the three previous events discussed, there is a sharp separation between large and small Lg/Pg amplitude ratios (figure 7.10) recorded for this Baja California earthquake (event six of figure 4.2). For the most part, the differences observed in the amplitude ratios are not obvious in the images of site-corrected Lg and Pg amplitudes, which are very similar (figures 7.11 and 7.12). Both figures indicate that propagation of the crustal phases is much less efficient in the thinning crustal waveguide near the coast.

Discussion of the application of site amplification corrections and future work

In the preceding section, I have demonstrated that the site amplification corrections computed for the SCSN stations enable isolation of propagation effects on regional phases. Application of the site amplification corrections indicate that observed variations in the $\log(\text{Lg/Pg})$ amplitude ratio discriminant can be better understood by analyzing their separate amplitude variations over a variety of paths. Specifically, for paths along different azimuths, through varying structure, we have seen

- 1) path segments where both Lg and Pg are blocked, but fairly equally, so that the Lg/Pg discriminant remains effective,
- 2) paths where Lg appears to be blocked to a greater extent than Pg, so that the discriminant value is lowered and earthquakes may be misclassified as explosions, and
- 3) paths where Pg appears to be blocked to a greater extent than Lg, so that the discriminant value is increased and explosions may be misclassified as earthquakes.

Although it is tempting to speculate on details of the amplitude variations observed in these figures, it is easy to be misled by preconceptions and I intend to systematically quantify the observations for a number of events. Specifically, I intend to develop an interpolation scheme so that changes in Lg amplitude may be estimated along short path segments in the propagation direction and correlated with path properties. This will provide the observations of Lg amplitude changes necessary to constrain models of Lg propagation, which is essential to understanding Lg blockage and to improving the performance of regional seismic discrimination.

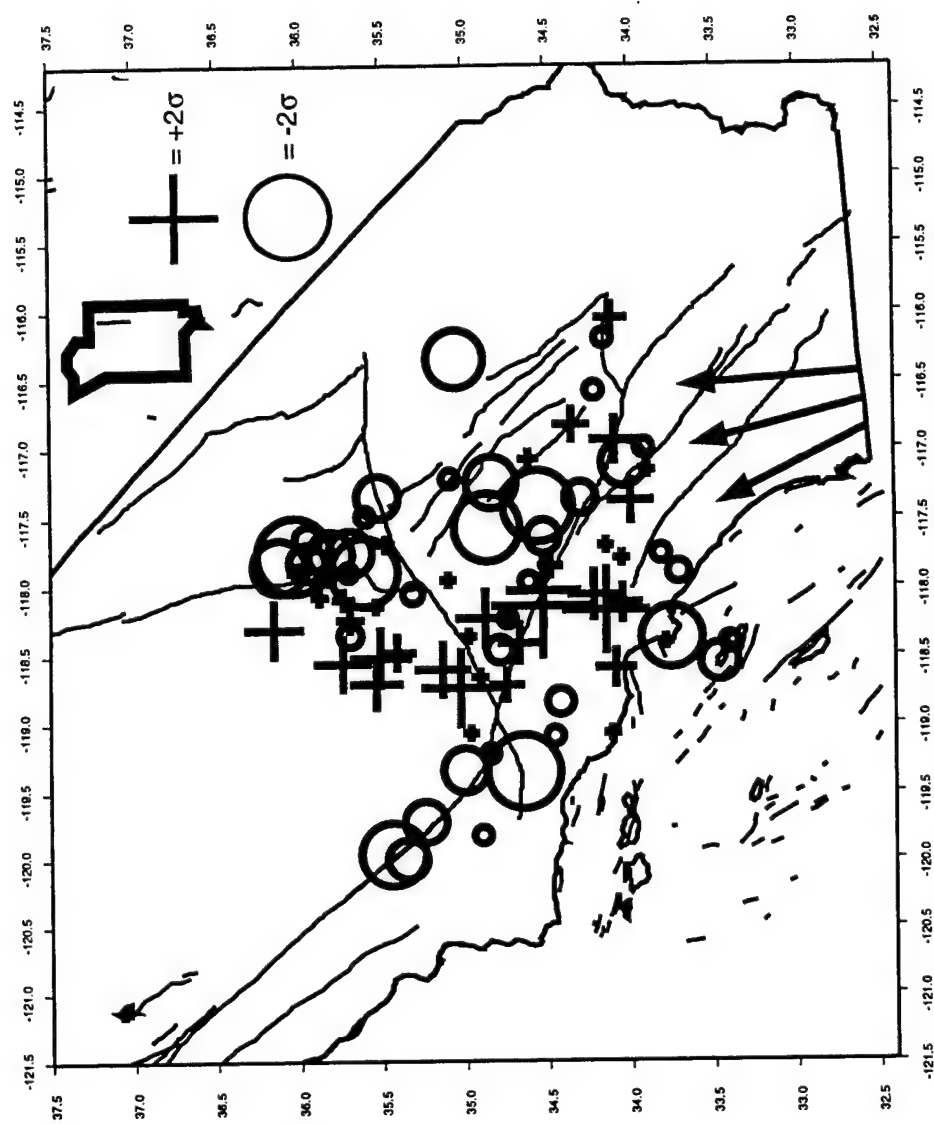


Figure 7.10: $\text{Log}(L_g/P_g)$ amplitude ratios for event number six of figure 4.2

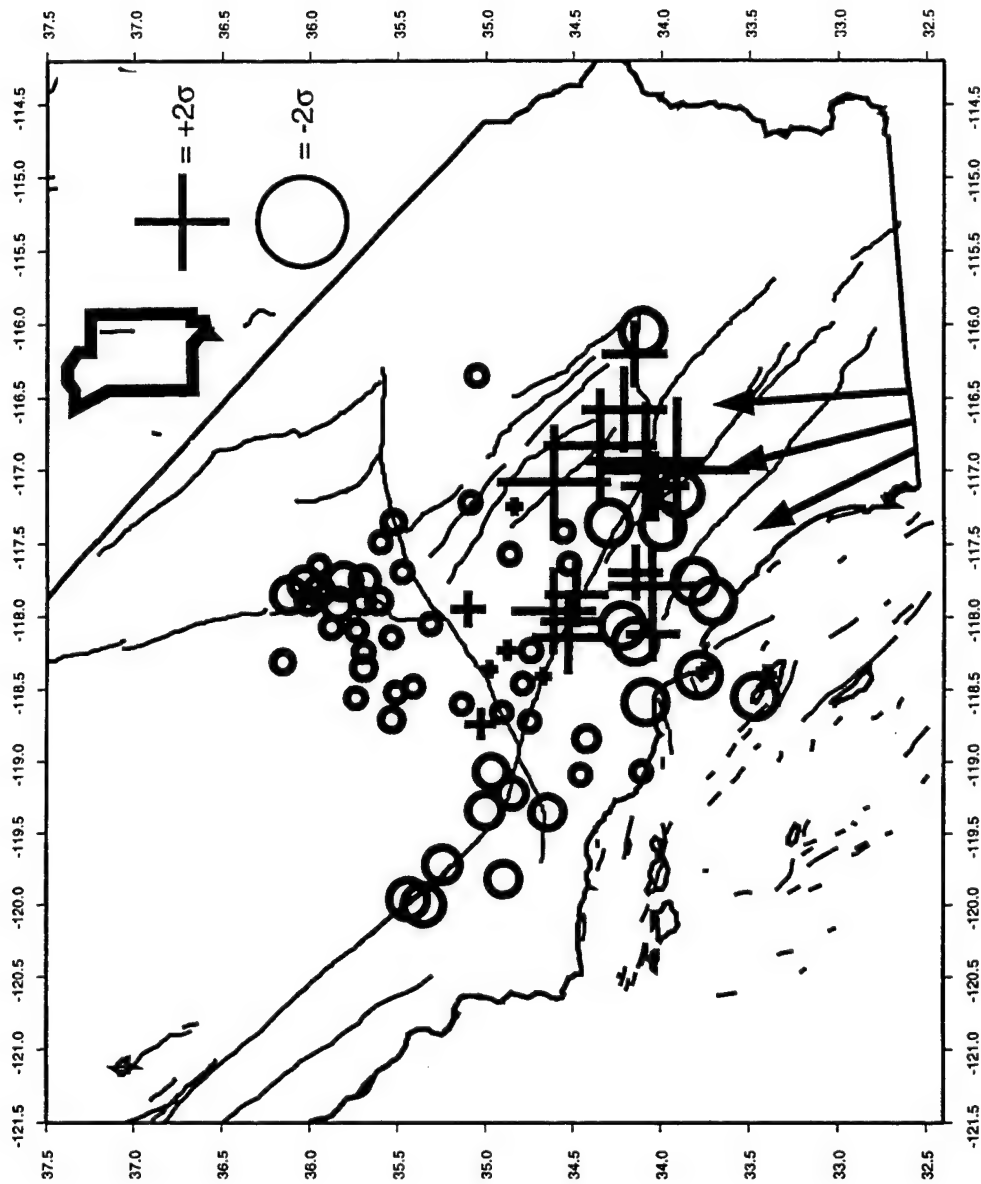


Figure 7.11: Lg amplitudes, after correction for site amplifications, for event six.

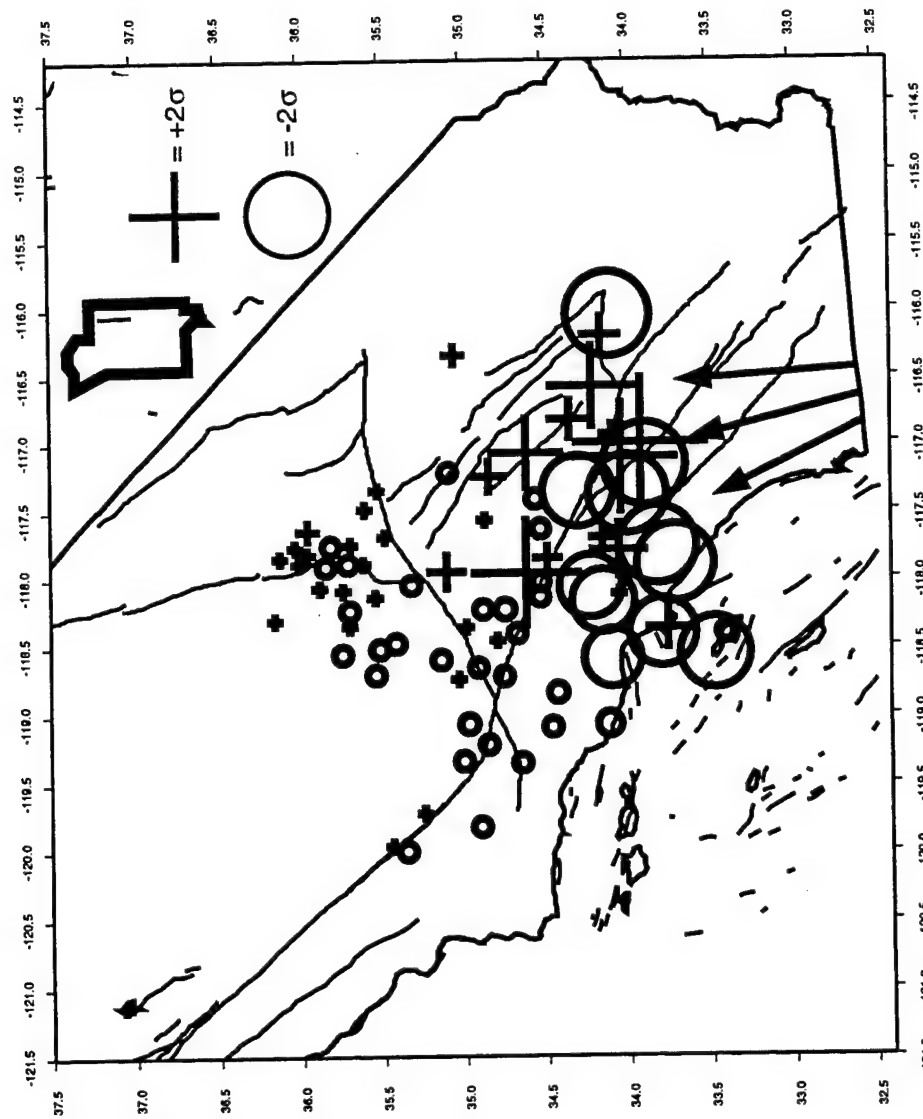


Figure 7.12: Pg amplitudes, after correction for site amplifications, for event six.

Several further projects are indicated as well, still specifically related to the goal of improving nuclear verification. The next step should be a rigorous assessment of the relative site amplifications of Lg and Pg. Then, a study of Pg propagation, similar to that described above for Lg, should be performed. Only when the mechanisms of Lg and Pg blockage are better understood will it be possible to assess their relative efficiency in blocking each phase and so develop highly accurate, transportable path corrections for the discriminant.

Conclusions

I will recapitulate what has been achieved in the course of completing this dissertation. The first half of the thesis dealt with the receiver function technique. We first improved the calculation of receiver functions by developing a simultaneous time-domain deconvolution (Appendix 1). We then provided a thorough analysis of the resolution of the technique, which indicated that receiver function amplitudes are extremely poorly constrained and should not be used to infer anything more than relative amplitude or dip of interfaces. This is important because it has been common to make direct inferences of dip and/or velocity jumps from receiver function amplitudes. On the other hand, we demonstrated that the arrival times of receiver function phases are quite robust to additive noise and the effects of deconvolution (Chapter 3). We extended the technique's application to an area with complex Moho topography by constraining possible models with other observations of the same data, including azimuthal variations in receiver function waveforms, and polarization of the initial unprocessed P-wave. From the technique's application to data recorded at Piñon Flat Observatory (PFO), on the boundary between the rifting Salton Trough and the 10,000 foot Peninsular Range, we were able to make several important inferences regarding the structure of the region. Specifically, the Moho appears to be gradational beneath the Salton Trough, and undergoes very rapid spatial changes in depth, apparently in large step offsets that maintain Airy isostasy. In the mid-crust we identified a significant low-velocity zone which may correspond to a highly conductive layer indicated by a nearby resistivity profile, possibly due to the pooling of saline fluids at the base of the pluton on which PFO rests.

The latter half of the thesis dealt with site amplifications at the SCSN. We adapted statistical techniques to the estimation of site amplifications and network magnitudes. These techniques could improve the accuracy of parameter estimates in other areas of geophysical data analysis, as they deal effectively with two problems common in geophysical data. One technique, robust reweighting of data, is straightforward in its application and can lead to significant improvement in the accuracy of parameters estimated from large sets of data drawn from a heavy-tailed distribution. The second method allows the incorporation of censored data into parameter estimates. Application of this technique is more involved than the first, but, where necessary, it can prevent biasing of parameter estimates. The site amplifications themselves are important for hazard assessment. We have verified previously estimated site amplifications, significantly expanded the base of known site amplifications, and perhaps most importantly, indicated a difference in the mechanisms by which resonance in sedimentary basins is generated.

In determining that the best way to improve the performance of the Lg/Pg regional discriminant would be to enable observation of variations of Lg blockage over a fine spatial scale, which the estimation of site amplifications does, we made several improvements in our understanding of regional propagation. Specifically, we showed that path effects dominate misclassification for most events and that changes in discriminant value are due to path effects that occur over ~20 km length scales. We demonstrated a need for the quantification of blockage, and that site amplifications were necessary for that. From application of the site amplification corrections, we showed that changes in the discriminant value are not necessarily due just to Lg blockage, but to changes in amplitudes of both phases. The application of the corrections showed that by calculating site amplifications for the SCSN, we have made it possible to measure changes in absolute Lg amplitudes due to propagation effects at the fine spatial scale at which Lg blockage occurs. Such measurements will provide the constraints necessary for further progress in modeling, and so in understanding, Lg blockage.

References

- Barker, B., Z. Der, and C. Mrazek, (1981), The effect of crustal structure on the regional phases Pg and Lg at the Nevada Test Site, *J. Geophys. Res.*, 86, 1686-1700
- Dowla, F., P. Goldstein, P. Harben, D. Harris, T. Hauk, S. Jarpe, E. Kansa, P. Lewis, D. McNamara, H. Patton, D. Rock, A. Ryall, C. Schultz, A. Smith, J. Sweeney, W. Walter, and L. Wethern (1996), Seismic regionalization in the Middle East and North Africa, *Proc. 18th Seism. Res. Symp.*, PL-TR-96-2153, 55-64
- Randall, G.E., H.E. Hartse, W.S. Phillips, and S.R. Taylor, Regional characterization of western China - II, *Proc. 18th Seism. Res. Symp.*, PL-TR-96-2153, 80-87
- Taylor, S.R., M. Denny, E. Vergino, and R. Glaser (1989), Regional discrimination between NTS explosions and western U.S. earthquakes, *Bull. Seism. Soc. Am.*, 79, 1142-1176
- Vernon, F.L., R.J. Mellors, J. Berger, A.M. Al-Amri, and J. Zollweg, Initial results from the deployment of broadband seismometers in the Saudi Arabian shield, *Proc. 18th Seism. Res. Symp.*, PL-TR-96-2153, 108-117
- Zhang, T., S. Schwartz, and T. Lay (1994), Multi-variate analysis of waveguide effects on short-period regional wave propagation in Eurasia and its application in seismic discrimination, *J. Geophys. Res.*, 99, 21929-21945
- Zhang, T., T. Lay, S. Schwartz, and W.R. Walter (1996), Variation of regional seismic discriminants with surface topographic roughness in the western U.S., *Bull. Seism. Soc. Am.*, in press

Simultaneous time-domain deconvolution with application to the computation of receiver functions

Harold Gurrola, G. Eli Baker and J. Bernard Minster

Institute of Geophysics and Planetary Physics, University of California at San Diego, La Jolla, CA 92093, USA

Accepted 1994 June 10. Received 1993 March 29

SUMMARY

Receiver functions are produced by deconvolving the horizontal components of a seismogram by the vertical component. Typically this is performed by spectral division of recordings of single events. Receiver functions from events with similar backazimuth and ray parameter are then stacked to improve the signal-to-noise ratio. To avoid the subjective and time-consuming method of prewhitening typically employed with spectral division, we have cast the deconvolution in the time domain. By performing the time-domain deconvolution as a regularized simultaneous inversion for a group of events that would normally have been stacked after deconvolution, we find that side lobes are reduced and resolution is improved. Furthermore, the regularized inversion allows the user to choose among a variety of objective model norms. In this paper, we present results from inversions employing the L_2 norm and lower-bounded least squares.

Key words: deconvolution, receiver function.

INTRODUCTION

Receiver functions are produced by deconvolving the radial and transverse horizontal components of a seismogram by the vertical component, thereby isolating P -to- S converted phases and reverberations ending in an S phase (Langston 1989, 1981, 1979; Owens, Crosson & Hendrickson 1988; Owens & Crosson 1988; Owens, Taylor & Zandt 1987; Owens, Zandt & Taylor 1984). To improve the signal-to-noise ratio, receiver functions are often binned by similar backazimuth and ray parameter (henceforth we will use the term 'bin' for this grouping of receiver functions or seismograms), and then stacked. It is well known that in the presence of noise, deconvolution is unstable (Sipkin & Lerner-Lam 1992). The instabilities of deconvolution due to noise are usually addressed by prewhitening the time series (usually for frequency-domain deconvolution; e.g. Owens *et al.* 1984) or applying damped least squares (e.g. Oldenburg 1981; Sipkin & Lerner-Lam 1992). We have found that the side lobes resulting from the deconvolution of a single seismogram, even with careful application of prewhitening, are coherent across the several receiver functions produced for a given bin and, therefore, stack coherently. To improve the signal-to-noise ratio as a step in the deconvolution, we perform a simultaneous deconvolution of events that would normally be stacked after deconvolution, thereby reducing the need for damping (prewhitening). Our approach is akin to that of Oldenburg (1981) who described a frequency-domain multichannel deconvolution. In particular, we have

modified the production of receiver functions by time-domain simultaneous deconvolution (Ammon 1991) to include damping terms similar to those outlined by Sipkin & Lerner-Lam (1992) for single-channel deconvolution. We will also give a brief illustration of the ease with which different penalty functions can be applied with the time-domain approach by showing results of a lower-bounded least-squares deconvolution.

In regions with horizontally stratified geology, all of the converted S energy will be found on the radial components. In areas with dipping layers or anisotropy, the tangential components of the receiver functions become important as well. The deconvolution procedure is, however, the same for both the radial and transverse components of the receiver functions. A major problem in producing receiver functions is to distinguish individual peaks that can be obscured by neighbouring larger peaks or their side lobes. Such problems are greatest on the radial components since they have larger arrivals than do the transverse ones. Since this paper focuses on the deconvolution technique rather than on the interpretation of receiver functions, we will only deal with radial components in the examples.

PROBLEMS NOTED WITH THE EXISTING DECONVOLUTION METHOD

Deconvolution is typically formulated in the frequency domain in terms of spectral division. A common

implementation for receiver functions (e.g. Owens, Taylor & Zandt 1983; Owens *et al.* 1984) uses the form:

$$r = \frac{hv^*}{vv^* + w} \quad (1)$$

where r is the Fourier transform of the receiver function, h and v are the Fourier transforms of the horizontal and vertical components of the seismogram respectively, $*$ indicates complex conjugation, and w is a prewhitening function. The prewhitening is carried out by replacing the

power level vv^* by a so-called 'water level' anywhere it falls below a specified value, usually a given fraction of the peak power level (e.g. Owens, Taylor & Zandt 1983). By filling the troughs in the denominator of eq. (1), we avoid spurious peaks that may appear in r and cause ringing in the receiver functions. Receiver functions are computed for a range of water levels, and a 'best' water level is selected on an individual basis, usually according to rather subjective criteria.

The top panel of Fig. 1 shows 14 receiver functions computed from seismograms recorded at Artii, Russia (ARU) using the frequency-domain deconvolution described above. The middle panel depicts the stack of these 14 receiver functions along with traces representing ± 2 standard deviations (determined by a jackknife technique, Efron & Tibshirani 1986) of the mean about the stack. We observe a broad trough on either side of the peak at 0 s which illustrates that artefacts of deconvolution tend to be coherent features and are enhanced by stacking after deconvolution. Since this peak is the first arrival we can be sure that the trough preceding it is a result of deconvolution. Because we expect side lobes to be symmetric about the main peak we suspect that later peaks and troughs are impinged upon by the side lobes of the primary peak. Sipkin & Lerner-Lam (1992) outline this problem in the context of deconvolution of instrument response from seismograms and describe techniques to minimize this effect on individual seismograms. By adapting their approach for simultaneous deconvolution, we significantly reduce these side lobes. The lowermost panel of Fig. 1 shows a receiver function computed using the simultaneous deconvolution method described below along with the standard deviation of the mean computed as in the middle panel.

In this figure, we observe that the side lobes leading into the initial peak can be greatly diminished by greater care in the deconvolution. A lower standard deviation does not necessarily indicate a better receiver function—especially in view of the fact that the repeatable features between receiver functions may result from artefacts in the deconvolution. The simultaneous deconvolution does, nevertheless, result in lower standard deviations in the pre-event noise as well as in the primary peak at 0 s and in the P_s conversion from the Moho at 5 s. The lowermost panel also exhibits greater resolution of the small peak at 2 s which only appears as a shoulder to the main peak in the frequency-domain stack. On the lowermost panel we do, however, notice that the standard deviation of the mean about troughs from 7 to 13 s is greater than on the stacked receiver functions computed individually by frequency-domain deconvolution.

As with any study using real data, visual inspection of the seismograms is required. In the case of receiver functions we typically determine the 'usable' data after applying the deconvolution. We compute individual receiver functions using the frequency-domain deconvolution with all data available from a given station and only present results from those data which produce a strong first arrival at time 0. The purpose of the simultaneous time-domain deconvolution is then to be able to apply an objective (reproducible) criterion for the damping function (prewhitening) and to be able to apply damping functions that are tailored to mitigate specific problems presented by a given data set.

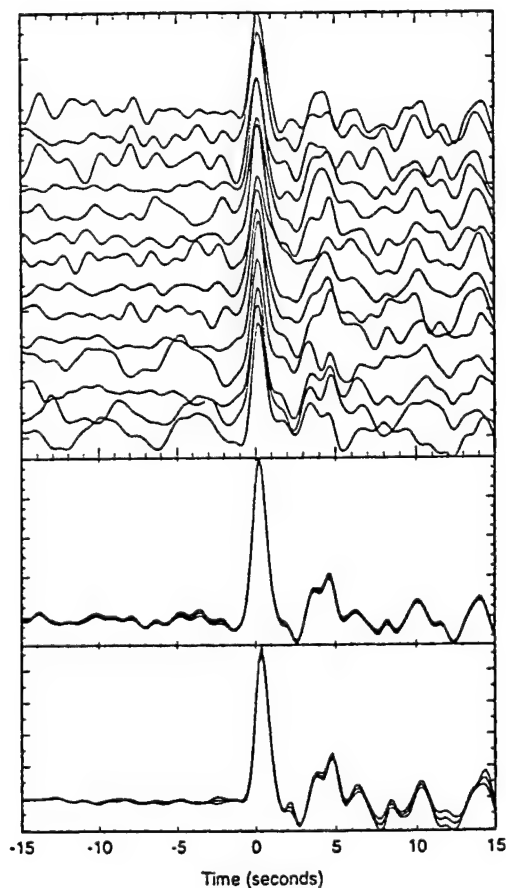


Figure 1. The top panel shows receiver functions computed by frequency-domain deconvolution of 14 events recorded at Artii, Russia (ARU). The middle panel shows the stack of these 14 receiver functions and the traces representing \pm two standard deviations of the mean. The bottom panel shows the receiver function computed using simultaneous time-domain deconvolution of the same 14 events and the traces representing \pm two standard deviations of the mean.

SIMULTANEOUS DECONVOLUTION

By casting the deconvolution as a linear inverse problem we are able to use more objective stabilization procedures than the somewhat subjective method of prewhitening described in eq. (1). For the ideal (noise free) case, we can write the convolution problem as:

$$\mathbf{V}\mathbf{r} = \mathbf{h}, \quad (2)$$

where \mathbf{h} (i elements) can be either the radial or transverse component of the seismogram, \mathbf{r} (m elements) is the corresponding component of the receiver function, and \mathbf{V} is composed of m columns each containing the vertical component of the seismogram (v with n elements) padded with zeros to fill the columns to a length i :

$$\mathbf{V} = \begin{pmatrix} v_1 & 0 & \vdots & \vdots & \cdots & 0 \\ \vdots & v_1 & 0 & \vdots & \vdots & \vdots \\ v_n & \vdots & v_1 & \ddots & \vdots & \vdots \\ 0 & v_n & \vdots & \vdots & \vdots & \vdots \\ \vdots & 0 & v_n & \vdots & \vdots & \vdots \\ \vdots & \vdots & 0 & \ddots & v_1 & 0 \\ \vdots & \vdots & \vdots & \vdots & \vdots & v_1 \\ \vdots & \vdots & \vdots & \vdots & \vdots & v_n \\ \vdots & \vdots & \vdots & \cdots & 0 & v_n \end{pmatrix}. \quad (3)$$

In the absence of noise, we could solve eq. (2) directly for the receiver function (similarly for noise-free data a stable solution can be found in principle by using a water level of 0.0 in eq. 1). As in the case of similar inversions (e.g. Constable 1987; Sipkin & Lerner-Lam 1992), noise is present in the \mathbf{h} term, therefore an exact solution of eq. (2) would overfit the data. It is desirable to find a solution in which the rms difference between the observations \mathbf{h} and predicted data $\mathbf{V}\mathbf{r}$ take an appropriate value, such as the standard deviation, T , of the pre-event noise. We therefore seek a receiver function \mathbf{r} which satisfies the following equation.

$$\|\mathbf{V}\mathbf{r} - \mathbf{h}\|^2 - T^2 = 0. \quad (4)$$

The notation $\|\mathbf{x}\|$ in the above equation denotes the L_2 norm of the vector \mathbf{x} . In the deconvolution for receiver functions, noise is also present in \mathbf{V} and we do not always expect to satisfy this constraint exactly. The solution of eq. (4) for \mathbf{r} is not unique and may be unstable. Therefore, we stabilize the problem by solving for a receiver function that satisfies a particular constraint. For the examples given in this paper, we seek the 'smallest' receiver function, in which the 'size', U , is defined by:

$$\|\mathbf{r}\|^2 = U. \quad (5)$$

By multiplying eq. (4) by a Lagrange multiplier (μ^{-1}) and adding it to eq. (5) we make the trade-off between both constraints explicit by minimizing the quantity

$$\|\mathbf{r}\|^2 + \mu^{-1}(\|\mathbf{V}\mathbf{r} - \mathbf{h}\|^2 - T^2) = U. \quad (6)$$

By differentiating the left-hand side with respect to \mathbf{r} and setting the result to zero, we obtain a vector \mathbf{r} which yields a

Simultaneous time-domain deconvolution

stationary value of U (Constable *et al.* 1987; Sipkin & Lerner-Lam 1992).

$$\mathbf{r} = (\mathbf{I} + \mu^{-1}\mathbf{V}^T\mathbf{V})^{-1}\mu^{-1}\mathbf{V}^T\mathbf{h} \quad (7)$$

\mathbf{I} is the $m \times m$ identity matrix. In an ideal situation, the appropriate value for μ would be that which satisfies the constraint given by eq. (4). However, as mentioned above, there is noise in both \mathbf{h} and \mathbf{V} in eq. (7), as well as basic imprecision in the formulation of receiver functions (resulting from the fact that the vertical component of the seismogram contains some S-wave energy, horizontal components contain P-wave energy, event binning is not a perfect procedure, etc.). For these reasons, we typically do not find exact solutions to eq. (4). Instead, we select an appropriate value for μ by repeating the inversion, each time using different values of μ , until convergence on a stable value of misfit (see discussion below).

To extend this method for the simultaneous deconvolution of several (N) events we modify eq. (2) to read:

$$\begin{pmatrix} \mathbf{V}_1 \\ \mathbf{V}_2 \\ \vdots \\ \mathbf{V}_N \end{pmatrix} \mathbf{r} = \begin{pmatrix} \mathbf{h}_1 \\ \mathbf{h}_2 \\ \vdots \\ \mathbf{h}_N \end{pmatrix}. \quad (8)$$

In which each \mathbf{V}_j , and \mathbf{h}_j ($j = 1, \dots, N$) are the same as \mathbf{V} , and \mathbf{h} , defined above, for the j th seismogram. Following the same steps as outlined in eqs (2) through (7) we obtain:

$$\mathbf{r} \left(\mathbf{I} + \mu^{-1} \sum_{j=1}^N \mathbf{V}_j^T \mathbf{V}_j \right)^{-1} \mu^{-1} \sum_{j=1}^N \mathbf{V}_j^T \mathbf{h}_j. \quad (9)$$

Simultaneous deconvolution (eq. 9) requires, therefore, no larger a matrix inversion than does the deconvolution of a single seismogram.

Figure 2 shows the misfit (first term of eq. 4) versus model size (eq. 5) for the simultaneous time-domain deconvolutions used to compute the lowermost receiver function in Fig. 1. In this case, we started by computing a receiver function using $\mu = 10^{10}$. We then computed additional receiver functions by repeated inversions, each time reducing the value of μ by one order of magnitude. This process was repeated until the value of misfit—the rms difference between the radial components of the observed seismograms and those computed by convolving the receiver function with the respective vertical components—was decreased from that of the previous receiver function by less than 0.05 per cent (typically resulting in a value for μ of between 100 and 1.0). The final receiver function depicted in Fig. 1 was computed using $\mu = 100$.

In the next section, the misfit values shown above the receiver functions in each figure are normalized by the standard deviations of the pre-event noise, T^2 . For the ideal case in which eq. (4) is satisfied, the normalized misfit would have a value of 1.0. It is obvious from Fig. 2, in which we converged on a value of misfit close to 15, that it is usually not possible to reach the ideal value of 1.0.

This method, as well as the frequency-domain method, are both examples of a damped least-squares deconvolution. In the frequency-domain inversion white noise is added (up to a given 'water level') to stabilize the inversion. The time-domain inversion is stabilized by only fitting the data to a specified misfit by using a Lagrange multiplier to balance misfit with some measure of model size (norm). In this

H. Gurrrola, G. E. Baker and J. B. Minster

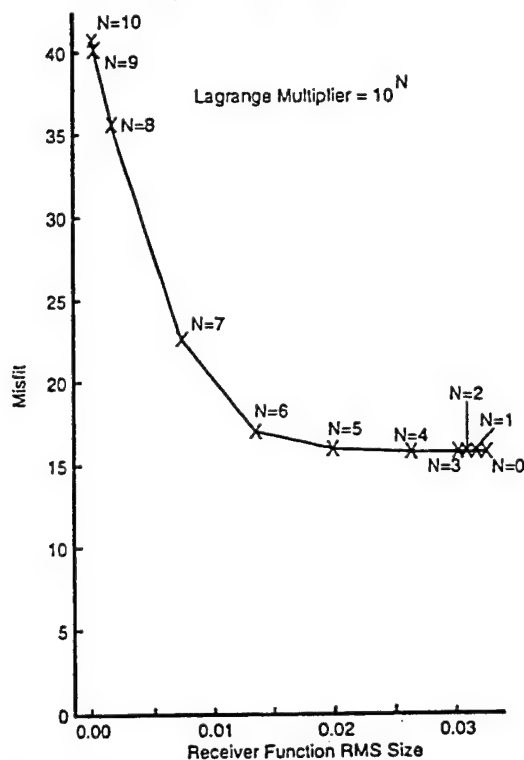


Figure 2. Misfit versus model-norm size for various Lagrange multipliers (μ) applied to the simultaneous deconvolution to compute the receiver function shown on the bottom of Fig. 1. The misfit is defined as the rms difference between the observed radial component of the seismograms and those predicted by a reconvolution of the receiver function with the vertical component. The model-norm size for this example is defined as the rms sum of all the components of the receiver function. To compute the receiver function shown on the bottom panel of Fig. 1 we used $\mu = 10^2$.

sense, the Lagrange multiplier serves the same purpose as the 'water level' in the frequency-domain deconvolution. The advantages are:

- (1) that we stabilize the inversion by making use of some property of the receiver function;
- (2) that the convergence criterion can be specified objectively and in simple terms so that the results are repeatable by other investigators.

Which particular property of the receiver function to use as the damping function is user-selectable, but, as we will demonstrate in the following section, this 'model norm' can be tailored to address specific problems.

The equivalent expression to eq. (9) for a frequency-domain simultaneous deconvolution (using the same notation as in eq. 1) is given by:

$$r = \frac{\sum_{j=1}^N h_j v_j^*}{\left\{ \sum_{j=1}^N v_j v_j^* \right\} + w} \quad (10)$$

It is obvious from eq. (10) that simultaneous deconvolution is equivalent to summing the cross-correlation of the vertical (input to the system) channels with the corresponding horizontal (the observed output of the system) and normalizing the result by the damped (prewhitened) sum of autocorrelations of the vertical components to produce a receiver function (the system). By summing prior to performing the inversion, we improve the signal-to-noise ratio of the auto-correlation and cross-correlation functions and reduce the amount of damping (prewhitening) needed. We recognize that the simultaneous frequency-domain deconvolution would be faster than the time-domain deconvolution, but it still requires the subjective 'water level' prewhitening. As stated earlier, our objective is to take advantage of the more objective and versatile regularization in the time domain. In the following section, we compare results of the simultaneous time-domain deconvolution with those of single-event frequency-domain deconvolution followed by stacking.

EXAMPLES

As a first test we applied the simultaneous deconvolution (eq. 9) to a synthetic data set. We computed a synthetic seismogram for a hypothetical earth structure (Table 1, Baker *et al.* 1995) with a delta-function source. To produce the 'true radial receiver function' for this structure (top receiver function on Figs 3 and 4), we deconvolved the radial component of the delta function synthetic seismogram by the vertical. We then constructed 25 synthetic seismograms by convolving 25 different observed *P*-wave trains with the vertical and radial components of the above delta-function synthetic seismogram. We then added 25 different observed vertical and radial seismic-noise samples to each of the 25 synthetic seismograms respectively. All the *P*-wave and noise samples were recorded at the Piñon Flat (PFO) broad-band seismic station. The signal-to-noise ratios of this synthetic data set, determined by the ratio of the peak amplitude to the standard deviation of the pre-event noise, ranged from about 25 to as low as 5. This range is typical of observed seismograms.

The time-domain deconvolution used in this paper is based on a linear convolution for the forward problem (eqs 2 and 3) in order to avoid effects of wrap around. In this type of deconvolution the receiver-function length is equal to the difference in the length of the horizontal and vertical components. A conservative approach to prepare the data before deconvolution would be first to cut the seismograms to as great a time length as possible before encountering the direct *S* phase, and then shorten the vertical component by the desired length of the receiver function. This would not

Table 1. Velocity model used to generate the synthetic seismograms.

Vs (km/sec)	Vp (km/sec)	layer thickness (km)
3.0	5.4	3.4
3.389	6.1	5.8
2.667	4.8	8.0
3.389	6.1	8.0
4.33	7.5	∞

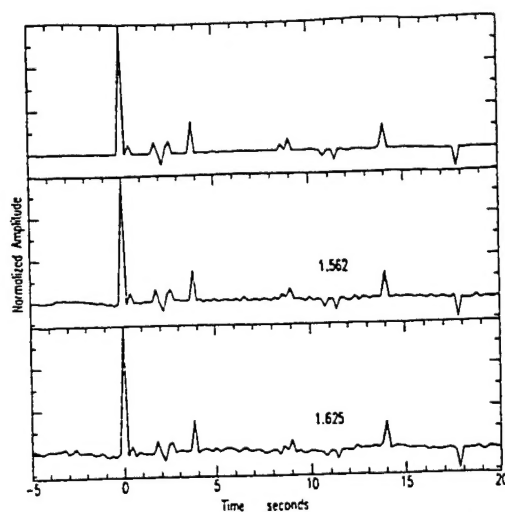


Figure 3. The uppermost 'idealized receiver function' was produced by deconvolution of noise-free synthetic seismograms (assuming a delta-function source). The bottom and middle receiver functions were computed by simultaneous deconvolution of five and 25 synthetic seismograms (described in the text) respectively. The numbers plotted above each of the receiver functions, on this as well as all the following figures, are the rms misfits between all of the observed horizontal components of the seismograms and the convolution products of the receiver function and the respective vertical components. The seismograms were weighted for the rms misfit calculation just as they were for the deconvolution.

only result in a very large matrix, but would include an unnecessary amount of noise. Better results would be obtained by cutting the vertical component at the end of the *P*-wave coda and then cutting the horizontal components to a length equal to that of the vertical plus the length of the desired receiver function. We have found that problems in reproducing the synthetics can only arise by cutting the data too short. As a result we suggest cutting the data long and tapering the last 5 s with a cosine function. We used the cut vertical components in all the time-domain and frequency-domain examples to follow unless otherwise specified. In the case of spectral-division deconvolution, this required padding the shortened vertical component with zeros to give both components an equal number of samples.

The receiver functions depicted in Fig. 3 were computed by simultaneous deconvolution of five (bottom) and 25 (middle) of the above synthetic seismograms. Fig. 4 depicts receiver functions computed by spectral-division deconvolution followed by stacking of the same five (second from bottom) and 25 (second from top) synthetics used in the computation of Fig. 3. The lowermost receiver function in Fig. 4 was computed by spectral-division deconvolution of the above 25 synthetics followed by stacking, using the entire vertical component (without cutting and padding it with zeros). The rms misfit between the predicted and observed radial component of the seismograms corresponding to each receiver function are given in these figures. We note that the receiver functions computed by simultaneous deconvolution using five and 25 synthetics are very similar:

Simultaneous time-domain deconvolution

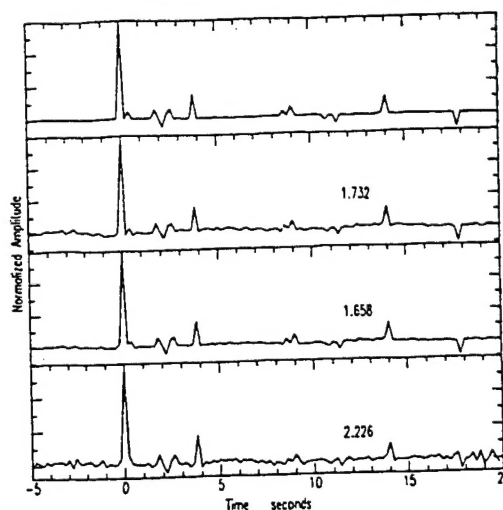


Figure 4. The uppermost 'idealized receiver function' was produced by deconvolution of noise-free synthetic seismograms (assuming a delta-function source). The second and third receiver functions from the top were computed by stacking 25 and five receiver functions (respectively), each computed by single-event frequency-domain deconvolution of the same synthetic seismograms as used to produce Fig. 2. The bottom receiver function was computed by the frequency-domain deconvolution of the uncut vertical components (see text) from the respective 25 horizontal components followed by stacking.

both resolve all the major peaks observed in the 'true radial receiver function'—the only major difference is a lower noise level on the receiver function computed with all 25 synthetic seismograms. Considering that for a given backazimuth and ray parameter we usually do not have as many as 10 seismograms, it is encouraging that simultaneous deconvolution produces virtually the same receiver function

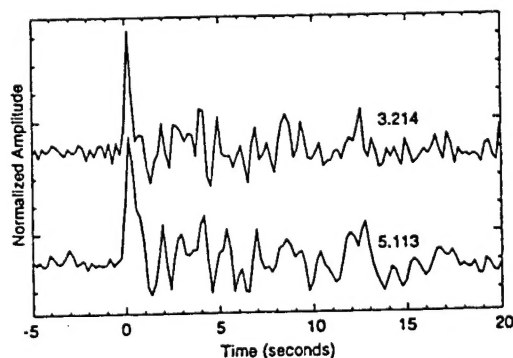


Figure 5. (Top) receiver function produced by simultaneous time-domain deconvolution of 25 events recorded at PFO. (Bottom) receiver function was computed by stacking 25 receiver functions computed individually from the same recordings by spectral division. Each of these traces was normalized by their peak amplitude.

for five seismograms as for all 25. In the lowermost receiver function of Fig. 4, we resolve only the largest peaks observed on the 'true radial receiver function', whereas in the case of the two middle receiver functions we resolve most of the features observed in Fig. 3. This indicates that much of the improved resolution is the result of windowing the vertical component more carefully to include only the *P*-wave source. The stacked receiver functions (Fig. 4) produced using both five and 25 of the synthetics exhibit noticeable side lobes leading into all the peaks (most noticeable on the small peaks between 8 and 12 s) whereas the peaks on the receiver functions produced by simultaneous deconvolution (Fig. 3) are generally sharper and, with the exception of the main peak at 0 s, have no side lobes. The small peak immediately behind the first arrival is much sharper on the time-domain receiver functions than on those of Fig. 4. The time-domain receiver functions computed using five and 25 synthetic seismograms (Fig. 3) have about 6 per cent lower rms misfits than those of the respective stacked frequency-domain receiver function (Fig. 4).

Figure 5 depicts a receiver function computed by the simultaneous time-domain deconvolution of 215 events recorded at PFO (top) and the stack of 25 receiver functions computed individually by spectral division (bottom). There were more than 25 seismograms available for this backazimuth and ray parameter, but we selected a subset of 25 usable seismograms. This selection was performed by computing the individual frequency-domain receiver functions and stacking those which had clear first arrivals (bottom, Fig. 5). Only those receiver functions used in the stacked receiver function were included in the simultaneous deconvolution (top, Fig. 5). The receiver function computed by simultaneous deconvolution appears to have broader frequency content but the stacked receiver function has larger amplitudes (relative to the main phase at time = 0) on almost all peaks.

Negative troughs in receiver functions are usually the result of a *Ppss* reverberation (or other higher order

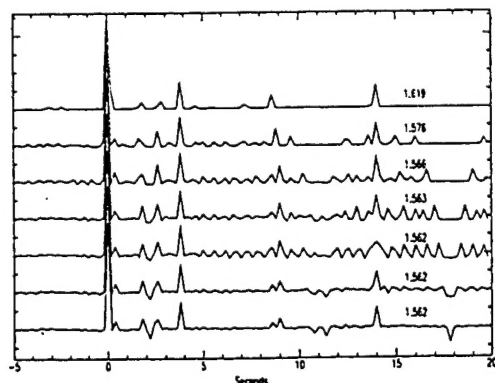


Figure 6. Receiver functions computed by simultaneous lower-bounded deconvolution of the 25 synthetic seismograms used in computing Figs 3 and 4. The top receiver function has a lower bound of zero. The lower-bound constraint decreases from top to bottom. The bottom receiver function has no lower-bound constraint. Numbers above the traces are the rms misfits.

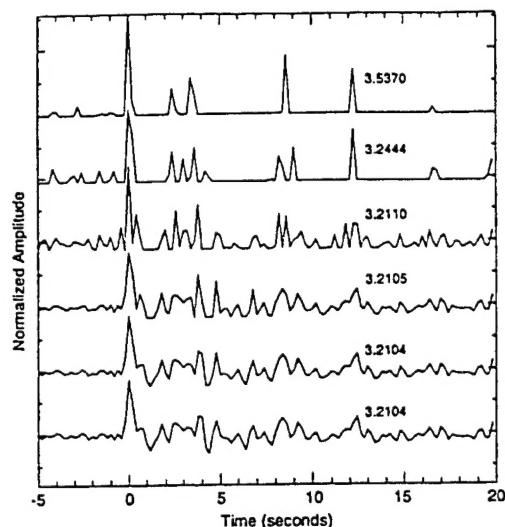


Figure 7. Receiver functions computed by simultaneous lower-bounded deconvolution of the same 25 seismograms as used in computing Fig. 5. The top receiver function has a lower bound of zero. The lower-bound constraint decreases from top to bottom. The bottom receiver function has no lower-bound constraint. Numbers above the traces are the rms misfits.

reverberations) or of a *P*-to-*S* conversion (*Ps*) from a velocity inversion.

To demonstrate an advantage of the time-domain formulation of the simultaneous deconvolution, we employ a lower-bounded least-squares algorithm (Lawson & Hanson 1974) to solve the inverse problem (eq. 9) and thereby test the possibility that the negative troughs are an artefact of the inherent non-uniqueness of the deconvolution problem. Fig. 6 shows receiver functions computed by lower-bounded least squares (of the same 25 synthetic seismograms as used in the previous examples) with more constraining lower bounds from bottom to top. We observe that as negative troughs are truncated by the lower bound, spurious positive peaks are added to the receiver function. This occurs before any significant variation in rms misfit is observed. Similar behaviour is observed in the receiver functions calculated from the 25 real seismograms (used in Fig. 5) computed using increasing lower bounds from bottom to top (Fig. 7). The similarity in growth of spurious peaks as a result of the truncation of troughs in both observed and synthetic receiver functions as a response to impinging lower bounds suggests that the negative troughs at 1.2 and 4.3 s in the observed receiver functions are in fact required to produce a reasonable receiver function.

CONCLUSION

Our goals in applying the simultaneous time-domain deconvolution were to: (1) reduce the side lobes about the main peak of the receiver functions; (2) to eliminate the human intervention needed in selecting a water level in the frequency-domain deconvolution. As with any study, human

intervention is still necessary to inspect the data and prepare it prior to deconvolution.

Further, a substantial advantage of time-domain deconvolution is the flexibility it allows in applying different model norms. In the examples given above, we minimized a linear combination of misfit and model size. The example using a lower bound constraint on the resulting receiver function demonstrates the flexibility of the time-domain deconvolution to determine the validity of troughs in the receiver functions. Sipkin & Lerner-Lam (1992) describe alternate roughening and smoothing norms that may also be appropriate depending on the problem. Finally, simultaneous deconvolution improves resolution of closely spaced phases.

ACKNOWLEDGMENTS

We thank Catherine DeGroot-Hedlin, Bob Parker and Steve Constable for providing inversion subroutines used in this research. We also thank Michael Hedlin for discussions related to this research. This research was supported by the Advanced Research Project Agency and monitored by the Air Force Phillips Laboratory under contract No. F29601-91-K-DB13, and by the Institute of Geophysics and Planetary Physics, Lawrence Livermore Laboratory under grant No. 92-47.

REFERENCES

- Ammon, C.J., 1991. The isolation of receiver effects from teleseismic *P*-waveforms, *Bull. seism. Soc. Am.*, **81**, 2504-2510.
- Baker, G.E., Gurrrola, H., Minster, J.B. & Zandt, G., 1995. Crustal Structure and Moho topography beneath Piñon Flat Observatory, *Tectonics*, submitted.
- Constable, S.C., Parker, R.L. & Constable, C.G., 1987. Occam's inversion: A practical algorithm for generating smooth models from electromagnetic sounding data. *Phil. Trans. R. Soc. Lond. Ser. A*, **266**, 123-192.
- Efron, B. & Tibshirani, R., 1986. Bootstrap methods for standard errors, confidence intervals, and other measures of statistical accuracy, *Stat. Sci.*, **1**, 54-77.
- Langston, C.A., 1979. Structure under Mount Rainier, Washington, inferred from teleseismic body waves, *J. geophys. Res.*, **84**, 4749-4762.
- Langston, C.A., 1981. Evidence for the subducting lithosphere under southern Vancouver Island and western Oregon from teleseismic *P* wave conversions, *J. geophys. Res.*, **86**, 3857-3866.
- Langston, C.A., 1989. Scattering of teleseismic body waves under Pasadena, California, *J. geophys. Res.*, **94**, 1935-1951.
- Lawson, C.L. & Hanson, D.J., 1974. *Solving Least Squares Problems*, Prentice Hall, Englewood Cliffs, NJ.
- Oldenburg, D.W., 1961. A comprehensive solution to the linear deconvolution problem, *Geophys. J. R. astr. Soc.*, **65**, 331-357.
- Owens, T.J., Crosson, R.S. & Hendrickson, M.A., 1988. Constraints on the subduction geometry beneath western Washington from broadband teleseismic waveform modeling, *Bull. seism. Soc. Am.*, **78**, 1319-1334.
- Owens, T.J. & Crosson, R.S., 1988. Shallow structure effects on broadband teleseismic *P* waveforms, *Bull. seism. Soc. Am.*, **78**, 96-108.
- Owens, T.J., Taylor, S.R. & Zandt, G., 1987. Crustal structure at regional seismic test network stations determined from inversion of broadband teleseismic *P* waveforms, *Bull. seism. Soc. Am.*, **77**, 631-662.
- Owens, T.J., Zandt, G. & Taylor, S.R., 1984. Seismic evidence for an ancient rift beneath the Cumberland plateau, Tennessee: a detailed analysis of broadband teleseismic *P* waveforms, *J. geophys. Res.*, **89**, 7783-7795.
- Owens, T.J., Taylor, S.R. & Zandt, G., 1983. Isolation and enhancement of the response of local seismic structure from teleseismic *P*-waveforms, *Internal report*, Lawrence Livermore Laboratory.
- Sipkin, A.A. & Lerner-Lam, A.L., 1992. Pulse-shape distortion introduced by broadband deconvolution, *Bull. seism. Soc. Am.*, **82**, 238-258.

This appendix, in full, is a reprint of the material as it appears in *Geophysical Journal International*, Volume 120, pp. 537-543, 1996, Gurrola, Harold, G. Eli Baker, and J. Bernard Minster. The dissertation author was the secondary investigator and second author of this paper.